Technische Universität München
TUM School of Natural Sciences

Dielectrics at Liquid-Liquid Interfaces

Karl David Egger

Vollständiger Abdruck der von der TUM School of Natural Sciences der Technischen Universität München zur Erlangung eines

Doktors der Naturwissenschaften (Dr. rer. nat.)

genehmigten Dissertation.

Vorsitz: Prof. Dr. Christopher Stein

Prüfer*innen der Dissertation:

1 Prof. Dr. Karsten Reuter
2 Prof. Dr. Martin Zacharias

Die Dissertation wurde am 27.09.2022 bei der Technischen Universität München eingereicht und durch die TUM School of Natural Sciences am 12.12.2022 angenommen.

Technische Universität München
TUM School of Natural Sciences
Lehrstuhl für theoretische Chemie

Dielectrics at Liquid-Liquid Interfaces

David Egger

PHD Thesis

Fachgebiet: Computational Chemistry
Themensteller: Prof. Dr. Karsten Reuter, Dr. Christoph Scheurer

2022

Abstract

For many years liquid-liquid interfaces (LLIs) - particularly between an aqueous and an organic solvent - have been identified as environments for important processes in biology and catalysis. Despite considerable advances in both computing power and modeling techniques in recent years, explicit quantum mechanical simulations of such solvated systems on the required length- and time-scales remain oftentimes out of reach. Coarse-graining the liquid environment of these systems into a continuum with less degrees of freedom whilst preserving its physical properties is therefore a necessity. In liquids consisting of neutral yet highly polar molecules like water, the dielectric response represented by the dielectric permittivity tensor represents a crucial modeling ingredient in every such coarse-graining approach.

In this work the dielectric behaviour at the LLI between water and 1,2-dichloro-ethane is investigated in immediate vicinity of the phase transition. Common polarization fluctuation approaches are adapted by discretizing the dielectric problem into a kernel convolution with the dipole-dipole interaction tensor on a regular grid. The presented method allows the black box calculation of the full local dielectric permittivity tensor for arbitrary system geometries and gives a quantitative explanation under which circumstances the plate capacitor picture is a valid approximation. It is found that an anisotropic treatment is imperative if a slab model shows lateral structure, a finding that besides LLIs might be of interest in many solid-liquid interfaces for example in electro-catalysis. Further investigations of molecular orientation towards the LLI as well as comparing electric fields and the dipole moment in molecular coordinate systems gives insight where the molecular liquids deviate from ideal Maxwellian dielectrics. It furthermore suggests a path towards improving the accuracy of implicit solvent approaches by delta-learning these deviations.

Contents

Chapter 1

Introduction

For many years the relevance of liquid-liquid interfaces (LLIs) - particularly between an aqueous and an organic solvent - has been recognized in fundamental scientific questions and technological applications. In catalysis and microbiology, many processes require a thorough understanding of water interfacing larger individual molecules as well as other liquids or soft matter. In biology, solvation of complex organic molecules like amino acids in aqueous environments greatly impacts their form and function, often mediated by the presence of ions. Here, the interplay of solvent and solute is key to understanding the functionality of biological membranes, proteins as well as a myriad of other processes that form the foundation of carbon based life on the planet [1–11].

LLIs are equally prominent in catalytic processes like photo-catalytic water splitting for hydrogen production in a post-fossil energy economy [12, 13]. Recent progress in the field of liquid-liquid electrochemistry has sparked interest in single-entity catalysis at the interface between two immiscible electrolyte solutions (ITIES). Typically forming an interface between $\mathrm{H_2O}$ and a polar organic solvent like 1,2-dicholorethane (DCE), ITIES are promising environments for catalysis of the oxygen reduction and hydrogen evolution reactions (ORR and HER) [14]. *In situ* deposited nanoparticles of paladium and platinum were successfully used as HER catalysts at ITIES [15], but also experiments with cheaper and more abundant transition-metal nanoparticles show promising results [16]. Since spontaneous adsorption of various nanoparticles at ITIES can be manipulated through external potential control [14, 17, 18] or variation of the aqueous phase pH [14, 19], these environments could potentially be very interesting for large scale industrial applications.

Even though only providing a background environment - the individual solvent molecule is of little interest after all - large volumes of liquid on both sides of the interface need to be accounted for in the analysis of the aforementioned systems. Treating this environment explicitly, greatly increases complexity and computational cost in atomistic computer models which limits the possible length- and time-scales of simulation. It is therefore desirable to coarse-grain structure and dynamical response of explicit liquids into a simplified continuum representation which greatly reduces its number of degrees of freedom. The embedded atomistic protein or catalytic complex of interest can then be coupled to the surrounding coarse-grained continuum liquid, typically via a mean-field response parametrized by a susceptibility function [20, 21]. Particularly for liquids consisting of

neutral yet highly polar molecules like water or DCE, the dielectric response represented by the dielectric susceptibility χ is an indispensable model ingredient in any coarse-graining approach. Historically defined in the context of Maxwell theory in matter, χ defines the relation between the polarization and the Maxwell field, which is a superposition of the fields created by external or "free" charge able to move independently and the smoothed out internal charges making up the dielectric [22]. It is a long-standing experimental fact that χ of bulk liquids constitutes an intrinsic material property that is independent of the shape of the dielectric [23]. However, while the Maxwell field constitutes a useful theoretical quantity, it is not directly accessible experimentally, especially in the sub-nanometer range towards interfaces. In molecular liquids, the interplay between short-range repulsive forces that establish local order and long-range attractive forces forming cohesion and stability is a long-standing concept [24]. Particularly for liquids with high molecular polarity, this can lead to the formation of strong inter-molecular bonding networks, like the hydrogen bonding network in water [25, 26]. Confinement or the introduction of interfaces breaks the bulk symmetry of these networks. In the immediate vicinity of such an interface this results in a generally non-linear, non-local and anisotropic change of several thermodynamic properties including density, viscosity, and dielectric response [27–34]. This change in dielectric behaviour enters the interpretation of phenomena like interfacial ion distribution [35, 36] or solvation free energy [35, 37–39].

Traditional experimental methods to measure ε of interfacial water relied on broadband dielectric spectroscopy of naturally occuring systems like nanoporous crystals [40] or zeolite powders [41] and were not able to experimentally resolve deviations from bulk behaviour with sub-nanometer precision. However, due to recent advances in scanning probe microscopy [42–44] Fumagalli *et al.* [29] were able to measure ε for H_2O in immediate vicinity of two-dimensional boron nitride films. They reported a dielectric dead layer of $\varepsilon \approx 2$ and a huge 100 nm wide transitional region in which ε retracted to its bulk value of $\varepsilon = 81$. This was rationalized later by Deissenbeck *et al.* [45] using an equivalent circuit picture of a series of plate capacitors. Since the capacitance of a plate capacitor is proportional to ε and capacitances are inversely summed in a serial circuit, the dead layer ε would dominate far into the bulk. In such a circuit model, a local ε can be calculated individually for every plate capacitor. A variety of successful approaches to calculate these plate capacitor ε based on polarization fluctuations have been developed in cartesian, cylindrical or spherical coordinates [46–49] as well as periodic slab systems [50] in the framework of linear response theory [24]. Since these polarization fluctuations have proven notoriously slow to converge, especially in polar liquids [39, 51–74] alternative approaches to calculate ε focus on measuring capacitance at constant potential [45], replace polarization with potential fluctuations [39, 75–78] or perform simulations at constant displacement field [53, 79–81]. Additionally, there exist multiple non-local approaches to calculate an interfacial dielectric constant in the liquid phase [82–84]. While all these approaches vary regarding their treatment of the molecular ensemble, all assume a separation of the dielectric response parallel and perpendicular to the interface, effectively using the substitution picture of two decoupled sets of in-series plate capacitors. The off-diagonal elements of the full 3x3 dielectric tensor $\boldsymbol{\varepsilon}$, often referred to as cross-terms, are set to zero. A comprehensive and general formalism how to coarse-grain molecular granularity below the nanoscale into a truly anisotropic continuum

dielectric tensor beyond this approximation has not been developed to the best of knowledge. For this reason, this work explores alternative approaches towards this goal.

In chapter 2 and 3 dielectric theory, the LLI concept as well as technical and simulation details are introduced and benchmarks are calculated for later comparison. Chapter 4 adapts common polarization fluctuation approaches by discretizing the dielectric problem into a kernel convolution with the dipole-dipole interaction tensor on a regular grid. While the issue of slow convergence remains, the presented method allows the black box calculation of the full local dielectric tensor for arbitrary geometries and gives a quantitative explanation under which circumstances the plate capacitor picture is a valid approximation. It is found that an anisotropic treatment is imperative if a slab model shows lateral structure, a finding that besides LLIs might be of interest in many solid-liquid interfaces for example in electro-catalysis. Chapter 5 explores the interfacial orientation of molecules towards the LLI. In chapter 6 the molecular coordinate system is employed to explore the relationship between intra- and extra-molecular charges in a one molecule reference system without the detour via a dielectric constant. While no direct path towards a cheaper calculation of the ε tensor was discovered, the findings of chapters 5 and 6 could be used to improve the accuracy of implicit solvent approaches by delta-learning in the future. Finally, chapter 7 explores the possibilities of reaction field models to calculate local dielectric constants and its chances as well as its limitations are discussed.

Chapter 2

Theoretical Background

The theoretical background and methodology relevant in this work is presented in this chapter. After a brief primer on units and notation, Molecular Dynamics simulation are introduced as the means to create the atomistic trajectories for coarse-graining in this work. The dielectric constant ε and dielectric susceptibility χ are then introduced in their traditional context of classical Maxwell electrostatics and subsequently in the linear response framework of statistical mechanics. Finally, a selection of common methods to calculate the dielectric constant in various geometries are presented and derived.

2.1 Units and notation

Regarding units and notation the following conventions are employed in this text. Throughout this work the Gaussian *cgs* unit system is employed which implies $4\pi\varepsilon_0 = 1$. Vectors and tensors are indicated by using bold letters. For the sake of clarity, Einstein summation is employed in formulas involving tensors, specifically the permittivity and dipole-dipole interaction tensor. Vector indices in Einstein summation are always indicated with a subscript and exclusively start at i ascending. The indices marking a quantity for two different instances of a molecule or atom start at a ascending. If both these i and a indices are present, the latter is written as a superscript. The partial derivative of a function $f(x)$ is written as

$$\frac{\partial f(x)}{\partial x} = \partial_x f(x) \tag{2.1}$$

The three dimensional divergence, rotation and gradient operators are expressed using the ∇-operator

$$\nabla = \begin{pmatrix} \partial_x \\ \partial_y \\ \partial_z \end{pmatrix} \tag{2.2}$$

If ∇ is treated like a three dimensional vector, divergence and rotation of a vector $\mathbf{A}$ can then be written via the scalar- and cross product, $\nabla \cdot \mathbf{A}$, $\nabla \times \mathbf{A}$, while the gradient of a scalar field ϕ is obtained from the multiplication $\nabla\phi$. The convolution between two functions f and g is written as $f * g$.

2.2 Molecular Dynamics

The trajectories for the dielectric analysis performed in this work were obtained via classical Molecular Dynamics (MD). Classical MD is a computational method for numerically solving Newton's equations of motion for a system of interacting particles or atoms, in the present case molecular liquids. Interaction potentials between particles are evaluated employing force fields, which define the interatomic energy as a function of particle positions, while the forces on each particle can be derived as the gradient of this energy function with respect to the spatial coordinates [85]. Costly evaluations of electronic or quantum mechanical interactions are parametrized into the atomic force field expression, greatly driving down computational cost. Naturally, accuracy and predictability of a force field model heavily depend on its parametrization, which is typically performed against experimental data or more accurate quantum chemical calculations. Transfer of a force field to different models as well as combinations of different force fields in simulations has to be performed with caution and needs to be carefully evaluated.

2.2.1 Force fields

In literature, the spectrum of different force fields is as wide as the the spectrum of systems to simulate. In recent years the rise of machine learning in computational chemistry has greatly contributed to the popularity of novel non-analytic neural-network-based frameworks over classical analytic force fields in biological and soft matter systems [86–88]. Still, these classical force fields have proven their capability to provide insights for aqueuous and organic liquids [89–91], soft matter [92] and complex biological [93–95] systems at atomistic resolution for comparatively low computational

cost. The inter-atomic energy term in many classical force fields typically distinguishes between covalent and non-covalent interaction terms.

$$U^{\mathrm{tot}} = U^{\mathrm{c}} + U^{\mathrm{nc}} \tag{2.3}$$

Non-covalent interactions aggregate all interaction terms between atoms that are not covalently bonded and correspond to inter-molecular interactions in molecular liquids, namely the electrostatic and van-der-Waals interaction as well as the short-range Pauli repulsion [96]. The electrostatic interaction is described by the pair-wise Coulomb potential between permanent charges introduced later in equation (2.21) of section 2.3. While its parametric form is well known, provided atomic charges are adequately fitted, its inverse proportionality to distance r prohibits the introduction of a cutoff without introducing large numerical errors. Typical methods to account for the long-range tail of the Coulomb interaction are presented in section 2.5.

The strong short-range Pauli repulsion is a quantum-mechanical phenomenon arising from overlap of the atomic outer electron shells and is mainly responsible for the short-range structure that is characteristic for the liquid state [24]. For relatively small r, this interaction can be approximated by an exponential function or an inverse power law, typically with powers between 9 and 15 [24].

At larger separations, the dominant contribution to the potential stems from the multi-polar dispersion interactions between the instantaneous electric moments on one atom, created by spontaneous fluctuations in the electronic charge distribution, and moments induced in the other [24]. This is typically referred to as the van-der-Waals interaction. All terms in this multipole series are attractive, where the leading dipole-dipole term, typically referred to as the London dispersion interaction [97], varies as r^{-6}.

Combining van-der-Waals and Pauli repulsion $\propto r^{-12}$ produces the popular 12-6 Lennard-Jones potential [98]

$$u^{\mathrm{LJ}}(r) = 4\varepsilon \left[\left(\frac{\sigma}{r}\right)^{12} - \left(\frac{\sigma}{r}\right)^{6} \right] \tag{2.4}$$

which involves two parameter: The collision diameter σ representing the distance $u^{\mathrm{LJ}}(\sigma) = 0$ where the interaction between two particles is zero and the depth ε of the potential minimum of u^{LJ}. Originally proposed to describe the cohesive energy of crystals of noble gases, its use in MD simulations of liquid argon proved to have unexpectedly good experimental agreement [99]. The use of pair potentials like (2.4) in calculations for the liquid state involves the neglect of many-body forces, which is hard to argue for and in the case of [99] was due to a fortitous cancellation of errors as argued in [100]. This is no generally valid assumption, particularly for more complex molecular liquids, but irrespective of the detailed assumptions made, the main features of the potential are always the same: a soft repulsion, a deep attractive well and a long-range oscillatory or asymptotic

tail [24] - properties that (2.4) possesses. Even though there is no evidence that a 12-6 Lennard-Jones performs better than other possible choices [101] it is widely used, including for the force fields employed in this work. Together with the pair-wise Coulomb interaction, the total non-covalent energy of a N-particle simulation can be written as

$$U^{\mathrm{nc}} = \sum_{a}^{N} \sum_{b<a}^{N} \left\{ 4\varepsilon_{ab} \left[\left(\frac{\sigma_{ab}}{r_{ab}} \right)^{12} - \left(\frac{\sigma_{ab}}{r_{ab}} \right)^{6} \right] + \frac{q_a q_b}{r_{ab}} \right\} \tag{2.5}$$

The covalent interaction potential accounts for covalent bonds between atoms with a specific hybridization state and its dependence on the relative arrangement of the involved atoms, regularly expanded in low order many-body terms such as bond lengths, angles, dihedrals, and out-of-plane deformations. In many pair-wise force-field models like the ones used for trajectory generation in this work, the functional form of U_c in (2.3) can be further grouped as

$$U^{\mathrm{c}} = U^{1-2} + U^{1-3} + U^{1-4} + \dots \tag{2.6}$$

In (2.6), the superscripts denote the interaction over one, two, three or four covalent bonds respectively. These interaction terms correspond to bonded (spanning two atoms or one covalent bond), angular (spanning three atoms or two covalent bonds) and dihedral (spanning four atoms or three covalent bonds) interactions. In principle higher terms can be added, but for the force fields considered in this work, the highest order covalent term for H_2O is the angular term U^{1-3} and in DCE the dihedral term U^{1-4}. Due to the relative rigidity of covalent bonds, covalently bonded atoms are not expected to deviate significantly from their reference distance. Many traditional force fields like TIP4P [102] thus employ rigid U_c potential terms, or use Hooke's law style harmonic expressions for bonded interactions like for example the widely used OPLS force field for hydrocarbons [89]. In the case of water it has been shown [103] that bond flexibility improves the agreement of the dielectric constant with experiment compared to rigid bond potentials.

2.2.2 Time propagation

In order to propagate particle ensembles forward in time, Newton's equations of motion need to be integrated from the particle positions and forces determined by the employed force field. While many integration algorithms exist, the Velocity-Verlet algorithm is often chosen for its speed, low memory requirements, good short-term energy conservation, little long-term energy drift, time-reversibility, and conservation of phase-space volume [85].

In Verlet-like integration schemes, the position of a particle at a point in time $r(t)$ that is subject to a force $f(t)$ can be approximated via the two symmetric Taylor series

$$\begin{aligned} r(t+\Delta t) &= r(t) + v(t)\Delta t + \frac{f(t)}{2m}\Delta t^2 + \frac{\Delta t^3}{3!}\partial_t^3 r + \mathcal{O}(\Delta t^4) \\ r(t-\Delta t) &= r(t) - v(t)\Delta t + \frac{f(t)}{2m}\Delta t^2 - \frac{\Delta t^3}{3!}\partial_t^3 r + \mathcal{O}(\Delta t^4) \end{aligned} \tag{2.7}$$

Here, m represents a particle's mass, $v(t)$ its velocity at time t, and $\mathcal{O}(\Delta t^4)$ all expansion terms of fourth order or higher. If the first and second equation of (2.7) are added, all terms involving uneven powers of Δt cancel out

$$r(t+\Delta t) + r(t-\Delta t) = 2r(t) + \frac{f(t)}{m}\Delta t^2 + \mathcal{O}(\Delta t^4) \tag{2.8}$$

which can be rearranged to

$$r(t+\Delta t) \approx 2r(t) - r(t-\Delta t) + \frac{f(t)}{m}\Delta t^2 \tag{2.9}$$

The Verlet algorithm in (2.9) thus provides an appoximation of the new position of a particle at time $r(t+\Delta t)$ from forces and positions at the earlier timesteps $t-\Delta t$ and t with an error of order Δt^4. Equation (2.9) does not include an explicit velocity calculation, since its terms cancel out in summing both series in (2.7). While $v(t)$ can in principle be evaluated by calculating the numerical derivative $\partial_t r$ in an extra step, this leads to comparatively high numerical errors for v on the order of Δt^2. Alternatively, the calculation of v can explicitly be included in (2.9)

$$\begin{aligned} r(t+\Delta t) &= r(t) + v(t)\Delta t + \frac{f(t)}{2m}\Delta t^2 \\ v(t+\Delta t) &= v(t) + \frac{f(t+\Delta t) - f(t)}{2m}\Delta t \end{aligned} \tag{2.10}$$

This is the velocity Verlet integration method, which through including the velocity calculation directly into the integration scheme by leap-frogging v and x calculations in time, is equivalent in accuracy to (2.9) without introducing an extra velocity calculation [85]. A half-stepped version of (2.10) is implemented in the LAMMPS simulation package [104], which is exclusively used for trajectory creation in this work.

Alternative integrators include higher order algorithms like the predictor-corrector method [85], where the Taylor series in (2.7) is truncated at higher orders. These provide superior short term energy conservation and thus allow for larger timesteps. However, the additional derivative evalu-

ations also drive computational cost up and the integration schemes often are not time-reversible and phase-space conserving [85], making them less robust for long-term sampling.

2.2.3 Open systems

The integration of Newton's equations of motion as presented above corresponds to the micro-canonical (NVE) ensemble where particle number and system volume are kept constant over the course of the trajectory. Depending on the application however, other control variables are more favorable. The linear-response formalism presented in section 2.6 however assumes trajectories simulated in the canonical (NVT) ensemble and many experimental setups use temperature T or pressure P instead of total energy and volume as their control variables. Simulations in NVT or the isothermal-isobaric (NPT) ensemble are realized with the help of thermostats.

The idea behind a constant temperature simulation is to couple the simulation system to a thermostat which can be thought of as an infinitely large heat bath with a fixed temperature [105]. Simulation system and bath are coupled in a way that heat but no particles can be exchanged. This coupling can be realized by stochastic collisions between particles of bath and system or by incorporating the bath degrees of freedom deterministically into the system Hamiltonian. The former approach can be implemented by a random collision model mimicking the influence of the heat bath - this is done by the Langevin thermostat [106] - or even by implicitly including its Brownian motion via an extension to the equations of motion as done in an Andersen thermostat [106]. Thermostatting by deterministically incorporating the bath degrees of freedom in the system Hamiltonian is achieved by adding a set of dynamic variables associated with the bath that are coupled to the simulation system's particle velocities. This is done in a Nose-Hoover thermostat [107, 108]. Langevin, Andersen, and Nose-Hoover type thermostats are all capable of simulating systems with canonical probability distribution and valid energy values, however time dependent parameters are reproduced more accurately with Nose-Hoover thermostats [105]. If the introduced dynamic variables of the Nose-Hoover thermostat are coupled to the simulation domain dimensions instead, it can be used for barostatting in constant pressure simulations.

The LAMMPS implementation [109] employs the equations of motion as formulated in [110], which combine the hydrostatic equations of Martyna *et al.* [111] with the strain energy proposed by Parinello and Rahman [112]. Its time integration schemes closely follow [113].

In cases where it is advantageous to regard the electric potential of a system as a thermodynamic control variable, potentiostats originally devised by Bonnet *et al.* [114] or the thermopotentiostat developed by Deißenbeck *et al.* [45] can be useful.

2.3 Maxwell electrostatics

For classical systems, the interaction of charge is described by Maxwell's theory of electromagnetism which can be derived from four basic equations defining the relation between electric and magnetic fields in vacuum. In differential form these equations read [22]

$$\nabla \cdot \mathbf{E} = 4\pi\rho \tag{2.11}$$

$$\nabla \cdot \mathbf{B} = 0 \tag{2.12}$$

$$\nabla \times \mathbf{E} = -\frac{1}{c}\frac{\partial \mathbf{B}}{\partial t} \tag{2.13}$$

$$\nabla \times \mathbf{B} = \frac{1}{c}\left(4\pi\mathbf{J} + \frac{\partial \mathbf{E}}{\partial t}\right) \tag{2.14}$$

where $\mathbf{E}$ and $\mathbf{B}$ represent the electric and magnetic fields in three dimensional space, ρ the charge distribution, $\mathbf{J}$ the current density and c the speed of light. In the absence of magnetic forces and if electric fields are assumed to be time-independent, Maxwell's four equations reduce by two to the electrostatic case governing the interaction between permanent charges and dipoles:

$$\nabla \cdot \mathbf{E} = 4\pi\rho \tag{2.15}$$

$$\nabla \times \mathbf{E} = 0 \tag{2.16}$$

Here $\mathbf{E}$ is a rotation-free - and hence a conservative - force field. It can be expressed by a scalar electrostatic potential ϕ

$$\mathbf{E} = -\nabla\phi \tag{2.17}$$

The electrostatic potential of a continuous charge distribution is given by

$$\phi(\mathbf{r}) = \int \frac{\rho(\mathbf{r}')}{|\mathbf{r} - \mathbf{r}'|} d\mathbf{r}' \tag{2.18}$$

where the integral spans all space. The electrostatic field is obtained by inserting (2.18) into (2.17)

$$\mathbf{E}(\mathbf{r}) = \int \rho(\mathbf{r}') \frac{\mathbf{r} - \mathbf{r}'}{|\mathbf{r} - \mathbf{r}'|^3} d\mathbf{r}' \tag{2.19}$$

Since above equation is linear with respect to charge, the charge distribution ρ and thus the integral can be split up arbitrarily without changing the resulting field observed at point $\mathbf{r}$. This principle of superposition is another consequence of $\mathbf{E}$ being a gradient field.

In the case of a set of point charges q_a at positions $\mathbf{r}_a$ the continuous charge distribution ρ can be written using Dirac's delta function:

$$\rho(\mathbf{r}) = \sum_a q_a \delta(\mathbf{r} - \mathbf{r}_a) \tag{2.20}$$

The integral in (2.18) then reduces to a sum and the electrostatic potential reads

$$\phi(\mathbf{r}) = \int \sum_a \frac{q_a \delta(\mathbf{r} - \mathbf{r}_a)}{|\mathbf{r} - \mathbf{r}'|} d\mathbf{r}' = \sum_a \frac{q_a}{|\mathbf{r} - \mathbf{r_a}|} \tag{2.21}$$

This sum of all point charges can also be interpreted as a multi-center, zero-order Taylor expansion of ρ. An equally valid but in many cases more convenient representation can be obtained by reducing the number of expansion centers while simultaneously increasing the Taylor expansion order. This means that instead of summing all charges individually, one could only sum over all molecules but include higher orders of the ρ expansion to obtain ϕ of a molecular liquid. This approach to patterned charge distributions introduced by Lorentz [115] and further developed by Rosenfeld, Mazur and de Groot [23, 116–118] can be used to translate from a microscopic description of individual charges in vacuum to a macroscopic continuum description of matter. The subsequent derivation follows the notation in [119].

Starting for example with a liquid of N molecules with M atoms each. Every of these atom carries a partial charge q^{nm} and is located at $\mathbf{r^{nm}}$ where $n \in N$, referring to the molecular index and $m \in M$, referring to the atomic index in the molecule. Then the total charge distribution is given by

$$\rho(\mathbf{r}) = \sum_n \sum_{m(n)} q^{nm} \delta(\mathbf{r} - \mathbf{r}^{nm}) \tag{2.22}$$

Here $m(n)$ runs over all partial charges inside molecule n. Inserting equation (2.22) into (2.19) and shifting the integration variable $\mathbf{r}'$ to $\mathbf{r}' + \mathbf{r}^{nm} - \mathbf{r}^n$ yields the expression

$$\mathbf{E}(\mathbf{r}) = \int \sum_n \sum_{m(n)} q^{nm} \delta(\mathbf{r}' - \mathbf{r}^{nm}) \frac{(\mathbf{r} - \mathbf{r}') - (\mathbf{r}^{nm} - \mathbf{r}^n)}{|(\mathbf{r} - \mathbf{r}') - (\mathbf{r}^{nm} - \mathbf{r}^n)|^3} d\mathbf{r}' \tag{2.23}$$

for the electric field. Here $\mathbf{r}^n$ represents the center of molecule n. The choice of this center is not unique but in a molecular liquid both the molecular center of mass or charge pose natural

candidates. Expanding above expression in a Taylor series in $\mathbf{r}'$ around the molecular centers $\mathbf{r}^n$ yields

$$\begin{aligned}\mathbf{E}(\mathbf{r}) &= \int \sum_n \sum_{m(n)} q^{nm}\delta(\mathbf{r}'-\mathbf{r}^n)\left[\frac{\mathbf{r}-\mathbf{r}'}{|\mathbf{r}-\mathbf{r}'|^3} + (\mathbf{r}^{nm}-\mathbf{r}^n)\cdot\nabla'\frac{\mathbf{r}-\mathbf{r}'}{|\mathbf{r}-\mathbf{r}'|^3}\right.\\ &= \left. +\frac{1}{2}(\mathbf{r}^{nm}-\mathbf{r}^n)(\mathbf{r}^{nm}-\mathbf{r}^n)^T : \nabla'\nabla'\frac{\mathbf{r}-\mathbf{r}'}{|\mathbf{r}-\mathbf{r}'|^3} + \ldots\right] d\mathbf{r}' \end{aligned} \tag{2.24}$$

Here ∇' represents the gradient with respect to $\mathbf{r}'$ and $\nabla'(\mathbf{r}-\mathbf{r}') = -\nabla(\mathbf{r}-\mathbf{r}')$. Also $(\mathbf{r}^{nm}-\mathbf{r}^n)(\mathbf{r}^{nm}-\mathbf{r}^n)^T$ defines an outer product. Through integration by parts of all gradient terms and requiring the electric field to approach zero at infinite distances from the charge positions, equation (2.24) can be rearranged to

$$\begin{aligned}\mathbf{E}(\mathbf{r}) &= \int \frac{\mathbf{r}-\mathbf{r}'}{|\mathbf{r}-\mathbf{r}'|^3}\left[\sum_n\sum_{m(n)} q^{nm}\delta(\mathbf{r}'-\mathbf{r}^n) + \nabla'\sum_n\sum_{m(n)} q^{nm}\delta(\mathbf{r}'-\mathbf{r}^n)(\mathbf{r}^{nm}-\mathbf{r}^n)\right.\\ &\quad \left. +\frac{1}{2}\nabla'\nabla' : \sum_n\sum_{m(n)} q^{nm}\delta(\mathbf{r}'-\mathbf{r}^n)(\mathbf{r}^{nm}-\mathbf{r}^n)(\mathbf{r}^{nm}-\mathbf{r}^n)^T + \ldots\right] d\mathbf{r}' \end{aligned} \tag{2.25}$$

The summands in equation (2.25) can be expressed in terms of the molecular multipole moments of order $l \in 1, 2, 3, ...$, which are defined in analogy to the mechanical moments as

$$\mathbf{p}^{ln} = \frac{1}{l!}\sum_{m(n)} q^{nm}(\mathbf{r}^{nm}-\mathbf{r}^n)^l \tag{2.26}$$

In this sense, p^{0n} is associated with the net charge, p^{1n} with the charge dipole, and p^{2n} with the charge quadrupole of molecule n. The product represented by the l-exponent has to be understood as an outer product in this notation, making the molecular multipoles $\mathbf{p}^{ln}$ tensors of rank l. The choice of origin for the lowest rank non-vanishing multipole moment, which in the case of neutral molecules is the dipole (l=1), is independent of the choice of origin, while all higher order multipoles are not [22]. Grouping all molecular multipoles $\mathbf{p}^{ln}$ by their order l introduces the macroscopic multipole densities

$$\mathbf{Q}^l(\mathbf{r}) = \sum_n \mathbf{p}^{ln}\delta(\mathbf{r}-\mathbf{r}^n) \tag{2.27}$$

The electric field $\mathbf{E}$ in equation (2.25) can then be expressed as

$$\mathbf{E}(\mathbf{r}) = \int \frac{\mathbf{r}-\mathbf{r}'}{|\mathbf{r}-\mathbf{r}'|^3}\left[\mathbf{Q}^0(\mathbf{r}') - \nabla'\cdot\mathbf{Q}^1(\mathbf{r}') + \nabla'\nabla' : \mathbf{Q}^2(\mathbf{r}') - \dots\right] d\mathbf{r}' \tag{2.28}$$

By substituting the analogy [22]

$$4\pi\delta(\mathbf{r}-\mathbf{r}') = \nabla\cdot\frac{\mathbf{r}-\mathbf{r}'}{|\mathbf{r}-\mathbf{r}'|^3} = -\nabla'\cdot\frac{\mathbf{r}-\mathbf{r}'}{|\mathbf{r}-\mathbf{r}'|^3} \tag{2.29}$$

in (2.28) for all but the $\mathbf{Q}^0$-term, all terms containing $\mathbf{Q}^l$ with $l > 0$ can be "pulled out" of the integral:

$$\mathbf{E}(\mathbf{r}) = \int \frac{\mathbf{r}-\mathbf{r}'}{|\mathbf{r}-\mathbf{r}'|^3}\mathbf{Q}^0(\mathbf{r}')d\mathbf{r}' - 4\pi\left[\nabla\cdot\mathbf{Q}^1(\mathbf{r}') + \nabla\nabla : \mathbf{Q}^2(\mathbf{r}') - \dots\right] \tag{2.30}$$

In (2.29) and (2.30), δ represents Dirac's delta function.

Returning to the example of the charge distribution of a molecular liquid that gets expanded around its molecular centers, the first term in (2.30) associated with the monopole term $\mathbf{Q}^0$ would correspond to the distribution of net molecular charge in the system of interest while the field due to all higher order terms are summarized as the total polarization response $\boldsymbol{\mathcal{P}}^{\mathbf{tot}}$:

$$\boldsymbol{\mathcal{P}}^{\mathbf{tot}} = \mathbf{Q}^1(\mathbf{r}') - \nabla'\cdot\mathbf{Q}^2(\mathbf{r}') + \dots \tag{2.31}$$

The field associated with the monopole term or the free charge distribution

$$\mathbf{D}(\mathbf{r}) = \int \frac{\mathbf{r}-\mathbf{r}'}{|\mathbf{r}-\mathbf{r}'|^3}\mathbf{Q}^0(\mathbf{r}')d\mathbf{r}' \tag{2.32}$$

is commonly referred to as the displacement vector $\mathbf{D}$ in classical electrostatics since if subject to constant $\mathbf{D}$, $\mathbf{Q}^0$ is constantly displaced. Because the functional form of (2.32) equals (2.23) for $\mathbf{E}$ in vacuum, the scalar $\mathbf{Q}^0$ is often also referred to as the "free" charge in a system. Since the higher moments summarized in $\boldsymbol{\mathcal{P}}^{\mathbf{tot}}$ do not carry net charge, they are not constantly displaced if subjected to a field. They are therefore referred to as the "bound" charge of the system [23].

Substituting (2.31) and (2.32) in equation (2.30) yields the constitutive relation of classical electrostatics

$$\mathbf{E} = \mathbf{D} - 4\pi\boldsymbol{\mathcal{P}}^{\mathbf{tot}} \tag{2.33}$$

Assuming the intramolecular length-scales $|\mathbf{r}^{nm} - \mathbf{r}^{n}|$ to be small compared to the distance of the multipole expansion centers from the point of observation $|\mathbf{r} - \mathbf{r}^{n}|$, a truncation of higher orders after the leading order - for a dielectric of neutral molecules, this is the dipole moment - can be sufficient. This truncation generally is not applicable for the polarization response arbitrarily close to real interfaces. At some point, the assumption of intramolecular length-scales being negligibly small breaks down and the atomistic granularity of a real medium starts to show. The terminology of "free" and "bound" charge thus loses its meaning.

It has been shown by sum-frequency vibrational spectroscopy studies for a variety of charged and uncharged water/lipid, water/air and water/quartz interfaces [120–122], as well as molecular dynamics simulations of water interfacing diamond [27, 46, 119], that quadrupole and octupole moments can have an influence on the orientational polarization response of interfacial water. For the sake of simplicity and while keeping this in mind, the total polarization is nevertheless assumed to be equal to the dipole density in the following, $\boldsymbol{\mathcal{P}}^{\mathbf{tot}} = \mathbf{P} = \mathbf{Q}^{1}$. Higher orders can be re-introduced when necessary. We furthermore focus on orientational polarization and neglect molecular polarizability.

Due to changes in position and orientation of the molecular constituents making up a macroscopic medium at finite temperatures, the electric field in matter $\mathbf{E} = \mathbf{E}^{\mathbf{m}}$ in (2.33) is strongly varying and anisotropic at the atomistic level. In order to smoothen out this field and move from a vacuum description of individual molecules to the picture of a homogeneous continuum, this microscopic field needs to be averaged out over a "physically small" volume Ω. This volume needs to be small compared to its distance to the point of observation but still large enough to contain a sufficient number of molecules [123]. The sum of the field due to external charge contributions $\mathbf{E}^{\mathbf{0}}$ as well as the smoothed out microscopic field $\langle \mathbf{E}^{\mathbf{m}} \rangle_{\Omega}$ due to atomistic charge contributions

$$\mathbf{E} = \mathbf{E}^{\mathbf{0}} + \langle \mathbf{E}^{\mathbf{m}} \rangle_{\Omega} \tag{2.34}$$

defines the Maxwell field $\mathbf{E}$. The exact shape and form of Ω remains an open question of debate [39] and finding the connection between $\mathbf{E}^{\mathbf{m}}$ and $\mathbf{E}$ is the objective of essentially all mean-field theories of dielectrics [23, 39].

Using the definitions for $\mathbf{P}$, $\mathbf{E}$ and $\mathbf{D}$, analogues to the vacuum electrostatic Maxwell equations (2.15) and (2.16) can be formulated:

$$\nabla \cdot \mathbf{D} = 4\pi Q^0 = 4\pi \rho^{\text{free}} \tag{2.35}$$
$$\nabla \times \mathbf{E} = 0 \tag{2.36}$$

From (2.35) and (2.36), the following boundary conditions at dielectric interfaces can be derived [22]:

$$\mathbf{E}_{\parallel,1} = \mathbf{E}_{\parallel,2} \tag{2.37}$$
$$\mathbf{D}_{\perp,1} = \mathbf{D}_{\perp,2} + 4\pi\sigma^{\text{free}} \tag{2.38}$$

with the subscript $\parallel$ and $\perp$ denoting the field components parallel and normal to the interface and σ^{free} the surface charge density at the interface. For interfaces lacking free charge carriers, this term is omitted. So while the components parallel to an interface are continuous for $\mathbf{E}$, just like in vacuum, the normal components are not. In matter, the normal components of $\mathbf{D}$ are continuous.

For a pure dielectric, i.e. in the absence of free charges,(2.35) states that $\mathbf{D}$ is a divergence-free, or transverse vector field. The Maxwell field $\mathbf{E}$ in (2.36) on the other hand is curl-free or longitudinal. These two fields can thus be seen as the transverse and longitudinal projections of the polarization vector field in the Helmholtz-decomposition (c.f. appendix B) of $\mathbf{P}$ [39, 52, 124]:

$$4\pi\mathbf{P} = \mathbf{D} - \mathbf{E} \tag{2.39}$$

It has been shown that the two polarization projections in (2.39) exhibit very different properties and statistics dependent on their corresponding dynamic structure factors [39, 125, 126]. The orthogonality of the longitudinal and transverse projections of $\mathbf{P}$ furthermore implies that only the longitudinal polarization can couple to an external electric field $\mathbf{E^0}$ since this is by definition a longitudinal field as equation (2.35) shows.

The electrostatic relations (2.35) and (2.36) were historically formulated by Maxwell and Kelvin starting from the macroscopic assumption of continuously homogeneous matter. By imagining virtual cavities in which test charges for measuring the electric field were inserted, the above electrostatic Maxwell equations can be derived from the vacuum Maxwell equations (2.15) and (2.16) and the constitutive relation (2.33) [22]. The reason that in many cases this continuum picture yields the same results as the multi-center multipole expansion ansatz of Lorentz above, which takes the granularity of the medium into account, relies on the fact that effects on molecular length-scales between 1 - 1000 Å oftentimes may be neglected on typical macroscopic distances of meters to millimeters. In this case the atomistic length-scales can be considered infinitesimally small, a volume of 1000 Å^3 may be regarded as a point and all operations of differential calculus are applicable

in good approximation [23]. For both approaches the difficulty lies in passing between a microscopic description in terms of individual particles to a macroscopic continuum.

2.4 Dielectric susceptibility and permittivity

In order to establish a relation between the polarization $\mathbf{P}$ and the Maxwell field $\mathbf{E}$ the dielectric susceptibility χ is introduced. In the most general sense, this relation can be written as the non-local after-effect function [24]

$$\mathbf{P}(\mathbf{r},t) = \int d\mathbf{r}' \int_{-\infty}^{t} \chi(\mathbf{r},\mathbf{r}',t,t')\mathbf{E}(\mathbf{r}',t')dt \tag{2.40}$$

If we limit ourselves to isotropic bulk materials, translational invariance is implied which means the above equation takes the form

$$\mathbf{P}(\mathbf{r}) = \int d\mathbf{r}' \int_{-\infty}^{t} \chi(\mathbf{r}-\mathbf{r}',t-t')\mathbf{E}(\mathbf{r}',t')dt \tag{2.41}$$

with the frequency ω, the k-space vector $\mathbf{k}$ and the Fourier transform definitions

$$\tilde{\mathbf{P}}(\mathbf{k},\omega) = \int \exp(i\mathbf{kr})d\mathbf{r} \int_{-\infty}^{\infty} \exp(i\omega t)\mathbf{P}(\mathbf{r},t)dt \tag{2.42}$$

$$\tilde{\mathbf{E}}(\mathbf{k},\omega) = \int \exp(i\mathbf{kr})d\mathbf{r} \int_{-\infty}^{\infty} \exp(i\omega t)\mathbf{E}(\mathbf{r},t)dt \tag{2.43}$$

$$\tilde{\chi}(\mathbf{k},\omega) = \int \exp(i\mathbf{kr})d\mathbf{r} \int_{0}^{\infty} \exp(i\omega t)\chi(\mathbf{r},t)dt \tag{2.44}$$

The reciprocal k-space vectors $\mathbf{k}$ are defined as linear combinations of integer multiples of the unit lattice vectors $\mathbf{e}_{\mathbf{k_i}} = 2\pi/L_i, i \in \{x,y,z\}$, where $\mathbf{L}$ represents the length of the simulation box. Inserting the Fourier transform expressions above, equation (2.41) transforms to

$$\tilde{\mathbf{P}}(\mathbf{k},\omega) = \tilde{\chi}(\mathbf{k},\omega) \cdot \tilde{\mathbf{E}}(\mathbf{k},\omega) \tag{2.45}$$

using the convolution theorem [127]. Here, $\tilde{\mathbf{E}}$ and $\tilde{\mathbf{P}}$ represent full transforms in time, while $\tilde{\chi}$ only represents a half-transform [124].

A similar Fourier space relation between the displacement field $\mathbf{D}$ and the Maxwell field $\mathbf{E}$ in form of the dielectric permittivity ε can also be introduced:

$$\tilde{\mathbf{D}}(\mathbf{k},\omega) = \tilde{\varepsilon}(\mathbf{k},\omega)\cdot\tilde{\mathbf{E}}(\mathbf{k},\omega) \tag{2.46}$$

Electrostatic permittivity and susceptibility are trivially linked by the relation

$$\tilde{\chi}(\mathbf{k},\omega) = \frac{1}{4\pi}(\tilde{\varepsilon}(\mathbf{k},\omega)-1) \tag{2.47}$$

For isotropic bulk liquids like water or DCE, it is considered an experimental fact that χ is an intensive material property, which means that measurements of χ for a given material are independent of sample size and shape [124]. This implies that their dependence on molecular orientations can only be short-ranged on macroscopic experimental length-scales [128]. However, χ denotes the response function to the internal and continuous Maxwell field $\mathbf{E}$, a quantity that as shown above, is not concisely defined microscopically if the separation into free and bound charge becomes ambiguous. Additionally, the Maxwell field is also not accessible experimentally. The measurable quantity is not the field itself, but rather the voltage defined as the line integral $V = \int \mathbf{E}\cdot d\mathbf{l}$ [39]. Traditionally the dielectric constant is measured by comparing the voltage drop in a capacitor with and without an inserted dielectric. Furthermore, as shown in appendix C, the application of linear response theory using the Maxwell field $\mathbf{E}$ is questionable because it technically does not qualify as an external field to the system. For these reasons, the dielectric response in (2.45) is more often formulated with respect to an external electric field $\mathbf{E^0}$ in terms of a quasi-susceptibility $\boldsymbol{\chi}^{\mathbf{0}}$

$$\tilde{P}_i(\mathbf{k},\omega) = \tilde{\chi}^0_{ij}(\mathbf{k},\omega)\cdot\tilde{E}^0_j(\mathbf{k},\omega) \tag{2.48}$$

The reason $\boldsymbol{\chi}^{\mathbf{0}}$ is represented as a tensor in (2.48) is to underscore the fact that the dielectric response to $\mathbf{E^0}$ is anisotropic, even for isotropic media with scalar χ. In order to obtain a relationship between χ and $\boldsymbol{\chi}^{\mathbf{0}}$, a relationship between $\mathbf{E}$ and $\mathbf{E^0}$ is needed. For moderate fields, this relation is given by [22, 23]

$$\tilde{E}_i(\mathbf{r},\omega) = \tilde{E}^0_i(\mathbf{r},\omega) + \tilde{T}^{\mathrm{dd}}_{ij}(\mathbf{k},\omega)\tilde{P}_j(\mathbf{k},\omega) \tag{2.49}$$

In the static limit of $\omega \to 0$, it can be shown [22, 128] that the propagator $\tilde{\mathbf{T}}^{\mathbf{dd}}$ is given by

$$\tilde{T}_{ij}^{\mathrm{dd}}(\mathbf{k},\omega) \approx \tilde{T}_{ij}^{\mathrm{dd}}(\mathbf{k}) = 4\pi k_i k_j \tag{2.50}$$

Here, $k_i k_j$ is to be understood as an outer product. It can be shown that the frequency dependence of $\tilde{\mathbf{T}}^{\mathbf{dd}}$ in above equation is neglectable if the retardation in time is constantly omitted [128, 129].

In real-space this takes the form

$$\begin{aligned} T_{ij}^{\mathrm{dd}}(\mathbf{r}) &= \nabla_i \nabla_j \frac{1}{r} \\ &= \begin{pmatrix} \frac{3x^2-r^2}{r^5} & \frac{3xy}{r^5} & \frac{3xz}{r^5} \\ \frac{3xy}{r^5} & \frac{3y^2-r^2}{r^5} & \frac{3yz}{r^5} \\ \frac{3xz}{r^5} & \frac{3yz}{r^5} & \frac{3z^2-r^2}{r^5} \end{pmatrix} \quad , \qquad r = \sqrt{x^2+y^2+z^2} \end{aligned} \tag{2.51}$$

The propagating 3x3 tensor $\mathbf{T}^{\mathbf{dd}}$ is also called the dipole-dipole interaction tensor because it defines the potential energy between two oriented dipoles $\boldsymbol{\mu}^{\boldsymbol{a}}$ and $\boldsymbol{\mu}^{\boldsymbol{b}}$

$$u^{ab} = \mu_i^a T_{ij}^{dd}(\mathbf{r}^{ab}) \mu_j^b \tag{2.52}$$

Contrary to the intrinsic material property χ, the quasi-susceptibility $\boldsymbol{\chi}^{\mathbf{0}}$ is neither local nor isotropic, even for an isotropic medium like liquid water. This follows from the intrinsity of χ and the generally non-isotropic and non-local relation between $\mathbf{E}$ and $\mathbf{E}^{\mathbf{0}}$ in equation (2.49).

Inserting equation (2.49) into (2.45), letting $\omega \to 0$ and making the locality assumption $\boldsymbol{\chi}^{\boldsymbol{l}}(\mathbf{r}) = \delta(\mathbf{r}-\mathbf{r}')\boldsymbol{\chi}^{\mathbf{0}}(\mathbf{r}')$ the response relation between $\mathbf{E}^{\mathbf{0}}$ and $\mathbf{P}$ in real space can be expressed as

$$P_i(\mathbf{r}) = \chi_{ij}^l(\mathbf{r}) E_j^0(\mathbf{r}) = \chi_{ij}^l(\mathbf{r}) \left[E_j^0(\mathbf{r}) + \int T_{jk}^{\mathrm{dd}}(\mathbf{r}-\mathbf{r}') P_k(\mathbf{r}') d\mathbf{r}' \right] \tag{2.53}$$

In gaussian units, both $\boldsymbol{\chi}^{\boldsymbol{l}}$ and the analogous to (2.46) derived property $\varepsilon^{\boldsymbol{l}}$ are unitless.

The dipole-dipole interaction tensor has a singularity at zero, which also introduces a singularity in the integral of (2.53). This singularity can be removed by splitting off the integration of a small sphere around the origin $|\mathbf{r}-\mathbf{r}'| < \rho$ and treating it separately:

$$\int T_{ij}^{\mathrm{dd}}(\mathbf{r}-\mathbf{r}') P_j(\mathbf{r}') d\mathbf{r}' = \int_{|\mathbf{r}-\mathbf{r}'|<\rho} T_{ij}^{\mathrm{dd}}(\mathbf{r}-\mathbf{r}') P_j(\mathbf{r}') d\mathbf{r}' + \int_{|\mathbf{r}-\mathbf{r}'|>\rho} T_{ij}^{\mathrm{dd}}(\mathbf{r}-\mathbf{r}') P_j(\mathbf{r}') d\mathbf{r}' \tag{2.54}$$

It can be shown [22, 23, 130] that for $\rho \to 0$

$$\lim_{\rho\to 0}\int_{|\mathbf{r}-\mathbf{r}'|<\rho} T_{ij}^{\mathrm{dd}}(\mathbf{r}-\mathbf{r}')P_j(\mathbf{r}')d\mathbf{r}' = -\delta_{ij}\frac{4\pi}{3}P_j(\mathbf{r}) \tag{2.55}$$

Above, all off-diagonal contributions vanish due to the lateral symmetry of $\mathbf{T}^{\mathbf{dd}}$. Inserted into equation (2.53) this gives for the relation between polarization and external field

$$P_i(\mathbf{r}) = \chi_{ij}^l(\mathbf{r})E_j^0(\mathbf{r}) = \chi_{ij}^l(\mathbf{r})\left[E_j^0(\mathbf{r}) + \lim_{\rho\to 0}\int_{|\mathbf{r}-\mathbf{r}'|>\rho} T_{jk}^{\mathrm{dd}}(\mathbf{r}-\mathbf{r}')P_k(\mathbf{r})d\mathbf{r}' - \frac{4\pi}{3}\delta_{jk}P_k(\mathbf{r})\right] \tag{2.56}$$

2.5 Long-range treatment of the the Coulomb interaction

In atomistic simulations of real systems the sheer number of charged particles imposes the need for efficient techniques to calculate the long-range Coulomb interaction. As a pairwise interaction between charged particles, the Coulomb interaction as defined by the potential (2.21) scales proportional with the square of the number of charged particles N in a simulation. Even with the rise in available computing power, this remains an issue as even simulations of small biological or catalytic systems can easily contain beyond $\mathcal{O}(10^5)$ interacting charged particles.

The seemingly most reasonable approach of truncating the interaction at a certain distance is only an option if the pairwise interaction potential decays faster than the inverse of the distance cubed. This can be demonstrated by separating pairwise interactions into short- and long-range contributions at a cutoff distance r_c. This cutoff radius is chosen such that below r_c, pairwise interactions are explicitly represented by a sum, while above the cutoff radius the remaining cumulative interactions are sufficiently approximated by a continuous integral. The potential energy U^{tot} of a particle in an infinite, three dimensional molecular liquid for $r > r_c$ can be expressed as [85]

$$U^{\mathrm{tot}} = \sum_{a<b} u^c(r_{ab}) + \frac{N\rho}{2}\int_{r_c}^{\infty} dr\, u(r)4\pi r^2 \tag{2.57}$$

with the number density ρ. The truncated short-range potential u_c is equal to u for $r < r_c$ and zero otherwise. Equation (2.57) shows that the tail integral of a potential $u(r)$ in three dimensions

$$U^{\mathrm{tail}} = \frac{N\rho}{2}\int_{r_c}^{\infty} dr u(r)4\pi r^2 \tag{2.58}$$

diverges unless the interaction potential $u(r)$ decays faster than r^{-3}. Comparing that to the r^{-1}-like decay of the Coulomb potential in equation (2.21), it becomes apparent that truncating the

Coulomb potential would lead to divergence of above integral and thus would introduce serious errors. A discussion of these artifacts can be found in [131]. In the following two sections, two techniques to handle long-range Coulomb interactions for polar liquids, the Ewald summation and reaction fields, are presented. Further methods include fast multipole methods [132–135] and particle-mesh-techniques [136–138].

2.5.1 Ewald summation

Originally formulated by Kornfeld [139], the Ewald summation treats the long-range interaction using a periodic lattice approach [57–59]. Infinite extension of the simulation box is achieved by repeating the primary simulation cell on an infinite periodic lattice. The Coulomb interaction can then be calculated by two rapidly converging sums in reciprocal and real space with a defined cutoff error [140, 141]. This has the advantage of reducing the $\mathcal{O}(N^2)$ scaling of an explicit pairwise Coulomb interaction calculation to $\mathcal{O}(N \log(N))$ [85].

For the derivation, assume a cuboid simulation cell with boxlength vector $\mathbf{L} = (L_x, L_y, L_z)$, volume $V^{\mathrm{box}} = L^3$ and periodic boundary conditions. The cell shall contain N charged particles while the total charge of the system is considered to be zero. The Coulomb potential experienced by one particle a due to all other N-1 particles in the primary cell as well as all $\mathrm{N_m}$ particles in the primary cell's periodically repeated images can then be written as

$$\phi^E(\mathbf{r}_a) = \sum_{b \neq a}^{N-1} \frac{q_b}{r} + \sum_{b}^{N} \sum_{\mathbf{m} \neq 0}^{\infty} \frac{q_b}{|\mathbf{r}_{ab} + \mathbf{mL}|} \tag{2.59}$$

The integer vector $\mathbf{m} = (m_x, m_y, m_z)$ serves as an index for each image cell on the 3D lattice. The sum over $\mathbf{m}$ runs over all permutations of this tuple and the condition $\mathbf{m} \neq 0$ expresses that the primary simulation cell with index $(0, 0, 0)$ is not included. It is already accounted for in the first sum of (2.59). The periodicity in $\mathbf{L}$ of the setup's infinite lattice suggests the definition of reciprocal lattice vectors $\mathbf{k} = 2\pi/\mathbf{L} \cdot \mathbf{m}$ for use in Fourier space.

The sum in above equation is poorly and only conditionally convergent when performed in real space alone. Instead, (2.59) can be rearranged and split into two faster converging sums with a controllable cutoff error, one in real space terminated at a distance r_c and one in Fourier space terminated at a distance k_c. Very briefly, this separation can be achieved by introducing Gaussian distributions of opposite charge around, and equal in magnitude to each point charge [85]. In this way no additional charge gets introduced into the system but the calculated electrostatic potential is smooth and rapidly decreasing with distance in both in real- and k-space. The nearest image convention used in the derivation requires $\mathbf{r_c} \leq \mathbf{L}/2$ to be met.

The width of these Gaussians, the Ewald screening parameter η, does not affect the calculated potential. It does however influence speed of convergence in both sums which is why an optimal choice of η is crucial with regard to computational efficiency when implementing the algorithm [85].

Expressions for the error sensitivity of the Ewald summation with respect to r_c, k_c and η have been formulated in [140] and [141].

The Ewald potential (2.59) can be written as [85]

$$\phi^E(\mathbf{r}_a) = \phi^{E1}(\mathbf{r}_a) + \phi^{E2}(\mathbf{r}_a) + \phi^{E3} \tag{2.60}$$

with the k-space contribution to the potential ϕ^{E1} solved in non-local Fourier space, the local contribution ϕ^{E2} solved in real-space and a self-interaction term ϕ^{E3} stemming from not counting the interaction of a particle with itself in the primary simulation cell. The k-space contribution is given by

$$\begin{aligned} \phi^{E1}(\mathbf{r}_a) &= \frac{4\pi}{V^{\text{box}}} \sum_{\mathbf{k}\neq 0} \sum_{b}^{N} \frac{q_b}{k^2} \exp\left(-\frac{k^2}{4\eta^2}\right) \exp(-\mathrm{i}\mathbf{kr}) \\ &= \frac{8\pi}{V^{\text{box}}} \sum_{\mathbf{k}>0} \sum_{b}^{N} \frac{q_b}{k^2} \exp\left(-\frac{k^2}{4\eta^2}\right) \cos(\mathbf{kr}) \qquad , \qquad k < k_c \end{aligned} \tag{2.61}$$

The real-space contribution by

$$\phi^{E2}(\mathbf{r}_a) = \sum_{b}^{N} \frac{q_b}{r_{ab}} \text{erfc}(\eta r_{ab}) \qquad , \qquad r < r_c \tag{2.62}$$

and the self-interaction contribution by

$$\phi^{E3} = \frac{2q_a\eta}{\sqrt{\pi}} \tag{2.63}$$

From ϕ^E the corresponding electrostatic field in Ewald geometry $\mathbf{E^E} = -\nabla\phi^E$ can be calculated. Its k-space contribution amounts to

$$\mathbf{E^{E1}}(\mathbf{r_a}) = \frac{8\pi}{V^{\text{box}}} \sum_{\mathbf{k}>0} \sum_{n}^{N} \frac{q_b}{k^2} \exp\left(-\frac{k^2}{4\eta^2}\right) \sin(\mathbf{kr})\hat{\mathbf{k}} \qquad , \qquad k < k_c \tag{2.64}$$

while its real-space share is given by

$$\mathbf{E^{E2}}(\mathbf{r_a}) = \sum_b^N \frac{q_b}{\sqrt{\pi}} \left(\frac{2\eta}{r^2} \exp\left(-\eta^2 r^2\right) + \frac{\sqrt{\pi}}{r^3} \mathrm{erfc}(\eta r) \right) \hat{\mathbf{r}} \qquad , \qquad r < r_c \tag{2.65}$$

The vectors $\hat{\mathbf{r}}$ and $\hat{\mathbf{k}}$ represent the unit vectors in $\mathbf{r}$ and $\mathbf{k}$ direction. Since ϕ^{E3} in (2.63) lacks spatial dependence and therefore its gradient is zero, the total Ewald field

$$\mathbf{E^E} = \mathbf{E^{E1}} + \mathbf{E^{E2}} \tag{2.66}$$

has no self-interaction contribution.

As shown in [142], the dipole-dipole interaction tensor in Ewald geometry is obtained by first calculating the Ewald Coulomb potential $\phi^{E,\mu}$ created by periodic arrays of boxes that contain dipoles instead of point charges. This is achieved by making the formal substitution $q_b \rightarrow \boldsymbol{\mu_b} \nabla$ in (2.60). An expression for the dipole-dipole interaction tensor $\mathbf{T^E}$ in Ewald geometry which is equivalent to $\mathbf{T^{dd}}$ in (2.51) can be obtained by comparing the potential energy of a dipole $\boldsymbol{\mu^a}$ subject to $\phi^{E,\mu}$

$$u^a = -\mu_i^a E_i^{E,\mu} = -\mu_i^a (-\partial_j \phi^{E,\mu}) = \sum_b \mu_i^a T_{ij}^E \mu_j^b \tag{2.67}$$

As its counterpart $\mathbf{T^{dd}}$, $\mathbf{T^E}$ is a symmetric 3x3 tensor.

Analog to the Ewald potential, $\mathbf{T^E}$ can be separated into the three separate contributions [48, 142]

$$T_{ij}^E = T_{ij}^{\mathrm{E1}} + T_{ij}^{\mathrm{E2}} + T_{ij}^{\mathrm{E3}} \tag{2.68}$$

Following the name convention introduced with (2.60), the k-space contribution is given by

$$T_{ij}^{\mathrm{E1}} = -\frac{8\pi}{V^{\mathrm{box}}} \sum_{\mathbf{k}>0} \exp\left(-\frac{k^2}{4\eta^2}\right) \cos\left(\mathbf{kr}\right) \frac{k_i k_j}{k^2} \qquad , \qquad k < k_c \tag{2.69}$$

where $k = |\mathbf{k}| = \sqrt{k_x^2 + k_y^2 + k_z^2}$ and $k_i k_j$ represents the outer product like in (2.50). The real-space contribution amounts to

$$T_{ij}^{\mathrm{E2}} = \left[\operatorname{erfc}(\eta r) + \frac{2}{\sqrt{\pi}}\left(\eta r + \frac{2}{3}\eta^3 r^3\right)\exp\left(-\eta^2 r^2\right)\right] T_{ij}^{\mathrm{dd}} = \rho(r) T_{ij}^{\mathrm{dd}} \quad , \quad r < r_c \tag{2.70}$$

with the general dipole-dipole interaction tensor $\mathbf{T^{dd}}$ of (2.51). The real-space Ewald contribution $\mathbf{T^{E2}}$ differs only in the radial factor $\rho(r)$ from $\mathbf{T^{dd}}$ for all its nine elements. Recalling $r = \sqrt{x^2+y^2+z^2}$, one can see that ρ is an even function in cartesian coordinates, thus preserving the odd symmetry of $\mathbf{T^{dd}}$ in $\mathbf{T^{E2}}$. Apart from symmetry, $\mathbf{T^{E2}}$ also inherits the singularity of $\mathbf{T^{dd}}$ at the origin.

To conclude, the Gaussian shielding term for compensation of the self-interaction only has an on-diagonal contribution and is given by

$$T_{ij}^{\mathrm{E3}} = T_{ii}^{\mathrm{E3}}\delta_{ij} = \frac{4\pi}{3}\left(\left(\frac{\eta}{\sqrt{\pi}}\right)^3 \exp\left(-\eta^2 r^2\right)\right) \quad , \quad r < r_c \tag{2.71}$$

Note, that contrary to the point-charge Ewald field $\mathbf{E^E}$ in (2.66), the Ewald dipole field and consequently $\mathbf{T^E}$, has a non-zero self-interaction contribution.

2.5.2 Reaction fields

Instead of a lattice summation over periodic images of the primary simulation cell, long-range electrostatics can also be treated using a cavity model. Only inside this cavity electrostatic interactions are modeled explicitly. The outside is coarse-grained into a continuum dielectric to which the inside charge distribution is coupled via an implicit mean-field response in the form of a reaction field. This has the advantage that only particles inside the primary simulation cell - the cavity - need to be modeled explicitly and the introduction of a cutoff for the Coulomb interaction is avoided.

The total electric field $\mathbf{E^{in}}$ inside such a setup can be partitioned into the contributions [23]

$$\mathbf{E}^{\mathrm{in}} = \mathbf{E^c} + \mathbf{E}^{\rho} + \mathbf{E^R} \tag{2.72}$$

Here the cavity field $\mathbf{E^c}$ denotes the field that would be present in an empty cavity without the dielectric charge distribution inside it. This includes external fields as well as fields arising due to maintaining the electrostatic boundary conditions (2.37) and (2.38) at the cavity interface. If a charge distribution is now introduced inside the cavity, it creates the additional field contribution $\mathbf{E}^{\rho}$. This induces a non-zero polarization density $\mathbf{P(r)}$ in the dielectric which in turn again polarizes the surrounding continuum according to $\varepsilon^{\mathbf{out}}$, resulting in a reaction field $\mathbf{E^R}$ inside the cavity. The reaction field can therefore be thought of as the mean-field response to the charge distribution

inside the cavity. Even though this representation might not produce physically correct fields outside the cavity, it aims at reproducing the dielectric response in the domain of interest inside the cavity. Ideally, this parametrization is independent of the charge distribution inside the cavity and parametrizes the response of the dielectric surrounding the cavity exclusively into the shape of the cavity and the dielectric constant of the surrounding continuum. Dependent on the cavity shape and the nature of the surrounding dielectric, the reaction field can in principle take arbitrary form. Provided $\mathbf{E^R}$ is known, it can be accounted for in the system Hamiltonian like any other potential contribution. If $\mathbf{E^R}$ is proportional to the total dipole of the cavity $\mathbf{M}$

$$E_i^R = f_{ij} M_j \tag{2.73}$$

the interaction between inside and outside polarization can even be incorporated in the pairwise dipole-dipole interaction tensor via the reaction field tensor $\mathbf{f}$. The energy of a dipole $\boldsymbol{\mu_a}$ at position $\mathbf{r_a}$ inside the cavity is given by

$$u^a = -\mu_i^a (E_i^c + E_i^\rho + E_i^R) = -\mu_i^a (T_{ij}^{\mathrm{dd}} \sum_b \mu_j^b + E_i^R) \tag{2.74}$$

If 2.73 holds, above equation can be written as

$$u^a = -\mu_i^a \left[\sum_b T_{ij} \mu_j^b + f_{ij} M_j \right] = -\mu_i^a \left[\sum_b (T_{ij} \mu_j^b + f_{ij} \mu_j^b) \right] = -\sum_b \mu_i^a (T_{ij} + f_{ij}) \mu_j^b \tag{2.75}$$

The entire mean-field interaction between cavity and surrounding dielectric can thus be handled by adding the diagonal tensor $\mathbf{f}$ to $\mathbf{T^d d}$, which is valid inside the cavity:

$$T_{ij}^{\mathrm{R}}(\mathbf{r}_{ab}) = \begin{cases} T_{ij}^{\mathrm{dd}}(\mathbf{r}_{ab}) + \delta_{ij} f_{ij} & a, b \text{ in cavity} \\ 0 & \text{otherwise} \end{cases} \tag{2.76}$$

For spherical or spheroidal cavities embedded in a scalar dielectric, it can be shown [23] that $\mathbf{E^R}$ fulfills the proportionality condition (2.73) An important example is a spherical cavity with radius r_c embedded in an isotropic dielectric with permittivity $\varepsilon^{\mathrm{out}}$. The reaction field tensor $\mathbf{f}$ in this case reduces to the scalar

$$f = \frac{1}{r_c^3} \frac{2(\varepsilon^{\mathrm{out}} - 1)}{2\varepsilon^{\mathrm{out}} + 1} \tag{2.77}$$

This expression first derived by Bell [143] in the treatment of electrolyte solutions holds for an arbitrary charge distribution inside the cavity.

2.6 The relation of the dielectric susceptibility to time-correlation functions

The relation between polarization and external electric field can be examined in the framework of linear response theory where a weak coupling between the response of a system to an external perturbing field is described by time-correlation functions characteristic of the equilibrated system in absence of the perturbation [24, 144]. The microscopic polarization density in an ensemble of N dipoles can be written as

$$\mathbf{P}(\mathbf{r}) = \sum_{n}^{N} \boldsymbol{\mu}^n \delta(\mathbf{r} - \mathbf{r}^n) \tag{2.78}$$

If an ensemble in microstate Γ is perturbed by a constant and weak external field $\mathbf{E^0}$, the Hamiltonian of this system can be written as

$$\begin{aligned} H'(\Gamma) &= H(\Gamma) + \int \mathbf{P}(\Gamma, \mathbf{r})\mathbf{E^0} d\mathbf{r} = H(\Gamma) + \int_V \mathbf{P}(\Gamma, \mathbf{n})\mathbf{E^0} dV + \int_{\partial V} \mathbf{P}(\Gamma, \mathbf{n})\mathbf{E^0} d\mathbf{n} \\ &= H(\Gamma) + \mathbf{M}(\Gamma)\mathbf{E^0} + \int_{\partial V} \mathbf{P}(\Gamma, \mathbf{r})\mathbf{E^0} d\mathbf{n} \end{aligned} \tag{2.79}$$

where $H(\Gamma)$ represents the Hamiltonian of the unperturbed system in microstate Γ and $\mathbf{M}$ the total dipole moment of the system. In order to avoid an explicit treatment of the surface integral in (2.79), it is typically ignored and introduced at a later stage in form of a reaction field contribution [47, 49, 50, 119]. In the following this is indicated by substituting the external field $\mathbf{E^0}$ for the cavity field $\mathbf{E^c}$, where these surface terms are already included. Phenomenologically it can be thought of as the field inside the simulation box when the external field $\mathbf{E^0}$ is applied but the dielectric filling is removed. As such it can still be considered an external field to $\mathbf{P}(\mathbf{r})$ to the bulk polarization inside the simulation box. Equation (2.79) then reads

$$H'(\Gamma) = H(\Gamma) + \mathbf{M}(\Gamma)\mathbf{E^c} \tag{2.80}$$

The average polarization density due to the cavity field $\mathbf{E^c}$ can then be expressed as the difference in polarization with field and without

$$\Delta P_i(\mathbf{r}) = \langle P_i(\mathbf{r}) \rangle_{E_j^c} - \langle P_i(\mathbf{r}) \rangle \tag{2.81}$$

where $\langle . \rangle_{\mathbf{E^c}}$ and $\langle . \rangle$ represent canonical averages for the system with and without external field applied. The average local polarization density for a system perturbed by a constant external field $\mathbf{E^c}$ is given by

$$\langle P_i(\mathbf{r}) \rangle_{E_j^c} = \frac{\int P_i(\mathbf{r}) \exp\left(-\beta H'\right) d^N\Gamma}{\int \exp\left(-\beta H'\right) d^N\Gamma} = \frac{\int P_i(\mathbf{r}) \exp\left[-\beta \left(H - M_j(\Gamma) E_j^c\right)\right] d^N\Gamma}{\int \exp\left[-\beta \left(H - M_j(\Gamma) E_j^c\right)\right] d^N\Gamma} \tag{2.82}$$

If the perturbing field is weak, $\langle \mathbf{P} \rangle_{\mathbf{E^c_c}}$ can be approximated by a first order Taylor series in $\mathbf{E^c}$ around the unperturbed equilibrium average:

$$\begin{aligned} \langle P_i(\mathbf{r}) \rangle_{E_j^c} &= \langle P_i(\mathbf{r}) \rangle + \left. \frac{\partial \langle P_i(\mathbf{r}) \rangle}{\partial E_j^c} \right|_{E_j^c = 0} E_j^c \\ &= \langle P_i(\mathbf{r}) \rangle + \beta \left[\langle P_i(\mathbf{r}) M_j \rangle - \langle P_i(\mathbf{r}) \rangle \langle M_j \rangle \right] E_j^c \end{aligned} \tag{2.83}$$

Inserting equation (2.83) into (2.81) then gives for the dielectric response of a system to a perturbing field $\mathbf{E^c}$

$$\Delta P_i(\mathbf{r}, E_j^c) = \beta \left[\langle P_i(\mathbf{r}) M_j \rangle - \langle P_i(\mathbf{r}) \rangle \langle M_j \rangle \right] E_j^c = h_{ij}(\mathbf{r}) E_j^c \tag{2.84}$$

Integrating equation (2.84) over the entire simulation box on both sides of the equation, gives the following expression for the change in total dipole moment

$$\Delta M_i(E_j^c) = \Delta M_i = \langle M_i \rangle_{E_j^c} - \langle M_i \rangle = H_{ij} E_j^c \tag{2.85}$$

with

$$H_{ij} = \int_V h_{ij} dV = \beta \left[\langle M_i M_j \rangle - \langle M_i \rangle \langle M_j \rangle \right] \tag{2.86}$$

A more rigorous derivation of the linear response ansatz, from which the static dielectric constant emerges as a special case, is presented in appendix C for a bulk dielectric and constant external field. As is shown, the linear response ansatz implies that a perturbation of a certain wavevector can only induce a response in the system with the same wavevector. It follows that for the calculation of the static dielectric constant, the consideration of static external fields is sufficient [24]. It furthermore shows that linear response theory using the Maxwell field $\mathbf{E}$ is not technically applicable because it does not represent an *external* field but one whose value depends on the state of the material [128]. This is why the contributions appearing in the fluctuation terms (2.84) and (2.86) are formulated with respect to the cavity field $\mathbf{E^c}$ and not the Maxwell field $\mathbf{E}$.

In order to derive fluctuation formulas to calculate the dielectric constant from (2.84), an expression for $\mathbf{E^c}$ in the respective system geometry needs to be derived from continuum electrostatics. In the following three sections this is described first for polar bulk systems using the reaction field, then for confined systems and finally periodic systems in slab geometry. All of these methods follow the same ansatz. First, the relation between an applied external constant field $\mathbf{E^0}$ to the cavity field $\mathbf{E^c}$ needs to be established. In a second step, the response of the dielectric to the cavity field needs to be formulated using Maxwell electrostatics. The resulting expression $\Delta\mathbf{P}(\mathbf{r}, \mathbf{E^c})$ is then equated to formula (2.84). After eliminating $\mathbf{E^c}$ on both sides of the resulting equation, one has obtained a relationship between the local dielectric constant and the fluctuation term in (2.84).

2.6.1 Calculation of the bulk dielectric constant

Neumann [49] derived a general expression for the dielectric constant for simulations employing periodic boundary conditions in the linear response framework. This combined the Clausius-Mossotti (CM) equation known to be applicable in spherical cutoff geometry [145, 146] and the Kirkwood-Fröhlich (KF) equation known to hold in a reaction field [147–150] or lattice summation setup [51, 57, 142]. The formalism is sketched in the following.

Equation (2.56) connects an isotropic bulk system's polarization response to an external field $\mathbf{E^c}(\mathbf{r})$ via

$$P_i(\mathbf{r}) = \lambda \left[E_i^c(\mathbf{r}) + \int d\mathbf{r}' T_{ij}^{\mathrm{dd}}(\mathbf{r} - \mathbf{r}') P_j(\mathbf{r}') \right] \tag{2.87}$$

where the singularity in the integral is removed and incorporated in

$$\lambda = \frac{3}{4\pi}\frac{\varepsilon - 1}{\varepsilon + 2} \tag{2.88}$$

Due to the convolution integral, (2.87) is best treated in Fourier space where it can be rearranged to

$$\tilde{P}_i(\mathbf{k}) = \lambda \left[\delta_{ij} - \lambda \tilde{T}_{ij}^{\mathrm{dd}}(\mathbf{k})\right]^{-1} \tilde{E}_j^c(\mathbf{k}) = \lambda \Lambda_{ij}^{-1}(\mathbf{k}) \tilde{E}_j^c(\mathbf{k}) \tag{2.89}$$

where $\mathbf{\Lambda^{-1}}$ should be interpreted as the inverse of the 3x3 matrix

$$\Lambda_{ij}(\mathbf{k}) = \delta_{ij} - \lambda \tilde{T}_{ij}^{\mathrm{dd}}(\mathbf{k}) \tag{2.90}$$

Since we are interested in the static dielectric constant, the perturbing field $\mathbf{E^c}(\mathbf{k}) = \mathbf{E^c}(\mathbf{0})$ is assumed to be constant. Furthermore we are looking for the bulk dielectric constant and hence the polarization response of the entire system $\mathbf{P}(\mathbf{k}) = \mathbf{P}(\mathbf{0})$ is completely delocalized. Equation (2.89) hence reduces to

$$\tilde{P}_i(0) = \lambda \left[\delta_{ij} - \lambda \tilde{T}_{ij}^{\mathrm{dd}}(0)\right]^{-1} \tilde{E}_j^0(0) \tag{2.91}$$

In order to solve for λ and hence the dielectric constant, $\mathbf{E^c}(\mathbf{0})$ and $\mathbf{P}(\mathbf{0})$ need to be specified. The Fourier transform of a constant external field $\tilde{\mathbf{E}}^{\mathbf{c}}(\mathbf{0})$ is given by

$$\tilde{\mathbf{E}}^{\mathbf{c}}(0) = \int_V \mathbf{E^c} d\mathbf{r} = V\mathbf{E^c} \tag{2.92}$$

with V representing the system volume.

An expression for the $\tilde{\mathbf{P}}$ is derived in the framework of linear response theory. According to (2.84), the polarization due to a perturbation in the form of an applied external electric field $\mathbf{E^c}$ reads in Fourier space

$$\tilde{P}_i(\mathbf{k}) = \int \tilde{h}_{ij}(\mathbf{k}) \tilde{E}_j^{\mathrm{c}}(\mathbf{k} - \mathbf{k}') \exp(-i\mathbf{k}\mathbf{r}) d\mathbf{k}' \tag{2.93}$$

For $\mathbf{k} = \mathbf{0}$ and constant $\mathbf{E^c}$ this can be written as

$$\tilde{P}_i(0) = H_{ij} E_j^c \tag{2.94}$$

Inserting (2.92) and (2.94) in (2.91) and eliminating $\mathbf{E^c}$ allows one to establish a relation between λ and the dipole moment fluctuations $\mathbf{H}$ if the zero-mode Fourier transform of the dipole-dipole interaction tensor $\tilde{\mathbf{T}}^{\mathbf{dd}}(\mathbf{0})$ is known:

$$\lambda = \frac{1}{V} \left[\delta_{ij} - \lambda \tilde{T}_{ij}^{\mathrm{dd}}(0) \right] H_{ij} \tag{2.95}$$

All elements of $\mathbf{T^{dd}}$ vanish due to symmetry of the integral

$$\tilde{T}_{ij}^{\mathrm{dd}}(0) = \int T_{ij}^{\mathrm{dd}}(\mathbf{r}) d\mathbf{r} = 0 \tag{2.96}$$

assuming the singularity of the dipole-dipole interaction tensor is already taken care of. By inserting this in (2.95) one arrives at the familiar CM relation for the dielectric constant that is known to be valid for simulations with vacuum boundary conditions [49]:

$$\begin{aligned} \lambda &= \frac{H_{ii}}{V} \\ \frac{\epsilon - 1}{\epsilon + 2} &= \frac{4\pi}{3} \frac{\bar{H}}{V} \end{aligned} \tag{2.97}$$

In the second line of above equation H_{ii} can be substituted with the mean over all three dimensions $\bar{H} = 1/3 \sum_i H_{ii}$ due to the assumed isotropicity of the medium.

However, this approach so far only considers explicit dipole-dipole interactions from within the designated cavity or simulation cell and the influence of a cavity-surrounding medium is not considered. Remember the surface integral in (2.79) is assumed zero. This is equivalent to vacuum boundary conditions which can be an inadequate assumption for the simulated system, even for a bulk liquid. Common lattice summation methods like the Ewald summation imply conducting boundary conditions at infinity [48] and a reaction field model of a cavity embedded in a dielectric $\varepsilon^{\mathrm{out}}$ would require $\varepsilon^{\mathrm{out}} \neq 1$ at the boundary. Neumann accounted for this by assuming a spherical cavity embedded

in a dielectric ε^{out} and using $\mathbf{T}^{\mathbf{R}}$ instead of $\mathbf{T}^{\mathbf{dd}}$ in (2.95). The general fluctuation formula for the cavity dielectric constant ε^{in} in this geometry is given by

$$\frac{\epsilon^{\text{in}}-1}{\epsilon^{\text{in}}+2} = \frac{4\pi}{3}\frac{\bar{H}}{V}\left[1 - \frac{\epsilon^{\text{in}}-1}{\epsilon^{\text{in}}+2}\frac{2(\varepsilon^{\text{out}}-1)}{2\varepsilon^{\text{out}}+1}\right] \tag{2.98}$$

The KF formula for the important special case of conducting boundary conditions is obtained by letting $\varepsilon^{\text{out}} \to \infty$ in (2.98)

$$\varepsilon^{\text{in}} = 1 + 4\pi\frac{\bar{H}}{V} \tag{2.99}$$

One might ask why (2.99) is equally valid for calculating the bulk dielectric constant for cubic boxes simulated using Ewald summation. After all, a spherical cavity is assumed in above derivation. The reason for this lies in the truncation of the k-space sum at radius k_c in lattice summation techniques, which in real space is nothing else than a large sphere filled with repetitions of the primary simulation cell. As such it can be interpreted as a large cavity in reaction field geometry if the boundary conditions are handled right. This is also true for non-cubic but rectangular simulation cells, due to the scaling of $\mathbf{k}$ with the boxlength.

2.6.2 Local dielectric constant calculation

A plethora of different fluctuation formulas for confined and interfacial system geometries has been derived. Fluctuation formulas to calculate the static dielectric constant for polar fluids confined in cylinders, slab systems and spheres with varying boundary conditions have been derived by Ballenegger et al. [46, 47] and are frequently employed [27, 33, 74, 119, 151–155].

In most of these simulation setups the dielectric properties do not change along two coordinate axes while varying over the third in the chosen coordinate system. The general 3x3 dielectric tensor then reduces to

$$\boldsymbol{\varepsilon} = \begin{pmatrix} \varepsilon_{\parallel} & 0 & 0 \\ 0 & \varepsilon_{\parallel} & 0 \\ 0 & 0 & \varepsilon_{\perp} \end{pmatrix} \tag{2.100}$$

All off-diagonal elements are zero and $\varepsilon_{\parallel}$ and $\varepsilon_{\perp}$ are decoupled.

A fluctuation formula for the local dielectric constant for periodic slab systems was derived by Stern and Feller [50] using an infinite lattice sum geometry like the one underlying the Ewald summation described in section 2.5.1. The derivation of this Stern-Feller (SF) fluctuation formula is outlined in

this section. Let the radius of a sphere S enclosing these periodic repetitions be $N \cdot L$ where N is an integer and L the length of the primary cell. The origin is chosen at an arbitrary point in the primary cell. Furthermore N is chosen to be sufficiently large for the sphere to be a valid approximation. The slab geometry of the primary cell is periodic in the xy-plane and varies along the z-dimension. This translates to a stack of infinitesimally thin, uniformly polarized discs that make up S. Each of these discs is uniformly polarized by a polarization density $\mathbf{P}(z)$, has a radius $\sqrt{N^2L^2 - z^2}$ and a thickness of dz. The electric field at the origin due to one of these discs with a distance $z \neq 0$ from the origin is then given by [50]

$$\begin{aligned} \xi_i(z) = E_i^{\mathrm{disc}}(0) &= \int_0^{\sqrt{N^2L^2-z^2}} d\rho \int_0^{2\pi} d\theta \rho T_{ij}^{\mathrm{dd}}(\rho, \theta, z) P_j(z) dz \\ &= \frac{\pi}{N^3 L^3} \left(N^2L^2 - z^2\right) \left[3\delta_{iz} P_z(z) - P_i(z)\right] dz \qquad , \qquad i \in \{x, y, z\} \end{aligned} \tag{2.101}$$

with $\mathbf{T}^{\mathbf{dd}}$ being the dipole-dipole interaction tensor of equation (2.51) and δ_{ij} being the Dirac delta function. Due to the singularity of $\mathbf{T}^{\mathbf{dd}}$ at the origin, the case $z = 0$ is not considered in above equation. Its contribution is added later. Above equation is then integrated over all discs which gives in the limit of large N [50]

$$E_i^{\mathbf{P}(z\neq 0)}(0) = \lim_{N\to\infty} \int_{-NL}^{NL} \xi_i(z) dz = \frac{4\pi}{V} \left[\delta_{iz} M_z - \frac{1}{3} M_i\right] \tag{2.102}$$

where V and $\mathbf{M}$ are the volume and the dipole moment of the primary cell. Analogously to the argumentation leading to formula (2.56), the contribution of the singularity is given by

$$E_i^{\mathbf{P}(z=0)}(0) = -4\pi \delta_{iz} P_z(z = 0) \tag{2.103}$$

for the uniformly polarized disc at the origin. Due to the lateral symmetry of $\mathbf{T}^{\mathbf{dd}}$ over the disc, this is the only contribution from the disc at $z = 0$. Combining equations (2.102) and (2.103) and recalling that the choice of origin was an arbitrary point within the primary cell, the total cavity field for a polarized system in the described periodic slab geometry is given by

$$E_i^{\mathbf{P}}(z) = 4\pi \left(\delta_{iz} \left[\frac{M_z}{V} P_z(z)\right] - \frac{M_i}{3V}\right) \tag{2.104}$$

Due to the use of $\mathbf{T^{dd}}$ so far, this assumes vacuum boundary conditions. However, a periodic lattice summation implies conducting boundary conditions [48]. By substituting $\mathbf{T^R}$ for $\mathbf{T^{dd}}$ in (2.101), and taking the limit $\varepsilon^{\text{out}} \to \infty$ the additional reaction field $\mathbf{E^R}$ for the spherical cavity (2.77)

$$E_i^R = \lim_{\varepsilon^{\text{out}} \to \infty} \frac{1}{r_c^3} \frac{2(\varepsilon^{\text{out}} - 1)}{2\varepsilon^{\text{out}} + 1} M_i = \frac{4\pi}{3} \frac{M_i}{V} \tag{2.105}$$

gets added to (2.104), which results in

$$E_i^{\mathbf{P}}(z) = 4\pi \left(\delta_{iz} \frac{M_z}{V} P_z(z) \right) \tag{2.106}$$

Inserting (2.104) in (2.53) and substituting $\mathbf{P}$ with the polarization fluctuation matrix $\mathbf{h}$ from (2.84) one obtains

$$\begin{aligned} h_{ij} E_j^c &= \chi_{ij}^l(z) \left[E_j^c + E_j^{\mathbf{P}} \right] \\ &= \chi_{ij}^l(z) \left[E_j^c + 4\pi \left(\delta_{jz} \frac{H_{jz}}{V} h_{jz}(z) \right) E_j^c \right] \end{aligned} \tag{2.107}$$

With $h_{\parallel}^l = h_{xx} + h_{yy}$ and $h_{\perp} = h_{zz}$ as well as analog notation for $\boldsymbol{\varepsilon^l}$ and $\mathbf{H}$ one obtains the slab-parallel fluctuation formula for the dielectric constant

$$\varepsilon_{\parallel}^l(z) = 1 + 4\pi h_{\parallel}(z) \tag{2.108}$$

Its slab-normal counterpart is given by

$$\varepsilon_{\perp}^l(z) = 1 + 4\pi h_{\perp}(z) \left[1 + \left(4\pi \frac{H_{\perp}}{V} - h_{\perp}(z) \right) \right]^{-1} \tag{2.109}$$

Even though equation (2.109) is correct, it is very sensitive to changes in $h_{\perp}$ and therefore subject to slow convergence as shown in [50]. This can be circumvented by instead calculating the inverse dielectric constant. Rearranging (2.109) then yields

$$(\varepsilon_{\perp}^l(z))^{-1} = 1 - 4\pi \frac{h_{\perp}(z)}{(1 + 4\pi H_{\perp}/V)} \tag{2.110}$$

Another approach to calculate $\varepsilon_{\perp}^{l}$ is to calculate the local capacitances C^{l} of a series of plate capacitors. C^{l} is given by the derivative

$$C^{l} = \frac{\partial \langle \sigma^{l} \rangle}{\partial \langle \phi^{l} \rangle} = \frac{1}{d} \varepsilon_{\perp}^{l} \tag{2.111}$$

where σ^{l} represents the local charge density and ϕ the local electrostatic potential in a slab. The slab thickness is represented by d. Since the change of σ^{l} with ϕ^{l} can be calculated from simple averages, this method is computationally more economic than a calculation of $\varepsilon_{\perp}^{l}$ via second-order polarization fluctuations. Using a thermo-potentiostat like the one by Deissenbeck *et al.* [45] further reduces the error since the potential can be assumed constant over the entire simulation box.

Chapter 3

Methods and Benchmarks

In this chapter simulation protocols for bulk and interfacial DCE or H_2O trajectories, as well as the creation and definition of the LLI are presented. Secondly, the fluctuation formulas derived in chapter 2 are applied to the generated trajectories. The dielectric constants for the H_2O and DCE bulk systems are calculated as a benchmark reference and the convergence of the total dipole fluctuations is examined. Subsequently, the local dielectric constant of the interfacial H_2O - DCE system is investigated. The parallel and perpendicular components of the dielectric constant are calculated, their convergence is tested and the applicability of the slab-model to this system is examined. Furthermore, numerical instabilities and conceptual limitations of a Maxwellian permittivity in atomistic vicinity of the interface are highlighted and discussed.

3.1 Simulation protocols

In this section the simulation and equilibration protocols for all trajectories used in this work are presented. Each was generated via classical MD, however all concepts presented in the following are equally applicable to any other type of canonical trajectory simulating bulk and interfaces of molecular liquids. Simulations of liquid water and DCE were carried out both in bulk and interface simulations. For clarity, each trajectory is referred to by its all-caps acronym in the rest of this work.

The force fields selected for trajectory generation in this work are SPC/Fw [156] for water and a reparametrized OPLS flavour force field [157] for DCE. These force fields were selected due to their improved experimental agreement regarding the dielectric constant [103, 157]. Both employ harmonic bond, angle and, in the case of DCE, dihedral terms to simulate intra-molecular covalent bonding. Non-covalent interactions are modeled according to (2.5), using a superposition of the 12-6 Lennard-Jones potential and pair-wise electrostatic interactions between atomic partial point-charges. Bond breaking is forbidden in both cases. As proposed for these force fields [157–159], Lorentz-Berthelot combination rules [115] were employed to evaluate inter-species Lennard-Jones parameters for H_2O and DCE atoms in interfacial simulations. Long-range electrostatics were simulated via Ewald summation as presented in section 2.5.1. As proposed by Liu *et al.* [154, 157]

a common cutoff distance of 10 Å for Lennard-Jones and short-range Ewald interaction was used and the truncation error for the Ewald sums was set to $10^{-6}\ \frac{\text{kcal}}{\text{mol}}$ in all simulations. Furthermore, rectangular simulation boxes and periodic boundary conditions were employed in all cases. All trajectories were simulated in the NVT ensemble with a timestep of 1 fs and simulations were carried out using the LAMMPS simulation package [109].

Bulk The H2OBULK and DCEBULK trajectories simulate bulk liquids consisting of 356 molecules of H_2O and 64 molecules of 1,2-dichloroethane (DCE), respectively. Both are thermostated at 298.15 K via a Nose-Hoover thermostat that is configured to match the target temperature every 100 timesteps. The length of each simulation is 30 ns and a snapshot is taken every 1 ps, totaling 30000 snapshots per trajectory. Pre-simulation, both trajectories are equilibrated subsequently in the NVT, NPT, NVE, and again the NVT ensemble for 2 ns each. The final NVT equilibration step is performed as a buffer before production. Past equilibration, the cubic simulation box had a side length of 22.18 Å in the case of H2OBULK and 20.79 Å in the case of DCEBULK.

Interface The interfacial trajectory DCEH2OINT consists of 356 H_2O and 252 DCE molecules simulated at 298.15 K. The H_2O and DCE phases are periodic in the xy-plane, the phase transition occurs along the z-direction. Thermostatting and equilibration was performed analogous to the bulk counterparts H2OBULK and DCEBULK. The simulation lasted 45 ns and a snapshot was taken every 1 ps, totaling 45000 snapshots. Past equilibration, the brick shaped simulation box had a sidelength of 22.41 Å in x- and y-direction and 91.69 Å in z-direction. This corresponds to a H_2O phase that spans roughly 22 Å and a DCE phase that spans roughly 60 Å in z-direction, even though the precise extents of each phase may vary over time. The use of periodic boundary conditions creates a lower and an upper interface between H_2O and DCE. This terminology refers to each interface's average z-coordinate. In order to utilize both the upper and the lower LLI, a copy of the entire trajectory was rotated by 180 degrees around the y-axis, essentially inverting upper and lower LLI. Both the original and flipped instance of the trajectory were furthermore periodically shifted along the z-axis to place the average z-coordinate of the LLI closest to the origin at $z = 0$. This results in the DCE phase occupying the z-axis negative halfspace and the H_2O phase occupying the z-axis positive half-space, separated by the lower LLI in the original instance and the upper LLI in its flipped copy. Assuming both the DCE and H_2O phase are sufficiently large to reach bulk behaviour, hence the upper and lower LLI are decorrelated, the effective length of the trajectory can be doubled for interface analysis. The effective sampling rate of the present 45 ns trajectory is therefore equivalent to a 90 ns trajectory where only one LLI is used.

3.2 Dipole clusterings

Coarse-graining from atomistic to dipole trajectories is performed by representing a group of atoms with net zero charge in the atomistic trajectory by their dipole moment calculated according to

(2.26). The two types of clusterings used in this work are portrayed in figure 3.1. Molecular clustering, where all atoms of a molecule form a dipole, was employed for coase-graining both H_2O and DCE phases. In the case of DCE, the additional 2xCCl clustering was used where each carbon-chlorine leg and its adjacent hydrogen atoms of a DCE molecule are clustered into two individual dipoles. Intensive investigations via diffraction methods and spectroscopy show that liquid DCE at room temperature occurs in two different main conformations [157, 160].

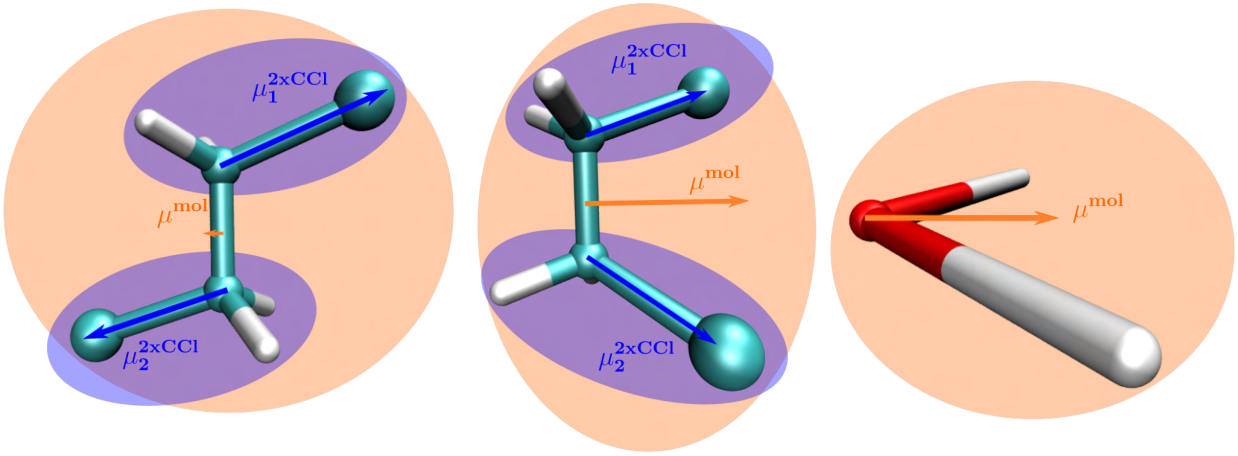

Figure 3.1 – Molecular and 2xCCl clustering for *trans* and *gauche* DCE (left and middle) and molecular clustering for H_2O (right). The molecularly clustered *trans* DCE conformer assumes a molecular dihedral angle of "around 180°", the chlorine atoms lie on opposite sides of the DCE carbon-carbon axis. For *gauche* DCE the dihedral angle lies between 30° and 90°, which means the chlorine atoms lie on the same side of the carbon-carbon axis. The molecular dipole of *trans* DCE is thus significantly smaller than *gauche* DCE.

For the leftmost *trans* DCE conformer in figure 3.1 with a molecular dihedral angle $\approx 180°$, the chlorine atoms lie on opposite sides of the DCE carbon-carbon axis. In the *gauche* conformer portrayed in the middle, with a dihedral angle between 30 and 90 degrees, the chlorine atoms lie on the same side of the carbon-carbon axis. As a result, a molecular clustering for the two dominant DCE conformers thus exhibits two very different average dipole magnitudes as the two chloromethyl groups of the DCE molecules either cancel or support each other's contribution to the dipole moment. This is visualized by the blue distribution in figure 3.2. For a 2xCCl clustered DCE phase these two peaks collapse as shown by the orange distribution in 3.2 since the length of a carbon-chlorine leg stays rigid in comparison. Comparing the 2xCCl to the molecular clustering in DCE thus provides a possibility to test the influence of dipole rigidity on dielectric properties of the coarse-grained trajectory. A comparison of the orange and green distributions in 3.2 furthermore reveals that dipoles in 2xCCl clustered DCE and molecular clustered H_2O are quite similar in magnitude. The 2xCCl dipoles are significantly less variable however, since they are dominated by the relative position of C and Cl in the chloromethyl groups.

In both molecular and 2xCCl clustering, the cluster center of mass was chosen as the space point of the dipole vector. Since all clusters are neutral and the dipole thus represents the leading order in the multipole expansion, the choice of the space point should not matter. Choosing the center of charge for example would be an equally valid alternative.

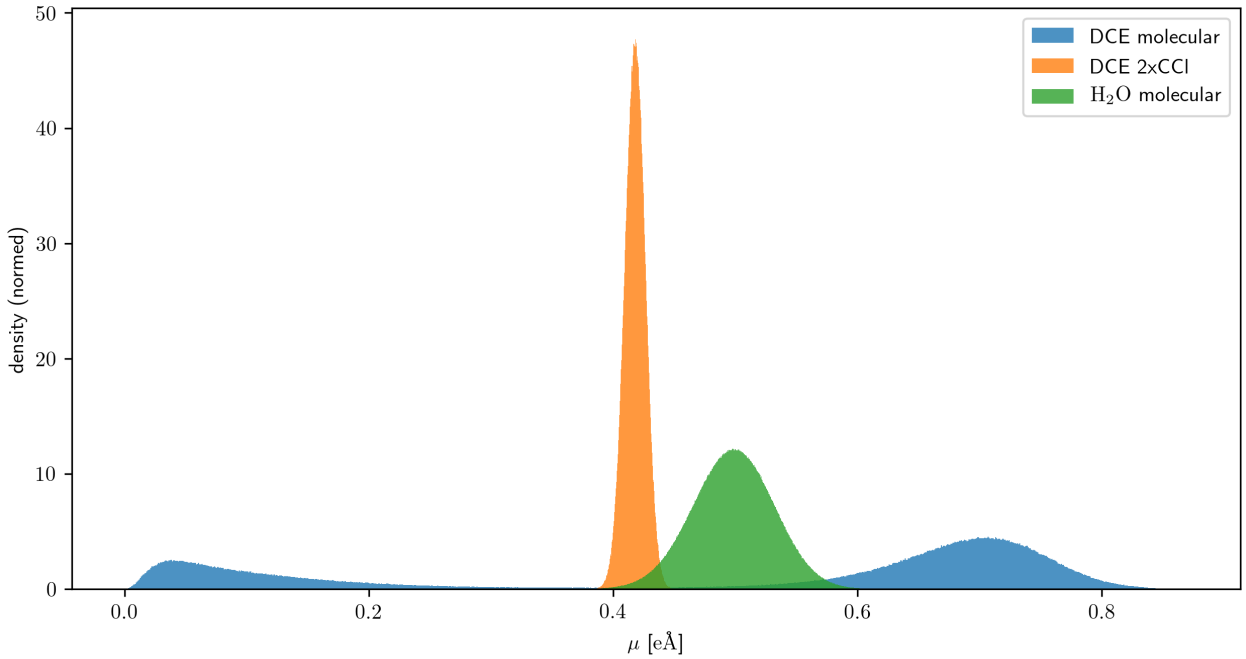

Figure 3.2 – Distribution of the dipole magnitude of DCE in molecular (blue) and 2xCCl clustering (orange) as well as H_2O in molecular clustering (green).The magnitude of the molecular DCE dipole changes significantly between *trans* and *gauche* conformation. For 2xCCl clustered DCE, the distribution of group diples is narrow since the length of a carbon-chlorine bond stays constant in comparison. The 2xCCl clustered DCE dipole and the H_2O molecular dipole are similar in magnitude, 2xCCl is significantly more rigid however.

3.3 Instantaneous interface calculation

In order to statistically sample the region of a phase transition between two immiscible liquids like H_2O and DCE, an interface is needed as a point of reference.

The topology of a solid-liquid or solid-solid interface is naturally defined by the rigid surface of the solid and changes comparatively little over the course of a trajectory. However, an interface between two immiscible molecular liquids like H_2O and DCE at ambient temperatures lacks this point of reference. It changes with time as capillary waves smooth out the interfacial structure [31, 161] and dissociating droplets can lead to interface fragmentation.

A rigid mathematical surface derived from density averages like the Gibbs dividing interface [106] looses relevant information as it does not accommodate for such roughness of the interface. To address that issue, we follow a procedure proposed by Willard and Chandler [162] for a liquid-vapor interface and employed by Liu *et al.* [154] for a DCE-H_2O LLI to capture said instantaneous fluctuations. This procedure coarse-grains the discrete instantaneous density of any *i*th cluster center at position $\mathbf{r}_i$ at time t: $\rho(\mathbf{r},t) = \sum \delta(\mathbf{r}-\mathbf{r}_i(t))$ into a continuous density by convoluting ρ with a normalized Gaussian and subsequently mapping it onto a regular grid. Following [154, 162], the half-width of the Gaussian kernel is chosen to be 2.5 Å which is approximately the molecular diameter of water and as such constitutes the smallest independently moving entity in the simulation. Additionally, this parameter is comparable to the empirical parameter used to truncate the capillary wave spectrum in capillary wave theory [163–166] as pointed out in [154]. Resolving a LLI in atomistic trajectories

beyond this resolution is meaningless, particularly since this work focuses on molecular polarization at the interface. Analogous to [154], the instantaneous interface is chosen by the "10-90" criterion [31, 167] which constitutes the iso-surface between the H_2O and DCE phase where water density

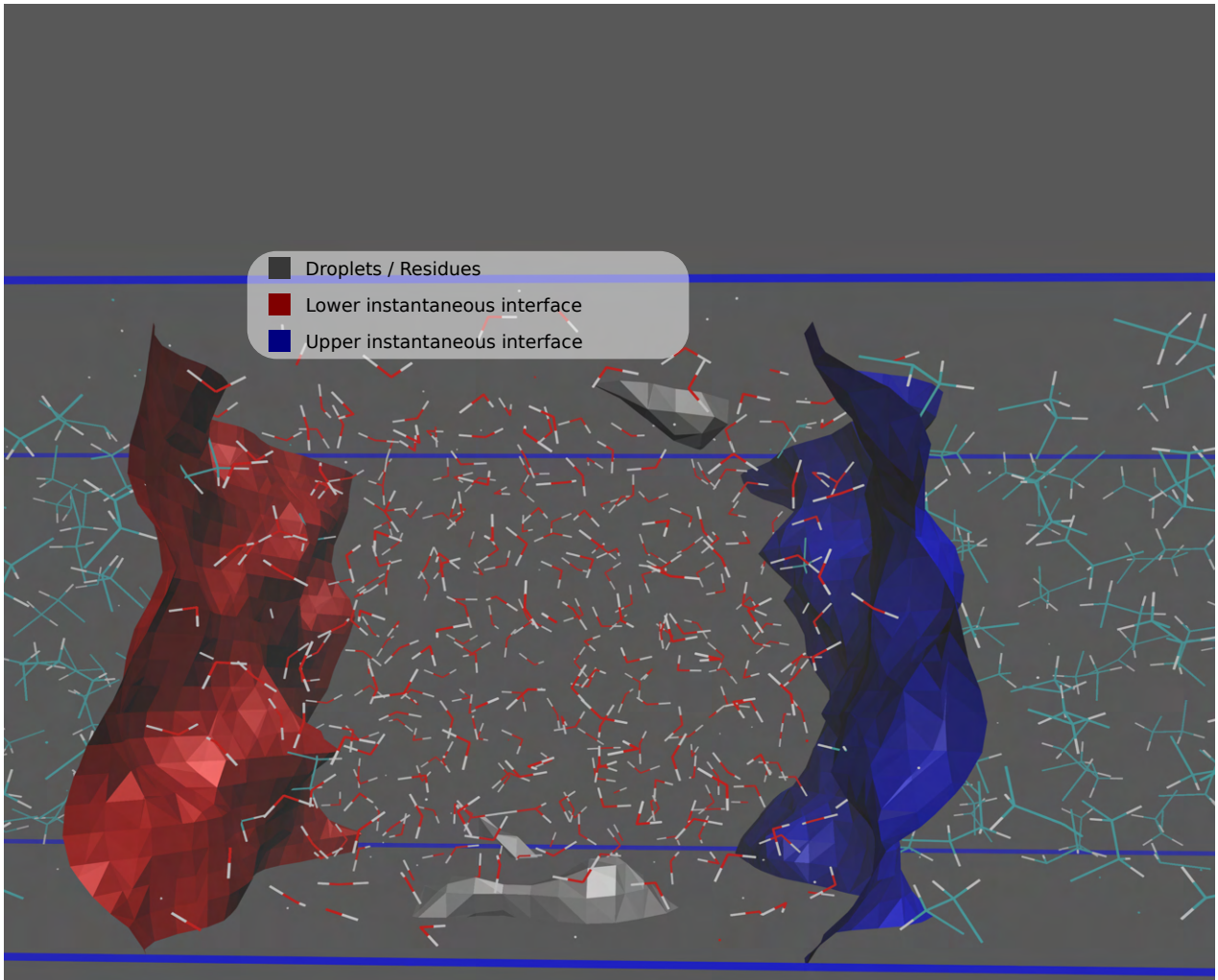

Figure 3.3 – The instantaneous DCE-H_2O LLI is chosen by the "10-90" criterion which constitutes the iso-surface between the H_2O and DCE phase where water density has decreased by 90% compared to its bulk value. The two largest sets of connected vertices are selected as the lower and upper triangulated instantaneous LLI, depending on their average z-coordinate vertex value. Vertices distinct from these two largest connected submanifolds are discarded. They can stem from single molecules or small droplets of one phase inside the other as well as numerical noise.

From the potentially total iso-surface obtained via the Marching Cubes algorithm, the two largest sets of connected vertices are selected as the lower and upper instantaneous interface, depending on their average z-coordinate vertex value. Vertices distinct from these two largest connected submanifolds are discarded. These smaller droplets and residues can stem from single molecules or small droplets of one phase inside the other and the degree of fragmentation is furthermore dependent on the width of the chosen Gaussian kernel. The lower instantaneous interfaces in red and the upper instantaneous interface in blue are depicted for a snapshot of a H_2O - DCE interface simulation in figure 3.3.

In figure 3.4 the probability distribution of the disconnected manifolds per iso-surface in each snapshot is shown on the left. Distribution peak and minimum coincide at a number of two disconnected manifolds. For higher counts of disconnected manifolds the distribution decays rapidly and no snapshot contains more than six disconnected manifolds. This confirms that a distinct upper and lower LLI can be identified in each snapshot and droplet formation is the exception. Discarding the smaller manifolds in our description as well as the choice of parameters for LLI creation are therefore considered to be valid. On the right the distribution of vertices per disconnected manifold exhibits two clearly distinct regimes. The higher regime resembling a Gaussian distribution is centered around 900 vertices per manifold and represents the large connected sheets of upper and lower LLI. The lower regime exhibits two peaks approaching zero vertices per manifold on its left and 100 on its right. The peak closer to zero most likely represents residues of the density iso-surface due to thermal fluctuations while the peak around 100 vertices per manifold is more likely to be associated with opposite phase molecules. The distinct peak furthermore suggests that only individual molecules of the opposite species penetrate the phase boundary.

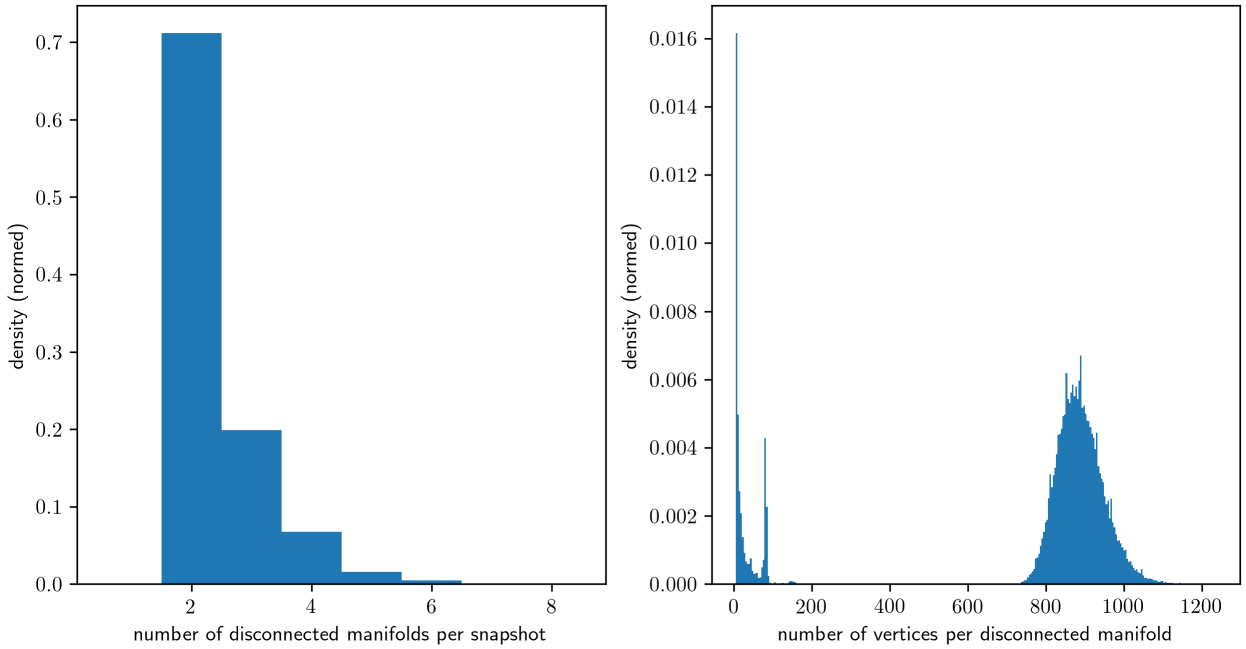

Figure 3.4 – Left side: Probability distribution of the disconnected manifolds per iso-surface in each snapshot. The distribution peak and minimum coincide at a number of two disconnected manifolds, for higher counts the distribution decays rapidly. This confirms that a distinct upper and lower LLI can be identified in each snapshot and droplet formation is the exception. Right side: Distribution of vertices per disconnected manifold, where two regimes are visible. The Gaussian distribution centered around 900 vertices per manifold represents the large connected sheets of upper and lower LLI.

The distance of a point in space to the instantaneous interface is obtained by projecting the cluster center onto the triangulated LLI along the z-axis and is independent of the laboratory frame of the simulation. This approach significantly reduces the dimensionality of the problem because it decouples a cluster's interfacial distance in z-direction from its exact 3D location with respect to the interface. The long range dynamic behavior of two so obtained instantaneous interfaces with respect to the upper and lower water phase boundaries, if not correlated, allows the calculation

of the dielectric response via ensemble averages only dependent on instantaneous LLI distance. As shown in the following section, the dielectric profiles with respect to the instantaneous interface differ significantly from the results obtained with respect to a rigid interface and captures significantly more detail. It should be noted however, that the reduction of the instantaneous interface to a 1D profile in z-direction also omits lateral cross correlation effects in the electrostatics which can not be cleanly separated from the influence of capillary smoothing.

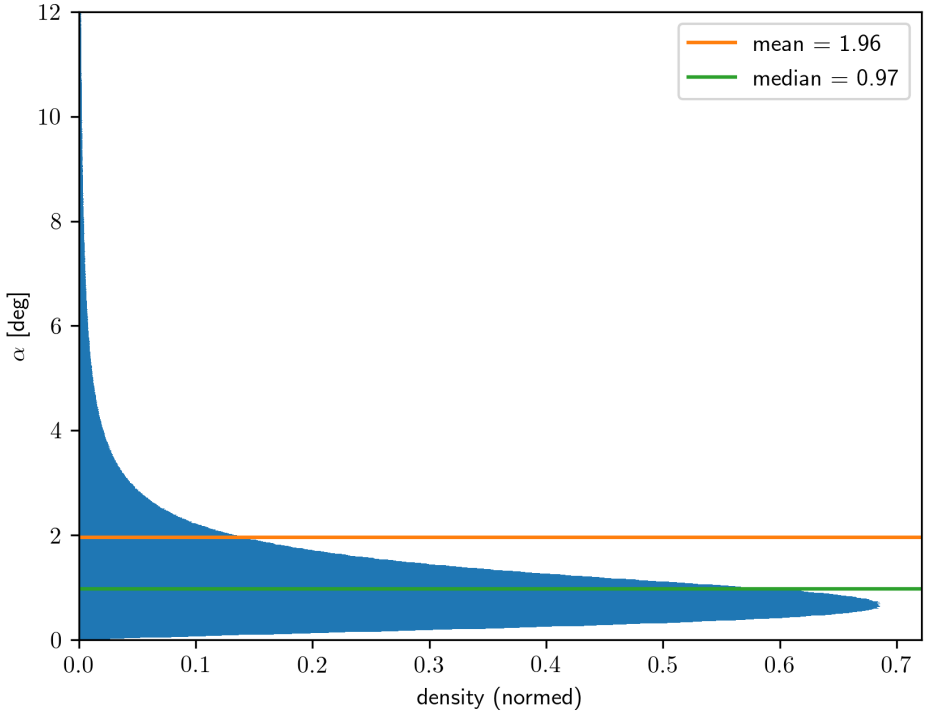

Figure 3.5 – Distribution of the angle between the triangulated LLI's normal vectors and the z-axis. A mean value of 2.01 degrees and a median value of 0.98 degrees of this distribution indicate that the deviation from the xy-plane, which would be a zero angle against the z-axis, is small.

The distribution of the angle α of the triangulated instantaneous LLI normal vectors against the z-axis is portrayed in figure 3.5. With a mean value of 2.01 degrees and a median value of 0.98 degrees this distribution indicates that the deviation from the xy-plane, which would be a zero angle against the z-axis, is small. The approximation of a slab-system that is infinitely extended in xy-direction is valid using the instantaneous LLI as reference. In addition to the LLI described above, a planar interface only dependent on the average density in each snapshot is used for comparison in this work. It is similar to the thermodynamically defined Gibbs dividing interface [31] and placed at the average z-position of all vertices of the instantaneous LLI in each snapshot. If derived from an instantaneous LLI created via the "10-90" criterion with respect to the water phase as described above, the plane is located where the water density has declined by 90% on average in each snapshot. It is referred to as the Gibbs LLI in the following.

In figure 3.6 the slab-averaged molecular number density profiles in z-direction are shown with respect to the Gibbs LLI in blue and the instantaneous LLI in orange. In both cases the total

number density is indicated by a solid, the DCE density by a dashed and the H_2O density by a dotted line.

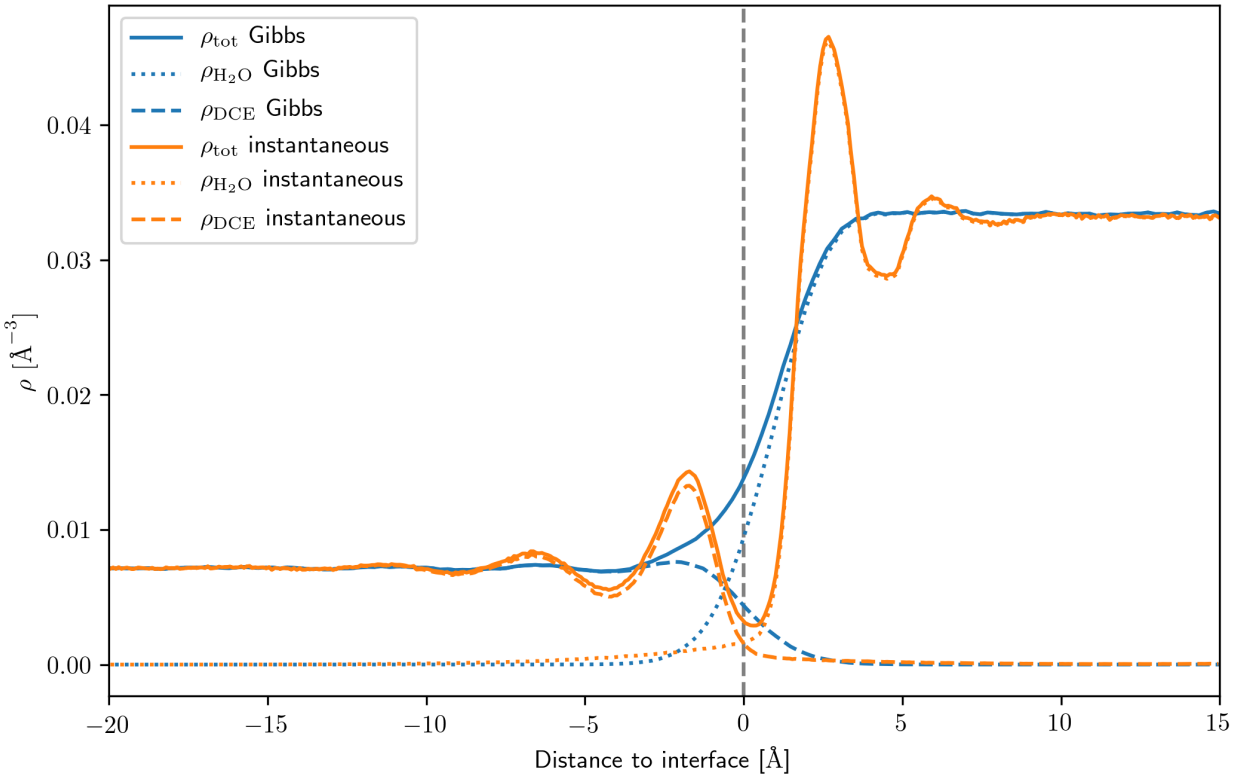

Figure 3.6 – Comparison of the slab-averaged molecular number density profiles in z-direction is shown with respect to the Gibbs LLI in blue and the instantaneous LLI in orange. The total number density is indicated by a solid, the DCE density by a dashed and the H_2O density by a dotted line.

Compared to the Gibbs LLI density profile, the instantaneous LLI density profile has significantly more structure. Here, solvation shell formation can be observed in both the DCE phase on the left and the H_2O phase on the right. These structural deviations from the bulk liquid phase densities are observed in many computer simulations [27, 28, 31, 33, 84, 119] of solid/liquid interfaces as well as in ion hydration [172–174] and are attributed to the mutual alteration of van-der-Waals interactions by the other phase. In the present example, the first two solvation shells up to an interfacial distance of ~10 Å away from the LLI are most prominent after which the oscillations decay rapidly and the density approaches the respective bulk values. Between the peaks of the first solvation shell in H_2O and DCE, a depletion zone where the number density is at its global minimum can is observed. In case of the Gibbs LLI slab system, the transition between the DCE and H_2O bulk phase is sigmoid as the instantaneous LLI structure gets entirely smoothed out.

3.4 Fluctuation formula benchmarks for the bulk permittivity

In the following we use the KF equation (2.99) derived in 2.6.1 to compute the scalar dielectric constant for the bulk trajectories of water and DCE:

$$\varepsilon = 1 + \frac{4\pi}{3V}\sum_i H_{ii} = 1 + \frac{4\pi}{V}\bar{H} \tag{3.1}$$

To recall, the derivation of this formula first requires equating two expressions for the change in polarization density $\Delta\mathbf{P}$ under application of an external electric field. The first expression for the polarization density $\Delta\mathbf{P}$ is derived using continuous Maxwell electrostatics as described in section 2.6.1. It is equivalent to the polarization build-up in the dielectric of a charged plate capacitor, a picture that becomes very intuitive if one remembers that $\Delta\mathbf{P}$ is enclosed by conducting boundary conditions as a response to an external electric field. Its statistical mechanics counterpart is derived in the linear response formalism as described in 2.6 and sets $\Delta\mathbf{P}$ in relation to H_{ii}. The applied electric field assumed in both expressions is subsequently eliminated on both sides of the equation which yields an expression for the permittivity only in terms of the equilibrium dipole fluctuations H_{ii} and is independent of the field applied.

Above equation furthermore implies a scalar dielectric constant expected for isotropic bulk liquids like $\mathrm{H_2O}$ and DCE. This assumes all non-diagonal elements of the total dipole fluctuations $H_{ij}, i \neq j$ to be zero and the on-diagonal elements H_{ii} to be equal if sufficiently converged. The bulk permittivity benchmarks were calculated using the H2OBULK trajectory in the case of H_2O and the DCEBULK trajectory in the case of DCE. The coarse-graining from atomistic to dipole trajectories was achieved by molecular clustering in both cases. In the case of DCE an additional 2xCCl clustering was performed in order to test the sensitivity of the bulk dielectric constant to the clustering type.

From these dipole trajectories the diagonal elements of the total dipole moment fluctuation tensor, H_{ii} and subsequently the dielectric constant was calculated using equation (3.1). The values for H_{ii}, $\bar{H}$ and ε are presented in table 3.7:

	H_{xx}	H_{yy}	H_{zz}	$\bar{H}$	ε	$\varepsilon^{\mathrm{ref}}$
$\mathrm{H_2O}$ molecular	117.80	118.47	115.76	117.34	77.87	78.1 [156]
DCE molecular	12.35	12.57	12.87	12.60	10.87	10.78 [175]
DCE 2xCCl	12.35	12.57	12.87	12.60	10.87	10.78 [175]

Figure 3.7 – Bulk dielectric constants for $\mathrm{H_2O}$ and DCE.

A comparison of the last two columns shows that the calculated bulk permittivities ε are in good agreement with the values for the bulk dielectric constant $\varepsilon^{\mathrm{ref}}$ reported in literature for both SPC/Fw [156] and DCE [157] at the given temperature.

Table 3.7 furthermore shows that the values for H_{ii} and subsequently ε are identical for both the molecular and 2xCCl clustering performed on the DCE trajectory. This is expected in the case of neutral clusters like the ones performed for DCE because the choice of the expansion centers has no influence on the leading order expansion term - which is the dipole for neutral clusters. The total dipole moment of the simulation cell in each snapshot thus stays the same and the different clusterings represent just two different ways to sum up this total dipole moment in each configuration. Furthermore, the H_{ii} values in x- y- and z-direction are identical within $\pm$ 1% of $\bar{H}$ for all dipole trajectories. This is expected because both $\mathrm{H_2O}$ and DCE are isotropic liquids and as such the dielectric permittivity, which parametrizes the response of a medium to an applied electric field, should be scalar. No preferred direction hence exists.

In figure 3.8, the convergence of H_{ii} is portrayed for the dipole trajectories considered. Here, the blue lines represent averages for $\bar{H}$ and the grey lines the directional H_{ii} over an averaging time T^{ave}. The blue channel in both plots indicates a $\pm$ 1%, the orange channel a $\pm$ 3% window around the maximal averaging time T^{max} of 30 ns.

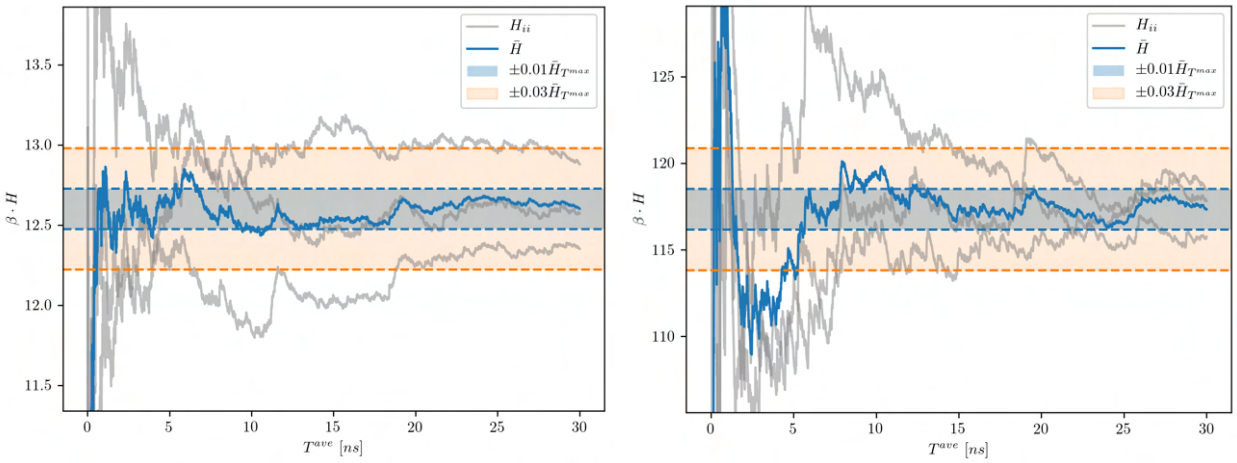

(a) DCE, 2xCCl clustering.

(b) $\mathrm{H_2O}$, molecular clustering.

Figure 3.8 – Relative convergence of the dipole fluctuation matrix $\mathbf{H}$ and the average over its trace, $\bar{H}$, for DCEBULK (left) and H2OBULK (right) bulk simulation boxes for $\mathrm{H_2O}$ and DCE. For DCEBULK a confident convergence of $\bar{H}$ into the $\pm$ 1% channel is achieved after roughly 10 ns, the time needed to converge the same expressions for H2OBULK is achieved after 20 ns.

It is visible that for both the H_2O and DCE case, the fluctuation terms are subject to a slow convergence of several nanoseconds. While in the case of DCEBULK a confident convergence of $\bar{H}$ into the $\pm$ 1% channel is achieved after roughly 10 ns, the time needed to converge the same expressions for H2OBULK is achieved after 20 ns, even though the number of H_2O molecules is almost six-fold the number of DCE molecules. Figure 3.8 also shows that the individual components H_{ii} still visibly fluctuate outside this channel. The slow convergence of the H_{ii} can be attributed to their quadratic nature since they represent time-correlation functions of second order. This observation is well understood and documented in literature [39, 51–74]. In order to account for the already considerable cost of simulating a 30 ns trajectory, the $\pm$ 3% confidence intervals for H_{ii} and $\pm$ 1% confidence intervals for $\bar{H}$ were considered sufficient.

3.5 Fluctuation formula benchmarks for the interfacial permittivity

In contrast to the isotropic bulk systems treated above, the dielectric response of less symmetric systems is anisotropic. The permittivity can then no longer be expressed as a scalar ε but needs to be treated as a space dependent 3x3 tensor $\boldsymbol{\varepsilon}$ in the most general case. In the case of the DCEH2OINT interfacial system, each phase is still infinitely expanded in the xy-plane. However, translational invariance is broken in z-direction. This implies that, in contrast to the bulk systems, translational invariance of $\boldsymbol{\varepsilon}$ can no longer be assumed over the entire simulation box because the $\mathrm{H_2O}$ and DCE phases' structure changes anisotropically towards the phase transition region.

To recall from section 2.6.2, the local permittivity tensor $\boldsymbol{\varepsilon^l}$ of such a slab-like system simulated in Ewald geometry takes the form

$$\boldsymbol{\varepsilon^l} = \begin{pmatrix} \varepsilon^l_{\parallel} & 0 & 0 \\ 0 & \varepsilon^l_{\parallel} & 0 \\ 0 & 0 & \varepsilon^l_{\perp} \end{pmatrix} \tag{3.2}$$

with the interface-parallel component $\varepsilon^l_{\parallel}$ given in (2.108) by

$$\varepsilon^l_{\parallel}(z) = 1 + 4\pi h_{\parallel}(z) \tag{3.3}$$

and the interface-perpendicular component $\varepsilon^l_{\perp}$ given in (2.110) by

$$(\varepsilon^l_{\perp})^{-1} = 1 - 4\pi \frac{h_{\perp}(z)}{(1 + 4\pi H_{\perp}/V)} \tag{3.4}$$

As mentioned in section 2.6.2, the reason for the inverse in (3.4) is numerical stability. It jumps the eye that equation (3.3) is functionally identical to the bulk formula (3.1) if the fluctuation term for the polarization density $h_{\parallel}$ is substituted for the fluctuation term of the total dipole moment H. This is intuitively understood if the periodic slab system is viewed as a plate capacitor enclosing a multi-layered dielectric stacked in z-direction. As shown by Neumann and Steinhauser [49], the use of the Ewald lattice summation imposes conducting boundary conditions at infinity. A conducting surface is equivalent to having a dielectric boundary with an infinite dielectric $\varepsilon = \infty$. A constant external field $\mathbf{E}^{\mathbf{0}}_{\parallel}$ applied in x-direction is thus equivalent to charging the yz-plane at $x = \pm\infty$. These boundary conditions are the same in both the bulk and the slab system. For the slab system, the charge on the capacitor plates at infinity would vary to fulfill Maxwell boundary conditions but the dielectric phase boundaries along the z-axis of the stacked dielectric slabs are never crossed by the field lines of $\mathbf{E}^{\mathbf{0}}_{\parallel}$. Both the bulk and slab system thus see the same boundary conditions for parallel fields.

This is not the case for a field $\mathbf{E}_\perp^0$ applied along the z-axis over the stacked dielectric layers. Here, the field lines do cross the boundaries between slabs while the bulk system still only sees its pair of conducting boundary conditions at $z = \pm\infty$. The fluctuation formulas for the slab and bulk system hence deviate functionally from one another.

If (3.3) and (3.4) are applied to a bulk trajectory like H2OBULK or DCEBULK with only one slab spanning the entire simulation box, they both collapse to the CM bulk fluctuation formula (3.1). If all off-diagonal elements of the permittivity tensor $\boldsymbol{\varepsilon}^l$ are zero, the fluctuation formulas for $\varepsilon_\parallel^l$ and $\varepsilon_\perp$ are furthermore completely decoupled.

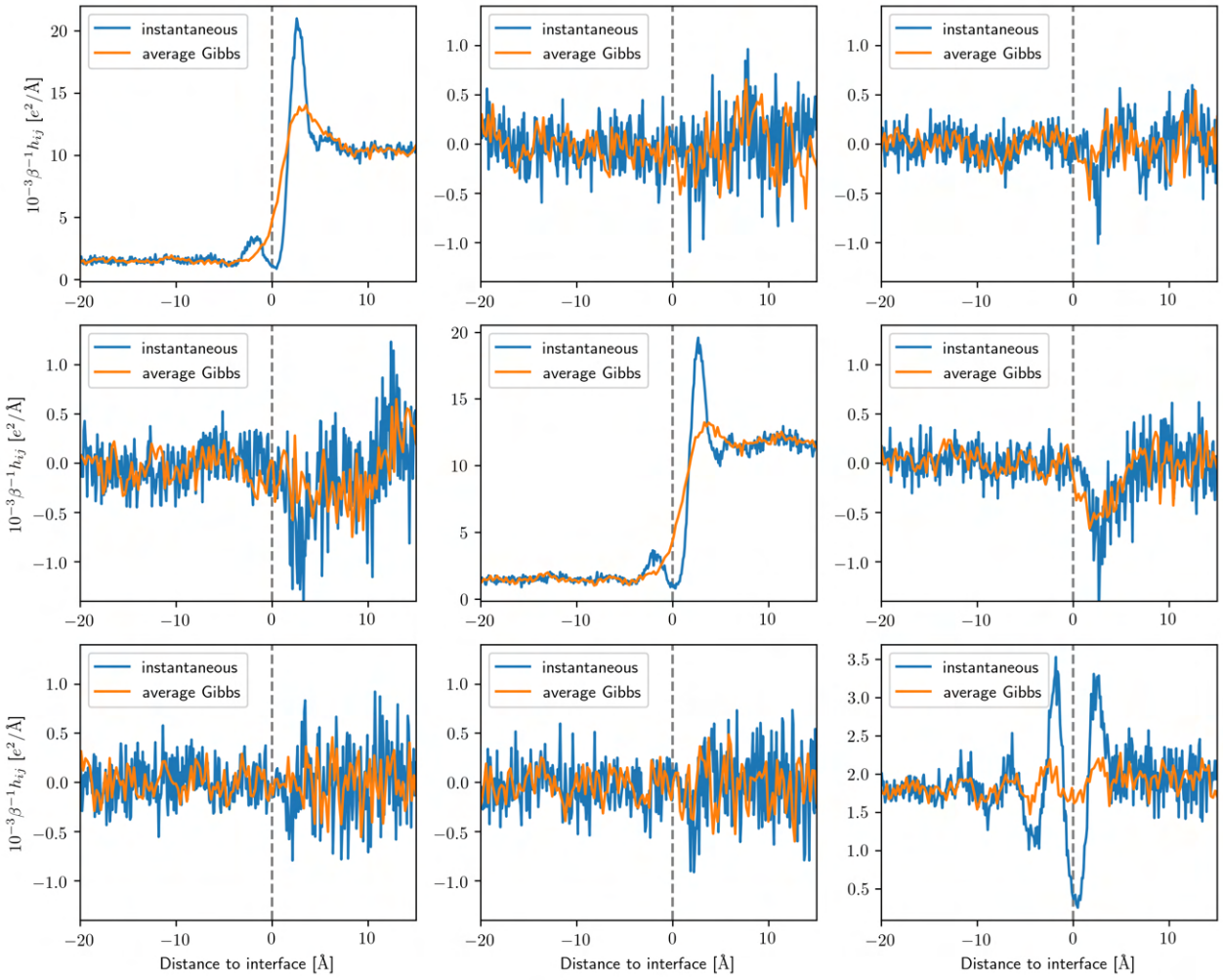

Figure 3.9 – Components of the polarization fluctuation matrix $\mathbf{h}$ as calculated from the DCEH2OINT trajectory, molecularly clustered. The H_2O phase occupies the positive half-space and the DCE phase occupies the negative half-space. In line with the observations made in figure 3.8, the results in the water phase are noisier. A clear phase transition separating the phases is additionally visible in windowed averages of $h_\parallel$ but not in $h_\perp$. All cross-contributions h_{ij} are negligible.

All nine components of the polarization fluctuation matrix $\mathbf{h}$ as calculated from the DCEH2OINT trajectory, molecularly clustered, are plotted in figure 3.9 with respect to interface distance. As discussed in section 3.3, the H_2O phase occupies the positive half-space while the DCE phase occupies the negative half-space. Each $\mathbf{h}$ component is portrayed with respect to instantaneous

LLI distance, represented by the blue line, and the average Gibbs LLI distance represented by the orange line. The fluctuation term for one specific z-distance is calculated from all molecules whose center of mass lies within a slab that is bounded by two z-shifted copies of the LLI. In both cases, this shift defining the the slab-thickness was chosen to be 0.23 Å . The slab volume of the instantaneous LLI is fluctuating over the course of the trajectory. The average slab volume over the entire trajectory is used for V in (3.3) and (3.4) in this case. The volume normalization in the polarization fluctuation terms $\mathbf{h}$ is performed using the instantaneous slab volume. As shown in figure 3.5, the deviations of the instantaneous LLI from a mathematical plane are rather small. The plate capacitor model thus remains a good approximation for the slab system, both with instantaneous and Gibbs LLI reference. From 3.9 various important observations can be made. The diagonal elements of $\mathbf{h}$ parallel to the interface, $h_{\parallel}$, equilibrate to distinct values at bulk distances, visibly separating the H_2O and DCE phase. As expected, these values are identical for both the Gibbs and instantaneous LLI reference. Towards the interface, both these parallel components of $\mathbf{h}$ exhibit multiple peaks in the blue line, that mainly follow the structure of the density solvation shells but are disproportionately more pronounced in the H_2O phase. The curves for both h_{xx} and h_{yy} are also comparable in value as the symmetry of the slab system suggests. Interestingly, the orange Gibbs LLI profiles for h_{xx} and h_{yy} also peak in the water phase at a distance of ~3.5 Å , even though these peaks do not show in the density profiles of figure 3.6. This suggests that the preferential orientation of molecular dipoles at the interface is not fully reflected in the number density profile, even in the Gibbs LLI reference system with its sinusoidal transition between constant bulk number densities. A notable change in value of $h_{\perp} = h_{zz}$ separating the bulk phases of H_2O and DCE is not observed, apart from fluctuations over the phase transition, which are significantly more pronounced in the instantaneous than the Gibbs LLI reference system. Compared to its parallel counterparts, the overall absolute values of $h_{\perp}$ are also significantly smaller.

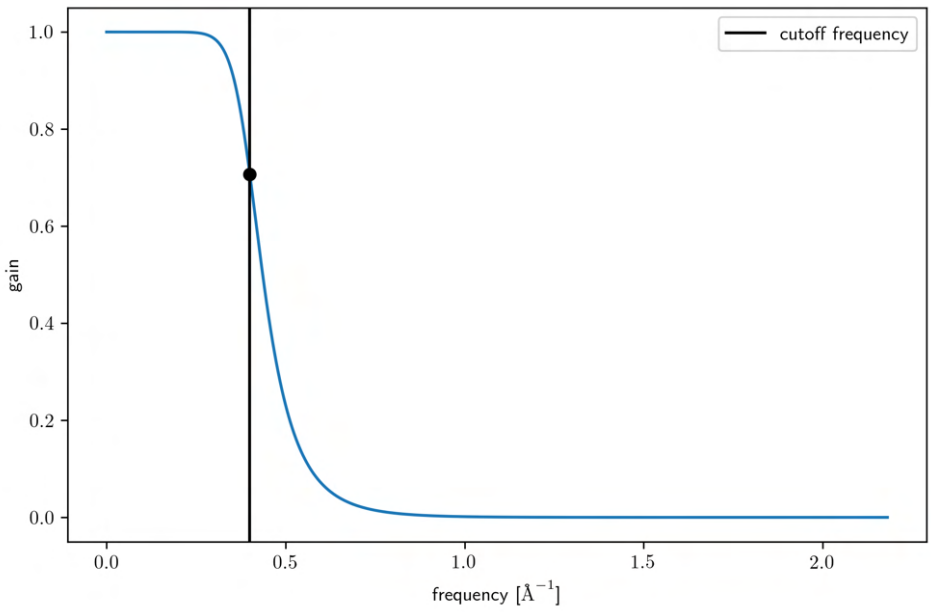

Figure 3.10 – Sixth order Butterworth lowpass filter with cutoff frequency at 1/2.5 Å^{-1} to reduce noise in ε.

While the average value of $h_\perp$ deep in the DCE phase is similar to its parallel equivalent $h_\parallel$, the values at bulk water distances is smaller by roughly a factor of five. The overall signal-to-noise ratio is also significantly worse in comparison, particularly in the H_2O phase. Figure 3.9 further shows that the off-diagonal cross terms h_{ij} are small compared to the on-diagonal elements. They never exhibit values greater than 5% of their on-diagonal counterparts in the same slab. This further supports the use of the plate capacitor fluctuation formulas (2.108) and (2.109) which assume all off-diagonal tensor elements to be zero due to symmetry reasons.

With $\mathbf{h}$, $\varepsilon^l_\parallel$ and $\varepsilon^l_\perp$ can be calculated according to the SF fluctuation formulas (3.3) and (3.4). The results for $\varepsilon^l_\parallel$ are shown in blue on the left axis, while number densities are plotted in grey on the right axis for reference. The horizontal red lines left and right of the origin mark the values measured for the dielectric constant of the bulk systems presented in table 3.7. The canonical average $\varepsilon^l_\parallel = (\varepsilon^l_{xx} + \varepsilon^l_{yy})/2$ is taken in order to improve statistics. This is valid due to the translational invariance in the xy-plane of the assumed slab model. A 6th order Butterworth lowpass filter as portrayed in figure 3.10 is additionally applied to the calculated permittivities and plotted in orange. The cutoff frequency is chosen at 1/2.5 $Å^{-1}$ since this corresponds to the extents of the H_2O molecule, the smallest cluster present in the simulation. Variations in ε on submolecular lengthscales are assumed to have no influence on the orientational polarization response of the medium. Higher frequencies are thus attributed to noise and suppressed. In order to prevent phase distortion in the filtered signal, the lowpass filter is combined with a forward-backward filter.

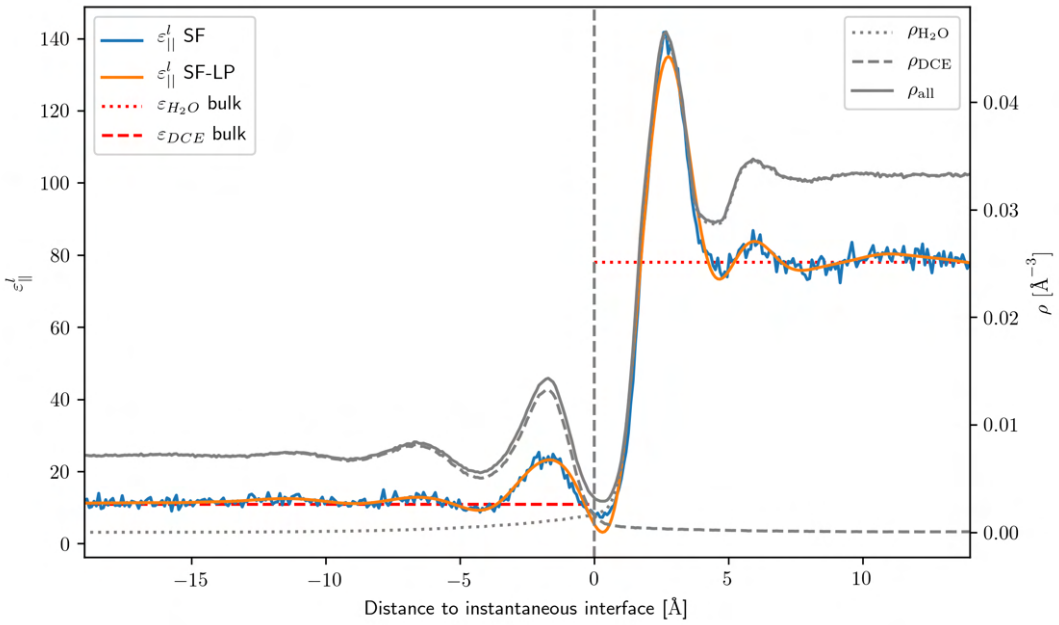

Figure 3.11 – $\varepsilon^l_\parallel$ profile calculated using equation (3.3) for DCEH2OINT, molecularly clustered, in the instantaneous LLI reference system. The pure signal is portrayed in blue and with a Butterworth lowpass filter applied in orange. The first solvation shell is the most pronounced in both the DCE phase on the left with a peak of $\varepsilon^l_\parallel = 22$ and the H_2O phase on the right with a peak of $\varepsilon^l_\parallel = 140$. Between the first solvation shells of the both phases, a depletion region where $\varepsilon^l_\parallel \approx 5$ forms the global minimum of the dielectric response.

The profiles for $\varepsilon^l_\parallel$ follow $h_\parallel$ since the two quantities are trivially linked by (3.3). Results in the instantaneous LLI reference system are portrayed in figure 3.11. The permittivity profile in this case

follows the number density profile with visible peaks towards the interface. The first solvation shell is the most pronounced in both the DCE phase on the left with a peak of $\varepsilon_{\parallel}^{l} = 22$ and the H_2O phase on the right with a peak of $\varepsilon_{\parallel}^{l} = 140$. After that the amplitude of oscillations decays rapidly further away from the interface and the value of $\varepsilon_{\parallel}^{l}$ approaches the scalar $\varepsilon^{\text{bulk}}$ in both phases. Oscillations in $\varepsilon_{\parallel}^{l}$ with minor amplitude prevail further into bulk than fluctuations in the molecular number densities. Between the first solvation shells of the both phases, a depletion region where $\varepsilon_{\parallel}^{l} \approx 5$ forms the global minimum of the dielectric response. This can be mostly attributed to a lack of orientable molecules in this region. Similar depletion regions have been observed in simulations of diamond interfacing water [119] and other solid/liquid interfaces [74, 151, 155] and recently reported experimentally by Fumagalli *et al.* for water in immediate vicinity of two-dimensional boron nitride films [29].

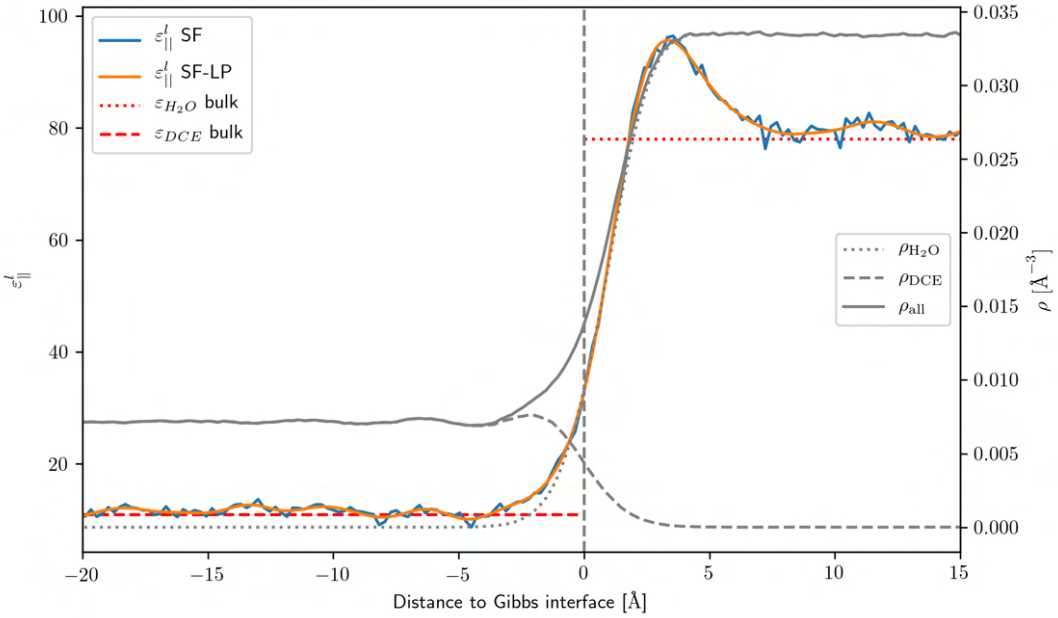

Figure 3.12 – $\varepsilon_{\parallel}^{l}$ profile calculated using equation (3.3) for DCEH2OINT, molecularly clustered, in the Gibbs LLI reference system. The pure signal is portrayed in blue and with a Butterworth lowpass filter applied in orange. Even though all density oscillations are averaged out, the dielectric constant exhibits a clear peak with a maximum value of $\varepsilon_{\parallel}^{l} = 96$ at 3.5 Å away from the interface before retracting to minor oscillations around the H_2O bulk value of $\varepsilon^{\text{bulk}} = 78.1$. Similar peaks in the DCE phase are not observed.

The corresponding results in the Gibbs LLI reference system are portrayed in figure 3.12, the raw profile as calculated by the SF equation (3.3) again represented by the blue line and with the lowpass filter applied in orange. Even though all density oscillations are averaged out as is visible in the sinusoidal density profile portrayed in grey on the right axis, the dielectric constant exhibits a clear peak with a maximum value of $\varepsilon_{\parallel}^{l} = 96$ at 3.5 Å away from the interface before retracting to minor oscillations around the H_2O bulk value of $\varepsilon^{\text{bulk}} = 78.1$. This clearly visualizes the difference in character of $\mathbf{h}$, and consequently $\boldsymbol{\varepsilon}$, as a second order correlation function compared to the zero-order density profile. Similar peaks in the DCE phase are not observed.

For both LLI reference systems, $\varepsilon_{\parallel}^{l}$ is always positive and greater than one. This means the polarization response is never greater than the $\mathbf{D}$ field created by the free charge carriers of the system.

It is thus compatible with the classical framework of Maxwellian electrostatics in matter. In both 3.11 and 3.12, fluctuations of $\varepsilon^l_{\parallel}$ around the bulk value are visible far into the H_2O phase, an effect that is a consequence of the locality assumption for $\boldsymbol{\varepsilon^l}$ as for example shown by Schaaf *et al.* [84] in the case of spherically confined water. Other reasons might include artifacts due to deviations from the perfect capacitor model due to interfacial irregularities or ripples which might result in perturbations of electric field lines.

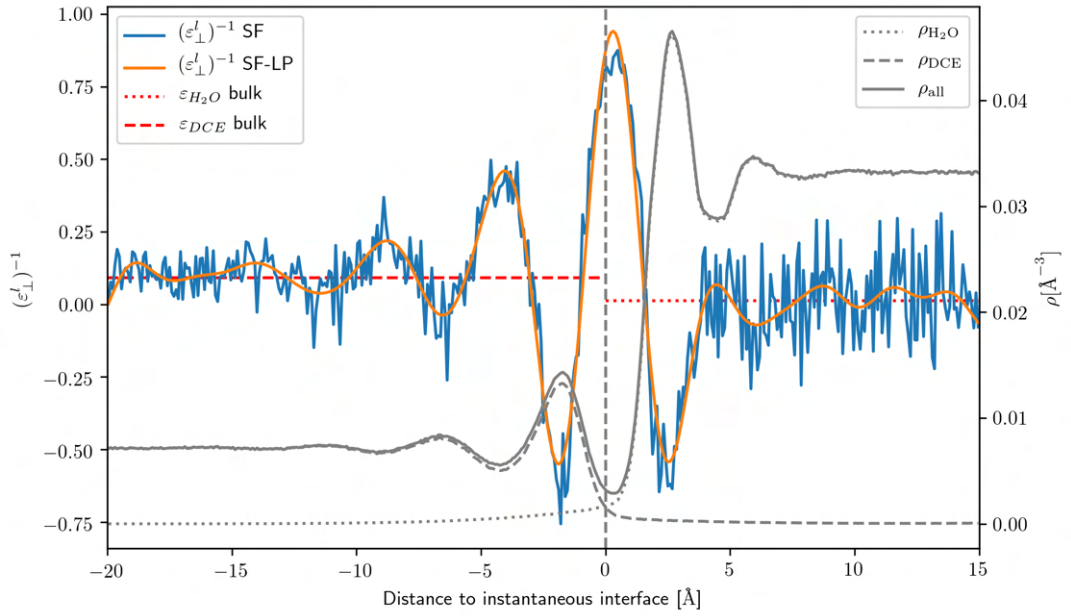

Figure 3.13 – $\varepsilon^l_\perp$ profile calculated using equation (3.4) for DCEH2OINT, molecularly clustered, in the instantaneous LLI reference system. The pure signal is portrayed in blue and with a Butterworth lowpass filter applied in orange. $(\varepsilon^l_\perp)^{-1}$ turns negative with its minimum located roughly at the peak of the first solvation shell in both phases. This negative correlation between the polarization $\mathbf{P}$ and the applied field $\mathbf{E^0}$ implies that $\mathbf{P}$ has an amplifying effect if $\mathbf{E^0}$ is applied, breaking energy conservation.

The inverse perpendicular component of the SF permittivity tensor $(\varepsilon^l_\perp)^{-1}$ can be calculated from h_{zz} according to (3.4). Its profile is portrayed in figure 3.13 for the instantaneous LLI reference system and in figure 3.14 for the Gibbs LLI reference system. Inspecting the $(\varepsilon^l_\perp)^{-1}$ profile for the instantaneous LLI, a clear qualitative difference to $\varepsilon^l_{\parallel}$ is visible. Most prominent, $(\varepsilon^l_\perp)^{-1}$ turns negative with its minimum located roughly at the peak of the first solvation shell in both phases. In both DCE and H_2O $(\varepsilon^l_\perp)^{-1}$ bottoms at roughly -0.5. This negative correlation between the polarization $\mathbf{P}$ and the applied field $\mathbf{E^0}$ implies that $\mathbf{P}$ has an amplifying effect if $\mathbf{E^0}$ is applied. In the absence of free charge, this would break the conservation of energy in classical electrostatics. In order to reach the positive reference bulk values indicated in red as well as its global maximum of 0.9 opposite the global density minimum, $(\varepsilon^l_\perp)^{-1}$ also exhibits multiple zero-crossings. This implies infinite permittivity $\varepsilon^l_\perp = \infty$, which in the present slab model correspond to tinfoil conducting sheets at the zero-crossings of $(\varepsilon^l_\perp)^{-1}$. Applying a constant field $\mathbf{E^0}$ from one direction would lead to a changing sign in the polarization profile. This would only be possible if the tinfoil sheets would carry free charge carriers. Even though the examined DCEH2OINT trajectory exclusively consists of neutral DCE and H_2O molecules, additional free charge would have to be introduced to accommodate for the non-Maxwellian behaviour of a granular dielectric.

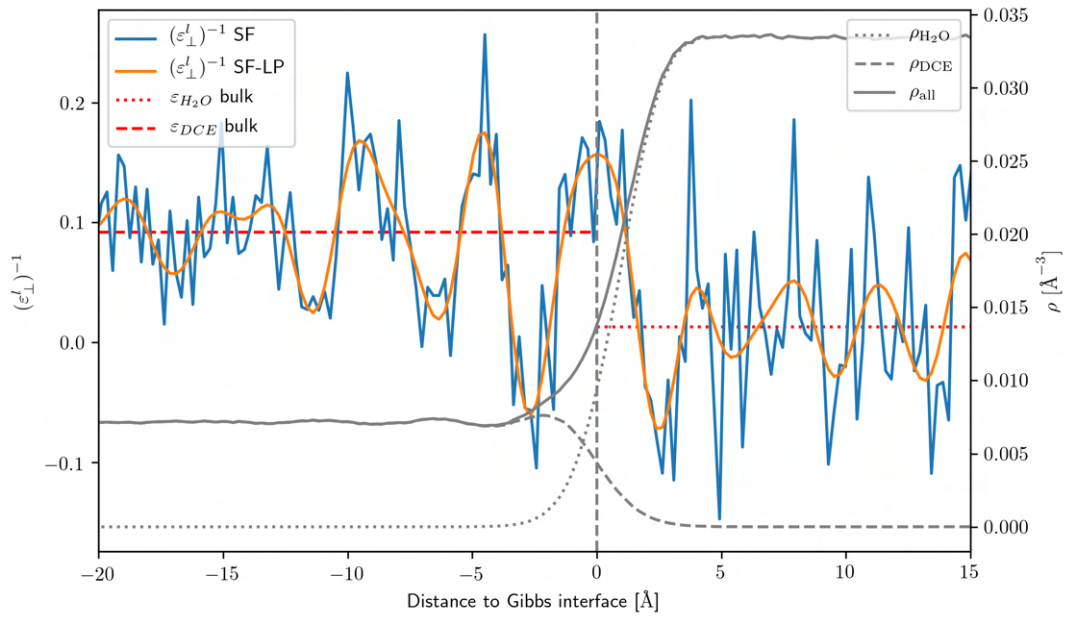

Figure 3.14 – $\varepsilon^l_\perp$ profile calculated using equation (3.4) for DCEH2OINT, molecularly clustered, in the Gibbs LLI reference system. The pure signal is portrayed in blue and with a Butterworth lowpass filter applied in orange. The profile is qualitatively identical compared to the instantaneous LLI reference system, albeit with more smeared out peaks.

A qualitatively identical assessment can be made for the $(\varepsilon^l_\perp)^{-1}$ profile for the Gibbs LLI reference system portrayed in figure 3.14, albeit with more smeared out peaks. Zero-crossings and negative $\varepsilon^l_\perp$ are still observed. The smaller amplitude of the oscillations highlights the considerable lower signal-to-noise ratio of $\varepsilon^l_\perp$ compared to $\varepsilon^l_\parallel$. The numerical noise even exceeds the difference between bulk permittivities. The perpendicular component of the permittivity tensor is thus harder to converge and the predicted polarization response deviates from a Maxwellian dielectric in case of adjacent granular liquid phases. Its apparent unphysicality does not mean however that the calculated local $\varepsilon^l_\perp$ can not be used to quantify the polarization response to an external field. It needs to be acknowledged however, that additional couplings to $\mathbf{E^0}$ take place in granular dielectrics that can not be represented by a local proportionality constant $\boldsymbol{\varepsilon^l}$ between $\mathbf{P}$ and $\mathbf{E^0}$. In the interfacial region, these contributions don't average out due to symmetry breaking which leads to coupled energy reservoirs not accounted for in a Maxwellian dielectric. At the core of the breakdown of the Maxwellian picture lies that at the small interfacial distances of several Angstrom, the separation into free and bound charge is no longer valid because intra-molecular distance can no longer be assumed to be sufficiently small compared to the distance between cluster center and observer.

Chapter 4

Folding the Polarization with the Dipole-Dipole Interaction Tensor

While approaches presented in the previous two chapters for calculating a local dielectric constant have been proven very successful and have been frequently employed in confined liquid systems, they nevertheless only apply to very specific system geometries. The derivation of these formulas is specific to each setup and the complexity of the derivation is determined by the analytical solution to the corresponding electrostatic problem. All of them rely on the decoupling of the dielectric tensor into parallel and perpendicular components, effectively solving a dielectric plate capacitor problem for various sets of coordinates. Among other assumptions, like the Ewald geometry dictating conducting boundary conditions, off-diagonal elements of the dielectric tensor are *a priori* assumed to be zero. In this chapter an alternative approach is presented, which solves the general electrostatic problem based on polarization fluctuations and gives access to a full, spatially resolved dielectric tensor for arbitrary geometries. This approach based on discretizing the dipole-dipole interaction tensor and subsequently turning the basic relation of electrostatics into a kernel-convolution problem is presented in the following. All formulas are derived for systems in Ewald geometry but the presented approach is transferable to any kind of pair-wise Coulomb potential.

4.1 Formalism

As was shown in section 2.4, a system's linear polarization response $\mathbf{\Delta P}$ to an external perturbation in form of a static cavity field $\mathbf{E^c}$ can be established via a local dielectric susceptibility function $\boldsymbol{\chi}^{\boldsymbol{l}}(\mathbf{r})$ via

$$\Delta P_i(\mathbf{r}, E_j^c) = \chi_{ij}^l(\mathbf{r}) \left[E_j^c + \int_V d\mathbf{r}' T_{jk}(\mathbf{r} - \mathbf{r}') \Delta P_k(\mathbf{r}', E_j^c) \right] \tag{4.1}$$

Both $\boldsymbol{\chi}^l$ and the dipole-dipole interaction tensor $\mathbf{T}$ represent 3x3 tensors while $\boldsymbol{\Delta}\mathbf{P}$ and $\mathbf{E^c}$ comprise 3-dimensional vectors. In addition to the above electrostatic relationship, linear response theory provides the expression (2.84) for the excess polarization $\boldsymbol{\Delta}\mathbf{P}$ in terms of the polarization fluctuation matrix $\mathbf{h}$:

$$\Delta P_i(\mathbf{r}, E_j^c) = \beta \left[\langle P_i(\mathbf{r}) M_j \rangle - \langle P_i(\mathbf{r}) \rangle \langle M_j \rangle\right] E_j^c = h_{ij}(\mathbf{r}) E_j^c \tag{4.2}$$

Inserting (4.2) in (4.1) yields

$$\begin{aligned} h_{ij}(\mathbf{r}) E_j^c &= \chi_{ij}^l(\mathbf{r}) \left[E_j^c + \int_V d\mathbf{r}' T_{jk}(\mathbf{r} - \mathbf{r}') h_{kj}(\mathbf{r}') E_j^c \right] \\ h_{ij}(\mathbf{r}) &= \chi_{ij}^l(\mathbf{r}) \left[1 + \int_V d\mathbf{r}' T_{jk}(\mathbf{r} - \mathbf{r}') h_{kj}(\mathbf{r}') \right] \end{aligned} \tag{4.3}$$

The electric field in above equation cancels out due to the linearity of the sum under the convolution integral and the fact that the external field $\mathbf{E^c}$ is identical in both (4.2) and (4.3).

Due to the spatial dependence of $\boldsymbol{\chi}^l$, equation (4.3) contains both a point-wise multiplication and a convolution in $\mathbf{r}$. A transformation to Fourier space in order to exploit the convolution theorem hence does not provide the desired simplification because the convolution under the integral would merely shift to a convolution with $\boldsymbol{\chi}^l$. The ansatz of Neumann [48, 49] used to calculate the bulk dielectric constant in (2.95) is not applicable to solve (4.3) for $\boldsymbol{\chi}^l$. In order to circumvent this issue, an attempt is made to directly solve the convolution integral in (4.3) by viewing it as a kernel-convolution problem.

Besides the ensemble average, the calculation of the polarization density fluctuations $\mathbf{h}$ require a spatial averaging over finite domains in space. If without loss of generality these domains are chosen to be regularly spaced 3-dimensional voxels, the integral I in (4.3) can be discretized and reads

$$I(\mathbf{r}) = \int_V d\mathbf{r}' T_{jk}(\mathbf{r} - \mathbf{r}') h_{kj}(\mathbf{r}') = \sum_{(m',n',p')} \int_{x_n^-}^{x_n^+} \int_{y_m^-}^{y_m^+} \int_{z_p^-}^{z_p^+} T_{jk}(\mathbf{r} - \mathbf{r}') h_{kj}(\mathbf{r}') dx' dy' dz' \tag{4.4}$$

The indices (m, n, p) represent the voxel indices in each dimension. Each voxel is defined such that its volume is given by

$$\begin{aligned} V^{\mathrm{vox}}[m,n,p] &= [x_n - \Delta_x, x_n + \Delta_x] \times [y_m - \Delta_y, y_m + \Delta_y] \times [z_p - \Delta_z, z_p + \Delta_z] \\ &= [x_n^-, x_n^+] \times [y_m^-, y_m^+] \times [z_p^-, z_p^+] \end{aligned} \tag{4.5}$$

where the discretized spatial vector $\hat{\mathbf{r}} = \mathbf{r}[n,m,p]$ constitutes the voxel center and Δ_i defines the voxel half-length. The polarization fluctuation term $\mathbf{h}(\mathbf{r}') = \mathbf{h}[m',n',p']$ is constant over V^{vox} as it represents the volume the polarization is spatially averaged over. It can hence be pulled out of the integral allowing for the integration over the dipole-dipole interaction tensor $\mathbf{T}$. Then (4.4) takes the form

$$\begin{aligned} I[m,n,p] &= \sum_{(m',n',p')} \int_{x_n^-}^{x_n^+} \int_{y_m^-}^{y_m^+} \int_{z_p^-}^{z_p^+} T_{jk}(\mathbf{r} - \mathbf{r}') dx' dy' dz' \; h_{kj}[m,n,p] \\ &= \sum_{(m',n',p')} \hat{T}_{jk}[n-n', m-m', p-p'] h_{kj}[m,n,p] \\ &= (\hat{T}_{jk} * h_{kj})[n,m,p] \end{aligned} \tag{4.6}$$

Using this result, (4.3) can be written in the discretized form

$$h_{ij}[n,m,p] = \chi_{ij}^l[n,m,p] \left(1 + (\hat{T}_{jk} * h_{kj})[n,m,p]\right) \tag{4.7}$$

which can be solved for $\boldsymbol{\chi}$ via

$$\chi_{ij}^l[n,m,p] = h_{ij}[n,m,p] \left(1 + (\hat{T}_{jk} * h_{kj})[n,m,p]\right)^{-1} \tag{4.8}$$

Since $\boldsymbol{\chi}$ and ε are trivially linked this also provides a discretized fluctuation formula for the local permittivity $\boldsymbol{\varepsilon^l}$,

$$\varepsilon_{ij}^l[n,m,p] = 1 + 4\pi h_{ij}[n,m,p] \left(1 + (\hat{T}_{jk} * h_{kj})[n,m,p]\right)^{-1} \tag{4.9}$$

The continuous convolution $\mathbf{T}$ and $\mathbf{h}$ in (4.1) is replaced by a discrete convolution of $\hat{\mathbf{T}}$ and $\mathbf{h}$ in (4.8) and (4.9). If regularly spaced voxels are chosen as the spatial averaging volume for $\mathbf{h}$, this discrete convolution can be efficiently solved via Fast Fourier Transform (FFT) [176]. The piecewise

integrated dipole-dipole interaction tensor $\hat{\mathbf{T}}$ is furthermore independent of $\mathbf{h}$ and only indirectly coupled to the simulation performed through the functional form of the long-range Coulomb interaction. As an example, in Ewald geometry $\hat{\mathbf{T}}$ depends on the size of the simulation box and the Ewald screening parameter employed but it is independent of temperature, number of particles or the phase composition in simulations containing interfaces. To view it as a pretrained kernel that is convoluted with the simulation-specific polarization fluctuation matrix $\mathbf{h}$ is thus a good comparison.

In order to use (4.9) in an actual integration, the MxNxP tensors $\mathbf{h}$ and $\hat{\mathbf{T}}$ need to be known. Analogously to the slabwise binning employed in previous chapters, the polarization fluctuation matrix $\mathbf{h}$ can be calculated binned in the desired resolution. Naturally a trade-off between numerical accuracy and spatial resolution remains, depending on system size and length of the trajectory used.

The elements of the discretized dipole-dipole interaction tensor integral $\hat{\mathbf{T}}$ are derived in the next chapter for the Ewald dipole-dipole interaction tensor $\mathbf{T^E}$. While the approach is in no way limited to this choice of $\mathbf{T}$, it is presented here since all trajectories are simulated using Ewald summation for long-range electrostatics. It furthermore should be noted that while a regular grid is advantageous because the discrete convolution can be solved via FFT, this approach is not limited by different spatial averaging volumes for $\mathbf{h}$.

4.2 Projection of the Ewald dipole-dipole interaction tensor onto a regular grid

As shown in section 2.5.1, the dipole-dipole interaction tensor in Ewald geometry can be separated into the three separate contributions

$$T_{ij}^{\mathrm{E}} = T_{ij}^{\mathrm{E1}} + T_{ij}^{\mathrm{E2}} + T_{ij}^{\mathrm{E3}} \tag{4.10}$$

where $\mathbf{T^{E1}}$ represents the k-space contribution, $\mathbf{T^{E2}}$ the real-space contribution and $\mathbf{T^{E3}}$ the self-interaction that needs to be subtracted [48, 142]. The individual contributions are truncated at the cutoff radii k_c for $\mathbf{T^{E1}}$ in reciprocal space as well as r_c for $\mathbf{T^{E2}}$ and $\mathbf{T^{E3}}$ in real space. In order to comply with the nearest image convention of the Ewald sum, the condition $r_c \leq L/2$ needs to be met [140].

Following the name convention introduced in chapter 2, the k-space contribution is given by

$$T_{ij}^{\mathrm{E1}} = -\frac{8\pi}{V^{\mathrm{box}}} \sum_{\mathbf{k}>0} \exp\left(-\frac{k^2}{4\eta^2}\right) \cos\left(\mathbf{kr}\right) \frac{k_i k_j}{k^2} \qquad , \qquad k < k_c \tag{4.11}$$

where the reciprocal vectors $\mathbf{k}$ are defined as linear combinations of integer multiples of the unit lattice vectors $\mathbf{e}_{\mathbf{k_i}} = 2\pi/L_i, i \in \{x, y, z\}$, η represents the Ewald screening parameter and V^{box} the volume of the simulation box.

The real space contribution is given by

$$T_{ij}^{\mathrm{E2}} = \left[\mathrm{erfc}\left(\eta r\right) + \frac{2}{\sqrt{\pi}}\left(\eta r + \frac{2}{3}\eta^3 r^3\right)\exp\left(-\eta^2 r^2\right)\right] T_{ij}^{\mathrm{dd}} = \rho(r) T_{ij}^{\mathrm{dd}} \quad , \quad r < r_c \tag{4.12}$$

where $\mathbf{T^{dd}}$ represents the general 3x3 dipole-dipole interaction tensor introduced in equation (2.51). The real-space Ewald contribution $\mathbf{T^{E2}}$ differs only in the radial factor $\rho(r)$ from $\mathbf{T^{dd}}$ for all nine elements of $\mathbf{T^{E2}}$. Recalling $r = \sqrt{x^2 + y^2 + z^2}$, one can see that ρ is an even function in cartesian coordinates, thus preserving the odd symmetry of $\mathbf{T^{dd}}$ in $\mathbf{T^{E2}}$. Apart from symmetry, $\mathbf{T^{E2}}$ also inherits the singularity of $\mathbf{T^{dd}}$ at the origin.

The Gaussian shielding term for compensation of the self-interaction only has an on-diagonal contribution and is given by

$$T_{ij}^{\mathrm{E3}} = T_{ii}^{\mathrm{E3}}\delta_{ij} = \frac{4\pi}{3}\left(\left(\frac{\eta}{\sqrt{\pi}}\right)^3 \exp\left(-\eta^2 r^2\right)\right) \quad , \quad r < r_c \tag{4.13}$$

In order to calculate the elements $\hat{\mathbf{T}}[m, n, p]$ for the Ewald dipole-dipole interaction tensor its three contributions in (4.10) need to be integrated over the voxel volume $V^{\mathrm{vox}}[m, n, p]$. Technically, the cutoff radius r_c may lead to discontinuities in the real-space integrands $\mathbf{T^{E2}}$ and $\mathbf{T^{E3}}$ for certain voxels. We will ignore this cutoff when formulating these integrals here and will return to their treatment in the following section.

The voxel integral over the k-space term $\mathbf{T^{E1}}$ has the solution

$$\begin{aligned}
\hat{T}_{ij}^{\mathrm{E1}}[m, n, p] &= \int_{x_n^-}^{x_n^+}\int_{y_m^-}^{y_m^+}\int_{z_p^-}^{z_p^+} T_{ij}^{\mathrm{E1}}(\mathbf{r})\, d\mathbf{r} \\
&= -\frac{8\pi}{V^{\mathrm{box}}}\sum_{|k|>0}\exp\left(-\frac{k^2}{4\eta^2}\right)\frac{k_i k_j}{k^2}\int_{x_n^-}^{x_n^+}\int_{y_m^-}^{y_m^+}\int_{z_p^-}^{z_p^+}\cos\left(\mathbf{kr}\right) d\mathbf{r} \\
&= -\frac{64\pi}{V^{\mathrm{box}}}\sum_{|k|>0}\exp\left(-\frac{k^2}{4\eta^2}\right)\frac{k_i k_j}{k^2}\cos\left(\mathbf{k\hat{r}}\right)\prod_{l\in\{x,y,z\}}\Delta_l \mathrm{sinc}(k_l\Delta_l)
\end{aligned} \tag{4.14}$$

The $\mathbf{k}$-summands differ from the summands of $\mathbf{T^{E1}}$ only in the product over the sinc functions

$$\mathrm{sinc}(k_l\Delta_l) = \frac{\sin(k_l\Delta_l)}{k_l\Delta_l} \tag{4.15}$$

where the value at the singularity $k_l\Delta_l = 0$ is defined as

$$\lim_{k_l\to 0} \frac{\sin(k_l\Delta_l)}{k_l\Delta_l} = 1 \qquad , \qquad \Delta_l \neq 0 \tag{4.16}$$

While individual components k_l of the k-space vector can be zero, we require a finite voxel size, $\Delta_l > 0$ always. This means that sinc is well defined and continuous as used in (4.14).

The roots of the sinc function are located at $k_l\Delta_l = n\pi, n \in \mathbb{Z}$. This is only achieved for $\Delta_l = L_l/2$, meaning in voxels spanning the entire simulation box in l-direction. This implicates that for such a voxel, the contribution to the sum (4.14) is zero for all $\mathbf{k}$-vectors with $k_l \neq 0$. As a consequence, if a single voxel spans the entire box, the k-space contribution (4.14) is zero since $\mathbf{k} = (0,0,0)$ is explicitly excluded. In a simulation setup, this situation would occur in a completely translationally invariant periodic bulk system like H2OBULK or DCEBULK.

The voxel integral over the self-interaction term $\mathbf{T^{E3}}$ is calculated similarly straightforward and has the analytic solution

$$\begin{aligned} \hat{T}^{\mathrm{E3}}_{ii}[m,n,p] &= \int_{x_n^-}^{x_n^+}\int_{y_m^-}^{y_m^+}\int_{z_p^-}^{z_p^+} T^{\mathrm{E3}}_{ij}(\mathbf{r})d\mathbf{r} \\ &= \frac{\pi}{6}\prod_{l\in\{x,y,z\}} (\mathrm{erf}(\eta(\hat{x}_l + \Delta_l)) - \mathrm{erf}(\eta((\hat{x}_l - \Delta_l))) \end{aligned} \tag{4.17}$$

where erf denotes the error function.

Contrary to $\hat{\mathbf{T}}^{\mathbf{E1}}$ and $\hat{\mathbf{T}}^{\mathbf{E3}}$ the calculation of the voxel integral over the real-space Ewald contribution $\hat{\mathbf{T}}^{\mathbf{E2}}$ requires additional diligence due to its singularity at the origin. The integration of (4.12) over the origin voxel $V^0 = V[0,0,0]$ needs to be treated individually. If we split off the integration over a sphere V^ϵ with radius $\epsilon < min\{\Delta_x, \Delta_y, \Delta_z\}$ around the origin, we can write

$$\begin{aligned}
\hat{T}_{ij}^{\mathrm{E2}}[0,0,0] &= \int_{-\Delta_x}^{\Delta_x}\int_{-\Delta_y}^{\Delta_y}\int_{-\Delta_z}^{\Delta_z} \rho(r) T_{ij}^{\mathrm{dd}}(\mathbf{r}) d\mathbf{r} \\
&= \int_{V^\epsilon} \rho(r) T_{ij}^{\mathrm{dd}}(\mathbf{r}) d\mathbf{r} + \int_{V^0 \setminus V^\epsilon} \rho(r) T_{ij}^{\mathrm{dd}}(\mathbf{r}) d\mathbf{r} \\
&= \frac{4\pi}{3}\int_{V^\epsilon} \rho(r)\delta_{ij}(\mathbf{r}) d\mathbf{r} + \int_{V^0 \setminus V^\epsilon} \rho(r) T_{ij}^{\mathrm{dd}}(\mathbf{r}) d\mathbf{r} \\
&= \frac{4\pi}{3}\rho(0) + \int_{V^0 \setminus V^\epsilon} \rho(r) T_{ij}^{\mathrm{dd}}(\mathbf{r}) d\mathbf{r} \\
&= \frac{4\pi}{3} + \int_{V^0 \setminus V^\epsilon} \rho(r) T_{ij}^{\mathrm{dd}}(\mathbf{r}) d\mathbf{r} \qquad (4.18)
\end{aligned}$$

where in the second line the definition of $\mathbf{T^{dd}}$ (2.51) and the identity (2.29) was used while δ is to be understood as a Dirac delta function. Since $\rho(0) = 1$, the contribution of the singularity to $\hat{T}_{ij}^{E2}$ is the same in Ewald and non-Ewald geometry and amounts to [23, 49, 130]

$$\lim_{\epsilon \to 0} \int_{V^\epsilon} T_{ij}^{\mathrm{E2}} d\mathbf{r} = \frac{4\pi}{3}\delta_{ij} \qquad (4.19)$$

Once the singularity is excluded, integrating $\mathbf{T^{E2}}$ over a spherical volume centered around the origin evaluates to zero due to the symmetry of $\mathbf{T^{dd}}$. The radius ϵ chosen in (4.18) therefore does not matter as long as it lies completely within the origin voxel V^0.

The integral of $\mathbf{T^{dd}}$ over V^0/V^ϵ is not automatically zero, even for homogeneous media. The reason that it evaluates to zero in the calculation of the bulk dielectric constant via the KF formula (2.99) even in rectangular simulation boxes using lattice summation techniques [47–49] is the use of the k-space cutoff k_c. In real-space, this geometry setup is equivalent to a large sphere filled by repeating primary simulation cells. Therefore ϵ can be chosen equal to this radius and the remainder integral vanishes.

For all other voxels, $\hat{\mathbf{T}}^{\mathbf{E2}}$ is well defined. However, the integral over the tensor elements must be computed numerically since there exists no analytical solution to the best of knowledge.

4.2.1 Grid geometry and classification of voxels

Depending on the continuity of the integrand and singularities in a voxel, different integration methods may apply. This classification is illustrated in figure 4.1 for cubic voxels sliced at $z = 0$. Here, four distinct voxel types can be identified.

The real-space integrands $\mathbf{T^{E2}}$ and $\mathbf{T^{E3}}$ are both truncated at $r = r_c$, hence their contribution to $\mathbf{T^{E}}[m,n,p]$ may vary. For the voxels marked blue in figure 4.1 that lie entirely within the sphere of r_c,

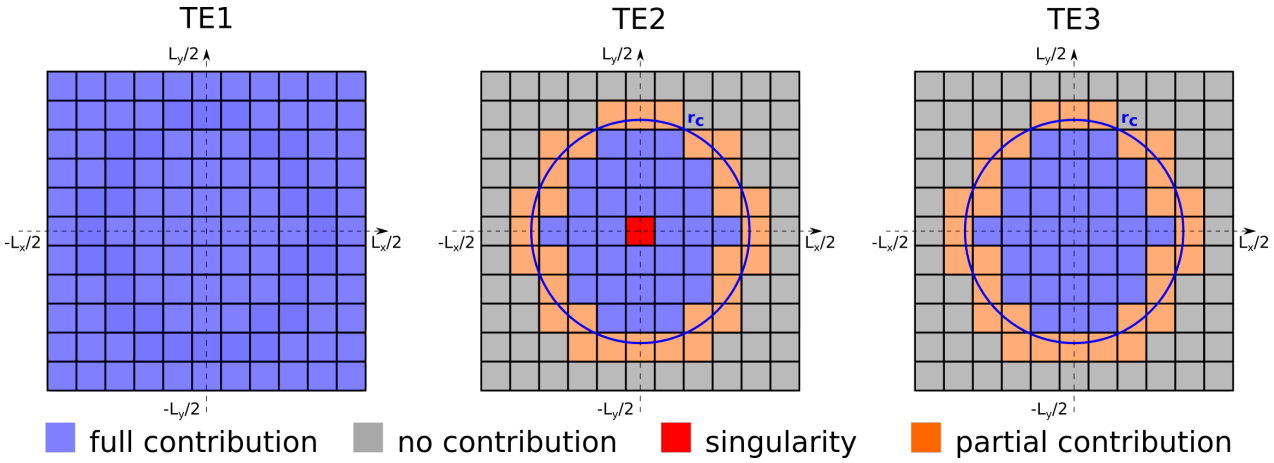

Figure 4.1 – Integration over $\mathbf{T^E}$ for cubic voxels sliced at $z = 0$. The real-space integrands $\mathbf{T^{E2}}$ and $\mathbf{T^{E3}}$ are both truncated at $r = r_c$ while $\mathbf{T^{E1}}$ has no cutoff in real space. If the entire voxel $[m, n, p]$ lies within the sphere of r_c, both (4.12) and (4.13) contribute fully to $\hat{\mathbf{T}}^{\mathbf{E}}[m, n, p]$ (blue). If the entire voxel lies outside r_c, they do not contribute at all (grey). Partially contributing voxels are sampled using Monte-Carlo integration (orange). $\mathbf{T^{E2}}$ has a singularity at the origin which is why the origin voxel needs to be treated separately.

the real-space integrands (4.12) and (4.13) are sufficiently smooth over the entire voxel integration volume because they are not truncated. If the entire voxel $[m, n, p]$ lies within the sphere of r_c, both (4.12) and (4.13) contribute fully to $\hat{\mathbf{T}}^{\mathbf{E}}[m, n, p]$. For these voxels marked blue in figure 4.1 the integrand is sufficiently smooth over the entire integration volume of the voxel. In this case, the analytical result (4.14) is used for $\hat{\mathbf{T}}^{\mathbf{E3}}$ and (4.12) is numerically integrated to obtain $\hat{\mathbf{T}}^{\mathbf{E2}}$. Another possibility is for the entire voxel to lie outside the cutoff sphere as indicated by the grey voxels in (4.1). Both $\hat{\mathbf{T}}^{\mathbf{E2}}$ and $\hat{\mathbf{T}}^{\mathbf{E3}}$ evaluate to zero in this case. In a third possibility branded orange, the sphere cuts through the voxel. This leads to either a rather complex integration volume of the sphere cutting through the voxel or discontinuous real-space integrands. The former drastically complicates the search for an analytic solution while the latter makes the numerical integration unstable due to the lack of continuous derivatives. In order to circumvent these problems, these voxels are integrated over using Monte-Carlo integration

$$\int_V f(\mathbf{r}) d\mathbf{r} = \frac{V}{N} \sum_n^N f(\mathbf{r}_n) \tag{4.20}$$

for N random points $\mathbf{r}_n$ inside the integration volume. Evaluating whether a voxel lies completely inside, partially inside or completely outside the sphere can be very efficiently calculated as shown in appendix F. Note that for $\hat{\mathbf{T}}^{\mathbf{E1}}[m, n, p]$ these distinctions are not necessary because the k-space contribution to the Ewald summation is only truncated in reciprocal space. Since (4.11) additionally has no singularities, the analytic solution (4.14) can be used for all voxels. The final voxel type concerns only $\hat{\mathbf{T}}^{\mathbf{E2}}[0, 0, 0]$ because it contains the singularity at the origin inherited from $\mathbf{T^{dd}}$. It is treated by splitting up the integral according to (4.18). This method requires that the singularity is located at the center of the voxel, which is why the number of voxels along each dimension is chosen to be always odd. Additionally, the voxel needs to be chosen in such a way that it completely lies

within the real-space cutoff sphere. This is not a limit to the applicability of this method to certain geometries but rather defines a minimal initial resolution of the convolution kernel $\hat{\mathbf{T}}^{\mathbf{E}}$. Multiple individual voxels can of course be recombined together if $\mathbf{h}$ for the system of interest is constant for such a recombined subdomain. On another note, this method is not limited to cubic voxels but is applicable to any orthorhombic voxel shape.

This method hence provides a general fluctuation formula for the full permittivity tensor of arbitrary dielectric systems as long as they are simulated in a rectangular geometry, which does not cause any practical limitations. The results presented here are valid for toroidal boundary conditions in Ewald geometry, but equation (4.9) can also be used for different setups if $\hat{\mathbf{T}}^{\mathbf{E}}$ is adapted accordingly. In figure 4.2 surface cuts at x =2.04 Å for all nine elements of $\hat{\mathbf{T}}^{\mathbf{E}}$ are portrayed in 0.22 Å resolution. The cuts reflect the persymmetry of its integrand, the dipole-dipole interaction tensor $\mathbf{T}^{\mathbf{E}}$. The on-diagonal elements are unique, while all off-diagonal elements are symmtetric to the diagonal.

4.3 Bulk and slab geometry as special cases

The fluctuation formula for ε^{l} in equation (4.9) represents the general case of the local dielectric response to an external electric field in Ewald geometry. Consequently, the KF fluctuation formula for the bulk permittivity (2.99) as well as the SF parallel (2.108) and perpendicular (2.109) fluctuation formulas for a periodic slab-like system should turn up as special cases of (4.9). This is derived and tested on the H2OBULK and a DCEH2OINT trajectories also used for the benchmark permittivity calculations in section 3.4 and 3.5. In accordance with the trajectories, rectangular simulation boxes and periodic boundary conditions are assumed in the following.

4.3.1 Derivation of bulk formula

The dielectric properties of the bulk simulation box introduced in section 3.4 are described by a scalar, spatially independent permittivity. The system's polarization response caused by an external electric field is constant and isotropic over the entire box and it follows from (4.1) and (4.2) that $\mathbf{h}[n,m,p] = \mathbf{h}$ can be assumed constant as well. Hence instead of using a regularly spaced grid, the entire simulation box can be represented by only a single voxel with a half-length of $\Delta_l = L_l/2$, $l \in \{x,y,z\}$. The scalar permittivity furthermore does not allow for cross-coupling between $\mathbf{P}$ and $\mathbf{E^0}$ which implies that all off-diagonal tensor elements of $\mathbf{h}$ are zero. Equation (4.9) then takes the form

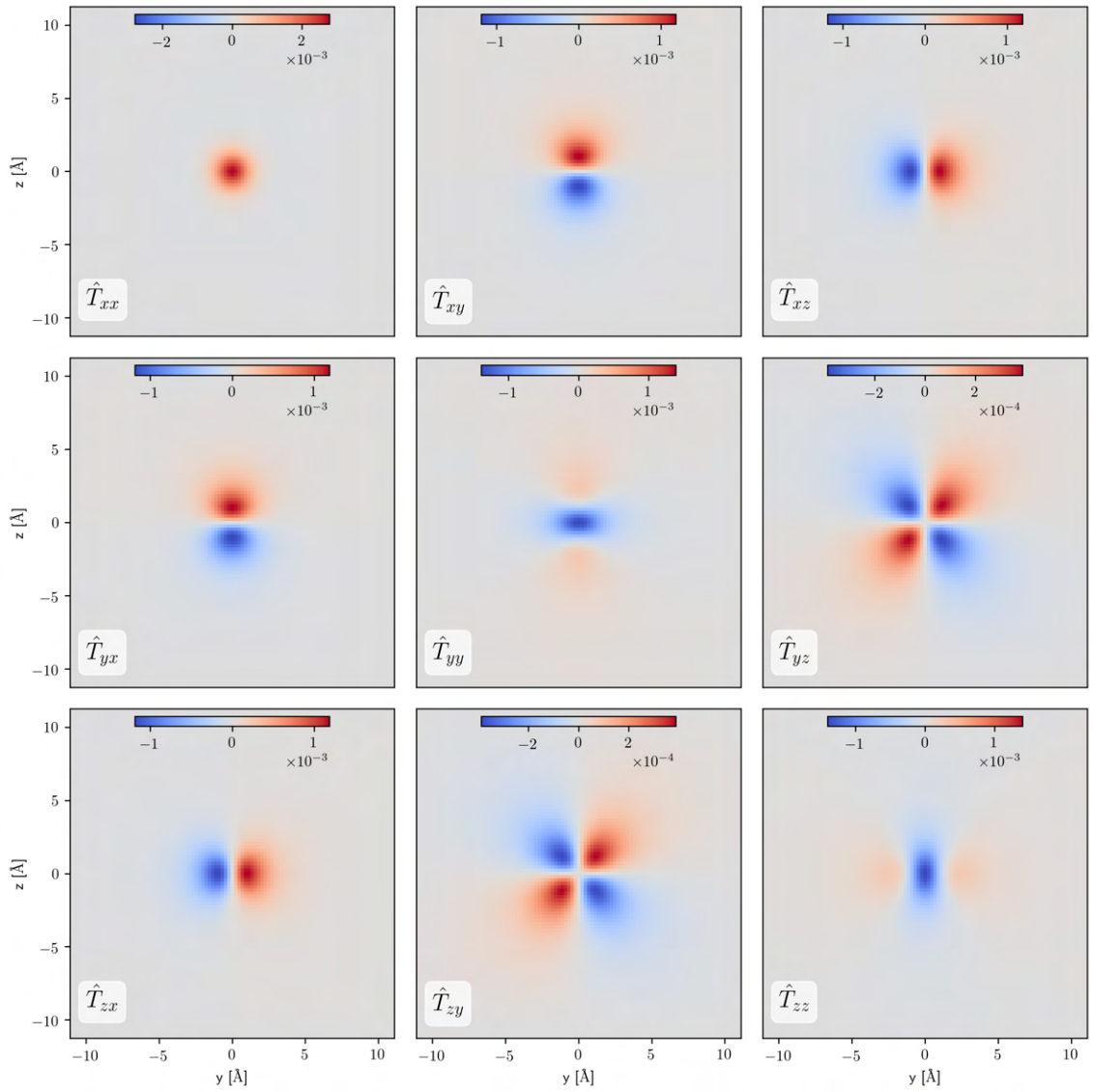

Figure 4.2 – Surface cuts at x =2.04 Å for all tensor elements of $\hat{\mathbf{T}}^{\mathbf{E}}$ with 0.22 Å resolution. The cuts reflect the persymmetry of $\mathbf{T}^{\mathbf{E}}$. The on-diagonal elements are unique, while all off-diagonal elements are symmetric to the diagonal.

$$\begin{aligned}
\varepsilon_{ii}[0,0,0] = \varepsilon &= 1 + 4\pi h_{ii}\left(1 + (\hat{T}_{ii} * h_{ii})\right)^{-1} \\
&= 1 + 4\pi h_{ii}\left(1 + h_{ii}\int_V (T_{ii}^{E1} + T_{ii}^{E2} + T_{ii}^{E3})d\mathbf{r}\right)^{-1} \\
&= 1 + 4\pi h_{ii}\left(1 + h_{ii}\left(-\frac{4\pi}{3} + \int_V T_{ii}^{E3} d\mathbf{r}\right)\right)^{-1}
\end{aligned} \tag{4.21}$$

As explained in the previous section, all elements of the k-space contribution $\hat{\mathbf{T}}^{\mathbf{E1}}$ vanish as a consequence of (4.14) if the voxel spans the entire box. Since the real space cufoff-radius of the

Ewald summation r_c fulfills $r_c \leq L/2$, the integral over this voxel $\hat{\mathbf{T}}^{\mathbf{E2}}$ reduces to an integral over a sphere with radius r_c. The only contribution to $\hat{\mathbf{T}}^{\mathbf{E2}}$ thus stems from the singularity at the origin, all other contributions vanish due to the angular symmetry of $\mathbf{T}^{\mathbf{dd}}$.

It follows that if $\hat{\mathbf{T}}^{\mathbf{E3}}$ is sufficiently approximated by the solution for $V \to \mathbb{R}^3$

$$\hat{T}_{ii}^{\mathrm{E3}} = \lim_{V\to\mathbb{R}^3} \int_V T_{ii}^{\mathrm{E3}} d\mathbf{r} = \frac{4\pi}{3} \tag{4.22}$$

it cancels the real-space contribution in the denominator integral of (4.21) and the KF formula (2.99) for a periodic system with conducting boundary conditions

$$\varepsilon \approx 1 + 4\pi h_{ii} = 1 + \frac{4\pi}{V}\, H_{ii} = 1 + \frac{4\pi}{V}\bar{H} \tag{4.23}$$

is recovered. It should be noted that no assumptions regarding the boundary conditions at infinity have been made. Rather, the equivalence to the fluctuation formula in reaction field geometry with conducting boundary conditions at infinity is a direct consequence of the functional form of the Ewald dipole-dipole interaction tensor. The present derivation of this result conveniently avoids the rather complex electrostatic substitution pictures used in the original derivation by Neumann and Steinhauser [48] and the concept is easily transferrable to other system geometries than Ewald. The H2OBULK reference simulation, which employs an Ewald screening parameter $\eta = 0.3659$ and a cutoff radius $r_c = 9$ Å, $\hat{T}_{ii}^{E3}$ evaluates to $4/3\pi$ within the simulation's set accuracy $a = 10^{-6}$ for the Ewald summation.

4.3.2 Derivation of slab formulas

Consistent with the reference DCEH2OINT interface simulation, we assume a periodic slab system that is stacked in z-direction and translationally invariant in the xy-plane. For such a system, equation (4.9) reduces to

$$\varepsilon_{ij}[0,0,p] = \varepsilon_{ij}[p] \quad = \quad 1 + 4\pi h_{ij}[p] \left(1 + (\hat{T}_{jk} * h_{kj})[p]\right)^{-1} \tag{4.24}$$

In order to compare this result to the SF fluctuation formulas (2.108) and (2.109), $\hat{\mathbf{T}} = \hat{\mathbf{T}}^{\mathbf{E}}$ has to be summed over in xy-direction.

Its elements in this projection are portrayed in figure 4.3. Here, off-diagonal elements $\hat{T}^{\mathrm{cross}} = \hat{T}_{ij}, i \neq j$ and the on-diagonal elements parallel to the slabs $\hat{T}_{||} = \hat{T}_{xx} = \hat{T}_{yy}$ are presented on the left. The slab normal components $\hat{T}_{\perp} = \hat{T}_{zz}$ are presented on the right.

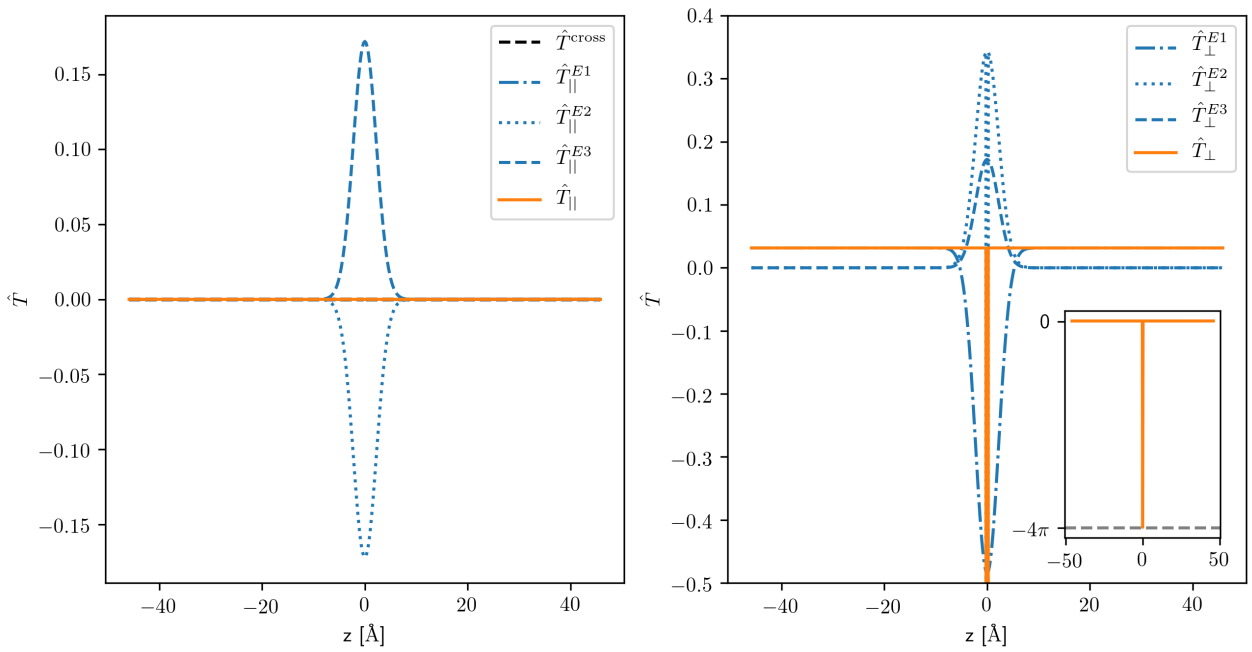

Figure 4.3 – Slabwise $\hat{\mathbf{T}}$ summed over in xy-direction. Off-diagonal elements $\hat{T}^{\text{cross}} = \hat{T}_{ij}, i \neq j$ and the on-diagonal elements parallel to the slabs $\hat{T}_{||} = \hat{T}_{xx} = \hat{T}_{yy}$ (both left) evaluate to zero over the entire box. The only non-zero contribution is $\hat{T}_{\perp}$ (right). The integral over the origin voxel returns $\hat{T}_{\perp}[0] = 4\pi$ and yields a value of $\hat{T}_{\perp}[p] \approx 4\pi\Delta_z/L_z$ in every other voxel.

The first thing that comes to eye in the left plot is that all cross-terms $\hat{T}^{\text{cross}}$ as well as the $\hat{T}_{||}$ are zero over the entire box. The k-space contribution $\hat{T}_{||}^{\text{E1}}$ evaluates to zero because the voxels span the entire box in xy-direction. The sinc function in (4.14) hits a root for $\Delta_l = L_l/2$, $l \in \{x, y, z\}$. All contributions in the k-space sum are therefore zero, except for k-vectors $\mathbf{k} = (0, 0, k_z)$ because $\text{sinc}(0) = 1$. These terms however are zero nonetheless for $\hat{T}^{\text{cross}}$ and $\hat{T}_{||}$ because of the term $\frac{k_i k_j}{k^2}$ in (4.14) and the only non-zero $\hat{\mathbf{T}}^{\mathbf{E1}}$ contribution is $\hat{T}_{\perp} = \hat{T}_{zz}$. The off-diagonal elements of $\hat{\mathbf{T}}^{\mathbf{E2}}$ in a slab with homogeneous $\mathbf{h}$ are zero due to the uneven symmetry of $\mathbf{T}^{\mathbf{dd}}$, while $\hat{\mathbf{T}}^{\mathbf{E3}}$ lacks non-zero off-diagonal components. All $\hat{T}^{\text{cross}}$ evaluate to zero in a homogeneously polarized slab. The independence of parallel and perpendicular components in slab geometry is thus a direct consequence of the functional form of $\mathbf{T}^{\mathbf{E}}$ and does not need to be introduced due to macroscopic symmetry reasons. This separation gets passed on into the formulas for calculating the $\boldsymbol{\chi}^l$ and $\boldsymbol{\varepsilon}^l$ tensors as shown below. It legitimizes the use of a series of plate capacitors as a substitution picture in slab geometry with perfectly homogeneous lateral polarization. If valid, $\boldsymbol{\varepsilon}^l$ can be calculated via the capacity of a plate capacitor (2.111) which only requires the average change in charge with potential. Since both of these are first-order quantities, this is much cheaper than calculating $\boldsymbol{\varepsilon}^l$ via slower converging second-order polarization fluctuations. Conversely, the $\hat{T}^{\text{cross}}$ behaviour also quantifies that the serial plate capacitor surrogate model breaks down if the polarization fluctuation term exhibits lateral structure within a slab. The $\hat{T}^{\text{cross}}$ can then no longer be assumed to be zero and the dielectric response becomes truly anisotropic. There is strong theoretical [177–180] and experimental [181–183] evidence that water forms ice-like structures particularly in the first solvation shells at solid-liquid interfaces. Also, the presence of ions as well as crystal or amorphous structure

of the solid interface might seed lateral structure in polarization fluctuation terms, particularly in immediate vicinity of the interface. Considering this, the presented method by discrete convolution (DC) might provide a more accurate way of coarse-graining the dielectric behaviour of the liquid phase in such systems.

The diagonal real-space components $\hat{T}_{||}^{\mathrm{E2}}$ and $\hat{T}_{||}^{\mathrm{E3}}$ both form Gaussians with opposite signs that cancel each other out. Hereby, the value of the $\hat{\mathbf{T}}^{\mathrm{E2}}$ singularity at the origin is compensated by the remainder integral in the origin voxel. This keeps $\hat{T}_{||}^{\mathrm{E2}}$ a smooth Gaussian-like function that mirrors the Gaussian of $\hat{T}_{||}^{\mathrm{E3}}$. The convolution in (4.24) thus evaluates to zero for the slab-parallel elements of the permittivity tensor $\varepsilon_{||}^{l} = \varepsilon_{xx}^{l} = \varepsilon_{yy}^{l}$ and the parallel fluctuation formula reads

$$\varepsilon_{||}^{l} = 1 + 4\pi h_{||} \tag{4.25}$$

This is precisely the SF fluctuation formula (2.108) for parallel slab-like systems. Naturally, the results for the parallel dielectric constant should be identical whether they are calculated by this formula derived from system symmetry or by directly using the projected dipole-dipole interaction kernel and formula (4.24). As shown in a $\varepsilon_{||}^{l}$ comparison for DCEH2OINT in the instantaneous LLI reference system in figure 4.4, this is the case to very good agreement. Apart from negligible numerical errors, the DC $\varepsilon_{||}^{l}$ result in orange is identical to reference $\varepsilon_{||}^{l}$ calculated with the SF formula (2.108) - note that the blue line is hidden underneath the orange line.

The perpendicuar projections of the Ewald voxel integrals $\hat{T}_{\perp}$ do not evaluate to zero as can be seen from the right hand plot in figure 4.3. While the integral over the origin voxel returns $\hat{T}_{\perp}[0] = -4\pi$ it yields a value of $\hat{T}_{\perp}[p] \approx 4\pi\Delta_z/L_z$ in every other voxel. Over the entire box, the origin and all other voxels compensate each other within the limits of numerical errors. This constant shift compared to the parallel components can be attributed to the $\hat{T}_{\perp}^{\mathrm{E1}}$ that are non-zero for slab-like voxels in z-direction. Note that $\hat{\mathbf{T}}^{\mathbf{E}}$ is also not a smooth function over the origin, the zero voxel remainder integral thus does not compensate the singularity.

Since all cross-terms are zero, inserting $\hat{T}_{\perp}$ into the convolution yields

$$\begin{aligned} \varepsilon_{\perp}^{l}[p] &= 1 + 4\pi h_{\perp}[p] \left(1 + (\hat{T}_{\perp} * h_{\perp})[p]\right)^{-1} \\ &= 1 + 4\pi h_{\perp}[p] \left(1 - 4\pi h_{\perp}[0] + \frac{4\pi}{L_z} \sum_{p} h_{\perp}[p]\right)^{-1} \end{aligned} \tag{4.26}$$

Rearranged for $(\varepsilon_{\perp}^{l})^{-1}$ this is

$$(\varepsilon_{\perp}^{l})^{-1} = 1 - 4\pi \frac{h_{\perp}(z)}{(1 + 4\pi H_{\perp}/V)} \tag{4.27}$$

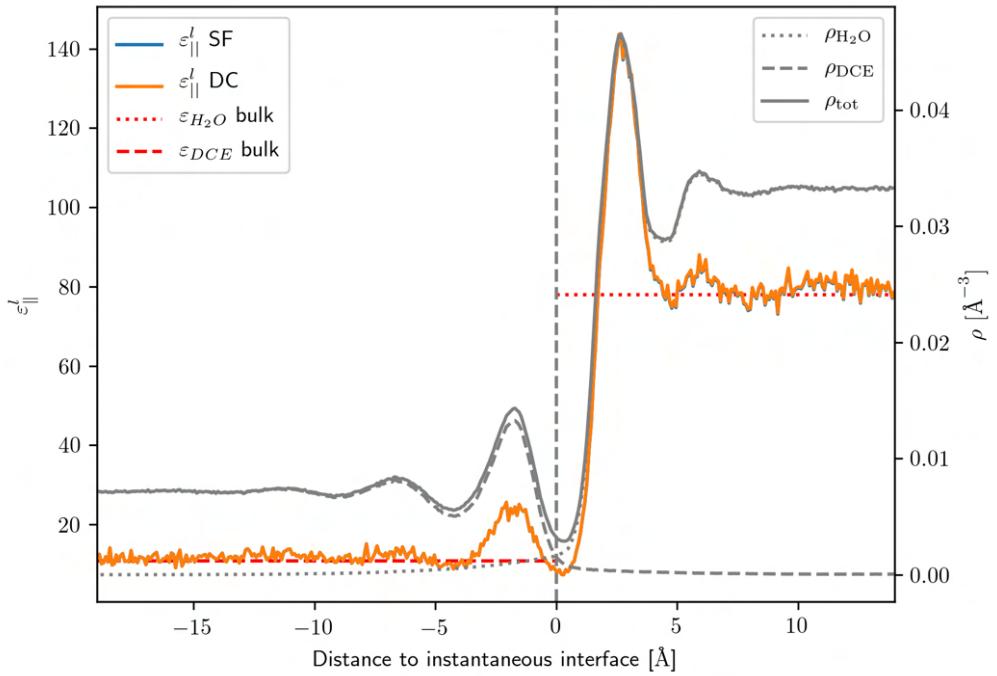

Figure 4.4 – Comparison of $\varepsilon^l_{||}$ profile calculated by discrete convolution (DC) (orange) to reference $\varepsilon^l_{||}$ profile calculated with the SF formula (2.108) (blue, hidden underneath orange) for DCEH2OINT in the instantaneous LLI reference system. Both profiles coincide apart from negligible numerical errors. The DC profile even reproduces the statistical noise of $\mathbf{h}$ due to the linearity of the convolution operation. No artificial introduction of boundary conditions is necessary since this information is already incorporated in $\hat{\mathbf{T}}^{\mathbf{E}}$.

which is the same as the SF fluctuation formula for the inverse local permittivity (2.109). Figure 4.5 shows a comparison of the inverse local permittivity $(\varepsilon^l_{\perp})^{-1}$ calculated using the DC method and its SF reference. Analogously to the parallel case in figure 4.4, both methods yield identical results within the margin of errors - note again that the blue line is hidden underneath the orange line.

Both results for $\varepsilon^l_{||}$ and $(\varepsilon^l_{\perp})^{-1}$ reproduce their reference for conducting boundary conditions, even though no explicit assumptions regarding the boundary conditions were made in the discrete convolution approach. Consistent with the bulk result, summing up both the parallel (4.25) and and perpendicular (4.27) ε elements over all slabs returns the bulk formula (4.23). This is a consequence of all elements of $\hat{\mathbf{T}}^{\mathbf{E}}$ evaluating to zero if this sum is performed. Both DC profiles even reproduce the statistical noise of $\mathbf{h}$ due to the linearity of the convolution operation.

All possible frequency filters like the lowpass filter portrayed in figure 3.10 used for smoothing out noisy intra-molecular frequencies in chapter 3.5 can be used as well. Using it in the DC formalism is computationally even more efficient since the filter can directly be multiplied with the $\hat{\mathbf{T}}$ - kernel prior to convolution.

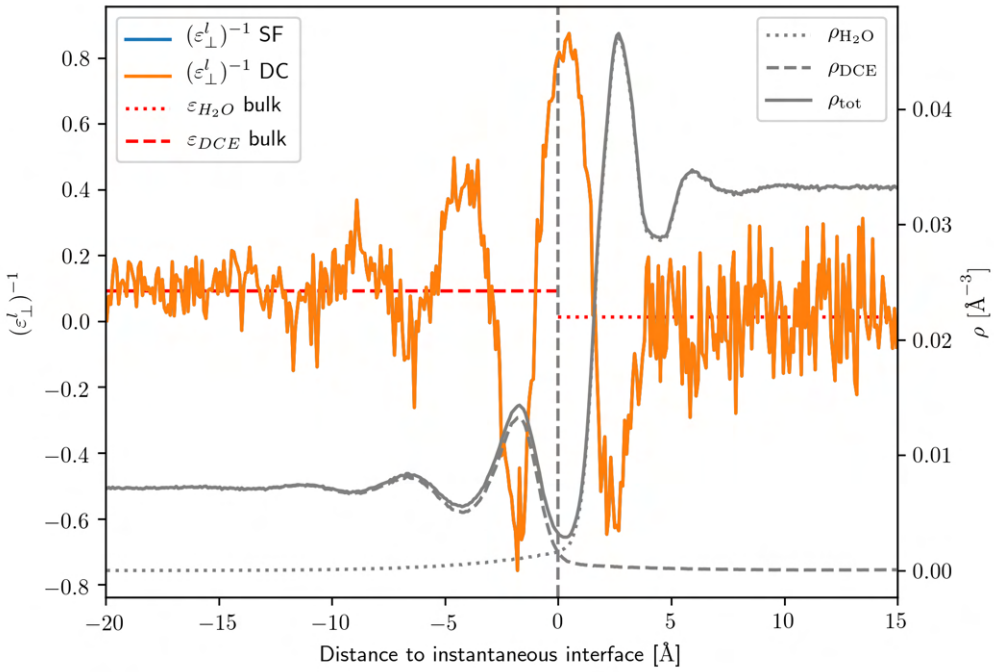

Figure 4.5 – Comparison of $(\varepsilon_\perp^l)^{-1}$ profile calculated by discrete convolution (DC) (orange) to reference $(\varepsilon_\perp^l)^{-1}$ profile calculated with the SF formula (2.108) (blue, hidden underneath orange) for DCEH2OINT in the instantaneous LLI reference system. Both profiles coincide apart from negligible numerical errors. The DC profile even reproduces the statistical noise of $\mathbf{h}$ due to the linearity of the convolution operation. No artificial introduction of boundary conditions is necessary since this information is already incorporated in $\hat{\mathbf{T}}^{\mathbf{E}}$.

Chapter 5

Distance-dependent molecular orientation at the Water-Dichloroethane interface

In this chapter the molecular structure of both the H_2O and DCE phase at the LLI is investigated. The structure is assessed in form of bivariate distributions of two independent angles per molecule against the instantaneous LLI reference of the H2ODCEINT trajectory. In section 5.1, the choice of these angles is discussed. In sections 5.2 and 5.3, the resulting distributions are presented and analyzed with respect to distance from the liquid-liquid interface. This chapter mainly reproduces and interprets results obtained by Zhu Liu in his doctoral thesis [184].

5.1 Formalism

In order to perform the statistical binning necessary to obtain insights into the molecular orientational distribution at the interface, the orientations of individual molecules need to be comparable. This requires a molecular coordinate system, which can be spanned by defining two orthonormal vectors $\hat{\mathbf{m}}$ and $\hat{\mathbf{p}}$ for both types of molecules as visualized in figure 5.1.

In the case of water, the primary orientational vector $\hat{\mathbf{p}}$ is chosen to align with the molecular dipole $\boldsymbol{\mu}$. The secondary vector $\hat{\mathbf{m}} = \hat{\mathbf{p}} \times \hat{\mathbf{l}}$ is perpendicular to the plane spanned by $\hat{\mathbf{p}}$ and the vector $\hat{\mathbf{l}}$ connecting both hydrogen atoms. For a planar molecule like water, $\boldsymbol{\mu}$ lies within the molecular plane, which makes $\hat{\mathbf{m}}$ the molecular plane surface normal. The three coordinate vectors $\hat{\mathbf{p}}$, $\hat{\mathbf{m}}$, and $\hat{\mathbf{p}} \times \hat{\mathbf{m}}$ thus span a right-handed orthonormal coordinate system.

In the case of DCE, the molecular dipole $\boldsymbol{\mu}$ is not a stable coordinate vector because molecular torsion has significant influence on its magnitude. Anchoring the molecular coordinate system at the dipole vector would thus greatly increase numerical errors because even thermal fluctuations in bondlengths could change the orientation of $\boldsymbol{\mu}$.

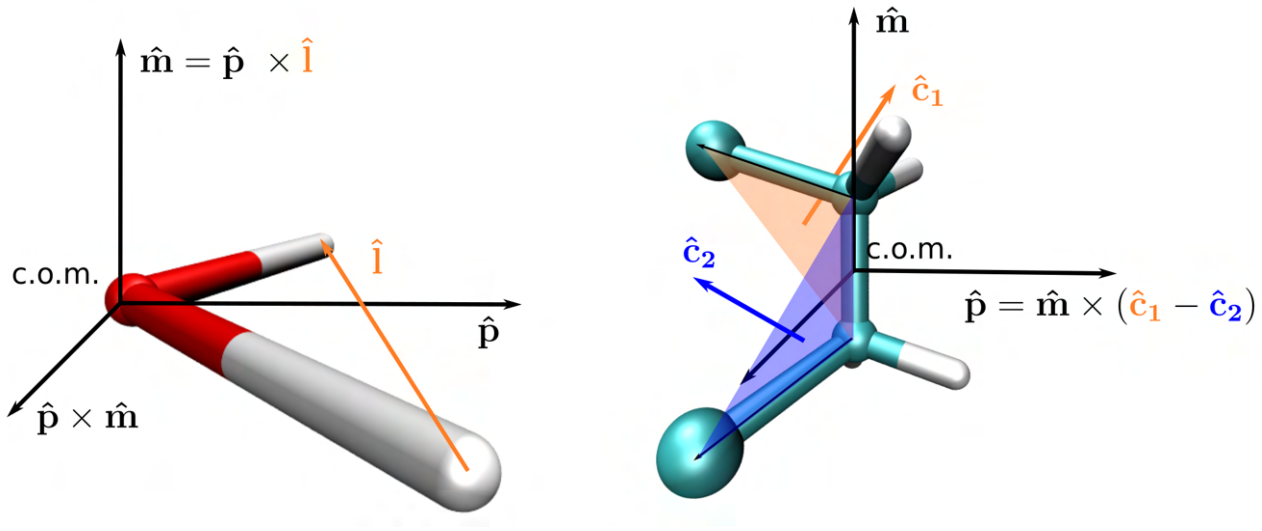

Figure 5.1 – Molecular coordinate systems for H_2O (left) and DCE (right). For H_2O the primary orientational vector $\hat{\mathbf{p}}$ is chosen to align with the molecular dipole $\boldsymbol{\mu}$. The secondary vector $\hat{\mathbf{m}} = \hat{\mathbf{p}} \times \hat{\mathbf{l}}$ is perpendicular to the plane spanned by $\hat{\mathbf{p}}$ and the vector $\hat{\mathbf{l}}$ connecting both hydrogen atoms. For DCE the vector $\hat{\mathbf{p}} = \hat{\mathbf{m}} \times (\hat{\mathbf{c_1}} - \hat{\mathbf{c_2}})$ is chosen instead of the dipole, since $\boldsymbol{\mu}$ changes with DCE conformation. The C-C axis constitutes the second coordinate vector $\hat{\mathbf{m}}$ for DCE.

Compared to water, DCE has two dominant conformers as can be seen in the distribution of the dihedral angle for the DCE phase as presented in figure 5.2 where the conformer probability is plotted against the dihedral angle on the left axis. In the conformer definition we follow [157], where DCE molecules with dihedral angles between 30 degrees and 90 degrees are defined as *gauche*, while a molecule with dihedral angle between 150 degrees and 210 degrees is declared *trans*. In the *gauche* case, the two carbon-chloride (C-Cl) bonds of the chloromethyl groups of DCE have parallel components when projected onto each other while in the *trans* case the orientation of the C-Cl bonds is almost anti-parallel. The limiting angles for each conformer are indicated by black dashed lines in figure 5.2. It is furthermore visible that the weight of the perfect *cis* conformer with a dihedral angle around zero is negligible in the probability distribution. The recorded *trans/gauche* ratio is consistent with first principle calculations [185, 186].

Comparing the dipole magnitudes of the *gauche* and *trans* conformers on the right axis of figure 5.2, it becomes visible, that the magnitude of the molecular dipole moment $|\boldsymbol{\mu}| = \mu$ is negatively correlated with the dihedral angle of DCE. While the C-Cl orientation in the *gauche* case is constructive and the DCE molecule thus has an overall greater dipole than the individual chloromethyl groups, their nearly anti-parallel orientation with respect to the molecular center of mass, which represents an idealized inversion center in the *trans* case, results in an almost zero-magnitude dipole of *trans* DCE molecules.

On a side note, figure 5.2 additionally shows that there are slightly more *gauche* conformers for the interfacial DCE - the blue line - as compared to the bulk reference simulation indicated in orange. This is in agreement with the observation that the DCE phase forms solvation shells and thus gets "polarized" when in contact with an also polarized water phase. This difference in figure 5.2 is observable but small as the influence of the interface diminishes at distances of ~8 Å into the bulk

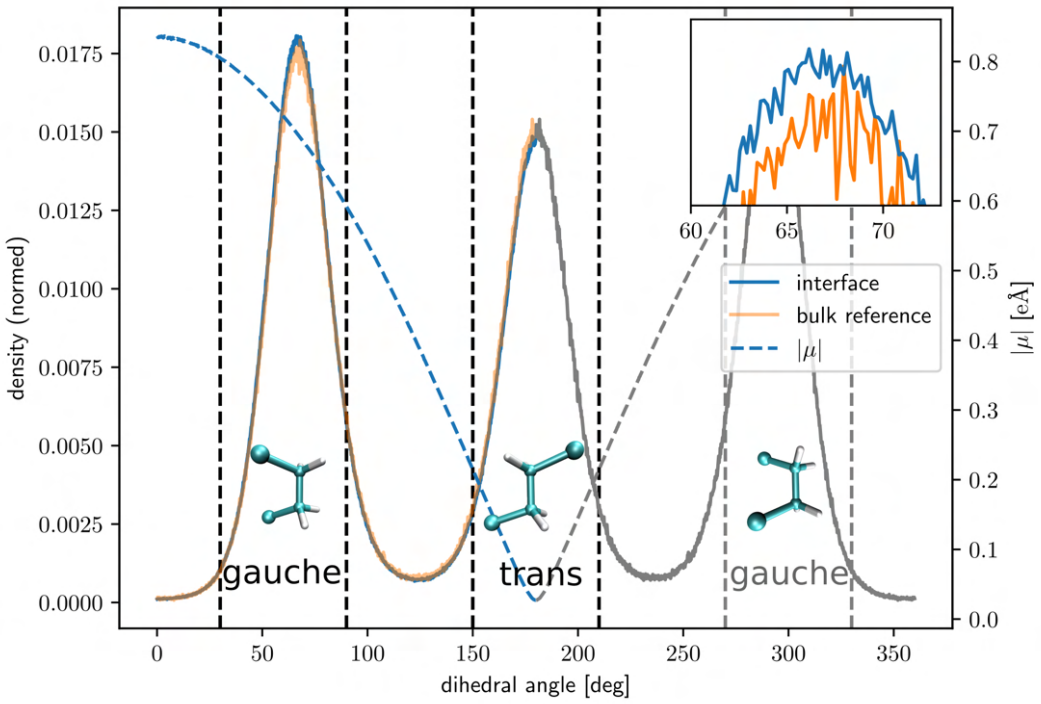

Figure 5.2 – DCE conformer distribution (left axis) and average magnitude of the DCE molecular dipole (right axis) plotted against dihedral angle. The limiting angles for *trans* and *gauche* conformer are indicated by black dashed lines.

compared to over 60 Å of the total phase. A spatially resolved profile of the interface/bulk ratios for number densities of *gauche* and *trans* DCE is examined later in this chapter.

Since $\boldsymbol{\mu}$ is not a stable coordinate vector in case of DCE the vector

$$\hat{\mathbf{p}} = \hat{\mathbf{m}} \times (\hat{\mathbf{c_1}} - \hat{\mathbf{c_2}}) \tag{5.1}$$

is chosen as a substitute, as shown on the right side of figure 5.1. Here $\hat{\mathbf{c_1}}$ and $\hat{\mathbf{c_2}}$ are defined as the normal vectors of the two planes that the C-Cl bonds span with the C-C axis of the DCE molecule. The choice of this vector as the primary molecular coordinate vector for DCE has two advantages. First, it is perpendicular to the C-C axis, which constitutes the second coordinate vector $\hat{\mathbf{m}}$ for the DCE molecule. $\hat{\mathbf{p}}$, $\hat{\mathbf{m}}$ and $\hat{\mathbf{p}} \times \hat{\mathbf{m}}$ thus form an orthonormal coordinate system. Second, choosing $\hat{\mathbf{p}}$ instead of $\hat{\boldsymbol{\mu}}$ as coordinate vector avoids the following numerical stability issues.

In figure 5.3, the distributions for three possible primary DCE coordinate vectors are portrayed, all calculated for the DCEBULK trajectory. On the bottom x-axis, the distribution for $|\mathbf{p}| = |\mathbf{m} \times (\mathbf{c_1} - \mathbf{c_2})|$ from (5.1) is displayed in orange and $|\mathbf{p}^\dagger| = |\mathbf{m} \times (\mathbf{c_1} + \mathbf{c_2})|$ in blue. The distribution of μ in grey is depicted on the top x-axis. All three distributions exhibit two dominant peaks.

However, the lower-magnitude peak of both the grey and blue distribution is very close to zero. This means that a significant portion of DCE molecules has $\boldsymbol{\mu}$ and $\mathbf{p}^{\dagger}$ vectors with close to zero magnitude. If chosen as molecular coordinate vectors, even small intramolecular atomic displacements are significant in comparison. Such displacements are always present at finite temperature and as a consequence would render the orientation of the coordinate system very unstable. Additionally, the normalization required for coordinate vectors would mean dividing by very small numbers, which would introduce further numerical errors. In the distribution of $\mathbf{p}$ on the other hand, the low-magnitude peak is shifted comfortably far away from the origin at $|\hat{\mathbf{p}}| = 4.4$ Å and the weight of the distribution at zero magnitude is negligible. Above instabilities are thus avoided if $\hat{\mathbf{p}}$ is chosen over $\hat{\boldsymbol{\mu}}$ or $\hat{\mathbf{p}}^{\dagger}$ as the primary DCE coordinate vector.

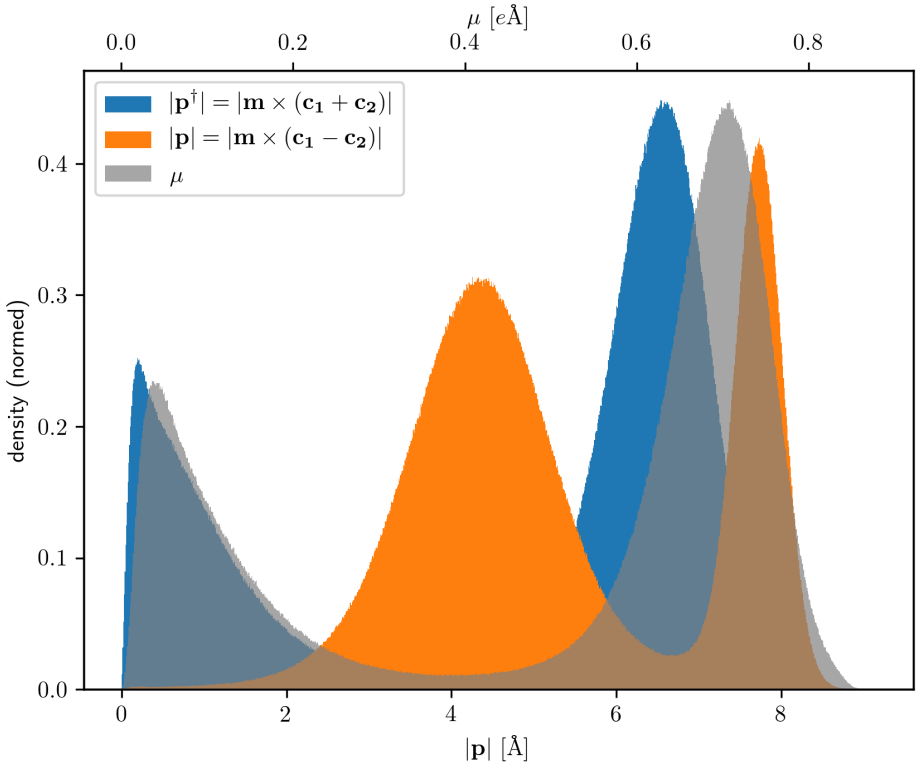

Figure 5.3 – Bottom axis: Distribution of $|\mathbf{p}^{\dagger}| = |\mathbf{m} \times (\mathbf{c_1} + \mathbf{c_2})|$ (blue) and $|\mathbf{p}^{\dagger}| = |\mathbf{m} \times (\mathbf{c_1} - \mathbf{c_2})|$ (orange). Top axis: Distribution of $|\boldsymbol{\mu}|$ (grey). Grey and blue distributions both have a dominant peak very close to zero magnitude. This introduces instabilities since even small thermal displacements of cluster atoms can change the orientation of such a coordinate vector. Additionally, the normalization required for coordinate vectors would mean dividing by very small numbers, which would introduce further numerical errors. The orange distribution for $|\mathbf{p}|$ does not share this problem, since its low-magnitude peak is shifted comfortably far from the origin at $|\hat{\mathbf{p}}| = 4.4$ Å and its weight at zero magnitude is negligible. For this reason $\hat{\mathbf{p}} = \hat{\mathbf{m}} \times (\hat{\mathbf{c_1}} - \hat{\mathbf{c_2}})$ is chosen as the primary coordinate vector for DCE.

In figure 5.4, the relation between the molecular dipole $\boldsymbol{\mu}$ and the primary and secondary DCE coordinate vectors $\hat{\mathbf{p}}$ and $\hat{\mathbf{m}}$ is visualized. Here, γ denotes the angle between $\boldsymbol{\mu}$ and $\hat{\mathbf{p}}$ and α the angle between $\boldsymbol{\mu}$ and $\hat{\mathbf{m}}$. Both angles, γ on the left and α on the right, are plotted against the molecular dihedral angle of DCE. The magnitude of the dipole μ increases gradually with the dihedral angle as indicated by the colorbars. Naturally, the *gauche* conformer within the light blue region exhibits a higher μ than the *trans* conformer in the orange region. For DCE in *gauche*

conformation, $\boldsymbol{\mu}$ is perpendicular to both $\hat{\mathbf{p}}$ and $\hat{\mathbf{m}}$ on average. The angular spread does not exceed $90 \pm 10°$, hence μ can be thought of as aligned with the third molecular coordinate vector $\hat{\mathbf{p}} \times \hat{\mathbf{m}}$ in good approximation. For DCE in *trans* conformation on the other hand, the spread in α and γ rises steeply. Both γ and α exhibit huge spreads in angle for small dipole magnitudes μ, which again illustrates why the dipole disqualifies as a molecular coordinate vector for DCE. The increasing instability of γ towards a perfect *cis* conformation which has a dihedral angle of 0° adds to that even though this influence is minor due to the negligible weight of dihedral angles below 10° in the distribution of figure 5.2.

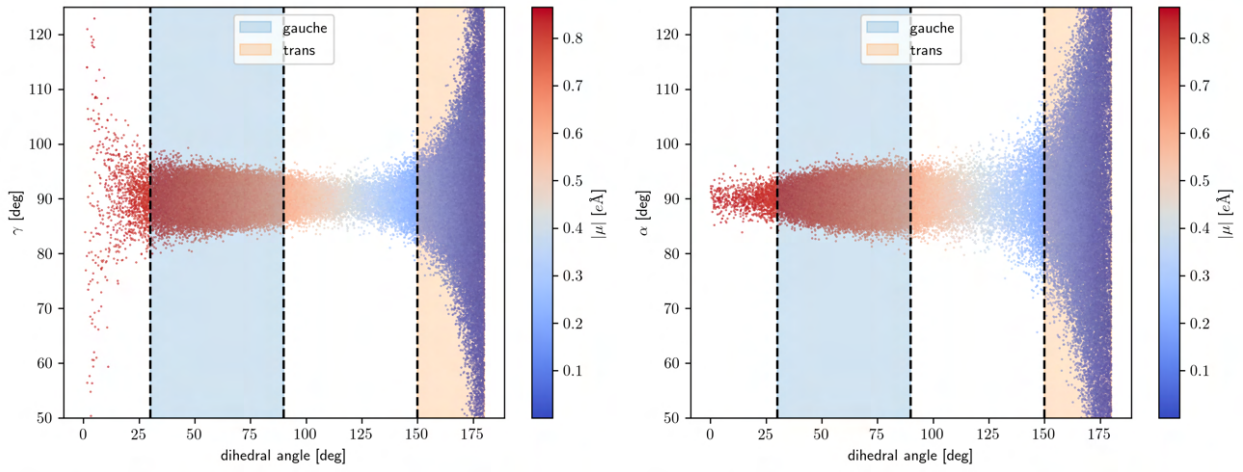

(a) Correlation between dihedral angle and γ.

(b) Correlation between dihedral angle and α.

Figure 5.4 – For DCE in *gauche* conformation, $\boldsymbol{\mu}$ is perpendicular to both $\hat{\mathbf{p}}$ and $\hat{\mathbf{m}}$ on average. The angular spread does not exceed $90 \pm 10°$, hence μ can be thought of as aligned with the third molecular coordinate vector $\hat{\mathbf{p}} \times \hat{\mathbf{m}}$ in good approximation. For *trans* DCE γ and α exhibit huge spreads in angle for small dipole magnitudes μ, which again illustrates why the dipole disqualifies as a molecular coordinate vector for DCE.

To summarize, the presented choices of $\hat{\mathbf{p}}$ and $\hat{\mathbf{m}}$ for H_2O and DCE introduce a right handed, orthonormal coordinate system per molecule type. Both of these coordinate systems are robust with regard to molecular torsion and bond bending which are present during finite temperature MD simulations with non-rigid bonds and angles.

In order to quantify the molecular structure of the interface at the origin, the joint bivariate distribution $H_z(\cos\theta, \phi)$ is calculated slabwise with respect to z-distance to the interface. Here, θ and ϕ represent the azimuthal and polar angle the LLI normal vector $\mathbf{n}$ takes on in the molecular coordinate systems introduced in figure 5.1. The angle θ is therefore given by the angle between $\hat{\mathbf{p}}$ and $\hat{\mathbf{n}}$ and ϕ represents the angle between the vector $\hat{\mathbf{m}}$ and the projection

$$\mathbf{n}_\perp = \mathbf{n} - \frac{\mathbf{n} \cdot \hat{\mathbf{p}}}{|\mathbf{n}|} \hat{\mathbf{p}} \tag{5.2}$$

A schematic representation of this is portrayed in figure 5.5.

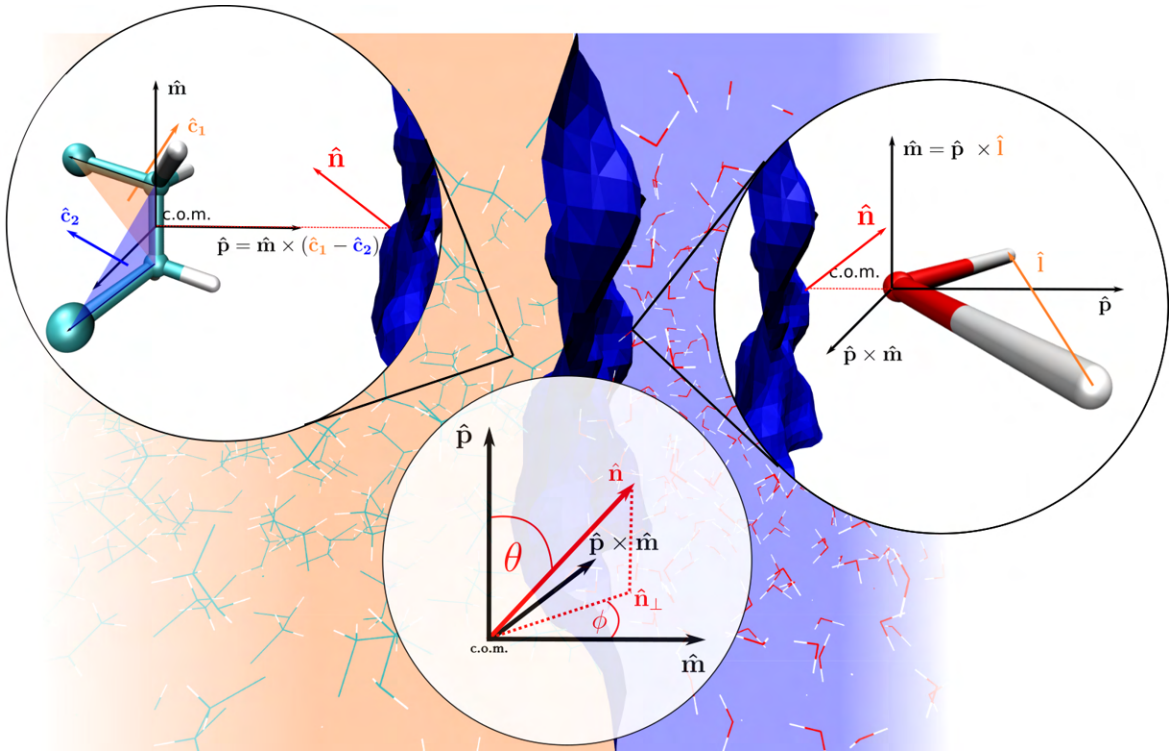

Figure 5.5 – The presented choices of $\hat{\mathbf{p}}$ and $\hat{\mathbf{m}}$ for H_2O and DCE introduce a right handed, orthonormal coordinate system per molecule type. θ and ϕ represent the azimuthal and polar angle the LLI normal vector $\mathbf{n}$ takes on in these molecular coordinate systems. The interfacial distance of a molecule is defined as the distance between the molecular center of mass and the corresponding projected point of reference on the liquid-liquid interface. Said point of reference is defined as the projection of the center-of-mass onto the triangulated continuous surface along the z-direction. The LLI normal vector applicable for each molecule is defined as the surface normal vector at the point of reference. $\cos\theta$ is chosen instead of θ in the joint bivariate slab distribution $H_z(\cos\theta, \phi)$ in order to ensure a constant bin volume over all angles.

As described above, the interfacial distance of a molecule is defined as the distance between the molecular center of mass and the corresponding projected point of reference on the liquid-liquid interface. Said point of reference is defined as the projection of the center-of-mass onto the triangulated continuous surface along the z-direction. The LLI normal vector applicable for each molecule is defined as the surface normal vector at the point of reference.

The reason $\cos\theta$ is chosen instead of θ to form the joint bivariate slab distribution $H_z(\cos\theta, \phi)$ is to ensure a constant bin volume over all angles. The infinitesimal surface element for an integration over the unit sphere in spherical coordinates is given by $dV = \sin\theta$. Performing a binning in evenly spaced intervals of θ and ϕ thus gives a different weight to individual bins that needs to be corrected. Performing the transformation $\theta \to \cos\theta$ removes the θ-dependence in the integration over the unit sphere:

$$\int_0^{2\pi} d\phi \int_0^{\pi} d\theta \sin\theta = \int_0^{2\pi} d\phi \int_{-1}^{1} d\cos\theta \tag{5.3}$$

The joint bivariate distribution $H_z(\cos\theta, \phi)$ therefore has the same bin volume for all bins $(\cos\theta : \cos\theta + \Delta\cos\theta, \phi : \phi + \Delta\phi)$. While $H_z(\cos\theta, \phi)$ maps the orientational profile at the LLI, a molecule's lateral position parallel to the interface is lost in this representation.

Due to the molecular C_{2v} symmetry of H_2O and DCE, the coordinate vector $\hat{\mathbf{m}}$ is only defined up to a change in sign. Molecules can therefore always be oriented in such a way that ϕ is restricted to the interval [0,90]. The approximation of ideal symmetry is valid since the timescale and energy separation between vibrations on the one hand and translation, rotation as well as, in the case of DCE, torsion on the other hand is sufficiently large at the DCEH2OINT LLI interface [187, 188].

5.2 Orientational binnings for H_2O

In figure 5.6, the H_2O joint bivariate distributions $H_z(\cos\theta, \phi)$ obtained from the DCEH2OINT trajectory in the instantaneous LLI reference system for nine different slabs with increasing interfacial distance are displayed. Following the convention introduced in section 3.3, the DCE phase occupies the negative half-space and H_2O occupies the positive halfspace.

For each slab a thickness of one nanometer was chosen. In the top row, the slab boundaries are indicated by vertical blue lines. Each slab's relative number density profile $\langle\rho\rangle/\langle\rho_{\mathrm{bulk}}\rangle$ compared to bulk is represented by a blue dot. For the reference bulk density the slab confined between 10nm - 11nm interfacial distance is selected. While the first two solvation shells with peaks in slab [2nm, 3nm] and [6nm, 7nm] are clearly visible, $\langle\rho\rangle/\langle\rho_{\mathrm{bulk}}\rangle$ converges to one for larger distances from the instantaneous interface. This is in accordance with the observations made in chapter 3. It is furthermore evident, that the signal-to-noise ratio decreases in slabs with low number density, which can be attributed to worse statistics.

The joint bivariate distributions are performed with a resolution of 50x50 pixels over $(\phi, \cos\theta) :\mapsto [0, 90] \times [-1, 1]$ and the bin counts in each of the nine $H_z(\cos\theta, \phi)$ in figure 5.6 are normed to the average bin count of the reference bulk slab $\langle H_{[10,11]}\rangle_{cos\theta,\phi}$. These relative bin count values are colorgraded low to high as indicated by the horizontal colorbar in each $H_z(\cos\theta, \phi)$. The extrema of this ratio are naturally correlated with each slab's number density profile represented by the blue dots in the top row of figure 5.6.

Besides the slab average, distinct orientational preferences of the water molecules with respect to the instantaneous interface can be deduced from the $H_z(\cos\theta, \phi)$. Directly at the interface, in slab $H_{[0,1]}$, a single peak in the distribution at around $\phi \approx 80°$ and $\cos\theta \approx -0.5$ (or $\theta \approx 120°$) is visible. Comparing this with the molecular coordinate system portrayed in figure 5.1, a value of $\theta \approx 120°$ corresponds to a water molecule with its dipole $\mathbf{p}$ pointing towards the interface at a $30°$ angle. A value of $\phi \approx 80°$ on the other hand indicates an almost parallel orientation of the molecular plane normal $\hat{\mathbf{m}}$ and the interface normal projection $\mathbf{n}_\perp$. This results in a molecular position of the water molecule, where one H-leg is tilted in an acute angle towards the interface, leaving the second one dangling.

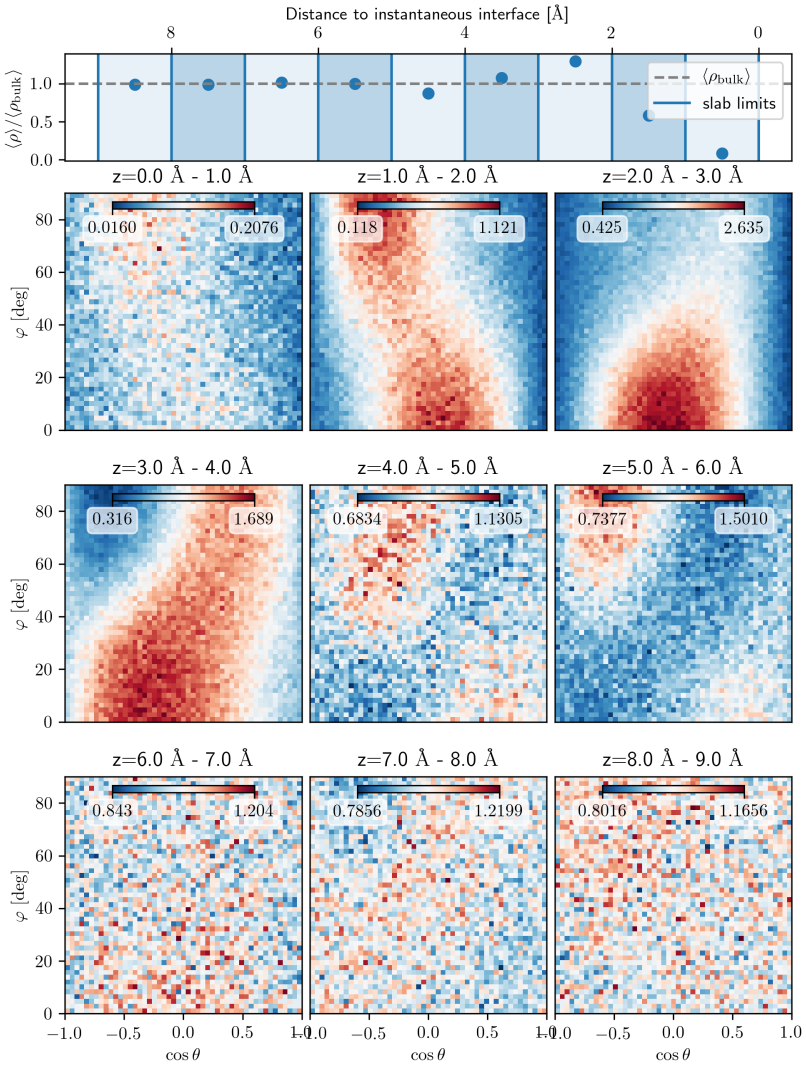

Figure 5.6 – H_2O joint bivariate distributions $H_z(\cos\theta, \phi)$ obtained from the DCEH2OINT trajectory in the instantaneous LLI reference system for nine different slabs with increasing interfacial distance. Slab boundaries (vertical blue lines) and relative number density profile $\langle\rho\rangle/\langle\rho_{\text{bulk}}\rangle$ compared to bulk (blue dots) are shown on top. $H_z(\cos\theta, \phi)$ are normed to the average bin count of the reference bulk slab $\langle H_{[10,11]}\rangle_{cos\theta,\phi}$.

Over a transition phase visible in $H_{[1,2]}$, this preferred positioning shifts to a second dominant orientation characterized by the peak appearing in the joint distribution $H_{[2,3]}$. This peak is located around $\phi \approx 10°$ and $\cos\theta \approx 0°$ and appears in the slab containing the top of the first density solvation shell. The peak is slightly narrower along the $\cos\theta$- than the ϕ-axis, which gives it an ellipsoid shape with the minor semi-axis oriented parallel to the $\cos\theta$-axis. A higher number density than bulk is not observed for $\phi > 40°$ and $|\cos\theta| > 0.65$. A comparison with the molecular coordinate system in figure 5.6 shows that the peak value for $\cos\theta$ around the origin corresponds to a parallel orientation of the molecular dipole $\hat{\mathbf{p}}$ to the interface. The acute angle $\phi \approx 10°$ indicates a slight tilt of the molecular plane, which means that one H-leg is slightly closer to the interface than the other.

This peak is somewhat broader than its counterpart appearing in the two slabs closest to the interface and remains a dominant, even broader, feature in $H_{[3,4]}$. Here in slab [3, 4], a third preferred orientation appears at $\cos\theta \approx 0.5$ and $\phi \approx 80°$. This position roughly corresponds to mirroring the

first peak at the axis $\cos\theta = 0$. Again comparing the $\cos\theta \approx 0.5$, which corresponds to an angle of $\theta \approx 60°$ with the molecular coordinate system in figure 5.1, one sees that it represents a dipole orientation, which is tilted by $60°$ against $\hat{\mathbf{n}}$ and is pointing away from the interface. In contrast to slab [1, 2], the peaks in slab [3, 4] are not separated anymore, mainly due to a broadening of peaks in ϕ. One explanation for this broadening with increasing distance from the interface could be a lessening influence of the DCE phase due to shielding. In slab [4, 5] and [5, 6], the preferred orientation of the H_2O molecules retracts to their peak first appearing in $H_{[1,2]}$ at $\phi \approx 80°$ and $\cos\theta \approx -0.5$. This periodic behaviour also coincides with the first oscillation of solvation shell formation as can be seen comparing $\langle\rho\rangle/\langle\rho_{\mathrm{bulk}}\rangle$ in the top row of figure 5.6. The molecular orientation towards the liquid-liquid interface becomes increasingly random in the second solvation shell for $z > 7$Å which is also reflected in the density fluctuations. Above findings are in line with orientational maps reported in literature [189, 190].

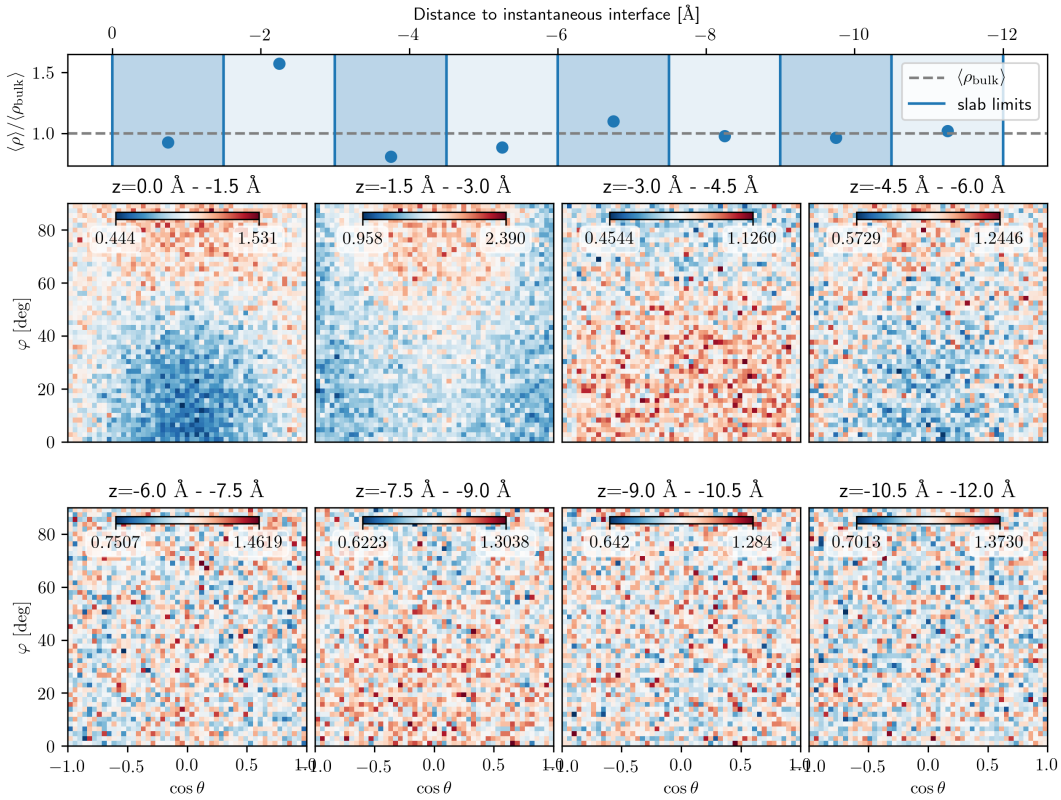

Figure 5.7 – Combined *gauche* and *trans* DCE joint bivariate distributions $H_z(\cos\theta, \phi)$ obtained from the DCEH2OINT trajectory in the instantaneous LLI reference system for nine different slabs with increasing interfacial distance. Slab boundaries (vertical blue lines) and relative number density profile $\langle\rho\rangle/\langle\rho_{\mathrm{bulk}}\rangle$ (blue dots) compared to bulk (dashed line) are shown on top. $H_z(\cos\theta, \phi)$ are normed to the average bin count of the reference bulk slab $\langle H_{[-18,16.5]}\rangle_{cos\theta,\phi}$.

5.3 Orientational binnings for DCE

Analogously to the previous section, the joint bivariate distributions $H_z(\cos\theta, \phi)$ including both *gauche* and *trans* DCE in nine slabs with increasing interface distance are shown in figure 5.7.

Same as for H_2O, the resolution of the distributions $H_z(\phi, \cos\theta)$ for the DCE phase was set to 50x50 pixels over $(\phi, \cos\theta) :\mapsto [0, 90] \times [-1, 1]$. Due to the larger size of the DCE molecules compared to H_2O , an increased slab thickness of 1.5nm was chosen to improve statistics. As in figure 5.6, in the top row slab boundaries are indicated by vertical blue lines while each slab's relative number density $\langle\rho\rangle/\langle\rho^{\text{bulk}}\rangle$ is depicted by a blue dot. To calculate the reference bulk density, the slab [-18,-16.5] was chosen. This is suffiently far away from the interface to be considered bulk as is easily visible from figure 5.8.

Even more pronounced than in the case of water, the first and second solvation shell with peaks in slab [-1.5, -3.0] and [-6, 7.5] are visible in $\langle\rho\rangle/\langle\rho^{\text{bulk}}\rangle$. Comparing figures 5.6 and 5.7, one can see that the relative density fluctuations are considerably larger in DCE than H_2O and stretch further into the bulk. Examining these distributions H_z, one can see that the interface has an ordering effect on the DCE molecules in the vicinity of the LLI. This effect is less pronounced compared to the water phase and is fading faster with interfacial distance. Nevertheless, the distribution for slab $H_{[0,1.5]}$ exhibits a distinct maximum around $\phi \approx 85°$ and a minimum around $\phi \approx 10°$. This preference persists until minimum and maximum reverse in slab [-3.0, -4.5]. The two anti-symmetric poles oscillate with distance from the LLI. This oscillation is correlated with the density fluctuations portrayed in the top row of figure 5.7, albeit differs in frequency.

Since the DCE molecular coordinate system is dependent on the conformational state of the DCE molecule, calculating the joint bivariate distributions $H_z(\cos\theta, \phi)$ separately for *trans* and *gauche* DCE could provide further insight. This is underlined further by the comparison of the $\langle\rho\rangle/\langle\rho^{\text{bulk}}\rangle$ profiles for both conformers and all DCE. This is portrayed in figure 5.8.

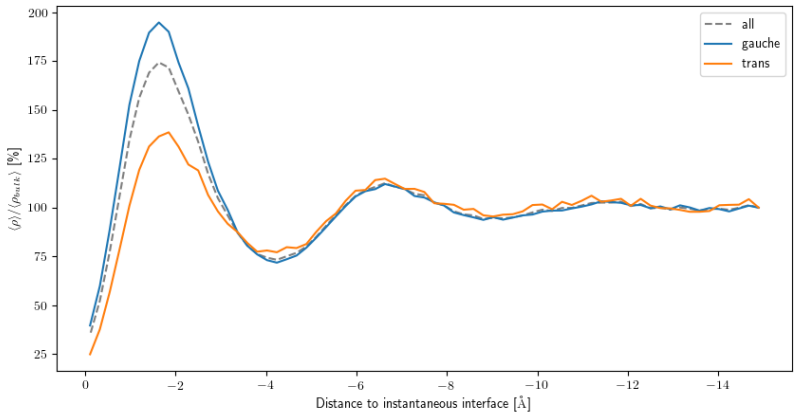

Figure 5.8 – $\langle\rho\rangle/\langle\rho^{\text{bulk}}\rangle$ profile for *gauche* (blue), *trans* (orange) and all (dotted grey) DCE molecules. The relative oscillations in density are significantly more pronounced for *gauche* than for *trans* DCE. This effect is most prevalent around the first peak for interfacial distances up to 4 Å.

While peaks occur roughly at identical distances from the LLI, it is apparent that the relative oscillations in density are significantly more pronounced for *gauche* than for *trans* DCE. This effect is most prevalent around the first peak for interfacial distances up to 4 Å. Here, *gauche* DCE reaches 195% bulk density compared to 140% bulk density in *trans*. This is expected since more *gauche* DCE

is generated at the interface due to electrostatic stabilization in response to an to an electrostatic potential imposed by the H_2O phase.

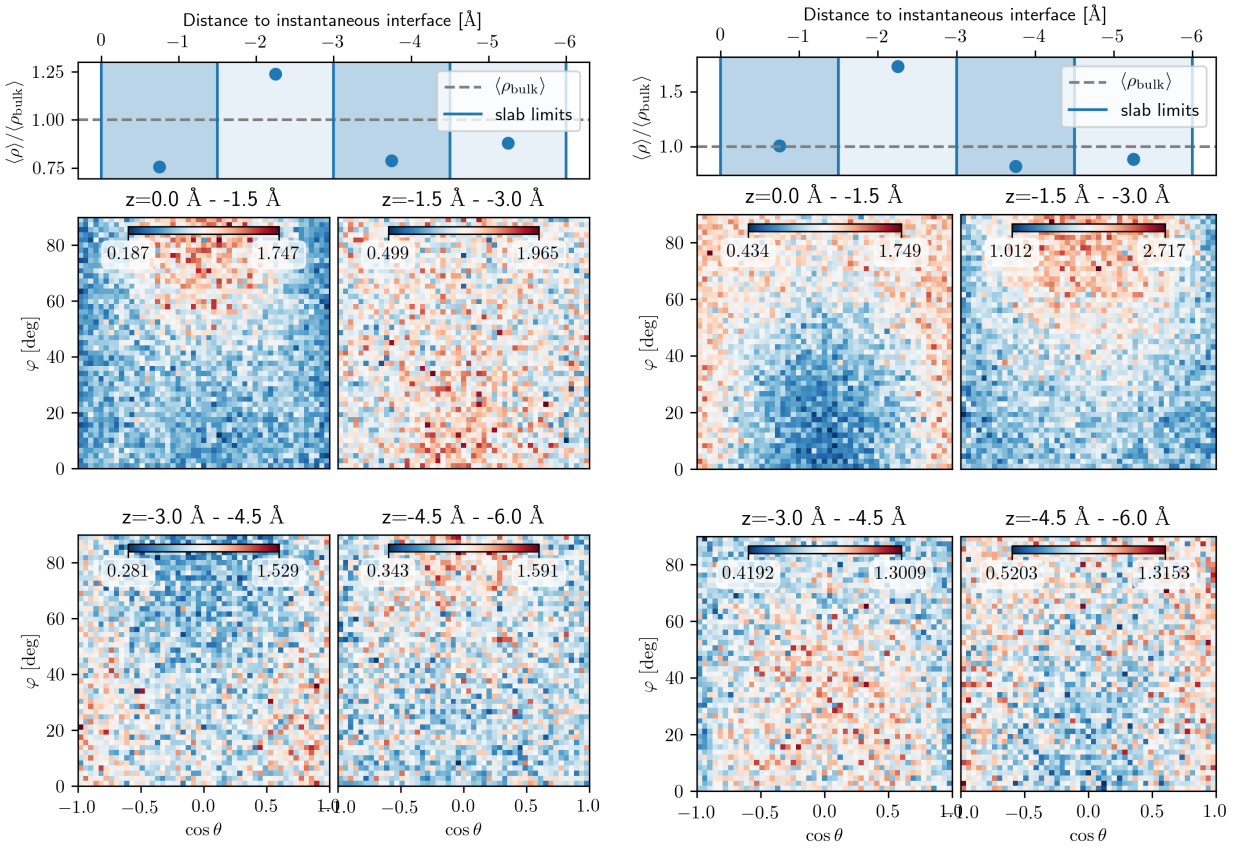

(a) Trans conformation.

(b) Gauche conformation.

Figure 5.9 – Separate *trans* (left) and *gauche* (right) DCE joint bivariate distributions $H_z(\cos\theta, \phi)$ with identical slab thickness and pixel resolution as in figure 5.7. The interfacial slab distribution $H_{[0,-1.5]}$ indicates a preferred orientation for polar angles $\phi > 70°$ for both conformers.

The $H_z(\cos\theta, \phi)$ with identical slab thickness and pixel resolution as in figure 5.7 are compared side by side in figure 5.9 for the four slabs closest to the interface. The H_z for *trans* DCE are portrayed in figure 5.9a and for *gauche* DCE in figure 5.9b. The relative density fluctuations portrayed in the top row of figures 5.9b and 5.9a support the observations made in figure 5.8. $\langle\rho\rangle/\langle\rho^{\mathrm{bulk}}\rangle$ of *gauche* DCE oscillates considerably stronger than *trans* DCE in the first solvation shell. The relative density of *gauche* DCE is larger by a factor of 1.1 than its bulk value in the interfacial slab [0,-1.5] and even increases to a factor of 1.57 in the following slab [-1.5, 3.0]. The same factors for *trans* DCE are considerably lower with 0.78 in [0, -1.5] and 1.24 in [-1.5, -3.0]. The interfacial slab distribution $H_{[0,-1.5]}$ indicates a preferred orientation for polar angles $\phi > 70°$ for both conformers. In the case of *trans* DCE, this takes the form of a spheroidal peak around $\phi \approx 85°$. In the case of *gauche* DCE this preference is best described by a spheroidal probability sink around $\phi \approx 15°$ and $\cos\theta \approx 0$. Comparing this to the correlation between molecular dipole $\boldsymbol{\mu}$ and the molecular coordinate vectors $\hat{\mathbf{p}}$ and $\hat{\mathbf{m}}$ in figure 5.4, one can deduce an anti-parallel alignment of molecular dipole and LLI surface normals within the interfacial layer of the organic DCE phase. This preference persists in slab [-1.5, -3.0] for *gauche* DCE as can be seen in figure 5.9b. In figure 5.9a, structure is almost entirely lost

for the same slab. In both cases, noticeable features in orientational structure decay faster than fluctuations in density in the organic phase compared to water. From figure 5.9 it can furthermore be concluded, that the *gauche* conformer is dominant for interfacial ordering in the DCE phase.

Chapter 6

Electric Field and Polarization in Proximity to Cluster Centers

In this chapter, the relation between the field and molecular polarity is investigated directly without prior coarse-graining into a dielectric mean-field response. Figure 6.1 shows the distribution of the angle θ between the cluster dipole $\boldsymbol{\mu}$ and the electric field $\mathbf{E}^{\mathbf{0}}$ created by all charges not belonging to the cluster as felt at the cluster center. All three distributions exhibit a clear maximum, indicating a preferred angular orientation between the field and dipole vectors. The sharpest peak at 12.06 degrees with a distribution mean angle of 15.33 degrees is visible for the distribution of θ in H2OBULK, molecularly clustered. The broadest peak at 49.14 degrees and the corresponding mean at 54.20 degrees for the distribution of θ is obtained for the DCEBULK trajectory with 2xCCl dipole clustering. Both resemble a Maxwell-Boltzmann distribution.

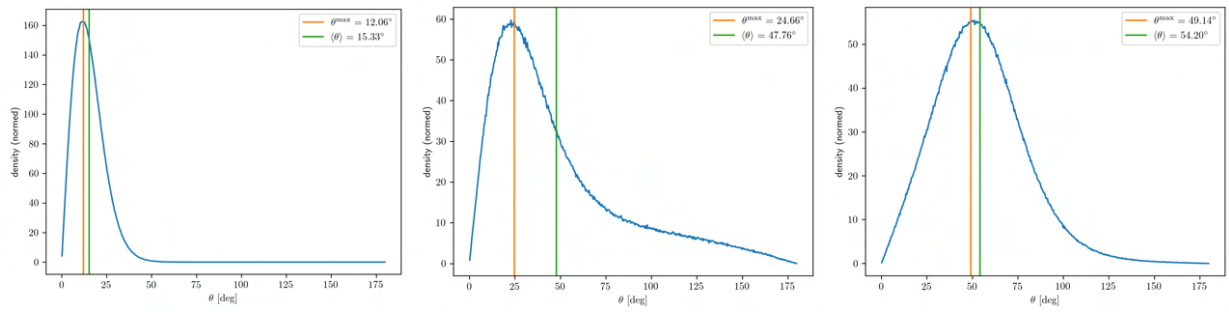

(a) H_2O molecular dipole clustering **(b)** DCE molecular dipole clustering **(c)** DCE 2xCCl dipole clustering

Figure 6.1 – Distribution of the angle θ between the cluster dipole $\boldsymbol{\mu}$ and the electric field $\mathbf{E}^{\mathbf{0}}$ created by all charges not belonging to the cluster as felt at the cluster center in H2OBULK and DCEBULK. All three distributions exhibit a clear maximum, indicating a preferred angular orientation between the field and dipole vectors. Contrary to the the molecularly clustered H_2O and 2xCCl clustered DCE, the θ distribution in this case has a pronounced tail towards higher angles. This effect can likely be attributed to superpositions of two different distributions arising due to the *gauche* and *trans* molecular configurations of DCE.

The distribution for molecularly clustered DCE in DCEBULK shows a peak at 24.66 degrees and a distribution mean angle of 47.66 degrees. Contrary to the the molecularly clustered H_2O and 2xCCl clustered DCE, the θ distribution in this case has a pronounced tail towards higher angles.

This effect can likely be attributed to superpositions of two different distributions arising due to the *gauche* and *trans* molecular configurations of DCE.

Naturally, a clear phase transition is visible in the angle and potential profiles for DCEH2OINT portrayed in figure 6.2. Interestingly the correlation with the solvation shell profile is significantly smaller compared to the permittivity profiles calculated in previous chapters. The change in polarization response between bulk and interface of the liquid phases is therefore most likely due to dipole orientation with the molecular fields mostly staying constant. Particularly since the permittivity is supposed to be a material property, comparing polarization and its electrostatic response on a molecular level might offer a path towards a mapping between bulk and interface for the dielectric constant.

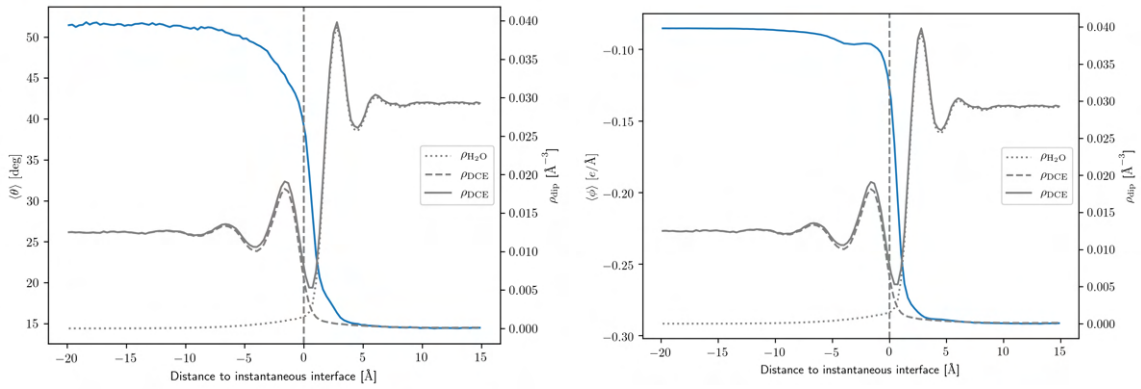

(a) $\langle\theta\rangle$ profile over interface.

(b) $\langle\theta\rangle$ at cluster center profile over interface.

Figure 6.2 – Profiles of $\langle\theta\rangle$ (left) and electrostatic potential $\langle\phi\rangle$ at the molecular center of mass (right) for DCEH2OINT, molecularly clustered. The correlation with the solvation shell profile is significantly smaller compared to the permittivity profiles calculated in previous chapters.

The significant dependence of the θ distribution on the clustering method of the same DCEBULK trajectory in figure 6.1 elucidates a key problem of only looking at the cluster centers. The cluster centers are the centers of mass and as such neither evenly distributed nor independent of the clustering type. After all the center of mass depends on the relative distribution of mass in the cluster and a 2xCCl clustered DCE molecule thus has different observation points than molecularly clustered DCE. Grouping a different set of atoms into a cluster furthermore alters which charge belongs to each cluster and thus gets ignored in $\mathbf{E^0}$. Examining the mean-field response to the molecular dipole only at the cluster centers thus falls short, the entire vicinity of each molecule should be analyzed instead.

Similar observations are made for the $\boldsymbol{\mu}$ vs. $\mathbf{E}$ average angle profile portrayed in figure 6.2a. No correlation with the solvation shell profile exhibited by the density is visible. The same is true for the average electrostatic potential profile measured at the dipole centers and excluding intra-domain contributions, as portrayed in figure 6.2b.

6.1 Formalism

The formalism to obtain volumetrically resolved averages for the electric field in vicinity of a molecule depending on its orientation is presented in the following. In all cases, a molecular clustering is chosen in order to guarantee independent movement of the cluster centers.

In an initial step, the electric field of all present charges is measured at a number of ghost atoms at each recorded snapshot of the original trajectory post simulation. These ghost atoms serve as pure measurement points, carry no charge and don't interact in any way with the actual particles of the simulation. Their position in the simulation box is randomly chosen in every snapshot in order to avoid any *a priori* spatial sampling preference in case the arrangement of molecules making up the simulation is locally correlated over snapshots in the laboratory frame. This might for example occur for the last solvation shell of water molecules in front of an interface. Especially for solid-water interfaces for example there is substantial evidence that in the immediate vicinity of the phase boundary, H_2O behaves more like ice than a liquid [25, 26, 54].

Introducing a large number of ghost atoms for sampling fields might seem like a very costly operation because in order to adequately sample the simulation box volume, a large number of these ghost-atoms needs to be added in comparison to the particles making up the simulation - especially if the $\mathcal{O}(N \log(N))$ scaling of the Ewald summation required to calculate the long-range electrostatic field contribution is considered. However, the interaction between ghost atoms can be excluded from pairwise calculations since interaction between ghost atoms is of no interest. The cost of the field calculation thus scales linear with the number of ghost atoms added. Additionally, a field calculation including ghost atoms only is performed at every snapshot and not every simulation timestep, resulting in a comparatively low computational cost of this ghost atom approach compared to the entire cost of running a MD simulation.

In a second step, every ghost atom is assigned to the cluster of the atom closest to it. Compared to a standard 3D Voronoi tesselation [191] with the cluster centers as generators, this has the advantage that the topology of the cluster type is taken into consideration. Furthermore the atomic clustering approach has the benefit of keeping the space division cluster agnostic. This is because it is performed with respect only to the particles that are actually present in the simulation and not introduced as part of a clustering step afterwards. The cluster ID as well as the connecting vector between ghost atom and cluster center is saved. Besides providing field measurements off cluster-center, this approach also samples the average space occupied by a single cluster thus providing a cavity definition without *a priori* assumptions. This corresponds to a spatial understanding of the actual cavity because the assignment to a cluster depends on the euclidian distance. It is in theory possible to use other definitions, but this choice has the advantage of clearly separating "outside" and "inside" charge. Only charge belonging to the cluster is ever present in the cavity. This approach also fits the intuitive assumption that a continuous medium should fill up the space it occupies completely.

Subsequently in a third step, the field contributions of charges belonging to the assigned closest cluster are subtracted at each ghost atom. In order to transform the trajectory from the laboratory

frame into a cluster-centric coordinate system, all clusters are oriented onto each other with the cluster center shifted to the origin. Similar to chapter 5, this requires the definition of a primary coordinate vector $\hat{\mathbf{p}}$ and a secondary coordinate vector $\hat{\mathbf{m}}$ orthogonal to it. This defines the right-hand orthonormal coordinate system $(\hat{\mathbf{p}}, \hat{\mathbf{p}} \times \hat{\mathbf{m}}, \hat{\mathbf{m}})$ for each individual cluster.

For the transformation $(\hat{\mathbf{x}}, \hat{\mathbf{y}}, \hat{\mathbf{z}}) \mapsto (\hat{\mathbf{p}}, \hat{\mathbf{p}} \times \hat{\mathbf{m}}, \hat{\mathbf{m}})$ from the laboratory frame to the cluster-centric coordinate system, all ghost atoms, as well as the corresponding potential-and electric fields, are rotated analogous to their assigned cluster center.

The matrix to reorient an individual cluster can be split in two rotations and is given by

$$R_n = R^x_{ij}(\phi_n) R^z_{ji}(\theta_n) \tag{6.1}$$

The rotation matrix $\mathbf{R^z}$ rotates vector $\hat{\mathbf{m}}$ onto the z-axis: $(\hat{\mathbf{p}}'', \hat{\mathbf{m}}'') \mapsto (\hat{\mathbf{p}}', \hat{\mathbf{z}})$ and is given by

$$R^z_{ij} = \delta_{ij} + v_{ij} + v_{ij} v_{ij} \frac{1}{1 + \cos(\theta)} = \delta_{ij} + v_{ij} + v_{ij} v_{ij} \frac{1}{1 + \hat{m}_z} \tag{6.2}$$

Here, θ constitutes the angle between $\hat{\mathbf{m}}$ and the z-axis and $\mathbf{v}$ the skew-symmetric cross product matrix

$$\mathbf{v} = \begin{pmatrix} 0 & -v_z & v_y \\ v_z & 0 & -v_x \\ -v_y & v_x & 0 \end{pmatrix} \tag{6.3}$$

with $\mathbf{v} = \hat{\mathbf{m}} \times \hat{\mathbf{z}}$. The matrix $\mathbf{R^z}$ then performs the rotation $(\hat{\mathbf{p}}', \hat{\mathbf{m}}') \mapsto (\hat{\mathbf{x}}, \hat{\mathbf{z}})$ around the z-axis by the angle ϕ between $\hat{\mathbf{p}}'$ and the x-axis and is given by

$$R^z_{ij} = \begin{pmatrix} \cos(\phi) & -\sin(\phi) & 0 \\ \sin(\phi) & \cos(\phi) & 0 \\ 0 & 0 & 1 \end{pmatrix} \tag{6.4}$$

In a final step, the average potential and electric fields as well as the cavity expression are mapped onto a regular grid via 3D binning. In case of the cavity, a subsequent normalization is performed by assuming that the number of hits is maximal in immediate vicinity of the atomic positions because of the repulsive nature of the employed Lennard-Jones and Coulomb pair-potential (2.5) which prevents atoms from falling into each other. The probability of these voxels belonging exclusively to the cluster made up by these atoms is assumed to be one and all other values are normed accordingly. This results in a continuous cavity density, where a value of one means this area in

space is definitely part of the cavity while a value of zero means that it is definitely not. The field and potential averages are simple geometric averages and only normalized by the number of timesteps.

6.2 Bulk Water in the cluster-centric coordinate system

All cavity as well as potential and electric field calculations in this section were performed on the trajectory H2OBULK, molecularly clustered. The choice of cluster-centric coordinate vectors is portrayed in figure 6.3.

The orientation is chosen in a way that the normalized dipole vector $\hat{\mathbf{p}}$ points in x-direction and an additional cluster-specific orientation vector $\hat{\mathbf{m}}$ points in positive z-direction. Analog to chapter 5, the primary coordinate vector $\hat{\mathbf{p}}$ is chosen to coincide with the direction of the molecular dipole, while the secondary coordinate vector $\hat{\mathbf{m}}$ is calculated via the cross product between $\hat{\mathbf{p}}$ and the connecting vector $\hat{\mathbf{l}}$ between both hydrogen atoms. Consequently, $\hat{\mathbf{m}}$ is perpendicular to the molecular plane. The cluster rotation is performed such that $\hat{\mathbf{p}}$ aligns with $\hat{\mathbf{x}}$ and $\hat{\mathbf{m}}$ with $\hat{\mathbf{z}}$ as shown on the right side of figure 6.3. Here the $\mathbf{R}^{\mathbf{z}}$ rotation is shown in blue and the $\mathbf{R}^{\mathbf{x}}$ rotation is red. The origin is set to the cluster center which is the center of mass.

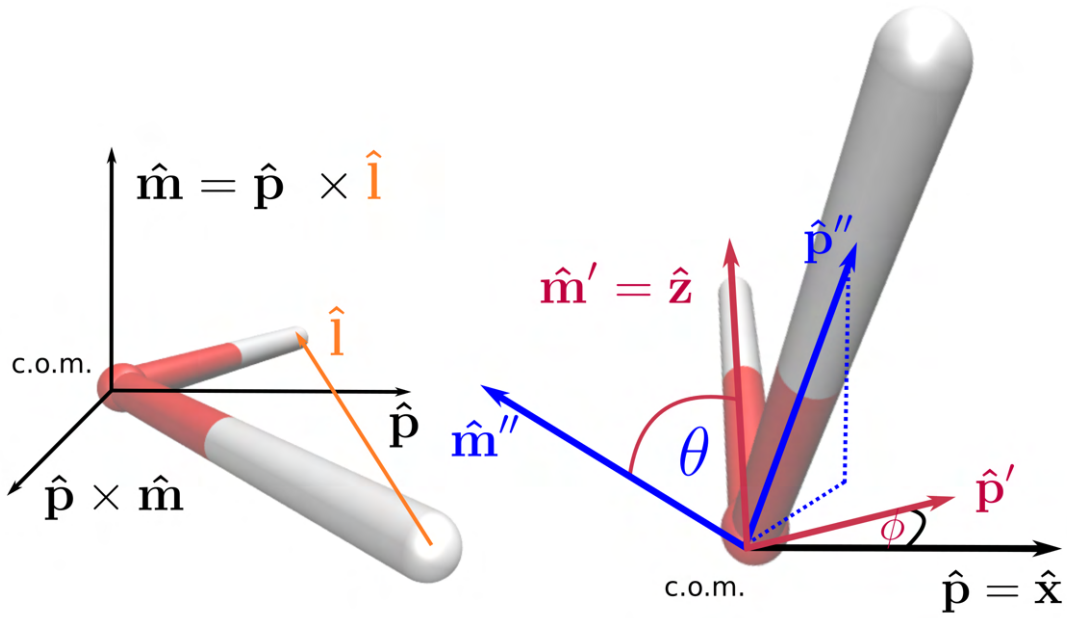

Figure 6.3 – Molecular coordinate system for $\mathrm{H_2O}$. The primary coordinate vector $\hat{\mathbf{p}}$ gets oriented along the x-axis while the secondary coordinate vector $\hat{\mathbf{m}}$ is oriented along the z-axis. The cluster center (molecular center of mass) gets shifted to the origin.

In each snapshot, 8000 ghost atoms where randomly introduced as measuring points over the box. A representation of the sampled cavity is portrayed in figure 6.4. The plots from left to right correspond to cuts along the coordinate planes for x, y, and z equal to zero. The cut z=0, represented by the right hand plot in figure 6.4, coincides with the H_2O molecular plane. For reference, the average charge density is projected onto each surface in black. Despite the point charges employed

in the SPC/Fw water model, the projection resembles an extended charge density due to intramolecular movements occuring because SPC/Fw uses harmonic bonds and angles. Furthermore, two contour lines, one solid at 0.2ρ and one dashed at 0.8ρ are marked in each plot.

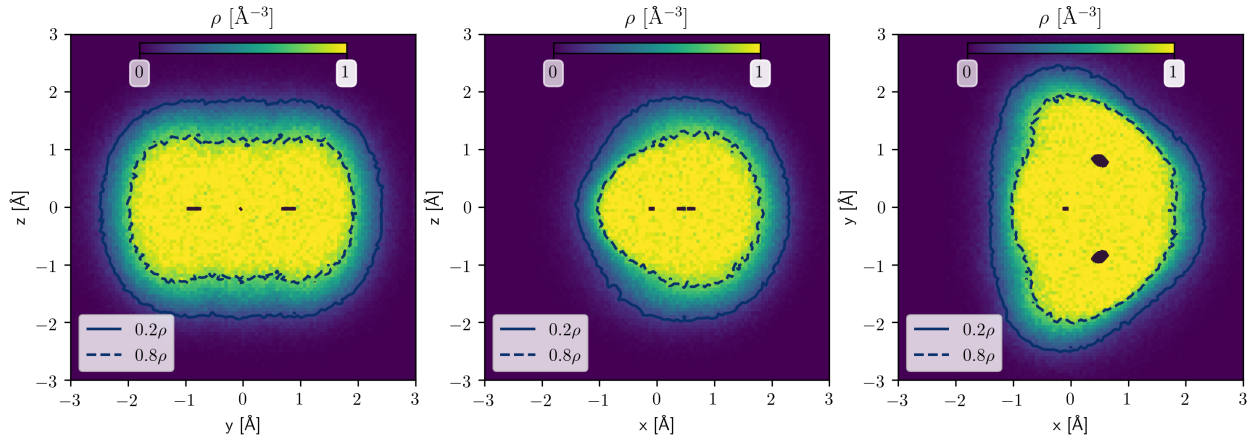

Figure 6.4 – Cavity density for H_2O for cuts along the coordinate planes. Plots from left to right correspond to cuts along the coordinate planes for x, y, and z equal to zero. The average charge density is projected onto each surface in black. Two contour lines, one solid at 0.2ρ and one dashed at 0.8ρ are marked in each plot. As expected, the shape of the cavity mainly follows the topology of a broad "ball-and-stick-model" of the planar water molecule. Examining the distance between the 0.8ρ and 0.2ρ contour lines indicates that the cavity probability ρ declines fairly homogeneously in all directions.

The shape of the cavity mainly follows the topology of a broad "ball-and-stick-model" of the planar water molecule. This is expected if one considers the radially repulsive nature of the Lennard-Jones and Coulombic interaction potential terms. It should however be noted, that the cavity interface seems to be more diffuse around the hydrogens than at the oxygen, possibly due to stronger vibrational displacement of the lighter H-nuclei. Examining the distance between the 0.8ρ and 0.2ρ contour lines indicates that the cavity probability ρ declines fairly homogeneously in all directions. The only notable exceptions are located behind the oxygen atom in the xz-plane portrayed in the middle plot and the flanks of the hydrogens visible in the xy-plane rightmost plot of figure 6.4. In these areas the decline from 0.8ρ to 0.2ρ is slightly steeper which reflects the repulsive nature of the SPC/Fw Lennard-Jones potential. The cavity density is furthermore axially symmetric with respect to the x-axis, i.e. the dipole, as well as the molecular plane. These symmetries are implied if one recalls the definition of the orientational vector $\hat{\mathbf{m}} = \hat{\mathbf{p}} \times \hat{\mathbf{I}}$. Since both hydrogens are identical, the sign of $\hat{\mathbf{I}}$ and hence $\hat{\mathbf{m}}$ is interchangeable.

The average Coulomb potential field within a H_2O molecule's cavity imposed by all other H_2O molecules in the simulation is presented in figure 6.5. Identical to figure 6.4, the cuts presented refer to the coordinate planes for x, y, and z equal zero and the projected mean charge as well as the cavity 0.8ρ and 0.2ρ contour lines are included for orientation. Beyond the 0.2ρ contour line, the average potential is blurred since the numerical errors deteriorate due to bad numerical sampling. As for the cavity, the potential field is also axially symmetric with respect to the x-axis as well as the molecular plane, thus following cluster symmetry.

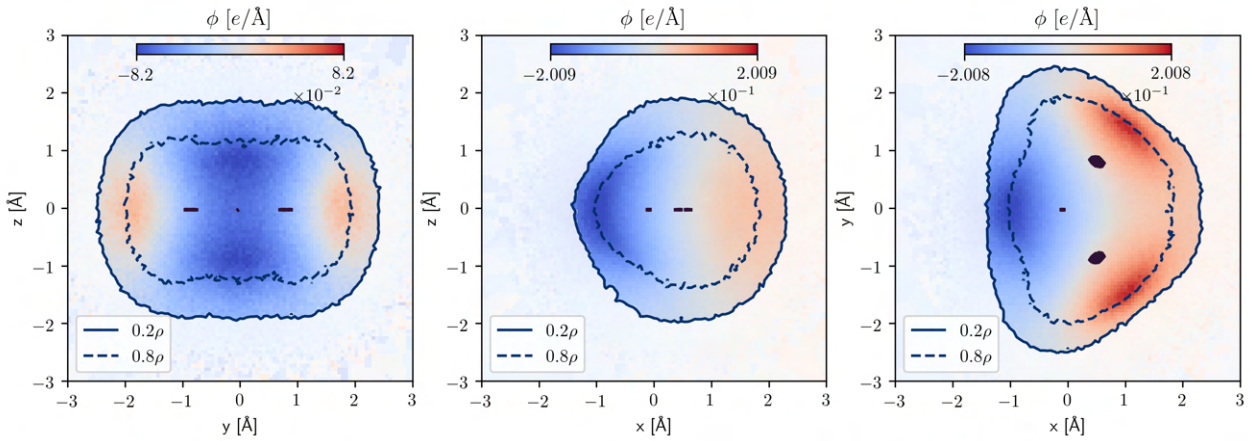

Figure 6.5 – Potential field due to all extra-molecular charges inside the cavity for cuts along the coordinate planes. Plots from left to right correspond to cuts along the coordinate planes for x, y, and z equal zero. The average charge density is projected onto each surface in black. Two contour lines, one solid at 0.2ρ and one dashed at 0.8ρ are marked in each plot. The largest magnitude potentials are not observed at the charge locations but further out in the cavity.

The center contour plot reveals a potential sink bending around the oxygen to the left side of the cavity. The left hand plot furthermore shows two distinct lobes at around $z = \pm 1.9$ Å on the y-axis. In the x>0 half space, the hydrogen atoms are each opposed by two lobe-like potential sources. The potential observed at the cluster center of figure 6.5 at the origin is consistent with the potential observed in figure 6.2b of $\phi = 0.03$, as expected. Interestingly, the largest magnitude potentials are not observed at the charge locations but further out in the cavity as the xy-projection on the right of figure 6.5 illustrates.

The corresponding average $\mathbf{E}$-field components for the cuts along the coordinate planes are portrayed in figure 6.6. In contrast to the average potential in figure 6.5 and cavity probability in figure 6.4, not all components of the electrical vector field are axially symmetric over the xy- and the xz-plane but are rather changing sign on opposite sides of these mirroring planes. This can be explained by recalling that the electric field is a gradient field of the potential $\mathbf{E} = -\nabla\phi$. The change in sign arises therefore through the change of sign of the partial derivatives in the nabla operator at the origin. If this change in sign is considered, the planar molecular symmetry is no longer violated. Another observation is that the x-component of $\mathbf{E}$ is positive throughout at the origin and E_y and E_z are both negligible in comparison.

If the observation is extended further out into the cavity it becomes apparent that both E_y and E_z have non-zero contributions, especially around the location of the oxygen and hydrogen atoms of the H_2O molecule. While typically an order of magnitude smaller than E_x, these contributions can not be neglected. E_y for example reaches magnitudes comparable to E_x around the lobes of the hydrogen atoms. This also confirms that only considering the relation between polarization and electric field at the cluster center is clearly not enough since the charged atoms of the molecule will interact with $\mathbf{E}$. Regarding the potential, the strongest fields by magnitude are observed not at the charge, i.e. the atom centers but rather further out in the cavity. While this might be less relevant in a point-charge force field model like SPC/Fw, the significance rises if electrons are included in the

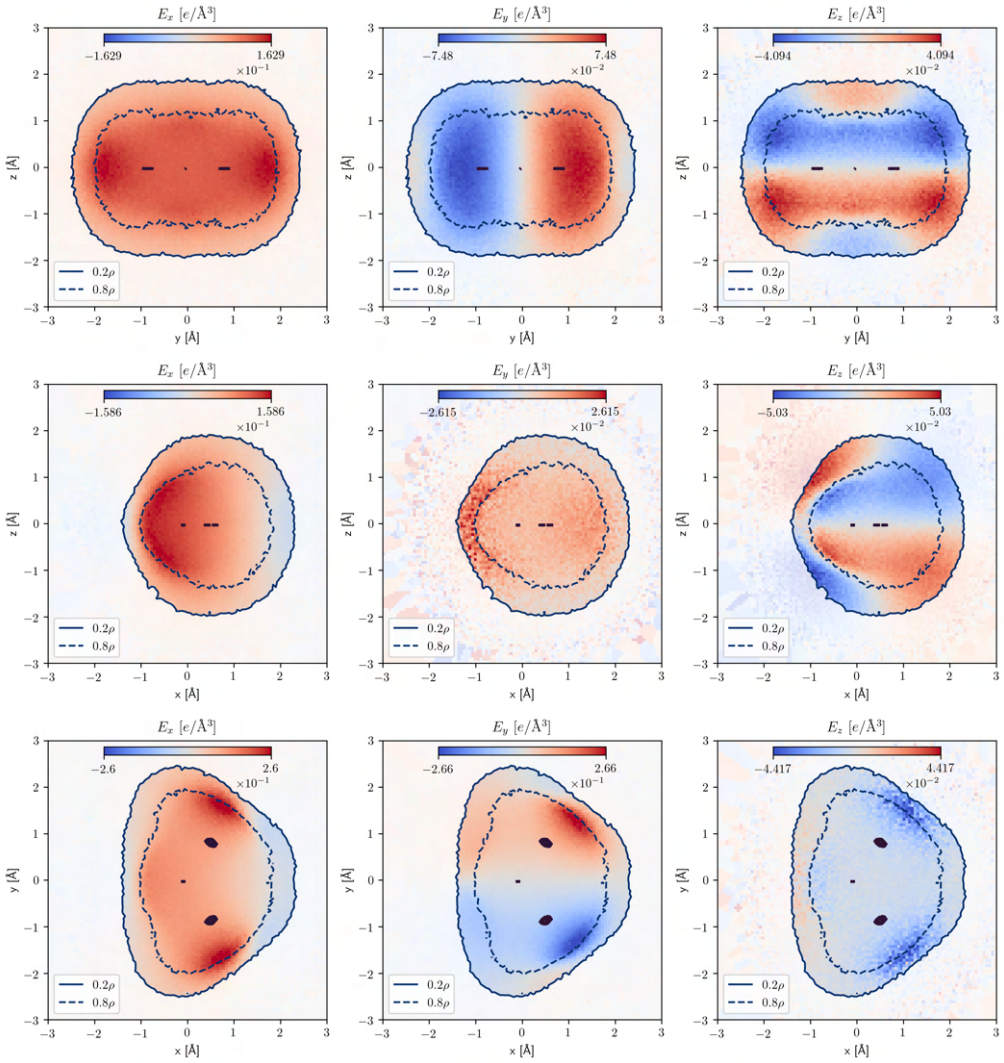

Figure 6.6 – $\mathbf{E}^0$ field due to all extra-molecular charges inside the cavity for cuts along the coordinate planes. Plots from left to right correspond to cuts along the coordinate planes for x, y, and z equal zero. The average charge density is projected onto each surface in black. Two contour lines, one solid at 0.2ρ and one dashed at 0.8ρ are marked in each plot. The x-component of $\mathbf{E}$ is positive throughout at the origin and E_y and E_z are both negligible in comparison.

calculations. Furthermore, all three components of $\mathbf{E}$ show non-constant patterns over the extent of the cavity.

A 3D rendering of charge densities, cavity and potential is portrayed in figure 6.7. The position of the oxygen atom is depicted in solid red while the position of the hydrogen atoms is depicted in solid blue. Even though H2OBULK employs a point-charge force-field, the average positions show as densities since the water molecules are simulated with harmonic bonds and angles. On a final note it should be mentioned that the cavity surface chosen is not really important. Due to the uniqueness of the Poisson equation, results can not differ if the potential is known on a closed surface around the cluster and this surface is chosen sufficiently large to prevent charge exiting or entering.

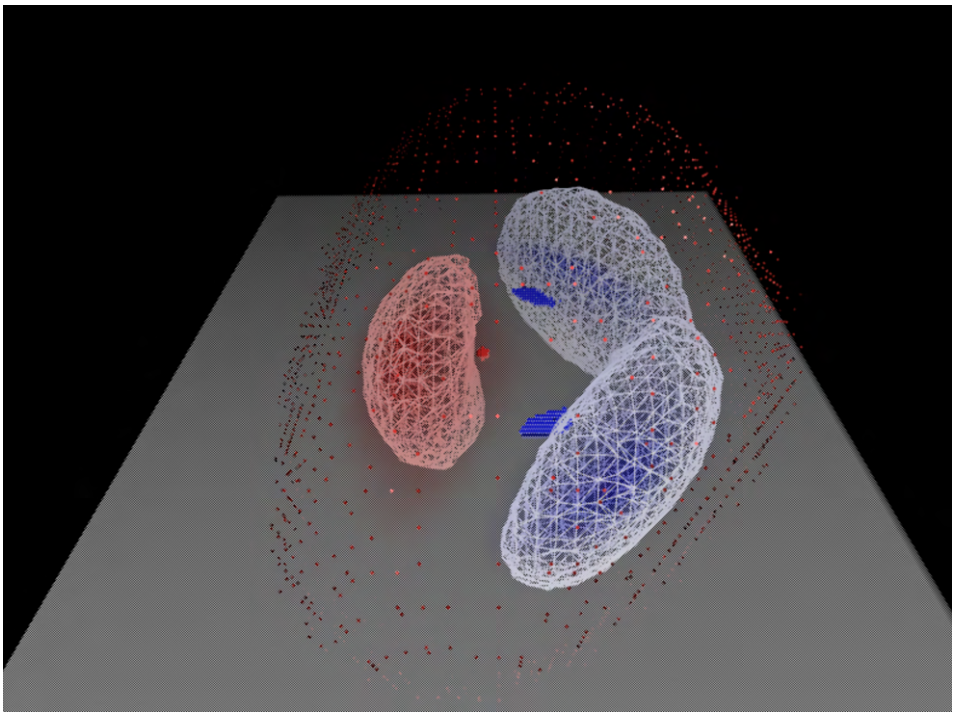

Figure 6.7 – 3D rendering of charge densities, cavity and potential. Even though H2OBULK employs a point-charge force-field, the average positions show as densities since the water molecules are simulated with harmonic bonds and angles.

6.3 Bulk DCE in the cluster-centric coordinate system

All cluster-centric field and potential averages in this section were calculated from the trajectory DCEBULK, molecularly clustered. As before, the choice of coordinate vectors follows the convention introduced in chapter 5 for the interfacial molecular binning and is portrayed on the left side of figure 6.8. The secondary cluster-coordinate vector $\hat{\mathbf{m}}$ is aligned with the C-C axis of the DCE molecule and the primary coordinate vector is given by $\hat{\mathbf{p}} = \hat{\mathbf{m}} \times (\hat{\mathbf{c}}_1 - \hat{\mathbf{c}}_2)$ where the $\hat{\mathbf{c}}_*$ denote the normals to the two planes spanned by the C-C axis and the two C-Cl bonds of the chloromethyl groups of DCE. Analog to $\mathrm{H_2O}$, the origin is set to the cluster center, which is the center of charge.

As depicted on the right side of figure 6.8 and analog to the H_2O case, each individual cluster as well as the corresponding potential and electric fields are rotated in order to align $\hat{\mathbf{m}}$ with the z-axis and $\hat{\mathbf{p}}$ with the y-axis. Due to the varying dihedral angle distribution in DCE, all averages are calculated separately in *gauche* and *trans* conformation.

Since DCE lacks the planar symmetry of $\mathrm{H_2O}$, the sign of $\hat{\mathbf{m}}$ is not interchangeable for DCE if all atoms are supposed to be rotated onto each other. The chosen convention here is for $\hat{\mathbf{m}} = \hat{\mathbf{z}}$ to point from the C-Cl bond with the chlorine atom in the positive $\mathbf{x} > 0$ half-space to the C-Cl bond with the chlorine atom in the negative $\mathbf{x} < 0$ half-space.

A 3D representation of cavity, as well as iso-densities of the average charge positions for both for both *gauche* and *trans* is shown in figure 6.9. Here, negative carbon and chlorine charge densities are depicted in red while positive charge densities due to hydrogens are colored blue. Due to inter-

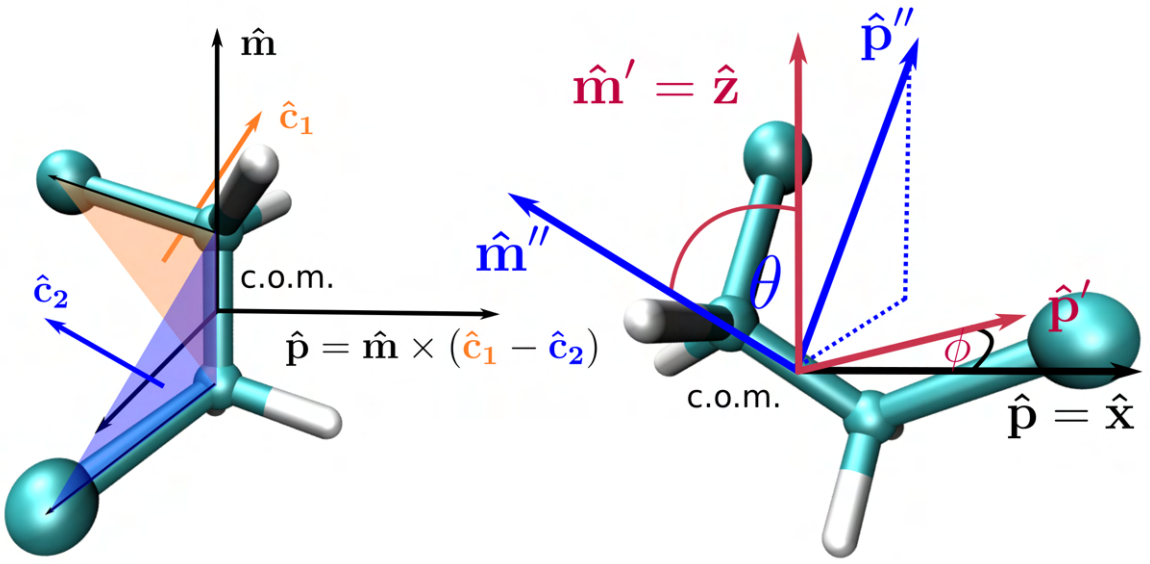

Figure 6.8 – Molecular coordinate system for DCE. The primary coordinate vector $\hat{\mathbf{p}}$ gets oriented along the x-axis while the secondary coordinate vector $\hat{\mathbf{m}}$ is oriented along the z-axis. The cluster center (molecular center of mass) gets shifted to the origin.

molecular vibrations occurring because of the harmonic pair-wise potentials for bond and angle interactions employed in the DCEBULK force-field, the average charge should again be regarded as a density distribution even if point charges are used in the simulation. In both figures 6.17a and 6.17b, the carbon atoms fall onto each other in this projection, the C-C axis represents the out of plane normal at the center red dot. The average dihedral angles for *gauche* and *trans* match the DCEBULK dihedral angle distribution in figure 5.2. The charge distribution in this rendering also confirms that the DCE dipole nicely aligns with the y-axis in both conformers. Furthermore it also visualizes why the *trans* DCE dipole is small compared to the *gauche* DCE dipole.

Analog to figure 6.5, the average potential ϕ in the cavity of a *gauche* DCE molecule imposed by all other DCE molecules of the simulation is portrayed in figure 6.10. From left to right, cuts of ϕ at $x = 0$, $y = 0$, and $z = 0$ are shown, and the cavity contour lines at 0.8ρ and 0.2ρ as well as projections of the average charge density are included. Outside the 0.2ρ contour, the potential is again blurred out due to bad sampling and thus high numerical errors. The rightmost cut at $z = 0$ aligns with the position of the observer in the 3D plot of figure 6.17a. Both the $x = 0$ and the $z = 0$ projection indicate two potential tubes of opposing sign running parallel to the C-C axis. One along the H-backbone of the *gauche* DCE in the $\mathbf{y} > 0$ half-space and the other enclosing the Cl-legs in the $\mathbf{y} < 0$ half-space.

Cuts of the same potential ϕ for *trans* DCE are plotted in figure 6.11. Again, the plots represent, from left to right, cuts of ϕ at $x = 0$, $y = 0$, and $z = 0$ are shown and the rightmost cut aligns with the position of the observer in figure 6.17b. The most notable difference to the *gauche* DCE case in figure 6.17a is that the continuous tubes of opposing sign along C-C are absent in 6.11. They are

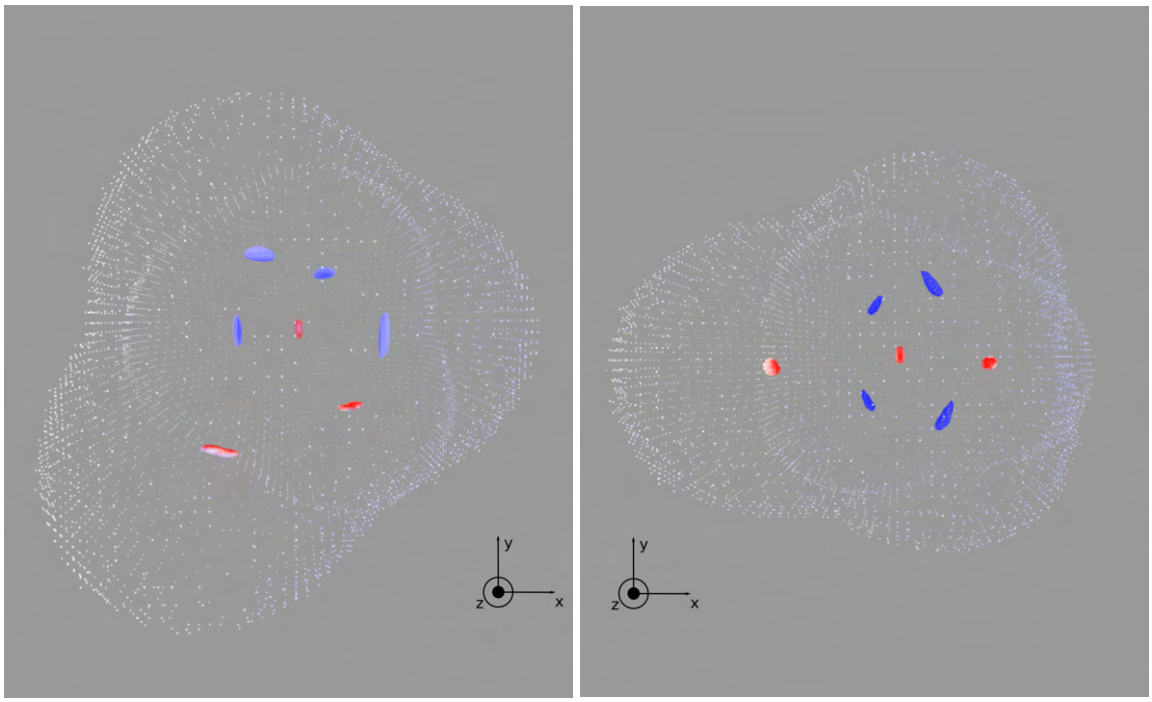

(a) gauche DCE **(b)** trans DCE

Figure 6.9 – 3D representation of cavity, as well as iso-densities of the average charge positions for both *gauche* (left) and *trans* (right) DCE. Since DCE lacks the planar symmetry of H_2O, the sign of $\hat{\mathbf{m}}$ is not interchangeable if all atoms are supposed to be rotated onto each other. The chosen convention is for $\hat{\mathbf{m}} = \hat{\mathbf{z}}$ to point from the C-Cl bond with the chlorine atom in the positive $\mathbf{x} > 0$ half-space to the C-Cl bond with the chlorine atom in the negative $\mathbf{x} < 0$ half-space.

replaced by crossing domains of equal potential, following the orientation of C-Cl bonds as most prominently visible in the center $y = 0$ projection.

Compared to the cavity potential in H_2O shown in figure 6.5, the maximal values of ϕ for both *gauche* and *trans* DCE are roughly one order of magnitude smaller. This greater potential field experienced by a water molecule in liquid water compared to DCE can be attributed to the higher density in water as compared to DCE and thus closer proximity of charges in the former case.

In figures 6.12 and 6.13, the electric field $\mathbf{E}$ inside the cavity imposed by all other participating DCE molecules of the simulation are portrayed component-wise for *gauche* DCE and *trans* DCE. Here, the same plane cuts used above for the potential constitute the rows while the components of $\mathbf{E}$ run over the columns. Analog to the potential plots, this means that in both figures 6.12 and 6.13 the third row aligns with the position of the observer in figure 6.9.

The most prominent feature of $\mathbf{E}$ for *gauche* DCE in figure 6.12 is that the E_y component is roughly two to three times greater in magnitude than E_x and E_z over all surface cuts. Furthermore, it is also positive over the entire cavity for all plane cuts, particularly at the origin. As for H_2O the average angle at the origin can be calculated by comparing $\mathbf{E}$ at the origin voxel to the molecular dipole oriented along the y-axis. With an electric field of $\mathbf{E}(0,0,0) = (0.4, 15.6, 0.7) \cdot 10^3\ e^2/\text{Å}^3$ and an average molecular dipole of $\boldsymbol{\mu} = (0, 0.70, 0)\ e\text{Å}$, this means an angle of $5.18°$ between $\mathbf{E}$ and $\boldsymbol{\mu}$.

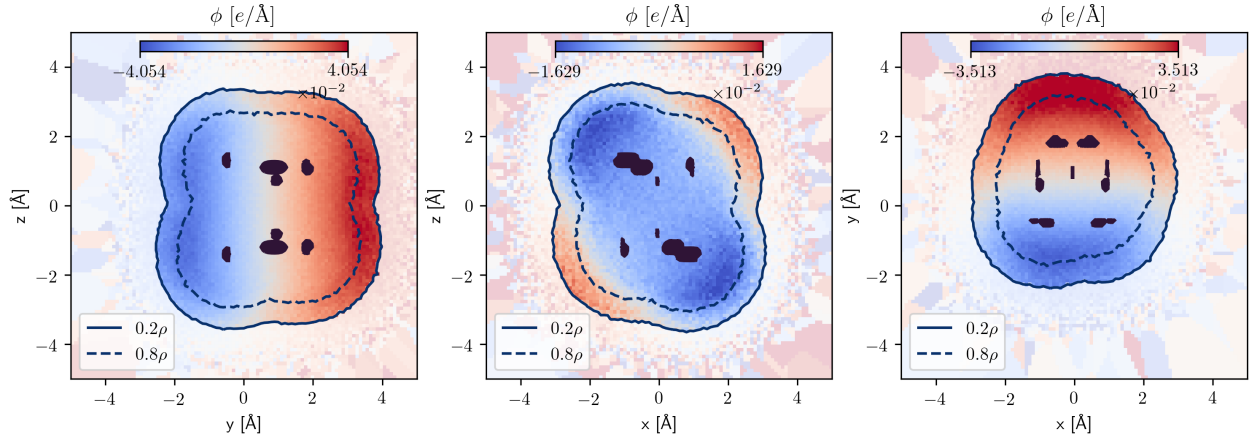

Figure 6.10 – *gauche* DCE potential field due to all extra-molecular charges inside the cavity for cuts along the coordinate planes $x = 0$, $y = 0$, and $z = 0$ from left to right. The average charge density is projected onto each surface in black. Two contour lines, one solid at 0.2ρ and one dashed at 0.8ρ are marked in each plot.

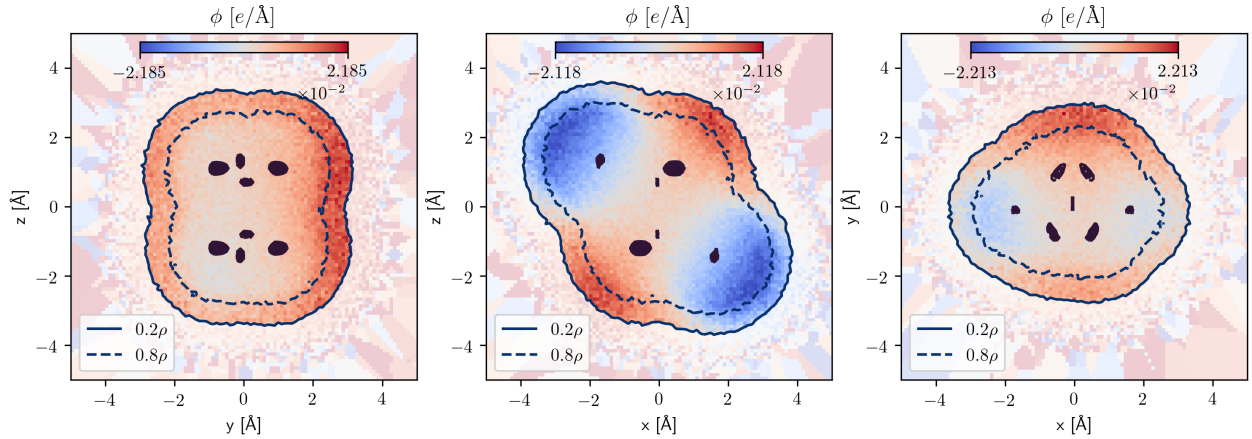

Figure 6.11 – *trans* DCE potential field due to all extra-molecular charges inside the cavity for cuts along the coordinate planes $x = 0$, $y = 0$, and $z = 0$ from left to right. The average charge density is projected onto each surface in black. Two contour lines, one solid at 0.2ρ and one dashed at 0.8ρ are marked in each plot.

The E_y component of the electric field for DCE in *trans* only keeps positive over the entire cavity for the y=0 plane in the center plot of figure 6.13. The average electric field vector at the origin is given by $\mathbf{E}(0,0,0) = (0.4, 2.7, 1.5) \cdot 10^3\ e^2/\text{Å}^3$, and stands at an angle of $31.3°$ with the average dipole vector $\boldsymbol{\mu} = (0, 0.04, 0)\ e\text{Å}$. Compared to the field magnitude $E^{\text{gauche}} = 15.7 \cdot 10^3\ e^2/\text{Å}^3$ in *gauche*, the magnitude of the electric field in *trans* formation $E^{\text{trans}} = 3.2 \cdot 10^3\ e^2/\text{Å}^3$ is smaller by roughly a factor of five.

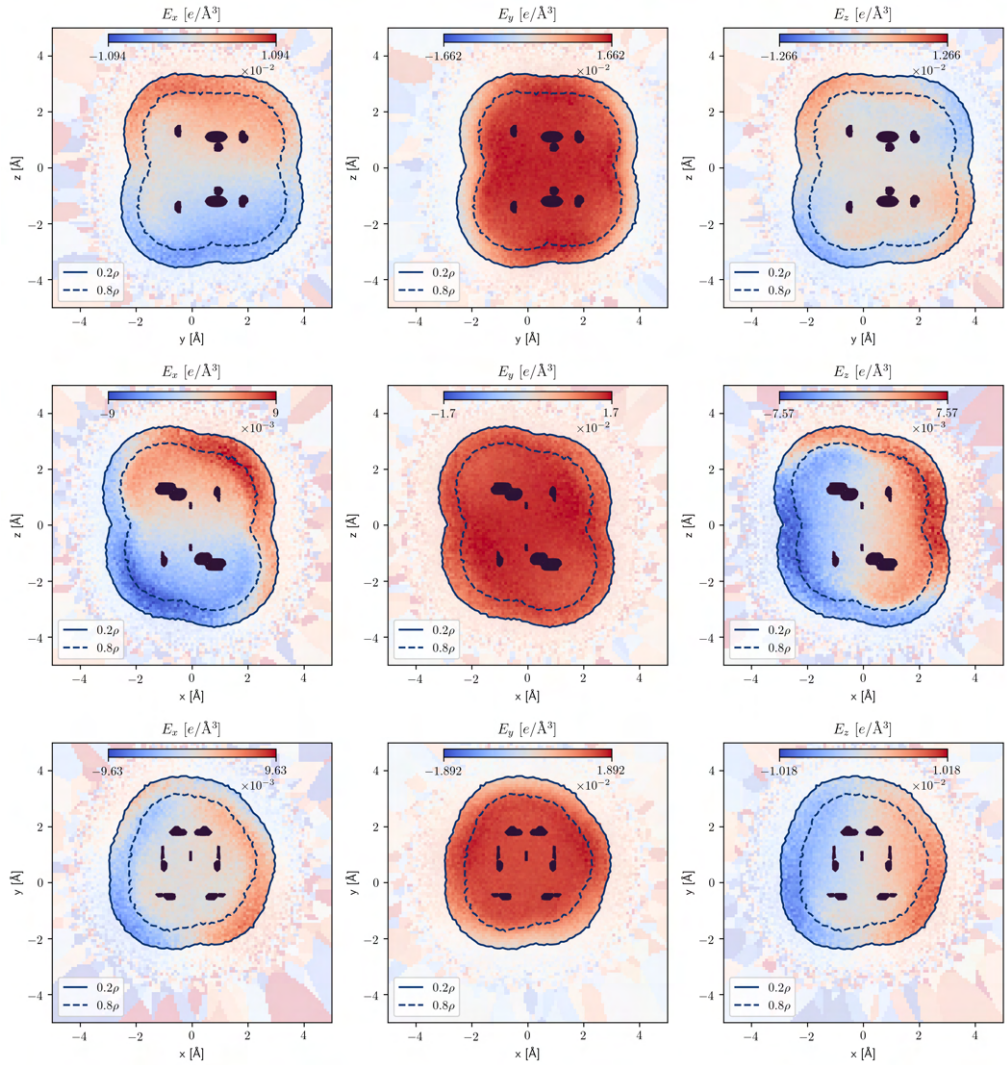

Figure 6.12 – *gauche* DCE $\mathbf{E^0}$ field due to all extra-molecular charges inside the cavity for cuts along the coordinate planes $x = 0$, $y = 0$, and $z = 0$ from left to right. The average charge density is projected onto each surface in black. Two contour lines, one solid at 0.2ρ and one dashed at 0.8ρ are marked in each plot.

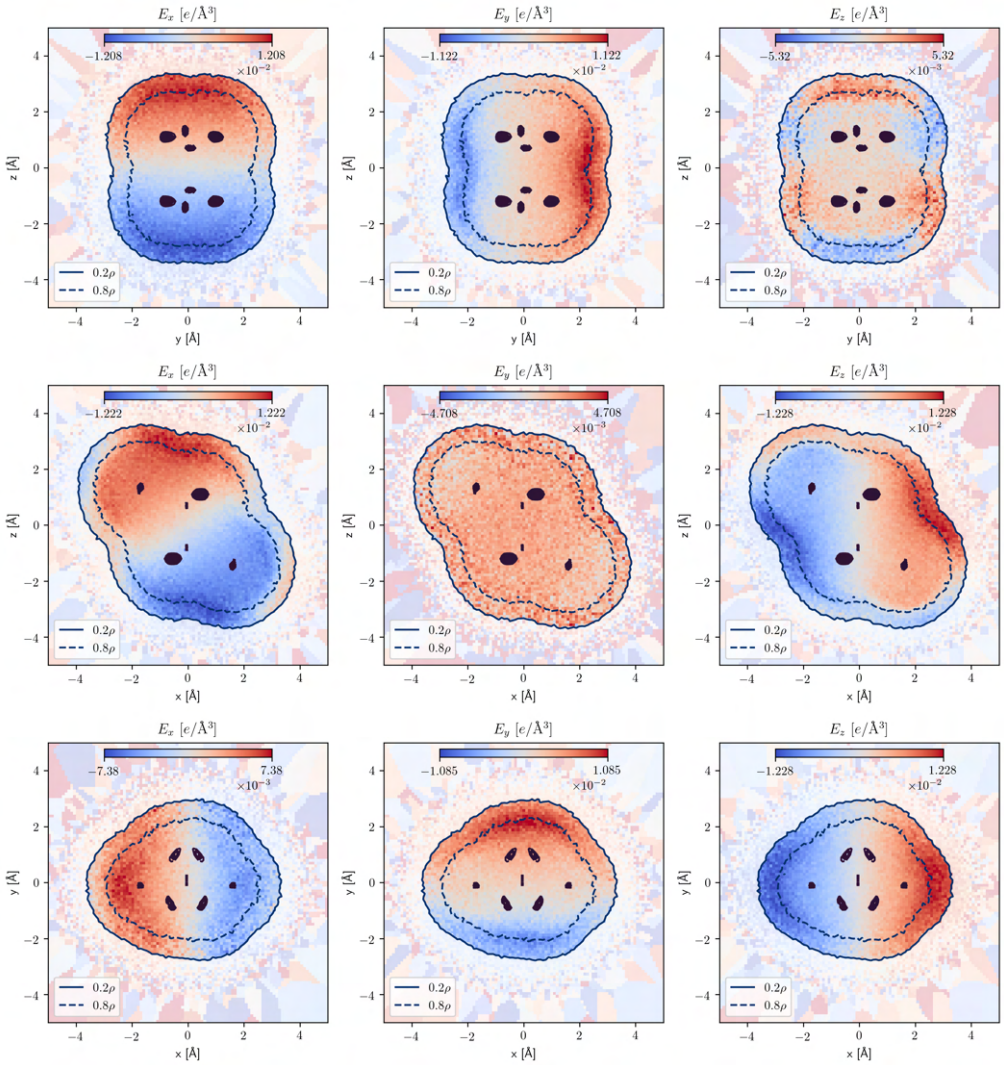

Figure 6.13 – *trans* DCE $\mathbf{E^0}$ field due to all extra-molecular charges inside the cavity for cuts along the coordinate planes $x = 0$, $y = 0$, and $z = 0$ from left to right. The average charge density is projected onto each surface in black. Two contour lines, one solid at 0.2ρ and one dashed at 0.8ρ are marked in each plot.

6.4 Interfacial field and potential in the cluster-centric coordinate system

After calculating the cavity as well as average potential and electric fields in the cluster-centric coordinate system for H2OBULK and DCEBULK, the change of these quantities towards the instantaneous LLI of DCEH2OINT is examined in this section. The trajectory was molecularly clustered and the molecular center of mass was chosen as the cluster origin. As above, the choice of coordinate vectors and rotation matrices is illustrated in figure 6.3 for H_2O and figure 6.8 for DCE.

In order to quantify the influence of the interface, the cavity field and the cavity potential in the first solvation shell are compared to bulk regimes for both H_2O and DCE as depicted in figure 6.14. The distinction between "bulk" and "interface" is made via the number density. Here, the dotted line represents the number density $\rho_{\mathrm{H_2O}}$ of H_2O , the dashed line the number density ρ_{DCE} of DCE and the solid line the total number density ρ_{tot} against the instantaneous distance to the interface. Following the usual convention, the instantaneous LLI is located at $x = 0$ while the DCE phase occupies the negative half-space and the H_2O phase the positive half-space. In figure 6.14 four different regimes are highlighted. In orange, regime "2" for instantaneous distances [-4.05 Å,0.56 Å] corresponds to the first solvation shell of DCE while "1" for instantaneous distances [-20 Å,16 Å] represents the regime to calculate the bulk baseline. The first solvation shell regime in the water phase in blue spans instantaneous distances [0.56 Å,4.55 Å] and the corresponding bulk baseline is located at distances [10 Å,14 Å]. The interfacial boundary was chosen at x=0.56 Å and not at $x = 0$ Å in order to confine the first solvation shells by the minima of ρ_{tot}.

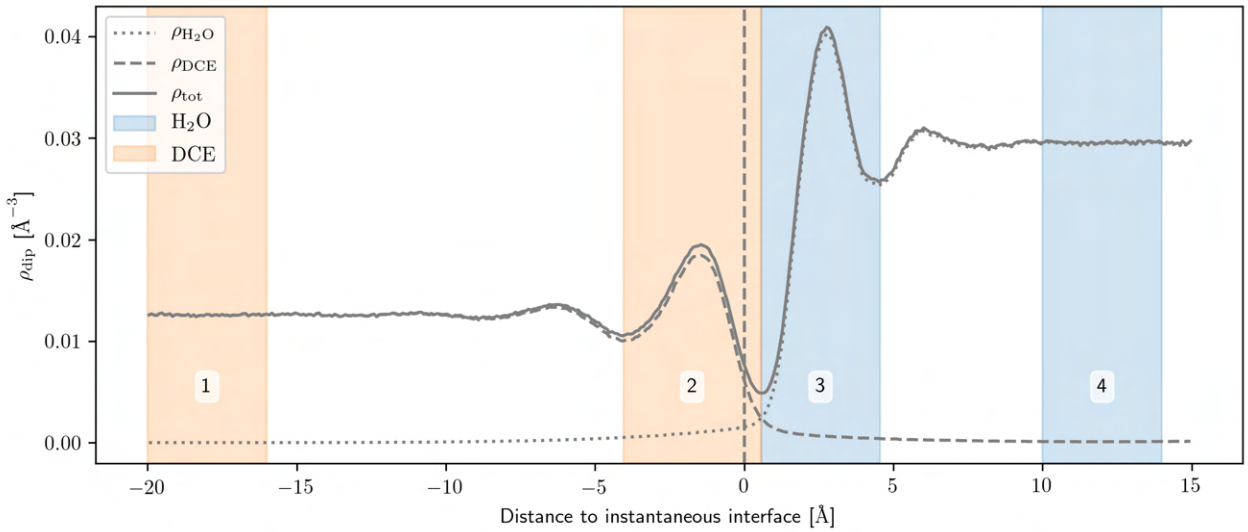

Figure 6.14 – Borders of the bulk regimes "1" (DCE) and "4" ($\mathrm{H_2O}$) to first interfacial regimes of the first solvation shell "2" (DCE) and "3" ($\mathrm{H_2O}$).

The ghost atoms necessary for the potential and $\mathbf{E}$-field measurements over the trajectory were distributed with respect to the instantaneous interface in order to guarantee optimal sampling. The ghost atoms for the DCE bulk regime "1" were distributed at interfacial distances [-25 Å, -12 Å] and the ghost atoms for the H_2O bulk regime "4" at interfacial distances [7 Å, 17 Å]. The ghost atoms

for the interfacial regimes "2" and "3" were distributed in [-10 Å, 10 Å] distance to the interface. The distance buffer of the ghost atoms over the selection regimes for the molecular centers "1"-"4" guarantees that the entire cavity is appropriately sampled. The size of this buffer should not be smaller than the maximal distance from cluster center to cavity boundary for each molecule. Comparing the cavity borders for both H_2O and DCE in the previous sections, this criterion is fulfilled.

6.4.1 Interfacial H_2O

The influence of the instantaneous interface on cavity probability and cavity potential is first examined for water. Figure 6.15 shows the cavity probability ratio between interface and bulk regimes ρ_3/ρ_4 for the surface cuts x, y, and z equal to zero from left to right. As above for the bulk trajectories, the average charge distribution is projected on to the plane for better orientation. Additional contour lines, solid for 0.2ρ and dashed for 0.8ρ, are plotted for "3" in red and and "4" in blue.

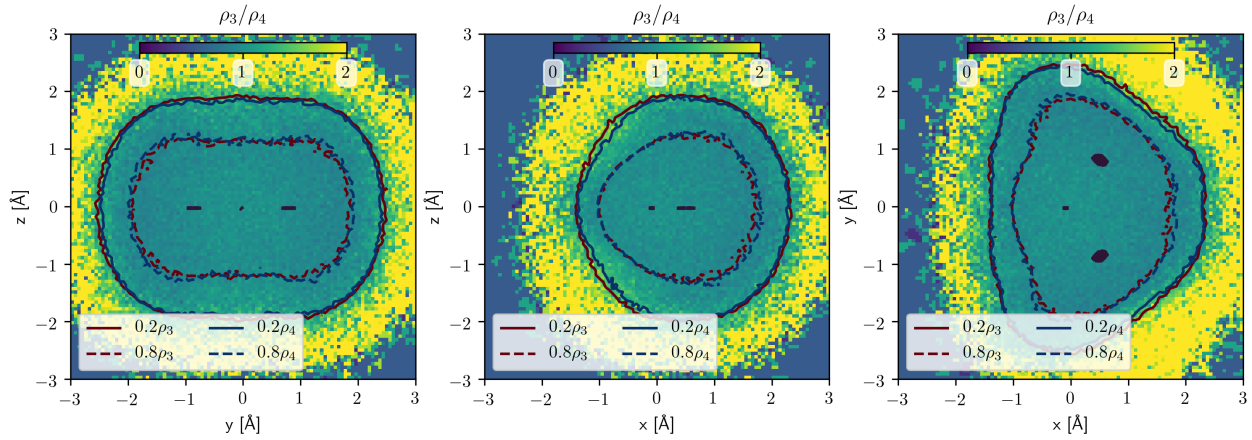

Figure 6.15 – Cavity probability ratio between H_2O interface and H_2O bulk regimes ρ_3/ρ_4 for the surface cuts x, y, and z equal to zero from left to right. Cavity probabilities $\rho > 0.2$ are roughly identical for both the interface and the bulk regime. While small deviations of the 0.2ρ contour are visible in the middle and rightmost projection, notable deviations only occur further out as signaled by the yellow corona representing a ratio of two or above.

Figure 6.15 reveals that cavity probabilities $\rho > 0.2$ are roughly identical for both the interface and the bulk regime. The shape of the cavity is roughly identical in bulk and at the interface as the green areas indicating a ratio of roughly one suggest. While small deviations of the 0.2ρ contour are visible in the middle and rightmost projection, notable deviations only occur further out as signaled by the yellow corona representing a ratio of two or above. The drawn out yellow corona with a value lower than 1 shows that the interfacial ρ_3 declines faster than the bulk benchmark ρ_4 which is to be expected when averaging over the first solvation shell. The space available to an individual H_2O molecule within the first solvation shell of regime "3" is higher on average compared to the volume available in the bulk regime "4". While immediately at the interface, this relation reverses, the number of H_2O molecules there is small. In an average over the first solvation shell, hence the high-density low-volume H_2O molecules dominate. However, compared to the total magnitude of

the bulk density, these deviations are comparatively small which is why no stronger changes in the average cavity probability density between bulk and interface are observed. The strong fluctuations in the yellow corona stem from numerical instabilities due to small value division.

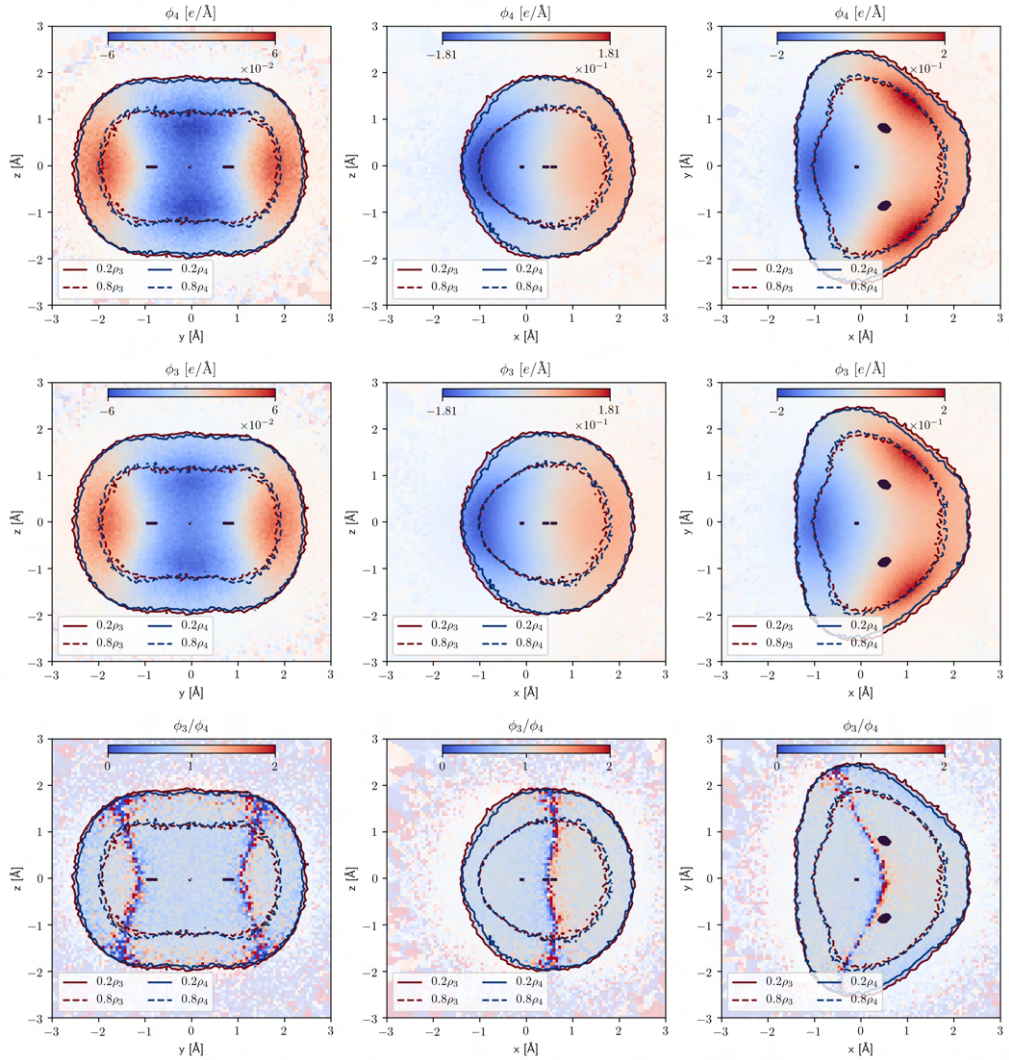

Figure 6.16 – Surface cuts through the potential fields ϕ_3 at the H_2O interface and ϕ_4 in H_2O bulk in the style of figure 6.5. The ratio ϕ_3/ϕ_4 plotted in the third row reveals an average potential slightly lower in regime "3" compared to regime "4".

In figure 6.16 the surface cuts through the potential fields ϕ_3 at the interface and ϕ_4 in bulk are portrayed in the style of figure 6.5 from the previous section. Here the first row represents the surface cuts for the bulk reference regime "3" while the second row represents the cuts for the interfacial regime "4". A visual comparison between the two regimes reveals an average potential slightly lower in regime "3" compared to regime "4". This is confirmed in the ratio ϕ_3/ϕ_4 plotted in the third row of figure 6.16. In all three surface cuts, the interfacial cavity potential is lowered compared to the bulk benchmark. This is observed over the entire cavity and seems to be relatively homogeneous. The bands of white in the third row correspond to values where $\phi_4 < 5\ me$Å as can be seen by comparing it to the first row. These values are excluded because the small values in the denominator lead to an exploding numerical error that would clutter the image. A direct depiction

of the interfacial $\mathbf{E}$-field is rather confusing since $\mathbf{E}$ is a vector field which is why it is not portrayed here.

6.4.2 Interfacial DCE

The same comparison of cavity probability and cavity potential at the interface versus the bulk can be performed in the DCE phase. As in the bulk case, the two DCE conformers *gauche* and *trans* are treated separately and discriminated via the dihedral angle according to figure 5.2. The ratio of cavity probability ρ_2/ρ_1 for both DCE conformers is portrayed in figure 6.17. For both *gauche* DCE on the left and *trans* DCE on the right, the $0.2\rho_1$ isosurface of the cavity probability in bulk is represented in white. Another isosurface of the ratio $0.2\rho_2/\rho_1$ is depicted in red. The most notable observation to draw from figure 6.17 is that the red isosurface of the interface to bulk ratio lies outside the white isosurface, indicating that the cavity is slightly more drawn out in bulk compared to the interface. This qualitatively matches the observations made for water but the drop in the interface to bulk ratio is smaller in comparison. Again, this matches the expectations due to the number density fluctuations shown in figure 6.14 since the relative change in density in the first solvation shell is higher in water compared to DCE. The skew in average cavity probability reflects that property. A second observation is that in both conformers the distance between white and red isosurface is fairly constant. The change in cavity shape, at least in an equally weighted average that is performed here, is therefore not significant.

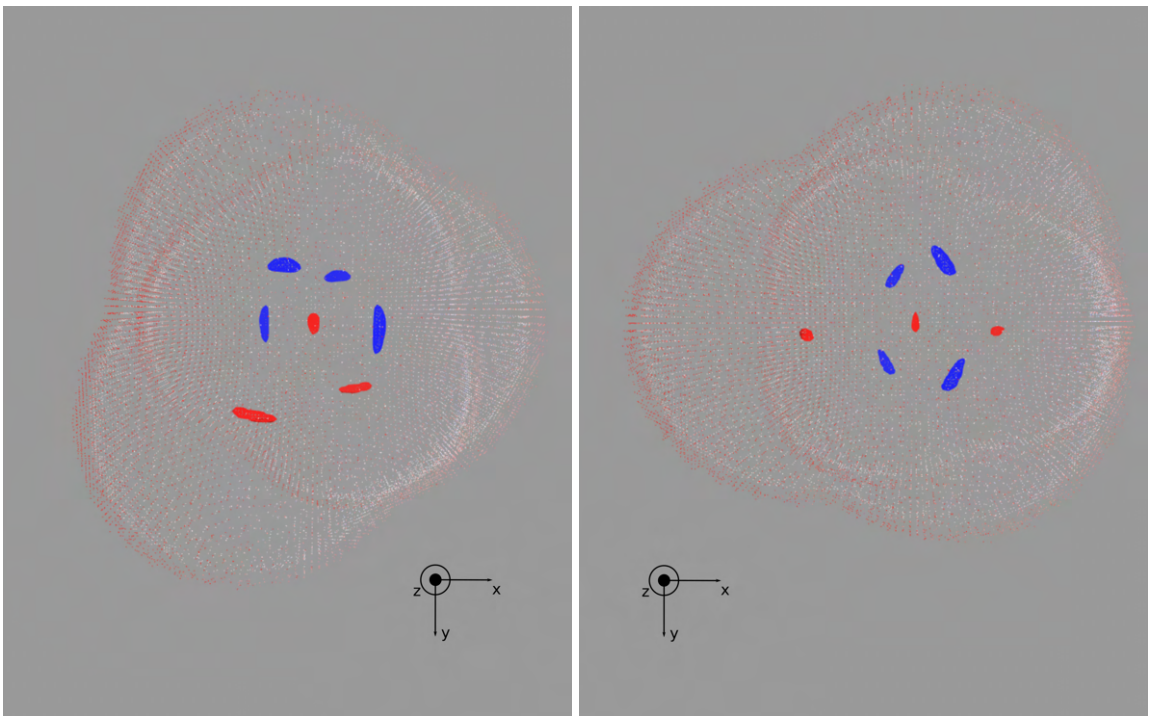

(a) gauche DCE **(b)** trans DCE

Figure 6.17 – Cavity probability for *gauche* and *trans* DCE. Bulk isosurface at $0.2\rho_1$ in white, corona at $0.2\rho_2/\rho_1$. Red corona lies outside of white, reflecting the higher density in the first solvation shell (and thus smaller volume).

The surface cuts for the average cavity potential at x, y, and z equal to zero for *gauche* DCE are portrayed in figure 6.18. Like in the corresponding plot for H_2O the average cavity potential in the DCE bulk regime ϕ_1 is plotted in the first row, while the potential in the interfacial regime ϕ_2 is plotted in the second row. A visual comparison of these first two rows with each other and the their bulk simulation counterpart in figure 6.10 shows no distinctive differences in the average cavity potential.

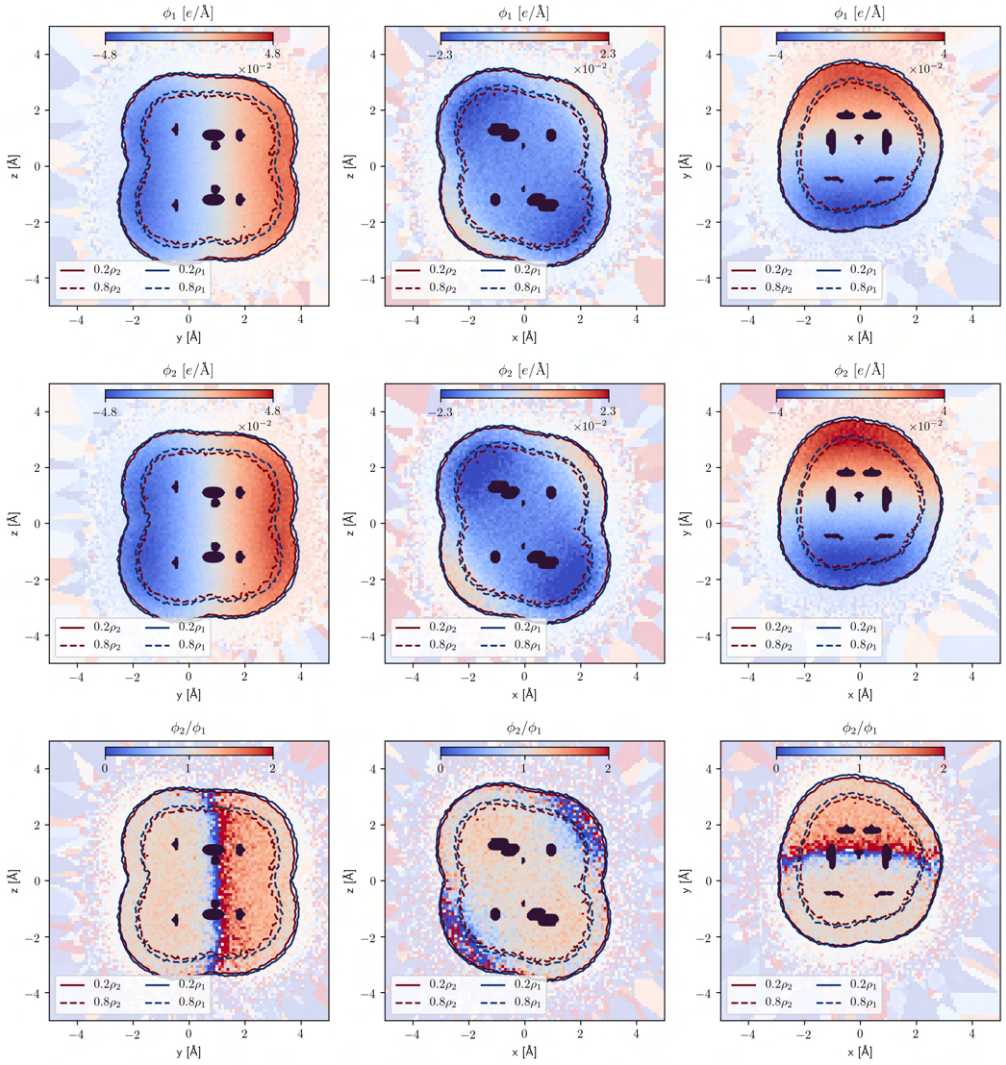

Figure 6.18 – Surface cuts through the potential fields for *gauche* DCE ϕ_2 at the interface and ϕ_1 in bulk. Opposite to water, the average cavity potential at the interface is larger than the bulk reference almost over the entire cavity. While the ratio (third row) on the chlorine side of the cavity is roughly homogeneous with a value of 1.3, the opposite side of the cavity occupied by the hydrogen atoms returns ratios of 1.4-1.6. Approaching the carbon axis from the hydrogen half of the cavity, the ratio even reaches values of two and higher.

In the third row of 6.18, the ratio ϕ_2/ϕ_1 is plotted. Opposite to water, the average cavity potential at the interface is larger than the bulk reference almost over the entire cavity. However, the interface to bulk ratio is considerably less homogeneous over the cavity. While the ratio on the chlorine side of the cavity is roughly homogeneous with a value of 1.3, the opposite side of the cavity occupied by the hydrogen atoms returns ratios of 1.4-1.6. Approaching the carbon axis from the hydrogen half of the cavity, the ratio even reaches values of two and higher. Doing the same from the chlorine half

of the cavity even shows ratios below one, indicating that the bulk reference cavity has a greater magnitude than the interfacial cavity potential in these areas. A similar effect is observed between the contours and the projection of the chlorine atoms in the middle xz-projection of the third row. This might be due to the preferential orientation of the polar *gauche* DCE molecules at the LLI as a response to the potential gradient created by the H_2O phase located on the other side of the LLI. Like for its H_2O counterpart, values with $\phi_1 < 5$ meÅ in figure 6.18 are blanked out due to numerical stability issues arising from division by small numbers.

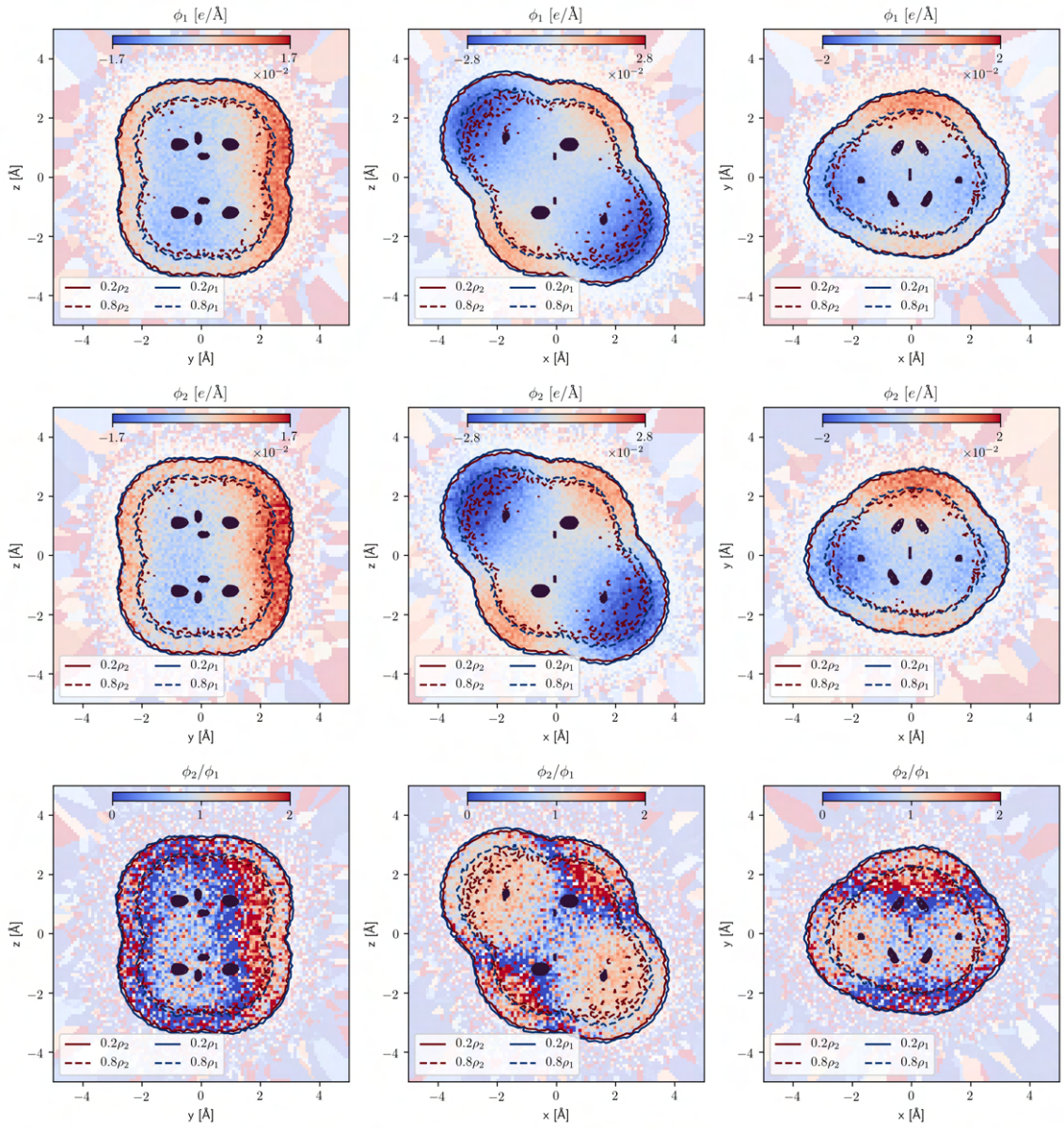

Figure 6.19 – Surface cuts through the potential fields for *trans* DCE ϕ_2 at the interface and ϕ_1 in bulk. The negative potential lobes around the chloride atom projections in the xz- and xy-plane are significantly more outspread than in the same potential for DCEBULK, leading to a neutral region in the center as compared to a distinctly positive one above. This suggests that even far into the bulk, at distances of 25 Å - 30 Å from the interface, *trans* DCE sees the influence of the interface in the cavity potential.

The corresponding surface cuts for the cavity potential of *trans* DCE are portrayed in figure 6.19. Again, the bulk reference cavity potential ϕ_1 is portrayed in the first row while its interfacial counterpart ϕ_2 is portrayed in the second row. Performing the same comparison between these two rows and the *trans* DCE results of the bulk trajectory in figure 6.11, one can notice several differences in the cavity potential. In surface cuts for the bulk trajectory above, the potential is entirely positive in the yz-plane with a neutral region in the center that skews to the lower left. In contrast, the same cuts in regimes "1" and "2" here exhibit a distinctively negative center region which is slightly more prominent for ϕ_1 in the first row. The second and third column here are more negative compared to its bulk trajectory counterpart, too. The negative potential lobes around the chloride atom projections in the xz- and xy-plane are significantly more outspread than in the same potential for DCEBULK, leading to a neutral region in the center as compared to a distinctly positive one above. This suggests that even far into the bulk, at distances of 25 Å - 30 Å from the interface, *trans* DCE sees the influence of the interface in the cavity potential. This behaviour can be interpreted as a consequence of the breaking in molecular symmetry for $\boldsymbol{\mu} \neq 0$ in *trans* DCE. Fields imposed by the presence of the /water LLI influence the presented averages in the molecular coordinate system disproportionately more in *trans* DCE compared to *gauche* DCE.

Chapter 7

Iterative Reaction Field Approach for Permittivity Calculation

In an effort to circumvent complicated electrostatic calculations arising in less regular system geometries like slabs, spheres or cylinders, an attempt to use an iterative, local reaction field approach was made that is presented in this chapter. Drawing from the fluctuation formula derivation for bulk dielectric constants by Neumann [48] presented in section 2.6.1, an attempt was made to employ local reaction fields in order to calculate a spatially resolved dielectric constant. This approach is sketched in figure 7.1.

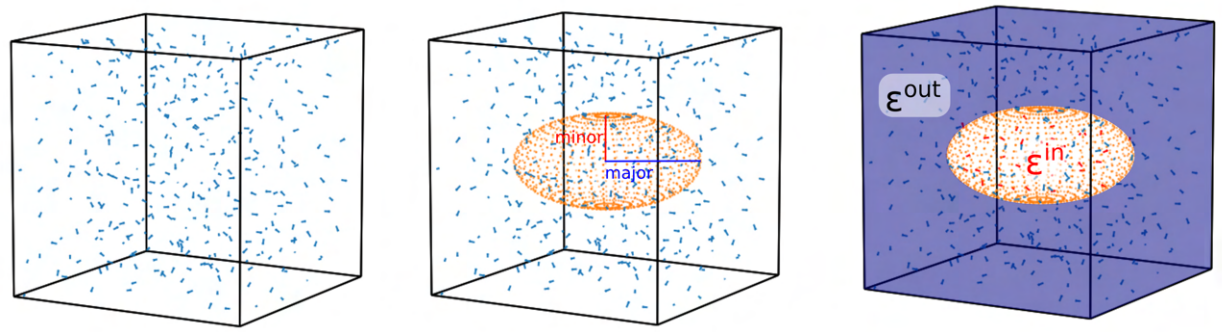

Figure 7.1 – Proposed formalism for iterative permittivity calcuation. Starting from a dipole trajectory (left), a cavity occupying a subspace of the entire simulation box is inserted (middle). This cavity is assumed to be embedded in the continuous dielectric ε^{out} (right). Only dipoles inside the cavity are treated explicitly while the interaction with the surrounding ε^{out} is coarse grained into a continuum reaction field response. The embedding dielectric ε^{out} gets then updated with this calculated ε^{in} in successive iterations until convergence.

Starting from a dipole trajectory, a cavity occupying a subspace of the entire simulation box is inserted. In the proposed reaction field picture, this cavity is assumed to be embedded in the continuous dielectric ε^{out}. Only dipoles inside the cavity are treated explicitly while the interaction with the surrounding ε^{out} is coarse grained into a continuum reaction field response.

If such a fluctuation formula is obtained, it can be employed iteratively using cavities of different shapes and orientations. The embedding dielectric ε^{out} gets then updated with this calculated ε^{in}

in successive iterations until convergence. This would allow to map out arbitrary dielectric configurations.

In search for suitable cavity geometries, oblate spheroidals were chosen for their flexibility. Through tuning of the minor and major semi-axes, cavities similar to slabs or spheres can be mimicked. Combined with cavity rotation and scaling this allows to adequately partition the dielectric to the desired spatial resolution. For a slab-like interfacial geometry between a solid and a liquid, one could for example choose a very short minor semi-axis normal to the interface and large major semi-axes parallel to the interface, resulting in a lentil shaped cavity. This would guarantee a high resolution with respect to interface distance while also exploiting the translational invariance in-plane for better statistics. Inside the cavity, the dipole-dipole interaction is explicitly calculated, analogous to the spherical cutoff case, and the interaction with the surrounding medium is coarse grained into a continuum reaction field response.

7.1 Formalism

In order to verify whether this iterative reaction field approach presents a viable option to calculate arbitrary dielectric profiles at all, its applicability to isotropic bulk systems is tested first.

As shown in section 2.6.1, the relation (2.95)

$$\lambda = \frac{1}{V}\left[\delta_{ij} - \lambda \tilde{T}_{ij}(0)\right] H_{ij} \tag{7.1}$$

between an isotropic system's bulk permittivity ε and its dipole moment fluctuations $\mathbf{H}$ can be established, if the zero-mode Fourier transform of the dipole-dipole interaction tensor $\tilde{\mathbf{T}}(\mathbf{0})$ is known. Here V represents the system volume and the parameter λ is given by

$$\lambda = \frac{3}{4\pi}\frac{\varepsilon - 1}{\varepsilon + 2} \tag{7.2}$$

The reaction field $\mathbf{E}^{\mathbf{R}}$ for a cavity system with oblate spheroid geometry with major semi-axis a and minor semi-axis b embedded in a medium with dielectric constant ε^{out} was first derived by Scholte [192]. It is constant over the cavity and proportional to the cavity dipole moment $\mathbf{M}$. It thus fulfills the necessary conditions (2.73) for $\mathbf{E}^{\mathbf{R}}$ to be incorporated into the pair-wise dipole-dipole interaction tensor

$$T_{ij}(\mathbf{r}_{ab}, \varepsilon^{\text{out}}) = \begin{cases} T_{ij}^{\text{dd}}(\mathbf{r}_{ab}) + \delta_{ij} f_{ij}(\varepsilon^{\text{out}}) & a, b \text{ in cavity} \\ 0 & \text{otherwise} \end{cases} \tag{7.3}$$

Here $\mathbf{T^{dd}}$ represents the explicit dipole-dipole interaction tensor (2.51) and $\mathbf{f}$ the reaction field tensor

$$\mathbf{f} = \begin{pmatrix} f_{\parallel} & 0 & 0 \\ 0 & f_{\parallel} & 0 \\ 0 & 0 & f_{\perp} \end{pmatrix} = \begin{pmatrix} \frac{3}{a^2 b} \frac{A^a(1-A^a)(\varepsilon^{\text{out}}-1)}{\varepsilon^{\text{out}}+(1-\varepsilon^{\text{out}})A^a} & 0 & 0 \\ 0 & \frac{3}{a^2 b} \frac{A^a(1-A^a)(\varepsilon^{\text{out}}-1)}{\varepsilon^{\text{out}}+(1-\varepsilon^{\text{out}})A^a} & 0 \\ 0 & 0 & \frac{3}{a^2 b} \frac{A^b(1-A^b)(\varepsilon^{\text{out}}-1)}{\varepsilon^{\text{out}}+(1-\varepsilon^{\text{out}})A^b} \end{pmatrix} \tag{7.4}$$

If the center coincides with the origin and the minor semi-axis is oriented along the z-axis, the integrals A^a and A^b are given by

$$A^a(a,b) = \frac{a^2 b}{2} \int_0^\infty \frac{ds}{\sqrt{(s+a^2)^4(s+b^2)}} = \frac{a^2 b}{2} \left(\frac{b}{a^2(b^2-a^2)} - \frac{\mathrm{i} \cdot \cosh^{-1}(\frac{b}{a})}{(a^2-b^2)^{3/2}} \right) \tag{7.5}$$

and

$$A^b(a,b) = \frac{a^2 b}{2} \int_0^\infty \frac{ds}{\sqrt{(s+a^2)^2(s+b^2)^3}} = \frac{a^2 b}{2} \left(\frac{2}{a^2 b - b^3} - \frac{2\cos^{-1}(\frac{b}{a})}{(a^2-b^2)^{3/2}} \right) \tag{7.6}$$

These dimensionless integrals are independent of the volume of the spheroidal cavity and exhibit the limiting behaviour

lim	$a \to b$	$a \to \infty$	$b \to 0$	$b \to a$
A_a	1/3	0	0	1/3
A_b	1/3	1	1	1/3

The reaction field tensor $\mathbf{f}$ is both constant over the cavity and independent of its volume. In the limit of the oblate spheroid approaching a sphere, $A_a = A_c = \frac{1}{3}$ and $\mathbf{f}$ is equal to expression (2.77). A summary of the derivation of equations (7.4), (7.5), and (7.6) as presented in [23] can be found in appendix D. It should be noted, that contrary to the spherical case, this expression only holds for constantly polarized cavities and not arbitrary distributions of $\mathbf{P^{cav}}(\mathbf{r})$.

Substituting the zero-mode Fourier transform of (7.3) for $\tilde{\mathbf{T}}(\mathbf{0})$ in (7.1) and solving for λ returns the fluctuation formula for the bulk dielectric constant ε^{in} in this system geometry. Parallel to the minor semi-axis, this yields

$$\frac{\varepsilon^{\text{in}}-1}{\varepsilon^{\text{in}}+2} = \frac{4\pi}{3} \frac{H_\perp}{V(1+f_\perp H_\perp)} \tag{7.7}$$

and parallel to the major semi-axis

$$\frac{\varepsilon^{\text{in}}-1}{\varepsilon^{\text{in}}+2}=\frac{4\pi}{3}\frac{H_{\parallel}}{V(1+f_{\parallel}H_{\parallel})} \tag{7.8}$$

with $H_{\perp}=H_{zz}$ and $H_{\parallel}=H_{xx}=H_{yy}$. Analog to the fluctuation formulas in slab geometry, symmetry in the xy-plane can be exploited to improve statistics.

However, an oblate spheroid of permittivity ε^{in} embedded in a homogeneous dielectric ε^{out} does not yet capture the desired system geometry portrayed in figure 7.1. Here, the spheroidal cavity is embedded in a cubic simulation box with periodic boundary conditions and long-range electrostatics are treated using the Ewald sum. Therefore, in order to translate the Ewald setup the trajectory was simulated in into the reaction field image of our analysis, the Ewald dipole-dipole interaction tensor would need to be mapped onto the reaction field dipole-dipole interaction tensor (7.3).

7.2 Sensitivity analysis of oblate spheroidal reaction field formula in bulk water

In order to test the validity of the fluctuation formulas for oblate spheroidal cavities (7.7) and (7.8), the sensitivity of the calculated ε^{in} towards cavity volume, eccentricity and orientation has to be examined. The sensitivity tests are performed using the isotropic bulk water trajectory H2OBULK described in section 3.1. To recall, this trajectory consists of 356 water molecules in a cubic simulation box with periodic boundary conditions and is thermostated at 300 K. Long-range electrostatics are treated using Ewald lattice summation which corresponds to tinfoil boundary conditions in reaction field geometry and means that its bulk dielectric constant ε^{bulk} can be calculated using the KF fluctuation formula (2.99).

Consequently, any ε^{in} calculated involving the fluctuation formulas derived above needs to be able to reproduce ε^{KF} for the same trajectory. In order for an iterative reaction field approach to converge, these fluctuation formulas should furthermore reproduce ε^{bulk} directly if the stationary condition $\varepsilon^{\text{out}}=\varepsilon^{bulk}$ is used in (7.7) and (7.8). Since H2OBULK represents a bulk simulation, shape, volume and orientation of the cavity should not affect the result.

In order to test the sensitivity towards volume and eccentricity, (7.7) and (7.8) are applied to various oblate spheroidal cavities all centered in the middle of H2OBULK at half the boxlength along each coordinate axis. In all cases, the minor semi-axis b is oriented in z-direction and the major semi-axis a lies in the xy-plane. From this geometry it follows that $\varepsilon^{\text{in}}_{\perp}=\varepsilon^{\text{in}}_{zz}$ and $\varepsilon^{\text{in}}_{\parallel}=\varepsilon^{\text{in}}_{xx}=\varepsilon^{\text{in}}_{yy}$.

The results for the sensitivity of ε^{in} towards volume and eccentricity are presented in figure 7.2. Here, the volume V of the oblate spheroidal cavity is given by

$$V = \frac{4\pi}{3} a^2 b \tag{7.9}$$

and it eccentricity ecc, which serves as a measure of shape and parametrizes the ratio between minor and major semi-axis is given by

$$ecc = \sqrt{1 - \frac{b^2}{a^2}} \tag{7.10}$$

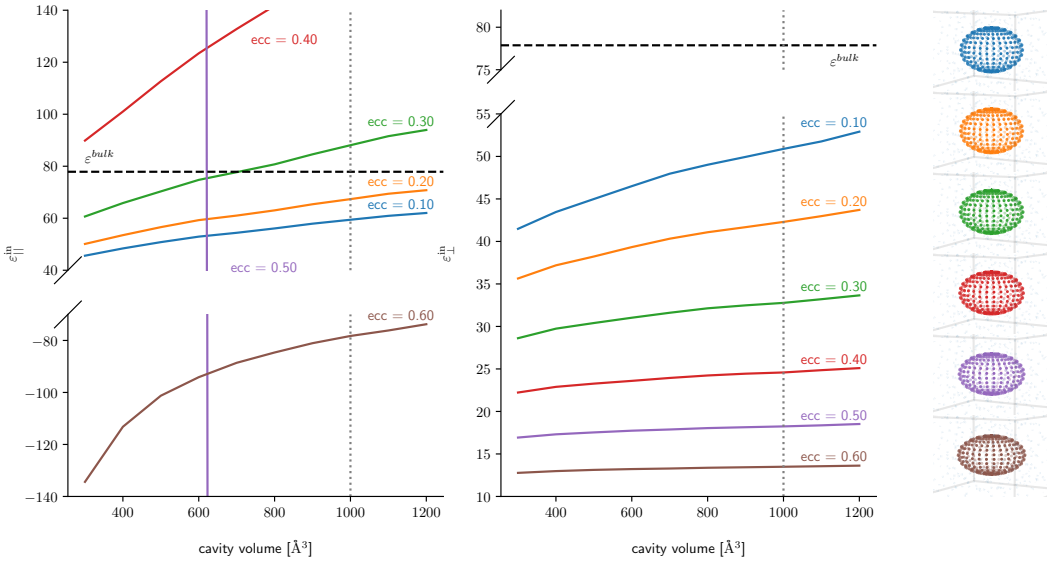

Figure 7.2 – Sensitivity of $\varepsilon^{\text{in}}_{\parallel}$ (left) and $\varepsilon^{\text{in}}_{\perp}$ (middle) towards volume and eccentricity of the oblate spheroidal cavity. Both $\varepsilon^{\text{in}}_{\parallel}$ and $\varepsilon^{\text{in}}_{\perp}$ are massively sensitive towards even moderate changes in eccentricity and volume. Additionally, the calculated dielectric constants $\varepsilon^{\text{in}}_{\parallel}$ and $\varepsilon^{\text{in}}_{\perp}$ differ for identical cavities in every case, even though they should produce the same results for an isotropic liquid like bulk water.

From the left and center plot of figure 7.2 two main observations can be made. Firstly, both $\varepsilon^{\text{in}}_{\parallel}$ and $\varepsilon^{\text{in}}_{\perp}$ are massively sensitive towards even moderate changes in eccentricity and volume. The dotted lines in both the left and center plot of figure 7.2 correspond to the cavities portrayed on the right. In the case of $\varepsilon^{\text{in}}_{\perp}$ no equality to ε^{bulk} is obtained in the probing range of 300 - 1200 Å^3 for volume and 0.1 - 0.6 for eccentricity. The two points satisfying $\varepsilon^{\text{in}}_{\parallel} = \varepsilon^{bulk}$ in the left plot have to be considered as coincidences. Secondly, the calculated dielectric constants $\varepsilon^{\text{in}}_{\parallel}$ and $\varepsilon^{\text{in}}_{\perp}$ differ for identical cavities in every case, even though they should produce the same results for an isotropic liquid like bulk water.

Regarding trends, one can see that both $\varepsilon_{\parallel}^{\mathrm{in}}$ and $\varepsilon_{\perp}^{\mathrm{in}}$ increase with cavity volume. Increasing eccentricity has a dampening effect on $\varepsilon_{\perp}^{\mathrm{in}}$ and a strengthening effect on $\varepsilon_{\parallel}^{\mathrm{in}}$ until an eccentricity of 0.4. For $ecc = 0.5$ this trend strongly reverses and $\varepsilon_{\parallel}^{\mathrm{in}}$ turns negative. For a bulk dielectric constant in the Maxwellian sense, this is an unphysical result.

Two potential reasons for this strong divergence of $\varepsilon^{\mathrm{out}}$ from its expected behaviour come to mind. One possible source of error arises due to a lack of particle conservation. While the H2OBULK trajectory is simulated in the canonical NVT ensemble and the total particle number N is constant over the course of the trajectory, the same can not be said for the number of particles n inside the spheroid cavity. The linear response formalism employed in the derivation of the fluctuation formulas (7.8) and (7.7) however assumes a NVT ensemble and thus particle conservation. The statistical averages calculated for the fluctuation matrix $\mathbf{H}$ therefore have a wrong, non-canonical energy weighting when performed over local spheroidal cavities. Since the system - the spheroid - is comparatively large compared to the bath formed by the rest of the simulation box, adapting the linear response framework for a grand-canonical μVT ensemble is not a viable solution. The influence of particle fluctuations in and out of the spheroid would therefore have a non-negligible influence on the bath and a chemical potential in the classical sense could not be defined.

A second possible source of error are wrong electrostatics. The H2OBULK system is simulated in a cubic box in Ewald geometry. Inserting an oblate spheroidal cavity into such a system deviates from the assumed electrostatic setup of a dielectric spheroid with dielectric constant $\varepsilon^{\mathrm{in}}$ embedded in an infinite dielectric $\varepsilon^{\mathrm{out}}$.

Neither of these two possibilities can be ruled out by an isolated analysis of figure 7.3. Here, an examination regarding the influence of cavity orientation on $\varepsilon^{\mathrm{in}}$ can offer valuable insights. The influence of cavity orientation on $\varepsilon_{\parallel}^{\mathrm{in}}$ and $\varepsilon_{\perp}^{\mathrm{in}}$ calculated via (7.8) and (7.7) is portrayed in figure 7.3 for an oblate spheroidal cavity with a volume of 1000 Å^3 and an eccentricity of 0.3. This corresponds to the green spheroid portrayed in the right plot of figure 7.2.

As illustrated on the right hand side, α represents the angle between the oblate spheroid's minor semi-axis and the z-axis. An angle of $\alpha = 0°$ thus corresponds to a spheroid with minor semi-axis aligned in z-direction while an angle of $\alpha = 90°$ corresponds to a spheroid with major semi-axis aligned in z-direction. Due to the symmetry of of the oblate spheroid, α is π-periodic.

As expected from the results in figure 7.2, $\varepsilon_{\parallel}^{\mathrm{in}}$ and $\varepsilon_{\perp}^{\mathrm{in}}$ do not coincide. A notable additional information is however, that both permittivity values change with α. The parallel component $\varepsilon_{\parallel}^{\mathrm{in}}$ decreases as the cavity's major semi-axis aligns with the z-axis, while $\varepsilon_{\perp}^{\mathrm{in}}$ decreases.

Any quantitative analysis of the results obtained for $\varepsilon_{\parallel}^{\mathrm{in}}$ and $\varepsilon_{\perp}^{\mathrm{in}}$ in figures 7.2 and 7.3 is difficult since the errors introduced via wrong statistical averaging and wrong electrostatics cannot easily be dissected.

Nevertheless their dependence on cavity orientation allows to draw one important conclusion. Since surface and volume of the rotated spheroid in figure 7.3 remain constant, so are the particle fluctuations in and out of the spheroid. After all, the cavity is placed in an isotropic bulk water simulation. So even if equation (7.8) and (7.7) are formulated around an n - dependent thermodynamic variable

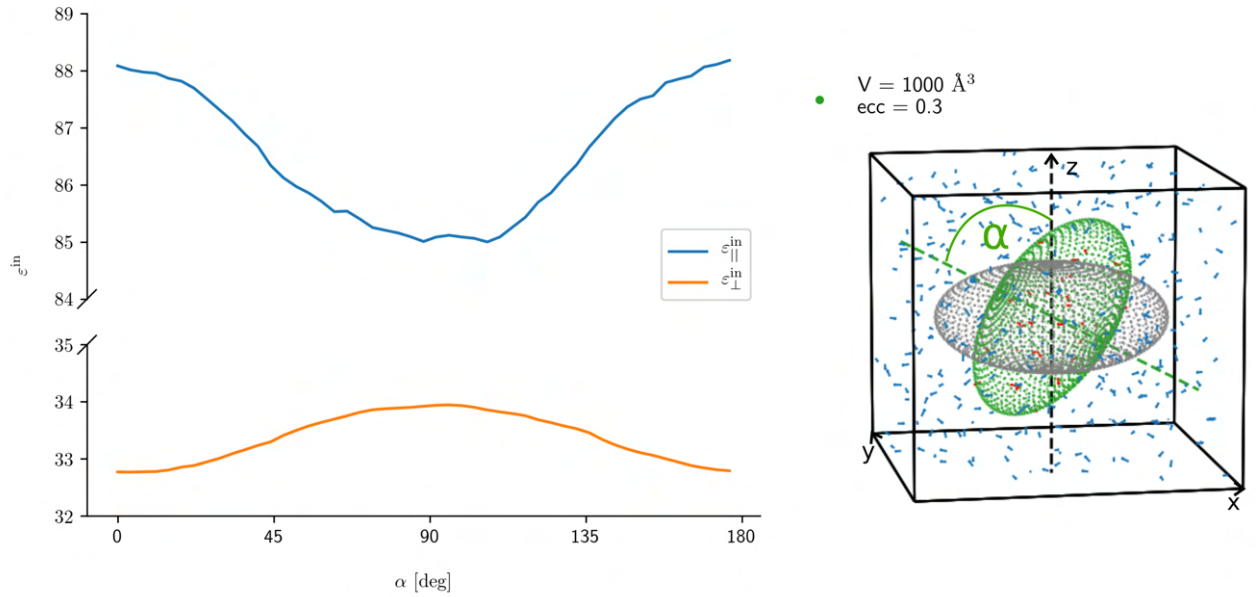

Figure 7.3 – Influence of cavity orientation on $\varepsilon^{\mathrm{in}}_{\parallel}$ (left) and $\varepsilon^{\mathrm{in}}_{\perp}$ (middle) for an oblate spheroidal cavity with a volume of 1000 Å^3 and an eccentricity of 0.3 (right). Both permittivity values change with the angle between the oblate spheroid's minor semi-axis and the z-axis.

equivalent to a chemical potential μ in a sort of semi-grand canonical approach that accounts for the comparatively small particle bath outside the cavity, the electrostatic error has an effect and can not be neglected. Alternatively the μ equivalent would need to be a direction dependent tensorial quantity. This would introduce an undesired level of complexity, require additional extensive sampling of the energy distribution to calculate accurate averages and introduce further sources of error due to non-linear coupling effects between the directions. For these reasons, the avenue of a tensorial n-dependent thermodynamic variable was not pursued further, especially keeping in mind that these problems already arise for an isotropic bulk liquid as simulated in H2OBULK.

Simply ignoring the Ewald geometry of the underlying trajectory is therefore not an option and an adequate mapping between the Ewald geometry of the trajectory and the reaction field geometry to calculate $\varepsilon^{\mathrm{in}}$ needs to be established.

7.3 Mapping of the reaction field dipole dipole interaction tensor to the Ewald interaction potential of the simulation

In order to incorporate the Ewald simulation geometry of H2OBULK into the derivation of the fluctuation formulas (7.8) and (7.7), a mapping from the Ewald dipole-dipole interaction tensor $\mathbf{T}^{\mathbf{E}}$ to the reaction field dipole-dipole interaction tensor $\mathbf{T}^{\mathbf{R}}$ is required. This is necessary since all electrostat-

ics that enter the derivation do so in the form of the zero-mode Fourier transform of the dipole-dipole interaction tensor $\tilde{\mathbf{T}}(\mathbf{0})$ in (7.1):

$$\lambda = \frac{1}{V}\left[\delta_{ij} - \lambda \tilde{T}_{ij}(0)\right] H_{ij} \tag{7.11}$$

To recall, in reaction field geometry only dipoles within the cavity interact explicitly while the interaction with the outside is coarse-grained into the mean-field dielectric response determined by ε^{out}. This is reflected in the formulation (7.3) of $\mathbf{T}^{\mathbf{R}}$ by two distinct contributions:

$$T^{R}_{ij}(\mathbf{r}_{ab}, \varepsilon^{\text{out}}) = \begin{cases} T^{\text{dd}}_{ij}(\mathbf{r}_{ab}) + \delta_{ij} f_{ij}(\varepsilon^{\text{out}}) & a, b \text{ in cavity} \\ 0 & \text{otherwise} \end{cases} \tag{7.12}$$

The first one $\mathbf{T}^{\mathbf{dd}}$ accounts for the explicit interaction of two dipoles inside the cavity while the second one aggregates all interaction between a dipole in the cavity and everything outside. In the reaction field formalism, the latter is incorporated into $\mathbf{T}^{\mathbf{R}}$ via the reaction field tensor $\mathbf{f}$.

The reason that this generally non-pairwise interaction with the environment can be incorporated into a pairwise interaction tensor like $\mathbf{T}^{\mathbf{R}}$ lies in the linear dependence of the reaction field $\mathbf{R}$ on the total dipole moment of the cavity $\mathbf{M}$ as shown in section 2.5.2.

In order to use the dipole-dipole interaction tensor $\mathbf{T}^{\mathbf{E}}$ as a substitute for $\mathbf{T}^{\mathbf{R}}$ in (7.11), the cavity-cavity and a cavity-outside dipole interactions have to be split accordingly. The desired form of $\mathbf{T}^{\mathbf{E}}$ would be written as

$$T^{ER}_{ij}(\mathbf{r}_{ab}) = \begin{cases} T^{E}_{ij}(\mathbf{r}_{ab}) + \delta_{ij} g_{ij} & a, b \text{ in cavity} \\ 0 & \text{otherwise} \end{cases} \tag{7.13}$$

where analog to (7.12) the first summand treats the pairwise interaction of explicit dipoles in the cavity while the second summand accounts for the interaction of an explicit dipole in the cavity with the cavity surroundings.

Before turning to the calculation of $\tilde{\mathbf{T}}(0)$ required in (7.11), the pseudo reaction field tensor $\mathbf{g}$ in (7.13) has to be specified. This tensor incorporates the interactions between a single dipole inside the spheroid cavity and all other dipoles in the box that are outside the cavity.

As required for its counterpart $\mathbf{f}$ in (7.12), $\mathbf{g}$ needs to fulfill the crucial condition of being proportional to the total dipole moment of the cavity. Whether or not this is an issue for the H2OBULK trajectory will be tested numerically in the next chapter.

The zero-mode Fourier transform of $\mathbf{T}^{\mathbf{ER}}$ required in (7.11) is obtained by integrating (7.13) over the cavity and can be split into two integrals:

$$\tilde{T}_{ij}^{ER}(\mathbf{0}) = \int_{V_{sph}} T_{ij}^{ER} d\mathbf{r} + \int_{V_{sph}} g_{ij} d\mathbf{r} = I_{ij}^{\text{in}} + I_{ij}^{\text{out}} \tag{7.14}$$

The first integral $\mathbf{I}^{\text{in}}$ has the solution

$$I_{\parallel}^{\text{in}} = I_{xx}^{\text{in}} = I_{yy}^{\text{in}} = \frac{4\pi}{3} P(\eta) + 8\pi \frac{V_{sph}}{V_{box}} \tag{7.15}$$

$$I_{\perp}^{\text{in}} = I_{zz}^{\text{in}} = \frac{4\pi}{3} P(\eta) - \frac{4a\sqrt{2\pi^3}}{(a+b)} S(\eta) + 8\pi \frac{V_{sph}}{V_{box}} \tag{7.16}$$

$$I_{i\neq j}^{\text{in}} = 0 \tag{7.17}$$

where a and b denote the lengths of the major and minor semi-axes of the spheroid and η the Ewald screening parameter. A detailed derivation as well as analytic expressions for the functions P and S can be found in appendix E.

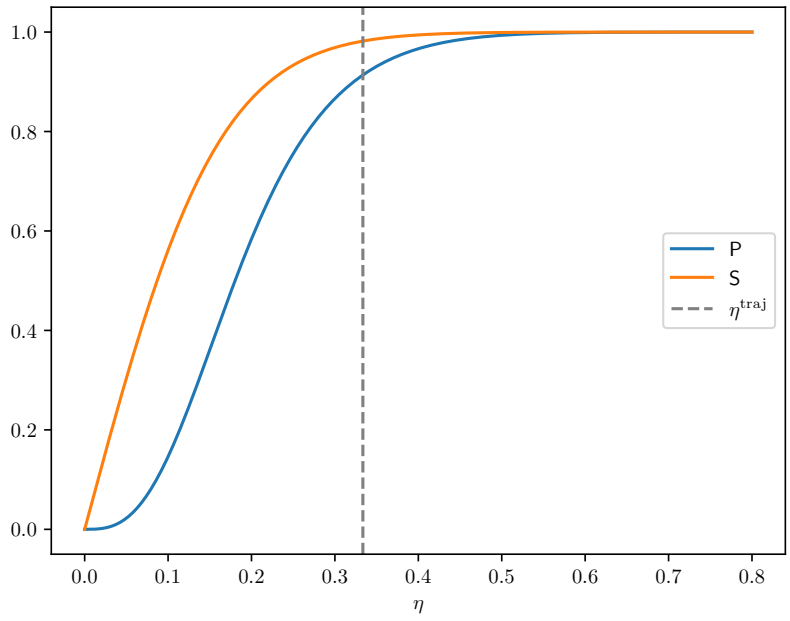

Figure 7.4 – Dependence of S and P on Ewald screening parameter η for a spheroid with major semi-axis of $a = 8$ Å and minor semi-axis of $b = 4$ Å. Both functions increase monotonously with η returning zero for $\eta = 0$ and plateauing at 1 for $\eta \approx 0.6$.

In figure 7.4, both $S(\eta)$ and $P(\eta)$ are plotted against the Ewald convergence parameter η for a spheroid with major semi-axis of $a = 8$ Å and minor semi-axis of $b = 4$ Å. Both functions increase monotonously with η returning zero for $\eta = 0$ and plateauing at 1 for $\eta \approx 0.6$.

7.3.1 Examination of the pseudo reaction field tensor g in bulk water

In order to calculate the second integral $\mathbf{I}^{\mathrm{out}}$ necessary for deriving permittivity fluctuation formulas for H2OBULK, the pseudo reaction field tensor g needs to be specified.

Analog to $\mathbf{f}$, g needs to serve as the proportionality constant between $\mathbf{E}^{\mathrm{out}}$ - the field produced inside the cavity by all dipoles outside - and the total dipole moment of the cavity $\mathbf{M}$:

$$E_i^{\mathrm{out}} = g_{ij} M_j = g_{ii} M_i \tag{7.18}$$

This linear dependence is a prerequisite to obtain any sensible expression for g that can be used to incorporate the interaction between cavity dipoles and outside polarization into $\mathbf{I}^{\mathrm{out}}$. Whether this is a reasonable assumption is examined for H2OBULK and, as before, a 1000 Å^3 cavity with an eccentricity of 0.3 and minor semi-axis oriented in z-direction. The total dipole moment of the cavity $\mathbf{M}$ is plotted against $\mathbf{E}^{\mathrm{out}}$ component-wise in figure 7.5. Here $\mathbf{M}$ constitutes the sum over all individual dipoles in the cavity while $\mathbf{E}^{\mathrm{out}}$ represents the average electric field due to all external charges felt at these cavity dipoles.

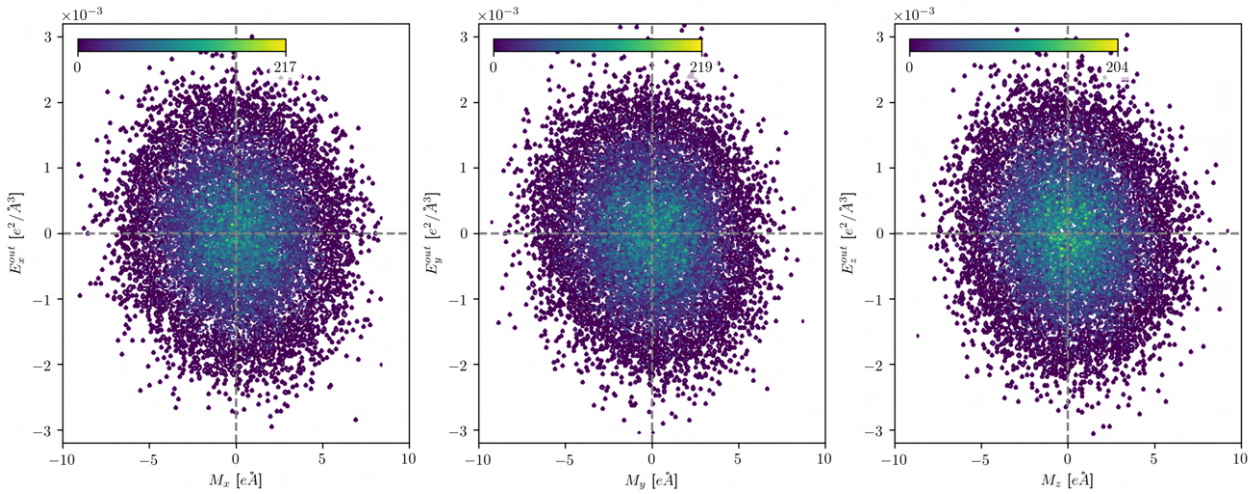

Figure 7.5 – Total dipole moment of the cavity $\mathbf{M}$ (sum over all individual dipoles in the cavity) plotted against $\mathbf{E}^{\mathrm{out}}$ (average electric field due to all external charges) component-wise. The two quantities exhibit no linear dependence.

This per-timestep comparison reveals no visible dependence between $\mathbf{M}$ and $\mathbf{E}^{\mathrm{out}}$, the two quantities appear to be entirely uncorrelated and condition (7.18) is not fulfilled.

Furthermore as illustrated in figure 7.6, the values for $\mathbf{E}^{\mathrm{out}}$ measured at the dipole centers strongly vary compared to the averages used in figure 7.5. A pseudo-reaction field tensor g that is constant over the cavity and fulfills (7.18) does therefore not seem to be obtainable.

The present case serves as an example that the iterative use of the reaction field formalism by Neumann [49] with the goal of calculating local permittivity profiles for trajectories simulated in

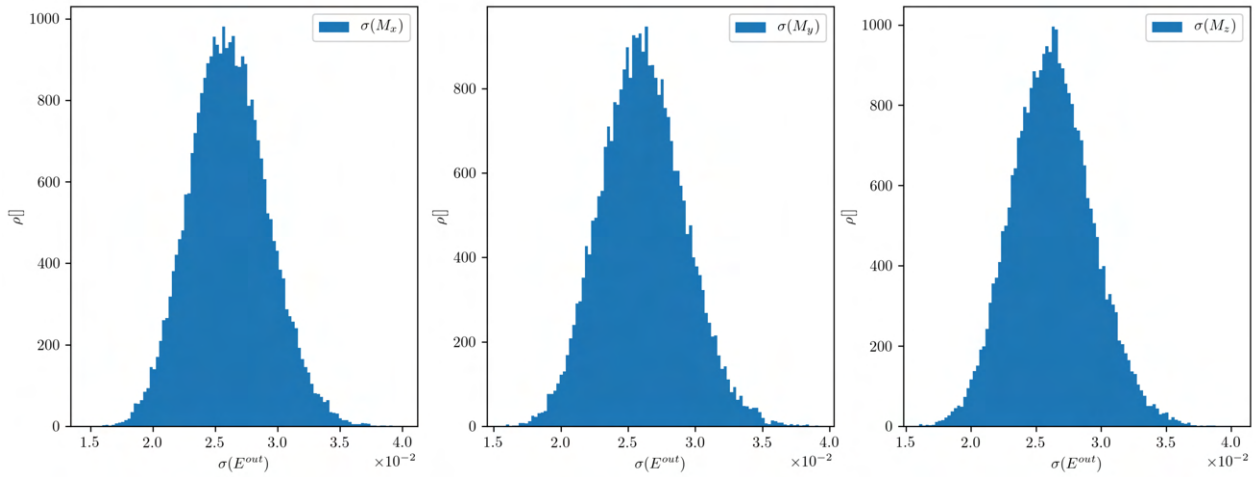

Figure 7.6 – Variance σ of $\mathbf{E}^{\mathrm{out}}$ measured at the dipole centers. σ is very large compared to the averages used in figure 7.5. A pseudo-reaction field tensor $\mathbf{g}$ that is constant over the cavity and fulfills (7.18) does therefore not seem to be obtainable.

Ewald geometry poses serious theoretical hurdles. It is not possible to separate the Ewald dipole-dipole interaction tensor $\mathbf{T}^{\mathbf{E}}$ into cavity-inside and cavity-outside contributions analog to its reaction field counterpart $\mathbf{T}^{\mathbf{R}}$. A mapping between the electrostatic realities of the simulated trajectory and the reaction field picture of a dielectric spheroid immersed in an infinite dielectric is hence impossible.

One could in principle include higher orders of $\mathbf{k}$ in the analysis and acknowledge the not conserved spheroid particle number throughout the derivation. However, these approaches would introduce high degrees of complexity and require further assumption regarding the nature of the particle bath for example. Since all these difficulties already appear for simple cases like bulk water, the iterative reaction field approach was not pursued further.

Chapter 8

Conclusion

Common strategies in coarse-graining the dielectric properties of interfacial polar liquids into a continuum mean-field response traditionally assume decoupled interface-parallel and interface-perpendicular elements in the permittivity response tensor. Among other assumptions, like the Ewald geometry dictating conducting boundary conditions, off-diagonal elements of the dielectric tensor are *a priori* assumed to be zero. This is identical to an equivalent circuit picture of a series of plate capacitor. While these approaches for calculating interfacial dielectric constants have been proven very successful and have been frequently employed in interfacial liquid systems, they nevertheless only apply to very specific system geometries.

In this work we derived an alternative approach based on discretizing the dipole-dipole interaction tensor and subsequently turning the basic relation of electrostatics into a kernel-convolution problem. This allows us to solve the general electrostatic problem based on polarization fluctuations and gives access to a full, spatially resolved dielectric tensor for arbitrary geometries. Furthermore, it provides a straightforward black box formalism that makes it very transparent where approximations enter the derivation. Traditional polarization fluctuation formulas for the local dielectric constant in bulk and in slab geometry for a H_2O / DCE LLI are derived as special cases in an Ewald simulation setup.

Additionally, the molecular orientation in both the H_2O and DCE phase against the interface were investigated in vicinity of the LLI in form of bivariate distributions of two independent angles per molecule against the instantaneous LLI. Our findings are in line with orientational maps reported in literature [189, 190].

The relation between the field and molecular polarity was also investigated directly without prior coarse-graining into a dielectric mean-field response. While a more efficient calculation of the dielectric behaviour of liquids was not found, combining these molecular fields with LLI orientation polarizations could open a path towards improving the accuracy of implicit solvent approaches by delta-learning in the future.

Finally in an effort to circumvent complicated electrostatic calculations arising in less regular system geometries like slabs, spheres or cylinders, an attempt to use an iterative, local reaction field

approach was made. An analysis of bulk water trajectories however revealed that even for relatively simple molecules like water, such an approach is futile and does not provide any advantages compared to the kernel-convolution approach.

Appendix A

Oblate spheroidal coordinates

Ellipsoidal coordinates for ellipsoid of semiprincipal axes a,b,c, assuming (a > b > c):

$$\frac{x^2}{a^2+\xi}+\frac{y^2}{b^2+\xi}+\frac{z^2}{c^2+\xi}=1, \qquad (\xi > -c^2) \tag{A.1}$$

$$\frac{x^2}{a^2+\eta}+\frac{y^2}{b^2+\eta}+\frac{z^2}{c^2+\eta}=1, \qquad (-c^2 > \eta > -b^2) \tag{A.2}$$

$$\frac{x^2}{a^2+\zeta}+\frac{y^2}{b^2+\zeta}+\frac{z^2}{c^2+\zeta}=1, \qquad (-b^2 > \eta > -a^2) \tag{A.3}$$

The surfaces of $\xi = const.$ are ellipsoids, $\eta = const.$ hyperboloids of one sheet and $\zeta = const.$ hyperboloids of 2 sheets. The relation to cartesian coordinates is given by

$$x = \pm\left[\frac{(\xi+a^2)(\eta+a^2)(\zeta+a^2)}{(b^2-a^2)(c^2-a^2)}\right]^{1/2} \tag{A.4}$$

$$y = \pm\left[\frac{(\xi+b^2)(\eta+b^2)(\zeta+b^2)}{(a^2-b^2)(c^2-b^2)}\right]^{1/2} \tag{A.5}$$

$$z = \pm\left[\frac{(\xi+c^2)(\eta+c^2)(\zeta+c^2)}{(b^2-c^2)(a^2-c^2)}\right]^{1/2} \tag{A.6}$$

and

$$h1 = \frac{1}{2}\left[\frac{(\xi-\eta)(\xi-\zeta)}{(\xi+a^2)(\xi+b^2)(\xi+c^2)}\right]^{1/2} \tag{A.7}$$

$$h2 = \frac{1}{2}\left[\frac{(\eta-\xi)(\eta-\zeta)}{(\eta+a^2)(\eta+b^2)(\eta+c^2)}\right]^{1/2} \tag{A.8}$$

$$h3 = \frac{1}{2}\left[\frac{(\zeta-\xi)(\zeta-\eta)}{(\zeta+a^2)(\zeta+b^2)(\zeta+c^2)}\right]^{1/2} \tag{A.9}$$

and the infinitesimal volume is given by

$$dV = dxdydz = h_1 h_2 h_3 d\xi d\eta d\zeta \tag{A.10}$$

Appendix B

Helmholtz theorem

Constituting a general mathematical theorem for sufficiently well behaved vector fields, the Helmholtz-theorem states that any inhomogeneous vector field $\mathbf{F}$ can be split into its longitudinal and transverse components [22]

$$\mathbf{F} = -\nabla\phi + \nabla \times \mathbf{A} = \mathbf{F_L} + \mathbf{F_T} \tag{B.1}$$

where both these components are orthogonal

$$\mathbf{F_L} \cdot \mathbf{F_T} = 0 \tag{B.2}$$

The longitudinal part of this decomposition is given by

$$\mathbf{F_L} = \frac{1}{4\pi}\int_V \frac{\nabla' \cdot \mathbf{F'}}{|\mathbf{r}-\mathbf{r'}|}dV' - \frac{1}{4\pi}\oint_{\partial V} \mathbf{n'} \cdot \frac{\mathbf{F'}}{|\mathbf{r}-\mathbf{r'}|}dS' \tag{B.3}$$

with ∂V being the surface enclosing volume V and $\mathbf{n}$ the corresponding outward facing normal vector. In case of the polarization field that becomes

$$4\pi\mathbf{P_L} = -\int_V \frac{\nabla' \cdot \mathbf{P'}}{|\mathbf{r}-\mathbf{r'}|}dV' - \oint_{\partial V} \mathbf{n'} \cdot \frac{\mathbf{P'}}{|\mathbf{r}-\mathbf{r'}|}dS' \tag{B.4}$$

$$= -\mathbf{E_p} - \oint_{\partial V} \frac{\sigma'_P}{|\mathbf{r}-\mathbf{r'}|}dS' \tag{B.5}$$

with the electric field $\mathbf{E_p} = -\nabla \cdot \phi_p$ due to all the charges in the dielectric and the surface charge $\sigma_P = \mathbf{n} \cdot \mathbf{P}$. The matching electrostatic potential ϕ_p is given by:

$$\phi_P = \int \frac{\rho'_P}{|\mathbf{r} - \mathbf{r}'|} dV' \tag{B.6}$$

with the charge distribution $\rho_P = -\nabla \cdot \mathbf{P}$.

Appendix C

Linear response theory in the canonical ensemble

The following derivation closely follows chapter 7.6 in [24]. Assuming a spatially uniform system is subjugated to an external space- and time-dependent field $\mathbf{F}$ weakly coupled to its conjugate variable A, the linear response algorithm calculates the resulting change in an observable B, whose mean value is assumed to be zero in the unperturbed system, i.e. in absence of the field.

The assumptions regarding A and B are quite general, they simply represent two functions dependent on the microstate of the system. In a 3D system of particles this microstate would mean its 6N coordinates and momenta. A and B can even be the same as is the case for polarization and electric field. The electric field $\mathbf{E}$ represents the derivative of the action with respect to the electric polarization density $\mathbf{P}$ [105] and thus constitute a conjugate pair.

In this case, the hamiltonian of the system is

$$\mathcal{H} = \mathcal{H}_0 + \mathcal{H}'(t) \tag{C.1}$$

with the unperturbed system represented by $\mathcal{H}_0$ and a perturbation hamiltonian

$$\mathcal{H}'(t) = -\int A(\mathbf{r})\mathbf{F}(\mathbf{r},t)d\mathbf{r} \tag{C.2}$$

Instead of a cartesian basis, the field $\mathbf{F}$ can also be expressed in a basis of plane waves. Since the calculated response of the system is supposed to be linear, the perturbations of individual plane wave components to the observable B are linearly independent. It is therefore sufficient to look at a single plain wave perturbing field with fixed wavevector $\mathbf{k}$ and frequency ω

$$\mathbf{F}(\mathbf{r},t) = \frac{1}{V}\mathbf{F}_{\mathbf{k}}e^{i(\mathbf{k}\cdot\mathbf{r}-\omega t)} \tag{C.3}$$

which if inserted in equation C.2 results in a perturbing hamiltonian of

$$\mathcal{H}'(t) = -\mathbf{F_k} e^{-i\omega t} \int A(\mathbf{r}) e^{i\mathbf{k}\cdot\mathbf{r}} d\mathbf{r} = -\mathbf{F_k} e^{-i\omega t} \cdot A_k \tag{C.4}$$

Since only a single plane wave is examined in this derivation, the wavevector indices $\mathbf{k}$ for $\mathbf{F}$ and $\mathbf{k}$ are omitted in the following and reintroduced later. It is furthermore assumed the system was in thermal equilibrium at $t = -\infty$, which is assured by a factor $\exp(\epsilon t)$ with $\epsilon > 0$. The perturbation hamiltonian then takes the form

$$\mathcal{H}'(t) = -A \cdot \mathbf{F_0} e^{-i(\omega + i\epsilon)t} \tag{C.5}$$

Since one is interested in the time-integrated response of the system as a whole, the time-evolution of shift in the phase-space probability density $f^{[N]}(t) = f^{[N]}(\mathbf{r}^N, \mathbf{p}^N; t)$ caused by the perturbation must be considered. The time evolution of $f^{[N]}$ is governed by the Liouville equation [24]

$$\frac{f^{[N]}(t)}{\partial t} = -i\mathcal{L} f^{[N]}(t) = \left\{\mathcal{H}, f^{[N]}(t)\right\} \tag{C.6}$$

where $\{A, B\}$ denotes the Poisson bracket:

$$\{A, B\} \equiv \sum_{i=1}^{N} \left(\frac{\partial A}{\partial \mathbf{r}_i} \cdot \frac{\partial B}{\partial \mathbf{p}_i} - \frac{\partial A}{\partial \mathbf{p}_i} \cdot \frac{\partial B}{\partial \mathbf{r}_i} \right) \tag{C.7}$$

and N represents all degrees of freedom of the system. Substituting equations (C.1) and (C.5) above equation can be written as

$$\begin{aligned}
\frac{f^{[N]}(t)}{\partial t} &= \left\{\mathcal{H}_0 + \mathcal{H}', f^{[N]}(t)\right\} \\
&= \left\{\mathcal{H}_0 - A\mathbf{F}(t), f^{[N]}(t)\right\} \\
&= \left\{\mathcal{H}_0, f^{[N]}(t)\right\} - \left\{A\mathbf{F}(t), f^{[N]}(t)\right\} \\
&= \left\{\mathcal{H}_0, f^{[N]}(t)\right\} - \left\{A, f^{[N]}(t)\right\} \mathbf{F}(t) \\
&= -i\mathcal{L}_0 f^{[N]}(t) - \left\{A, f^{[N]}(t)\right\} \mathbf{F}(t)
\end{aligned} \tag{C.8}$$

where $\mathcal{L}_0$ denotes the Liouville operator of the unperturbed system. Because we are only concerned with a weak perturbation, the probability density can be written as

$$f^{[N]}(t) = f_0^{[N]} + \Delta f^{[N]}(t) \tag{C.9}$$

where $f_0^{[N]} = f^{[N]}(-\infty)$ represents the unperturbed system. Inserted into equation (C.8) this can be linearized as

$$\begin{aligned}
\frac{\Delta f^{[N]}(t)}{\partial t} &= \frac{f^{[N]}(t)}{\partial t} - \frac{f_0^{[N]}(t)}{\partial t} \\
&= -i\mathcal{L}_0 \Delta f^{[N]}(t) - \left\{A, f^{[N]}(t)\right\} \mathbf{F}(t) \\
&= -i\mathcal{L}_0 \Delta f^{[N]}(t) - \left\{A, f_0^{[N]} + \Delta f^{[N]}(t)\right\} \mathbf{F}(t) \\
&= -i\mathcal{L}_0 \Delta f^{[N]}(t) - \left\{A, f_0^{[N]}\right\} \mathbf{F}(t) - \left\{A, \Delta f^{[N]}(t)\right\} \mathbf{F}(t) \\
&= -i\mathcal{L}_0 \Delta f^{[N]}(t) - \left\{A, f_0^{[N]}\right\} \mathbf{F}(t)
\end{aligned} \tag{C.10}$$

where the last summand is omitted because it represents a second order perturbation. The solution to this differential equation is

$$\begin{aligned}
\Delta f^{[N]}(t) &= -\int_{-\infty}^{t} \exp\left[-i(t-s)\mathcal{L}_0\right] \left\{A, f_0^{[N]}\right\} \mathbf{F}(s) ds \\
&= \beta \int_{-\infty}^{t} \exp\left[-i(t-s)\mathcal{L}_0\right] \dot{A} f_0^{[N]} \mathbf{F}(s) ds
\end{aligned} \tag{C.11}$$

That this is the correct solution to equation (C.10) can be checked by differentiation of the first line of (C.11) and the fact that the boundary condition $f_0^{[N]} = f^{[N]}(-\infty)$ is also fulfilled - or to be plugged in a symbolic programming platform. The substitution of the Poisson bracket in the last line of (C.11) is due to the following:

If we assume to be in a canonical ensemble (NVT), we have $f_0^{[N]} \propto \exp[-\beta \mathcal{H}_0]$ with $\beta = (k_b T)^{-1}$ and the Poisson equation in (C.10) takes the form

$$\begin{aligned}\left\{A, f_0^{[N]}\right\} &= \sum_{i=1}^{N}\left(\frac{\partial A}{\partial \mathbf{r}_i}\cdot\frac{\partial f_0^{[N]}}{\partial \mathbf{p}_i} - \frac{\partial A}{\partial \mathbf{p}_i}\cdot\frac{\partial f_0^{[N]}}{\partial \mathbf{r}_i}\right)\\ &= \beta\sum_{i=1}^{N}\left(\frac{\partial A}{\partial \mathbf{r}_i}\cdot\frac{\partial \mathcal{H}_0}{\partial \mathbf{p}_i} - \frac{\partial A}{\partial \mathbf{p}_i}\cdot\frac{\partial \mathcal{H}_0}{\partial \mathbf{r}_i}\right) f_0^{[N]}\\ &= -\beta(i\mathcal{L}_0 A) f_0^{[N]} = -\beta\dot{A} f_0^{[N]}\end{aligned} \tag{C.12}$$

In the last step we use that the time derivative of any function of the phase space variables $A(\mathbf{r}^N, \mathbf{p}^N)$ can be written as

$$\frac{\partial A}{\partial t} = \dot{A} = \sum_{i=1}^{N}\left(\frac{\partial A}{\partial \mathbf{r}_i}\cdot\dot{\mathbf{r}} - \frac{\partial A}{\partial \mathbf{p}_i}\cdot\dot{\mathbf{p}}\right) = \sum_{i=1}^{N}\left(\frac{\partial A}{\partial \mathbf{r}_i}\cdot\frac{\partial \mathcal{H}}{\partial \mathbf{p}_i} - \frac{\partial A}{\partial \mathbf{p}_i}\cdot\frac{\partial \mathcal{H}}{\partial \mathbf{r}_i}\right) = i\mathcal{L}A \tag{C.13}$$

as a result of Hamilton's equations [24].

With the help of (C.11), the mean change in variable $B(\mathbf{r}^N, \mathbf{p}^N)$ due to the field perturbation $\mathbf{F}(t)$ in the canonical ensemble can therefore be expressed as

$$\begin{aligned}\langle \Delta B(t)\rangle &= \int\int d\mathbf{r}^N d\mathbf{p}^N B(\mathbf{r}^N, \mathbf{p}^N)\Delta f^{[N]}(t)\\ &= \beta\int_{-\infty}^{t}\mathbf{F}(s)ds\int\int d\mathbf{r}^N d\mathbf{p}^N f_0^{[N]} B\exp\left[-i(t-s)\mathcal{L}_0\right]\dot{A}\\ &= \beta\int_{-\infty}^{t}\mathbf{F}(s)ds\int\int d\mathbf{r}^N d\mathbf{p}^N f_0^{[N]}\dot{A}\exp\left[i(t-s)\mathcal{L}_0\right]B\\ &= \beta\int_{-\infty}^{t}ds\Phi(t-s)\mathbf{F}(s)\end{aligned} \tag{C.14}$$

with the after-effect function $\Phi_{BA}(t)$ defined as

$$\Phi_{BA}(t) = \beta\langle B(t)\dot{A}\rangle_0 = -\beta\langle\dot{B}(t)A\rangle_0 \tag{C.15}$$

The thermal averages $\langle.\rangle_0$ represent the unperturbed system, because unperturbed phase-space density f_0 and propagator $\exp(i\mathcal{L}_0 t)$ are used under the integrals in equation (C.15).

Equation (C.14) means that the response of the system represented by the change in B due to a perturbation is a superposition of delayed effects. The response to a unit δ-function force applied at time $t = 0$ is consequently proportional to the after-effect function itself.

Equation (C.14) represents the solution for a monochromatic field perturbation due to the limit introduced in equation (C.3). If the field is spatially varying, equation (C.14) can trivially be generalized to

$$\langle \Delta B(\mathbf{r},t)\rangle = \int_{-\infty}^{t} ds \int d\mathbf{r}' \Phi_{BA}(\mathbf{r}-\mathbf{r}', t-s)\mathbf{F}(\mathbf{r}', s) \tag{C.16}$$

This convolution can be expressed as

$$\langle \Delta B_{\mathbf{k}}(t)\rangle = \int_{-\infty}^{t} ds \Phi_{BA}(\mathbf{k}, t-s)\mathbf{F}_{\mathbf{k}}(s) \tag{C.17}$$

in terms of its Fourier components. In this case, the after-effect function is accordingly defined as

$$\Phi_{BA}(\mathbf{k},t) = -\frac{\beta}{V}\langle \dot{B}_{\mathbf{k}}(t) A_{-\mathbf{k}}\rangle \tag{C.18}$$

As a consequence of above equation, a perturbation of a certain wavevector can only induce a response in the system with the same wavevector.

Assuming the external field $\mathbf{F}$ is of dampened plane wave nature as described in equation (C.5), the response expression in equation (C.17) takes the form

$$\begin{aligned}
\langle \Delta B_{\mathbf{k}}(t)\rangle &= \beta \int_{-\infty}^{t} \Phi_{BA}(\mathbf{k}, t-s) \exp\left[-i(\omega + i\epsilon)s\right] ds \\
&= \mathbf{F}_{\mathbf{k}} \exp\left[-i(\omega+i\epsilon)t\right] \int_{-\infty}^{t} \Phi_{BA}(\mathbf{k}, t-s) \exp\left[-i(\omega+i\epsilon)(s-t)\right] ds \\
&= \mathbf{F}_{\mathbf{k}} \exp\left[-i(\omega+i\epsilon)t\right] \int_{0}^{\infty} \Phi_{BA}(\mathbf{k}, t) \exp\left[i(\omega+i\epsilon)t\right] dt
\end{aligned} \tag{C.19}$$

If we take the limit $\epsilon \to 0$ - which would amount to pushing the time the system was in equilibrium infinitely far into the past - this becomes

$$\langle \Delta B_{\mathbf{k}}(t)\rangle = \chi_{BA}(k,\omega)\mathbf{F}_k \exp(-i\omega t) \tag{C.20}$$

with the *dynamic susceptibility*

$$\begin{aligned}\chi_{BA}(\mathbf{k},\omega) &= \chi'_{BA}(\mathbf{k},\omega) + i\chi''_{BA}(\mathbf{k},\omega) \\ &= \lim_{\epsilon\to 0^+}\int_0^\infty \Phi_{BA}(\mathbf{k},t)\exp\left[i(\omega+i\epsilon)t\right]dt \end{aligned} \tag{C.21}$$

The expression for Φ_{BA} from equation (C.18) can be substituted in above equation and then partially integrated:

$$\begin{aligned}\chi_{BA}(\mathbf{k},\omega) &= \lim_{\epsilon\to 0^+}\int_0^\infty \Phi_{BA}(\mathbf{k},t)\exp\left[i(\omega+i\epsilon)t\right]dt \\ &= -\frac{\beta}{V}\lim_{\epsilon\to 0^+}\int_0^\infty \langle\dot{B}_{\mathbf{k}}(t)A_{-\mathbf{k}}\rangle\exp\left[i(\omega+i\epsilon)t\right]dt \end{aligned} \tag{C.22}$$

The time integral in above equation can be integrated by parts:

$$\begin{aligned} I &= \int_0^\infty \langle\dot{B}_{\mathbf{k}}(t)A_{-\mathbf{k}}\rangle\exp\left[i(\omega+i\epsilon)t\right]dt \\ &= \left[\langle B_{\mathbf{k}}(t)A_{-\mathbf{k}}\rangle\exp\left[i(\omega+i\epsilon)t\right]\right]_0^\infty - \int_0^\infty \langle B_{\mathbf{k}}(t)A_{-\mathbf{k}}\rangle i(\omega+i\epsilon)\exp\left[i(\omega+i\epsilon)t\right]dt \\ &= -\langle B_{\mathbf{k}}(0)A_{-\mathbf{k}}\rangle - i(\omega+i\epsilon)\int_0^\infty \langle B_{\mathbf{k}}(t)A_{-\mathbf{k}}\rangle\exp\left[i(\omega+i\epsilon)t\right]dt \end{aligned} \tag{C.23}$$

The expression for the dynamic susceptibility thus takes the form

$$\chi_{BA}(\mathbf{k},\omega) = \frac{\beta}{V}\lim_{\epsilon\to 0^+}\left[\langle B_{\mathbf{k}}(0)A_{-\mathbf{k}}\rangle - i(\omega+i\epsilon)\int_0^\infty \langle B_{\mathbf{k}}(t)A_{-\mathbf{k}}\rangle\exp\left[i(\omega+i\epsilon)t\right]dt\right] \tag{C.24}$$

For the special case if A and B are the same variable and in the zero-frequency limit, the static susceptibility $\chi_{AA}(k)$ can then be expressed as

$$\chi_{AA}(k) = \frac{\beta}{V}\langle A_{\mathbf{k}}(0)A_{-\mathbf{k}}\rangle \tag{C.25}$$

and the relation between the perturbing field and the shift in variable A is given by

$$\langle \Delta A_{\mathbf{k}} \rangle = \frac{\beta}{V} \langle A_{\mathbf{k}} A_{-\mathbf{k}} \rangle \mathbf{F}_{\mathbf{k}} \tag{C.26}$$

If the electric field $\mathbf{E}$ is considered to be $\mathbf{F}$ and the polarization density $\mathbf{P}$ to be A in equations (C.26) and (C.25), $\chi = \chi_{AA}$ corresponds to the static dielectric susceptibility for a uniform dielectric. The application of linear response theory using the Maxwell field $\mathbf{E}$ is not technically applicable however because it does not constitute a true *external* field but one whose value depends on the state of the material[124]. This is why the fields appearing in the fluctuation formulas of the following sections always represent an external field $\mathbf{E^0}$.

Appendix D

Derivation for the reaction field of ellipsoidal cavities

The following derivation is a summary of the derivation performed in Boettcher [23].

D.1 Free Charge on conducting Elllipsoid

By introducing the abbreviation

$$R_s = \sqrt{(s+a^2)(s+b^2)(s+c^2)} \tag{D.1}$$

The Laplace equation in 3D in the oblate spheroidal coordinates introduced in appendix A can be written as

$$(\eta-\zeta)R_\xi\frac{\partial}{\partial\xi}\left(R_\xi\frac{\partial\Phi}{\partial\xi}\right)+(\zeta-\xi)R_\eta\frac{\partial}{\partial\eta}\left(R_\eta\frac{\partial\Phi}{\partial\eta}\right)+(\xi-\eta)R_\zeta\frac{\partial}{\partial\zeta}\left(R_\zeta\frac{\partial\Phi}{\partial\zeta}\right)=0 \tag{D.2}$$

Any solution to D.2 must be constant on the surface of the ellipsoid and regular at infinity. D.2 therefore reduces to

$$\frac{\partial}{\partial\xi}\left(R_\xi\frac{\partial\Phi}{\partial\xi}\right)=0 \tag{D.3}$$

where R_ξ is of the form D.1. Integration leads to

$$\Phi(\xi)=C_1\int_\xi^\infty\frac{d\xi}{R_\xi} \tag{D.4}$$

For large ξ, this expression approaches $\frac{2C_1}{\sqrt{\xi}}$, which is regular for $\xi \to \infty$.

D.2 Conducting Ellipsoid in Parallel Field

Assume a uniform external electric field $\mathbf{E_0}$, which is directed along the x-axis. If a conducting ellipsoid were to be placed in such a field (let's assume without loss of generality, that its major axis also coincides with the x-axis), $\mathbf{E_0}$ would induce a nonuniform charge distribution counteracting the external field. According to A.3, the potential of this applied field can be written as

$$\Phi_0 = -E_0 x = -E_0 \left[\frac{(\xi + a^2)(\eta + a^2)(\zeta = a^2)}{(b^2 - a^2)(c^2 - a^2)} \right]^{\frac{1}{2}} \tag{D.5}$$

in ellipsoidal coordinates. This primary potential is a product of three functions, each dependent on one ellipsoidal variable:

$$\Phi_0 = C_1 F_1(\xi) F_2(\eta) F_3(\zeta), \qquad C_1 = -\frac{E_0}{\sqrt{(b^2 - a^2)(c^2 - a^2)}} \tag{D.6}$$

This is equivalent to a separation of variables and therefore independent of the directions of the potential. This potential however lacks regularity at infinity. If the boundary conditions at a general ellipsoidal surface are to be satisfied, the induced potential Φ_1 must vary functionally over every surface of the family $\xi = const.$ in exactly the same way as Φ_0. It must, however, differ in its regularity at infinity. Therefore, the following functional form is assumed:

$$\Phi_1 = C_2 G_1(\xi) F_2(\eta) F_3(\zeta) \tag{D.7}$$

with

$$F_2(\eta) = \sqrt{\eta + a^2} \qquad and \qquad F_3(\zeta) = \sqrt{\zeta = a^2} \tag{D.8}$$

Substituting D.7 and D.8 into D.2 gives

$$R_\xi \frac{\partial}{\partial \xi} \left(R_\xi \frac{\partial G_1}{\partial \xi} \right) - \left(\frac{b^2 + c^2}{4} + \frac{\xi}{2} \right) G_1 = 0 \tag{D.9}$$

This is an ordinary differential equation of second order and therefore must have 2 independent solutions. We already know one of them to be

$$F_1(\xi) = \sqrt{\xi + a^2} \tag{D.10}$$

From theory of differential equations it is known, that if y_1 is a solution of

$$\frac{\partial^2 y}{\partial^2 x} + p(x)\frac{\partial y}{\partial x} + q(x)y = 0 \tag{D.11}$$

then an independent solution y_2 is given by

$$y_2 = y_1 \int \frac{e^{(} - \int p dx)}{y_1^2} \tag{D.12}$$

In our case, we have

$$p(\xi) = \frac{1}{R_\xi}\frac{\partial R_\xi}{\partial \xi} = \frac{\partial}{\partial \xi}\ln(R_\xi) \tag{D.13}$$

and therefore

$$G_1(\xi) = F_1 \int \frac{d\xi}{F_1^2 R_\xi} \tag{D.14}$$

The above equation is regular at infinity and therefore the potential due to the induced charge, Φ_1 is therefore

$$\Phi_1 = \Phi_0 \frac{C_2}{C_1}\int_\xi^\infty \frac{d\xi}{(\xi + a^2)R_\xi} \tag{D.15}$$

The constant C_2 is obtained by the condition that on the conducting ellipsoid $\xi = 0$ the potential is a constant Φ_s:

$$\Phi_s = \Phi_0 \left[1 + \frac{C_2}{C_1}\int_0^\infty \frac{d\xi}{(\xi + a^2)R_\xi}\right] \tag{D.16}$$

The potential at any external point is therefore given by

$$\Phi_1 = \Phi_0 + \frac{\Phi_s - \Phi_0}{\int_0^\infty \frac{d\xi}{(\xi+a^2)R_\xi}} \frac{C_2}{C_1} \int_\xi^\infty \frac{d\xi}{(\xi+a^2)R_\xi} \tag{D.17}$$

This works analogously for an electric field parallel to one of the other two axes of the ellipsoid.

D.3 Dielectric Ellipsoid in Parallel Field

Based on sections D.1 and D.2 one can now calculate the perturbation of a uniform parallel field due to a dielectric ellipsoid with static dielectric constant ε^{in} immersed in a dielectric ε^{out}. The applied external electric field $\mathbf{E_0}$ is applied arbitrarily with respect to the reference system of the ellipsoid and has the components E_{0x}, E_{0y}, E_{0z} along the axes of the ellipsoid.
Consider first the component field E_{0x}, the cases for the other directions derive analogously. Since we are still assuming a conducting ellipsoid surface, the resulting potential must exhibit the same general functional behavior like the potential in section D.2 and will differ from it only in the value of the constant C_2. Outside the ellipsoid, we therefore have

$$\Phi^+ = \Phi_0 + \Phi_1^+ = F_1(\xi)F_2(\eta)F_3(\zeta)\left[C_1 + C_2\int_\xi^\infty \frac{ds}{(s+a^2)R_s}\right] \tag{D.18}$$

The interior of the ellipsoid corresponds to the range $c^2 \leq \xi \leq 0$ if $a \geq b \geq c$. In this region Φ^- must vary with η and ζ as determined by the function $F_2(\eta)F_3(\zeta)$ in order to hold boundary conditions over the entire ellipsoid surface and, since D.9 has only two independent solutions, the dependence on ξ must be represented either by $F_3(\xi)$ or $G_1(\xi)$. The latter is degenerate at $\xi = -c^2$, thus the potential within the ellipsoid must have the functional form

$$\Phi^- = C_3F_1(\xi)F_2(\eta)F_3(\zeta) \tag{D.19}$$

The constants C_2 and C_3 are to be adjusted to satisfy the boundary conditions

$$\Phi^+(0) = \Phi^-(0) \qquad , \qquad \varepsilon^{\text{in}}\left[\frac{1}{h_1}\frac{\partial\Phi^-}{\partial\xi}\right]_{\xi=0} = \varepsilon^{\text{out}}\left[\frac{1}{h_1}\frac{\partial\Phi^+}{\partial\xi}\right]_{\xi=0} \tag{D.20}$$

This leads to

$$C_3 = C_1 + C_2 \int_0^\infty \frac{ds}{(s+a^2)R_s} \tag{D.21}$$

and

$$C_2 = \frac{abc}{2} \frac{(\varepsilon^{\text{out}} - \varepsilon^{\text{in}})}{\varepsilon^{\text{out}}} C_3 \tag{D.22}$$

Since $\Phi_0 = -E_{0x}$ one thus finds for the interior potential (D.19) inside the ellipsoid

$$\Phi^- = \frac{-E_{0x}x}{1 + \frac{abc}{2\varepsilon^{\text{out}}}(\varepsilon^{\text{in}} - \varepsilon^{\text{out}})A_1} = \frac{-E_{0x}x}{1 + \frac{abc}{2\varepsilon^{\text{out}}}(\varepsilon^{\text{in}} - \varepsilon^{\text{out}})A} \qquad , \qquad A = \frac{abc}{2}A_1 = \frac{abc}{2}\int_0^\infty \frac{ds}{(s+a^2)R_s} \tag{D.23}$$

which corresponds to a field of

$$E_x^- = \frac{E_{0x}}{1 + \frac{1}{\varepsilon^{\text{out}}}(\varepsilon^{\text{in}} - \varepsilon^{\text{out}})A} = \frac{\varepsilon^{\text{out}}}{\varepsilon^{\text{out}} + (\varepsilon^{\text{in}} - \varepsilon^{\text{out}})A} E_{0x} \tag{D.24}$$

The components E_y^- and E_z^- are obtained analogously. The perturbed field inside a dielectric oblate spheroid, whose axes are defined as $a = b > c$, can therefore be written as

$$\begin{pmatrix} E_x y^- \\ E_x y^- \\ E_z^- \end{pmatrix} = \begin{pmatrix} \frac{\varepsilon^{\text{out}}}{\varepsilon^{\text{out}} + (\varepsilon^{\text{in}} - \varepsilon^{\text{out}})A_{ab}} \\ \frac{\varepsilon^{\text{out}}}{\varepsilon^{\text{out}} + (\varepsilon^{\text{in}} - \varepsilon^{\text{out}})A_{ab}} \\ \frac{\varepsilon^{\text{out}}}{\varepsilon^{\text{out}} + (\varepsilon^{\text{in}} - \varepsilon^{\text{out}})A_c} \end{pmatrix} \begin{pmatrix} E_{ox} \\ E_{0y} \\ E_{0z} \end{pmatrix} \tag{D.25}$$

with

$$A_{ab} = \frac{a^2 c}{2} \int_0^\infty \frac{ds}{\sqrt{(s+a^2)^4(s+c^2)}} \tag{D.26}$$

and

$$A_c = \frac{a^2 c}{2} \int_0^\infty \frac{ds}{\sqrt{(s+a^2)^2(s+c^2)^3}} \tag{D.27}$$

The field inside the spheroid is therefore constant but its direction only aligns with the external field if the latter is aligned with one of the axes of the spheroid. Otherwise its direction is tilted according to the A-Integral.

D.4 Interpretation as Reaction Field

In case of an oblate spheroid with major semi-axis a and minor semi-axis c, the reaction field can be calculated by assuming a homogenous polarization inside an ellipsoid cavity resulting in a dielectric constant ε^{in}, immersed in a continuum dielectric ε^{out}.
The field of the total dipole moment $\mathbf{m}$ embedded in a continuum dielectric polarizes the surrounding matter and results in an inhomogenous polarization which, in turn creates an reaction field that is felt inside the cavity and is defined as

$$\mathbf{R} = \mathbf{F}\mathbf{m} \tag{D.28}$$

This reaction field is strongly dependent on size and shape of the cavity. The polarization induced by the electric field inside the cavity is according to electrostatics and equation D.25

$$\mathbf{P_{in}} = \frac{\varepsilon^{\text{in}} - 1}{4\pi}\mathbf{E^{in}} = \frac{1}{4\pi}\frac{(\varepsilon^{\text{in}} - 1)\varepsilon^{\text{out}}}{\varepsilon^{\text{out}} + (\varepsilon^{\text{in}} - \varepsilon^{\text{out}})A}\mathbf{E_0} \tag{D.29}$$

Hence the dipole moment of the spheroid amounts to

$$\mathbf{m} = \frac{4\pi}{3}a^2 c\mathbf{P^{in}} = \frac{a^2 c}{3}\frac{\varepsilon^{\text{out}}(\varepsilon^{\text{in}} - 1)}{\varepsilon^{\text{out}} + (\varepsilon^{\text{in}} - \varepsilon^{\text{out}})A}\mathbf{E_0} \tag{D.30}$$

It is also possible to calculate this moment from α_a, the polarizability of the ellipsoid along the a-axis. We obtain the induced moment m by multiplying this polarizability with the total polarizing field. This total field consists of the cavity field $\mathbf{E_c}$, which would occur in the empty cavity, and the reaction field R of the homogeneous dipole density P^{in}, with total dipole moment $\mathbf{m}$. Therefore with formula (D.28):

$$\mathbf{m} = \alpha_a(\mathbf{E_c} + \mathbf{R}) = \alpha_a(\mathbf{E_c} + f_a\mathbf{m}) \tag{D.31}$$

Since $\mathbf{m}$ and $\mathbf{E_c}$ are in the same direction with a field along one of the axes, we get

$$f_a = \frac{1}{\alpha_a} - \frac{E_c}{m} \tag{D.32}$$

Using equation D.25 for $\mathbf{E_c}$ and equation D.30 for $\mathbf{m}$ one arrives at

$$\mathbf{E_c} = \frac{\varepsilon^{\text{out}}}{\varepsilon^{\text{out}} + (1-\varepsilon^{\text{out}})A}\mathbf{E_0} \tag{D.33}$$

$$\mathbf{m} = \frac{a^2 c}{3}\frac{\varepsilon^{\text{out}}(\varepsilon^{\text{in}}-1)}{\varepsilon^{\text{out}} + (\varepsilon^{\text{in}}-\varepsilon^{\text{out}})A}\mathbf{E_0} \tag{D.34}$$

The relation between induced polarization/dipole moment, polarizabilty and applied field is in general given by

$$\mathbf{m} = \alpha\mathbf{E_0} \tag{D.35}$$

α_a from equation D.32 for a dielectric spheroid in vacuum is therefore given by

$$\alpha_a = \frac{a^2 c}{3}\frac{\varepsilon^{\text{in}}-1}{1+(\varepsilon^{\text{in}}-1)A} \tag{D.36}$$

Inserting equations D.34 and D.36 into equation D.32 one arrives at the following formulation for the reaction field factor f_a:

$$f_a = \frac{3}{abc}\frac{1+(\varepsilon^{\text{in}}-1)A}{\varepsilon^{\text{in}}-1} - \frac{\varepsilon^{\text{out}}E}{\varepsilon^{\text{out}}+(1-\varepsilon^{\text{out}})A}\frac{3(\varepsilon^{\text{out}}+(\varepsilon^{\text{in}}-\varepsilon^{\text{out}})A)}{a^2 c\varepsilon^{\text{out}}(\varepsilon^{\text{in}}-1)E} \tag{D.37}$$

$$= \frac{3}{a^2 c}\frac{A(1-A)(\varepsilon^{\text{out}}-1)}{\varepsilon^{\text{out}}+(1-\varepsilon^{\text{out}})A} \tag{D.38}$$

The derivation of f_c is analoguous and the reaction field tensor according to equationeqn:RF for an oblate spheroid takes the form

$$\mathbf{F} = \begin{pmatrix} \frac{3}{a^2 c}\frac{A_a(1-A_a)(\varepsilon^{\text{out}}-1)}{\varepsilon^{\text{out}}+(1-\varepsilon^{\text{out}})A_a} & 0 & 0 \\ 0 & \frac{3}{a^2 c}\frac{A_a(1-A_a)(\varepsilon^{\text{out}}-1)}{\varepsilon^{\text{out}}+(1-\varepsilon^{\text{out}})A_a} & 0 \\ 0 & 0 & \frac{3}{a^2 c}\frac{A_c(1-A_c)(\varepsilon^{\text{out}}-1)}{\varepsilon^{\text{out}}+(1-\varepsilon^{\text{out}})A_c} \end{pmatrix} \tag{D.39}$$

Appendix E

Integration of T^{E} over an oblate spheroidal cavity

For a simulation in a box with volume V_{box}, toroidal boundary conditions and an Ewald treatment of long-range Coulombics, the effective dipole-dipole interaction tensor is given by [142]

$$T_{ij}^{E} = T_{ij}^{E1} + T_{ij}^{E2} + T_{ij}^{E3} \tag{E.1}$$

with the k-space contribution

$$T_{ij}^{E1} = -\frac{4\pi}{V} \sum_{|k|\neq 0} \exp\left(-\frac{k^2}{4\eta^2}\right) \exp\left(-\mathrm{i}k_i r_i\right) \frac{k_i k_j}{k^2} \tag{E.2}$$

$$= -\frac{8\pi}{V} \sum_{|k|>0} \exp\left(-\frac{k^2}{4\eta^2}\right) \cos\left(k_i r_i\right) \frac{k_i k_j}{k^2} \qquad , \qquad k < k_c \tag{E.3}$$

the real-space contribution

$$T_{ij}^{E2} \quad = \quad \left[\mathrm{erfc}\left(\eta r\right) + \frac{2}{\sqrt{\pi}} \left(\eta r + \frac{2}{3}\eta^3 r^3\right) \exp\left(-\eta^2 r^2\right)\right] T_{ij}^{dd} = \rho(r) T_{ij}^{dd} \qquad , \qquad r < r_c \tag{E.4}$$

and the gaussian shielding term for compensation of the self-interaction

$$T_{ij}^{E3} = T_{ii}^{E3} = \frac{4\pi}{3} \left(\left(\frac{\eta}{\sqrt{\pi}}\right)^3 \exp\left(-\eta^2 r^2\right)\right) \qquad , \qquad r < r_c \tag{E.5}$$

with the dipole-dipole interaction tensor $\mathbf{T^{dd}}$ defined in equation (2.51) and a convergence parameter η that has no physical meaning and only balances the individual errors of the contributions.

In order to obtain an expression for $\tilde{\mathbf{T}}(0)$ in Ewald geometry we need to integrate equation (E.1) over the volume of the cavity chosen (oblate spheroid in our case). For this purpose we assume the spheroid to be centered at the origin, its minor semi-axis oriented along the z-direction and the major semi-axes lying in the xy-plane.

E.1 k-space contribution

$$\begin{aligned}\mathbf{TE1} = \tilde{\mathbf{T}}_{\mathbf{E1}}(0) &= \int_{V_{cav}} d\mathbf{r}\mathbf{T}_{\mathbf{E1}} \\ &= -\frac{8\pi}{V_{box}} \sum_{|k|>0} \exp\left[-\frac{k^2}{4\eta^2}\right] \int_{V_{cav}} d\mathbf{r} \cos\left[\mathbf{k}\cdot\mathbf{r}\right] \frac{|\mathbf{k}\rangle\langle\mathbf{k}|}{k^2} \qquad \text{(E.6)}\end{aligned}$$

(E.7)

The interaction energy $u_{DD} = \mu_i T_{ij} \mu_j$ of a dipole μ_i oriented along the x-axis with all images of another dipole μ_j is given by

$$\begin{aligned}\langle\mu_\mathbf{i}|\mathbf{TE1_x}|\mu_\mathbf{j}\rangle &= -\frac{8\pi}{V_{box}} \sum_{|k|>0} \exp\left[-\frac{k^2}{4\eta^2}\right] \int_{V_{cav}} d\mathbf{r} \cos\left[\mathbf{k}\cdot\mathbf{r}\right] \frac{\mu_{ix} k_x \langle\mathbf{k}||\mu_\mathbf{j}\rangle}{k^2} \\ &= -\frac{8\pi}{V_{box}} \sum_{|k|>0} \exp\left[-\frac{k^2}{4\eta^2}\right] \int_{V_{cav}} d\mathbf{r} \cos\left[\mathbf{k}\cdot\mathbf{r}\right] \frac{\mu_{ix} k_x \cdot \mathbf{e_k}}{k} |\mu_\mathbf{j}\rangle \qquad \text{(E.8)}\end{aligned}$$

It is therefore reasonable to identify

$$TE1_x = -\frac{8\pi}{V_{box}} \sum_{|k|>0} \exp\left[-\frac{k^2}{4\eta^2}\right] \frac{k_x}{k} \int_{V_{cav}} d\mathbf{r} \cos\left[\mathbf{k}\cdot\mathbf{r}\right] \mathbf{e_k} \qquad \text{(E.9)}$$

as the x-component of $\mathbf{TE1}$. The expression $\cos\left[\mathbf{k}\cdot\mathbf{r}\right]\mathbf{e_k}$ denotes a plane wave moving in direction $\mathbf{e_k}$. The integral expression in formula (E.9) can therefore be more easily represented by parametrizing the integral along the intersection of the plane cosine wave with the spheroid. In case the spheroid is centered at the origin and its semi-axes align with the cartesian axes, the area of intersection of a plane with this spheroid is given by [193]

$$A_{inter} = \frac{\pi a^2 b}{\kappa_t} \left(1 - \frac{\kappa^2}{\kappa_t^2}\right) \qquad \text{(E.10)}$$

where κ denotes the distance of the plane to the origin and $\kappa_t = \sqrt{a^2 n_x^2 + a^2 n_y^2 + b^2 n_z^2}$ with n_i denoting the normal vector components of the plane. κ_t equals the point where the plane wave front is tangential to the spheroid as can be easily seen by setting $\kappa = \kappa_t$ in equation (E.10) (area of intersection becomes zero). Using the above relation, (E.9) can then be written as

$$\begin{aligned} TE1_x &= -\frac{8\pi}{V_{box}} \sum_{|k|>0} \exp\left[-\frac{k^2}{4\eta^2}\right] \frac{k_x}{k} \int_{-\kappa_t}^{\kappa_t} d\kappa A_{inter} \cos\left[k\kappa\right] \\ &= -\frac{8\pi}{V_{box}} \sum_{|k|>0} \exp\left[-\frac{k^2}{4\eta^2}\right] \frac{k_x}{k} \frac{\pi a^2 b}{\kappa_t} \int_{-\kappa_t}^{\kappa_t} d\kappa \left(1 - \frac{\kappa^2}{\kappa_t^2}\right) \cos\left[k\kappa\right] \\ &= -\frac{32\pi^2 a^2 b}{V_{box}} \sum_{|k|>0} \exp\left[-\frac{k^2}{4\eta^2}\right] \frac{k_x}{k} \frac{\sin\left[k\kappa_t\right] - k\kappa_t \cos\left[k\kappa_t\right]}{k^3 \kappa_t^3} \\ &= -24\pi \frac{V_{sph}}{V_{box}} \sum_{|k|>0} \exp\left[-\frac{k^2}{4\eta^2}\right] \frac{k_x}{k} \frac{\sin\left[\tilde{k}\right] - \tilde{k}\cos\left[\tilde{k}\right]}{\tilde{k}^3} \end{aligned} \tag{E.11}$$

In the last line we substituted the spheroidal volume of our cavity $V_{sph} = \frac{4\pi}{3} a^2 b$ and substituted $k\kappa_t$ with $\tilde{k} = \sqrt{a^2 k_x^2 + a^2 k_y^2 + b^2 k_z^2}$, basically denoting the k-vector, deformed according to the semi-axes of the spheroid.

If we do the substitution

$$\begin{pmatrix} k_x \\ k_y \\ k_z \end{pmatrix} \mapsto \begin{pmatrix} a k_x \\ a k_y \\ b k_z \end{pmatrix} \tag{E.12}$$

in the sum of equation (E.11) we arrive at

$$\begin{aligned} TE1_x &= -24\pi \frac{V_{sph}}{V_{box}} \sum_{|k|>0} \exp\left[-\frac{\mathbf{k}B\mathbf{k}}{4\eta^2}\right] \frac{k_x}{a\sqrt{\mathbf{k}B\mathbf{k}}} \frac{\sin\left[k\right] - k\cos\left[k\right]}{k^3} \\ &= -24\pi \frac{V_{sph}}{V_{box}} \sum_{|k|\geq 0} \exp\left[-\frac{\mathbf{k}B\mathbf{k}}{4\eta^2}\right] \frac{k_x}{a\sqrt{\mathbf{k}B\mathbf{k}}} \frac{\sin\left[k\right] - k\cos\left[k\right]}{k^3} + 8\pi \frac{V_{sph}}{V_{box}} \end{aligned} \tag{E.13}$$

with the deforming matrix

$$B = \begin{pmatrix} \frac{1}{a^2} & 0 & 0 \\ 0 & \frac{1}{a^2} & 0 \\ 0 & 0 & \frac{1}{b^2} \end{pmatrix} \tag{E.14}$$

The last step in equation (E.13) can be performed, since the limit of the summand for $k->0$ equals 1/3. Switching to spherical coordinates this becomes

$$TE1_x = -24\pi \frac{V_{sph}}{V_{box}} \sum_{|k|\geq 0} \exp\left[-\frac{k^2\xi^2(\theta)}{4\eta^2}\right] \frac{\sin[\theta]\cos[\varphi]}{a\xi(\theta)} \frac{\sin[k]-k\cos[k]}{k^3} + 8\pi\frac{V_{sph}}{V_{box}} \tag{E.15}$$

with

$$\xi^2(\theta) = \frac{b^2\sin^2[\theta] + a^2\cos^2[\theta]}{a^2b^2} \tag{E.16}$$

The discrete sum in equation (E.15) can be transformed into a continuous integral by introducing a k-space density for the space of deformed k-vectors we are summing over. For a rectangular simulation box this density can be expressed as

$$\rho(k,\theta,\varphi) = \frac{1}{V_{state}} = \frac{1}{\frac{2\pi a}{L_x}\cdot\frac{2\pi a}{L_y}\cdot\frac{2\pi b}{L_z}} = \frac{V_{box}}{8\pi^3a^2b} = \frac{V_{box}}{6\pi^2V_{sph}} \tag{E.17}$$

Equation (E.15) expressed in a continuous integral then becomes

$$\begin{aligned} TE1_x &= -\frac{4}{\pi}\int_0^\infty dk \int_0^\pi d\theta \int_0^{2\pi} d\varphi \exp\left[-\frac{k^2\xi^2(\theta)}{4\eta^2}\right] \frac{\sin^2[\theta]\cos[\varphi]}{a\xi(\theta)} \frac{\sin[k]-k\cos[k]}{k} + 8\pi\frac{V_{sph}}{V_{box}} \\ &= 8\pi\frac{V_{sph}}{V_{box}} \end{aligned} \tag{E.18}$$

The integral in equation (E.18) is zero due to the periodicity in φ, stemming from the factor k_x in the original sum. The same argument holds for $TE1_y$:

$$TE1_x = TE1_y = 8\pi\frac{V_{sph}}{V_{box}} \tag{E.19}$$

The only case with non-vanishing integral is the z-component

$$
\begin{aligned}
TE1_z &= -\frac{4}{\pi}\int_0^\infty dk \int_0^\pi d\theta \int_0^{2\pi} d\varphi \exp\left[-\frac{k^2\xi^2(\theta)}{4\eta^2}\right] \frac{\sin[\theta]\cos[\theta]}{b\xi(\theta)} \frac{\sin[k]-k\cos[k]}{k} + 8\pi\frac{V_{sph}}{V_{box}} \\
&= -\frac{8}{b}\int_0^\infty dk \int_0^\pi d\theta \exp\left[-\frac{k^2\xi^2(\theta)}{4\eta^2}\right] \frac{\sin[\theta]\cos[\theta]}{\xi(\theta)} \frac{\sin[k]-k\cos[k]}{k} + 8\pi\frac{V_{sph}}{V_{box}} \\
&= -\frac{4}{b}\int_0^\pi d\theta \frac{\sin[\theta]\cos[\theta]}{\xi(\theta)} \int_{-\infty}^\infty dk \exp\left[-\frac{k^2\xi^2(\theta)}{4\eta^2}\right] \frac{\sin[k]-k\cos[k]}{k} + 8\pi\frac{V_{sph}}{V_{box}} \\
&= -\frac{4}{b}\int_0^\pi d\theta \frac{\sin[\theta]\cos[\theta]}{\xi(\theta)} \int_{-\infty}^\infty dk G(k)F(k) + 8\pi\frac{V_{sph}}{V_{box}}
\end{aligned} \tag{E.20}
$$

A multiplication in real space can be interpreted as a convolution in Fourier space. Therefore, by using the definitions

$$
\mathscr{F}[f(x)](k) = \frac{1}{\sqrt{2\pi}}\int_{-\infty}^\infty dx f(x)\exp[-\mathrm{i}kx] = F(k) \tag{E.21}
$$

$$
\mathscr{F}^{-1}[F(k)](x) = \frac{1}{\sqrt{2\pi}}\int_{-\infty}^\infty dx f(x)\exp[\mathrm{i}kx] = f(x) \tag{E.22}
$$

and the convolution theorem

$$
F(k)\cdot G(k) = \frac{1}{\sqrt{2\pi}}[f(r)\circ g(r)](k) \tag{E.23}
$$

the integral over k in (E.20) can be written as

$$
\begin{aligned}
&\int_{-\infty}^\infty dk G(k)F(k) = \int_{-\infty}^\infty dk \frac{1}{\sqrt{2\pi}}\mathscr{F}[f(r)\circ g(r)](k) \\
&= \frac{1}{2\pi}\int_{-\infty}^\infty dk \int_{-\infty}^\infty dr \exp[-\mathrm{i}kr]\int_{-\infty}^\infty d\tau f(\tau)g(r-\tau) \\
&= \frac{1}{2\sqrt{2\pi}}\int_{-\infty}^\infty dk \int_{-\infty}^\infty dr \exp[-\mathrm{i}kr]\int_{-1}^1 d\tau g(r-\tau)
\end{aligned} \tag{E.24}
$$

since $f(\tau)$ is the rectangle function

$$
\mathscr{F}[F(k)](\tau) = f(\tau)\begin{cases}\sqrt{\frac{\pi}{2}} & \text{for } |\tau|\le 1 \\ 0 & \text{otherwise}\end{cases} \tag{E.25}
$$

Employing the displacement law

$$\mathscr{F}\left[f(\alpha t+\beta)\right]=\frac{1}{\alpha}\exp\left[-\mathrm{i}\beta\omega\right]F\left(\frac{\omega}{\alpha}\right) \tag{E.26}$$

with $\alpha=-1$ and $\beta=1$ for $G(r-\tau)$, (E.27) can be further simplified to

$$\begin{aligned}
&\frac{1}{2\sqrt{2\pi}}\int_{-\infty}^{\infty}dk\int_{-\infty}^{\infty}dr\exp\left[-\mathrm{i}kr\right]\int_{-1}^{1}d\tau G(r-\tau)\\
&=\frac{1}{2\sqrt{2\pi}}\int_{-1}^{1}d\tau\int_{-\infty}^{\infty}dk\int_{-\infty}^{\infty}dr\exp\left[-\mathrm{i}kr\right]G(\tau)\exp\left[-\mathrm{i}\tau r\right]\\
&=\frac{1}{2\sqrt{2\pi}}\int_{-1}^{1}d\tau G(\tau)\int_{-\infty}^{\infty}dr\exp\left[\mathrm{i}\tau r\right]\int_{-\infty}^{\infty}dk\exp\left[-\mathrm{i}kr\right]\\
&=\pi\int_{-1}^{1}d\tau G(\tau)\int_{-\infty}^{\infty}dr\exp\left[\mathrm{i}\tau r\right]\delta(r)=\pi\int_{-1}^{1}d\tau G(\tau)=\pi\int_{-1}^{1}drG(r)
\end{aligned} \tag{E.27}$$

Where $G(r)$ is

$$G(r)=\mathscr{F}\left[\exp\left[-\frac{k^2\xi^2(\theta)}{4\eta^2}\right]\right](r)=\sqrt{2}\left(\frac{\eta}{\xi(\theta)}\right)\exp\left[-\frac{\eta^2r^2}{\xi^2(\theta)}\right] \tag{E.28}$$

Inserting that back into (E.20), the final expression for $TE1_z$ is given by

$$\begin{aligned}
TE1_z&=-\frac{4\sqrt{2}\pi}{b}\int_0^{\pi}d\theta\frac{\sin\left[\theta\right]\cos\left[\theta\right]}{\xi(\theta)}\int_{-1}^{1}dr\left(\frac{\eta}{\xi(\theta)}\right)\exp\left[-\frac{\eta^2r^2}{\xi^2(\theta)}\right]+8\pi\frac{V_{sph}}{V_{box}}\\
&=-\frac{4\sqrt{2}\pi}{b}\int_{-\pi}^{\pi}d\theta\frac{\sin\left[\theta\right]\cos\left[\theta\right]}{\xi(\theta)}\int_{0}^{1}dr\left(\frac{\eta}{\xi(\theta)}\right)\exp\left[-\frac{\eta^2r^2}{\xi^2(\theta)}\right]+8\pi\frac{V_{sph}}{V_{box}}\\
&=-\frac{4\sqrt{2}\pi}{b}\int_{-1}^{1}dt\frac{a^2b^2\eta t}{b^2+t^2(a^2-b^2)}\int_{0}^{1}dr\exp\left[-\frac{\eta^2a^2b^2r^2}{b^2+t^2(a^2-b^2)}\right]+8\pi\frac{V_{sph}}{V_{box}}\\
&=-\frac{8\sqrt{2}\pi}{b}\int_{0}^{1}dt\frac{a^2b^2\eta t}{b^2+t^2(a^2-b^2)}\int_{0}^{1}dr\exp\left[-\frac{\eta^2a^2b^2r^2}{b^2+t^2(a^2-b^2)}\right]+8\pi\frac{V_{sph}}{V_{box}}\\
&=-\frac{4a\sqrt{2\pi^3}}{(a+b)}S(\eta)+8\pi\frac{V_{sph}}{V_{box}}
\end{aligned} \tag{E.29}$$

with $S(\eta)$ given by

$$S(\eta)=\frac{1}{\sqrt{\pi}(a-b)}\left(\sqrt{\pi}\left(a\,\mathrm{erf}\left[\eta b\right]-b\,\mathrm{erf}\left[\eta a\right]\right)+ab\eta\left(\Gamma\left[0,\eta^2b^2\right]-\Gamma\left[0,\eta^2a^2\right]\right)\right) \tag{E.30}$$

The expression $S(\eta)$ is bounded by 1 and monotonically increasing for $\eta -> \infty$.

E.2 Real-space contribution

The integral over the real-space contribution to the Ewald dipole-dipole interaction tensor is zero due to the angular symmetry of the unmodified T-tensor $\mathbf{T^{dd}}$ (check formulas (2.51) and (4.12)):

$$\mathbf{TE2} = \tilde{\mathbf{T}}_{\mathbf{E2}}(0) = \int_{V_{cav}} d\mathbf{r}\mathbf{T}_{\mathbf{E2}} = 0 \tag{E.31}$$

and hence has no contribution to $\tilde{\mathbf{T}}_{\mathbf{E}}(0)$.

E.3 Self-interaction contribution

The integral over the shielding contribution has the analytical solution

$$\begin{aligned}
\mathbf{TE3} = \tilde{\mathbf{T}}_{\mathbf{E3}}(0) &= \int_{V_{cav}} d\mathbf{r}\mathbf{T}_{\mathbf{E3}}\mathbf{1} \\
&= \frac{4\pi}{3}\left(\operatorname{erf}\left[\eta b\right] - \frac{b}{\sqrt{a^2-b^2}}\exp\left[-\eta^2 a^2\right]\,\mathrm{erfi}\left[\eta\sqrt{a^2-b^2}\right]\right)\mathbf{1} \\
&= \frac{4\pi}{3}\left(\operatorname{erf}\left[\eta b\right] - \frac{2b}{\sqrt{\pi(a^2-b^2)}}\exp\left[-\eta^2 b^2\right]\,\mathrm{Dawson}\left[\eta\sqrt{a^2-b^2}\right]\right)\mathbf{1} \\
&= \frac{4\pi}{3}P(\eta)\mathbf{1}
\end{aligned} \tag{E.32}$$

where erfi(x) denotes the imaginary error function and Dawson(x) Dawson's integral. The second formulation is preferrable to the first since it is numerically more stable for spheroidal cavities with high eccentricities and large η. Same as $S(\eta)$, $P(\eta)$ is bounded to one and monotonically increasing for $\eta -> \infty$.

The overall components to the Ewald expression of $\tilde{\mathbf{T}}(0)$ can therefore be given as

$$\tilde{\mathbf{T}}_{\mathbf{E}\parallel}(0) = TE_x = TE_y = TE_\parallel = \frac{4\pi}{3}P(\eta) + 8\pi\frac{V_{sph}}{V_{box}} \tag{E.33}$$

$$\tilde{\mathbf{T}}_{\mathbf{E}\perp}(0) = TE_z = TE_\perp = \frac{4\pi}{3}P(\eta) - \frac{4a\sqrt{2\pi^3}}{(a+b)}S(\eta) + 8\pi\frac{V_{sph}}{V_{box}} \tag{E.34}$$

E.4 Limits of Slab Geometry

In the limit of an infinite major semi-axis, the spheroidal cavity is analogous to a slab geometry where the thickness and orientation of the slabs is defined by the minor semi-axis of the spheroid. The expressions for $\tilde{\mathbf{T}}_{\mathbf{E}}(0)$ in (E.33) and (E.34) then take the form

$$\lim_{x\to\infty} \tilde{\mathbf{T}}_{\mathbf{E}\parallel}(0) = \frac{4\pi}{3}\operatorname{erf}[\eta b] + 8\pi\frac{V_{sph}}{V_{box}} \tag{E.35}$$

$$\lim_{x\to\infty} \tilde{\mathbf{T}}_{\mathbf{E}\perp}(0) = 4\pi\operatorname{erf}[\eta b]\left(\frac{1}{3} - \frac{\sqrt{\pi a}}{a+b}\right) + \Gamma\left[0, \eta^2 b^2\right] + 8\pi\frac{V_{sph}}{V_{box}} \tag{E.36}$$

Appendix F

Voxel selection algorithm

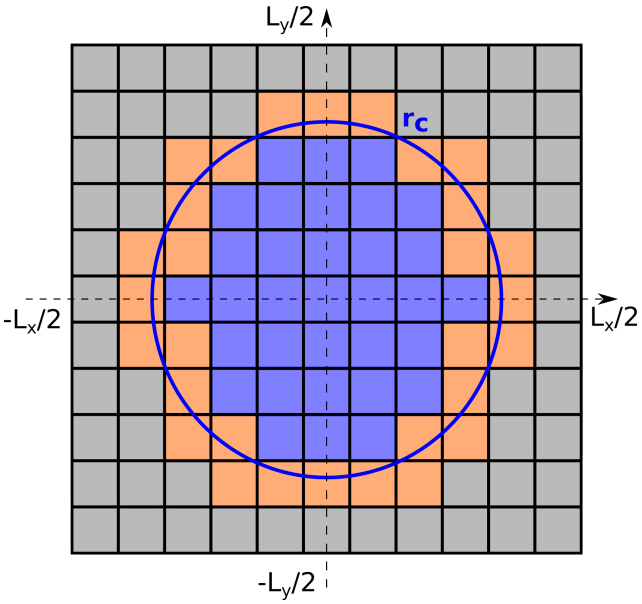

Figure F.1 – Classification whether a voxel lies completely inside (blue), partially inside (orange) and completely outside (grey) a sphere with radius r_c. The sketch represents a surface cut at $z = x_3 = 0$. It is assumed that the center of the sphere lies within the center of one voxel. It is not coinciding with voxel borders.

In order to calculate whether a 3D voxel defined by the volume

$$V = [x_1 - \Delta_1, x_1 + \Delta_1] \times [x_2 - \Delta_2, x_2 + \Delta_2] \times [x_3 - \Delta_3, x_3 + \Delta_3] \quad \text{(F.1)}$$

lies completely inside, partially inside or completely outside a sphere with radius r_c around the origin can be evaluated by minimizing the in-voxel distance

$$r^{\text{vox}}(u_1, u_2, u_3) = (x_1 + u_1\Delta_1)^2 + (x_2 + u_2\Delta_2)^2 + (x_3 + u_3\Delta_3)^2 = \sum_{i=1}^{3}(x_i + u_i\Delta_i)^2 \tag{F.2}$$

subject to the inequality constraints

$$\begin{aligned} u_i &\leq 1 \\ u_i &\geq -1 \end{aligned} \tag{F.3}$$

Here, we assume that the origin of the sphere lies in the center of a voxel - the central voxel - and not on the intersection of corners, edges or faces. A 2D cut at $z = x_3 = 0$ of this setup is sketched in figure F.1.

Applying the method of Lagrange multipliers the augmented objective function

$$L = \sum_{i=1}^{3}\left[(x_i + u_i\Delta_i)^2 + \lambda 1_i(x_i - 1) - \lambda 2_i(x_i + 1)\right] \tag{F.4}$$

can be formulated. Taking the partial derivatives

$$\begin{aligned} \frac{\partial L}{\partial x_i} &= 2\Delta_i(x_i + \Delta_i u_i) + \lambda 1_i - \lambda 2_i \\ \frac{\partial L}{\partial \lambda 1_i} &= x_i - 1 \\ \frac{\partial L}{\partial \lambda 2_i} &= -x_i - 1 \end{aligned} \tag{F.5}$$

returns three linear equations for three unknowns $u_i, \lambda 1_i, \lambda 2_i$. Above linear system of equations (LGS) is decoupled in every spatial coordinate and can thus be solved independently for every i. Three cases are possible. The first one $\lambda 1_i = \lambda 2_i$ assumes no constraint is active in this coordinate and above LGS gives the solution $u_i = -x_i/\Delta_i$. Since u_i is constrained to a magnitude smaller or equal to one by (F.3) and Δ_i represents half the length of a voxel, this solution is only valid if $x_i = 0$, in which case $u_i = 0$. The second case of either $\lambda 1_i = 0$ or $\lambda 2_i = 0$ being active returns either $u_i = -1$ or $u_i = 1$, meaning the minimal in-voxel radius coincides with the voxel borders in this

dimension. This means that in the present setup, the minimal in-voxel distance falls on the voxel corners, except for the coordinate planes where either x, y, or z equals zero. A voxel is therefore entirely inside the sphere, if all its corners are inside and entirely outside the sphere if all corners are outside. If neither of these cases apply, the voxel is partially inside. In the special case of one or two $x_i = 0$ equaling zero, these dimensions need to be excluded from (F.2) (i.e. $u_i = 0$) and the 3D corners need to be projected onto the corresponding 2D or 1D equivalents for voxel classification. The case where r_c lies entirely within the central voxel, i.e. $x_i = 0 \; \forall i$ is ignored since in this case the voxel resolution should simply be increased.

Finally, the third case leads to a plausible contradiction, meaning that not both constraints can be active at the same time. This case is irrelevant for the voxel classification. Since the voxel classification essentially comes down to a simple comparison of voxel corner distance to the radius r_c it can be very efficiently implemented.

Acknowledgement

Writing and finishing up this work would not have been possible without the direct and indirect support of many people over the better half of a decade. I am deeply grateful to you all.

Starting out I want to thank our "chief" Prof. Karsten Reuter for the opportunity to do my PhD in his group and the great and productive working environment he continuously manages to provide. Many thanks also go out to my direct supervisor Dr. Christoph Scheurer who by his calm nature and invaluable scientific input kept me motivated and on track, including prolonged therapeutic sessions in his office or the gardens of the FHI:) Thanks to both of you for your continued trust, advice, patience and time. You remain an inspiration to me both scientifically and personally and I consider it a great privilege to have been learning from both of you over all these years. I also want to thank our secretaries Ruth and recently Julia as well as our IT-admin Steffen for always helping out in case we needed something and even more for managing and maintaining the probably much larger pile of stuff we didn't even realize we needed. Many thanks to my office mates Christoph, Mitch, Hias, Xristoph, Sina in Munich and Hanna (and for a brief time Frederic, Limei and Yonghyuk) at the FHI for the great time together, all the chats, the laughs, the scientific and non-scientific discussions...and sometimes simply listening. In addition to the office crew, the same goes for all my other colleagues over the years, especially Carsten, Cristina, Christian, Jakob, Martin, Patrick, Simi and Simon R. as well as the many awesome new people I met in Berlin. Be it in Munich, Ulm, Berlin, Tallinn, Italy or Amsterdam, day or night, sober or not so sober, on the occasional stroll around the building working out in the park, singing (shouting) on a beer table or simply having a coffee (or recently tea:) I grew good friends with many of you and I hope we stay in touch for many years to come. You made coming to the office something to look forward too, even in times my project was not treating me too well. Special thanks also goes out to Hendrik, who with his unwaivering optimism and writing advice helped my alot when I was a little lost as well as Mitch who I learned a great deal from in the beginning. You were the big PhD brothers to look up to during my master thesis and just starting out as a PhD. Also many thanks to Mitch, Martin, Hias, Cristina and Simon W. for the great team-work and in the admin team and the workshop organization!

Finally I also have to thank my family and all my friends "out of the bubble", all of your love and friendship kept and keeps me sane and without you I never would have been able to finish this. Special shoutout goes to all my friends including Club der Menschen, Elve Monkeys, the old C32 crew, Pippo and Bine who would otherwise be missing in this list and the Berlin "expats" Anni, Liss and Nic who made (and make) my start in Berlin so much better. Finally finally my deepest thank

you goes to the people who know me the longest and have always been there for me: My mum, my dad and my brother Kili.

David Egger, December 2022

Bibliography

[1] V. Corradi, B. I. Sejdiu, H. Mesa-Galloso, H. Abdizadeh, S. Y. Noskov, S. J. Marrink, D. P. Tieleman, *Chemical Reviews* **2019**, *119*, 5775–5848.

[2] C. M. Davis, M. Gruebele, S. Sukenik, *Current Opinion in Structural Biology* **2018**, *48*, 23–29.

[3] D. M. Eckmann, R. P. Bradley, S. K. Kandy, K. Patil, P. A. Janmey, R. Radhakrishnan, *Current Opinion in Structural Biology* **2020**, *64*, 104–110.

[4] G. Enkavi, M. Javanainen, W. Kulig, T. Róg, I. Vattulainen, *Chemical Reviews* **2019**, *119*, 5607–5774.

[5] H. I. Ingólfsson, M. N. Melo, F. J. van Eerden, C. Arnarez, C. A. Lopez, T. A. Wassenaar, X. Periole, A. H. de Vries, D. P. Tieleman, S. J. Marrink, *Journal of the American Chemical Society* **2014**, *136*, 14554–14559.

[6] S. J. Marrink, V. Corradi, P. C. Souza, H. I. Ingólfsson, D. P. Tieleman, M. S. Sansom, *Chemical Reviews* **2019**, *119*, 6184–6226.

[7] M. Mathesh, D. A. Wilson, *Advanced Intelligent Systems* **2020**, *2*, 2000028.

[8] M. L. Verteramo, O. Stenström, M. M. Ignjatović, O. Caldararu, M. A. Olsson, F. Manzoni, H. Leffler, E. Oksanen, D. T. Logan, U. J. Nilsson, U. Ryde, M. Akke, *Journal of the American Chemical Society* **2019**, *141*, 2012–2026.

[9] Y. Wang, S. Sukenik, C. M. Davis, M. Gruebele, *The Journal of Physical Chemistry B* **2018**, *122*, 11762–11770.

[10] T. A. Wassenaar, H. I. Ingólfsson, R. A. Böckmann, D. P. Tieleman, S. J. Marrink, *Journal of Chemical Theory and Computation* **2015**, *11*, 2144–2155.

[11] P. Yang, *Nano Letters* **2021**, *21*, 5453–5456.

[12] M. Mendez, R. Partovi-Nia, I. Hatay, B. Su, P. Ge, A. Olaya, N. Younan, M. Hojeij, H. H. Girault, *Physical Chemistry Chemical Physics* **2010**, *12*, 15163–15171.

[13] D. Schaming, Z. Nazemi, P. Voyame, H. Deng, P. Y. Ge, M. A. Méndez, A. Olaya, F. Cortez, I. Hatay, H. Girault, *CHIMIA* **2011**, *65*, 356–356.

[14] A. N. J. Rodgers, S. G. Booth, R. A. W. Dryfe, *Electrochemistry Communications* **2014**, *47*, 17–20.

[15] J. Nieminen, I. Hatay, P. Ge, M. A. Méndez, L. Murtomäki, H. H. Girault, *Chemical Communications* **2011**, *47*, 5548–5550.

[16] M. Scanlon, X. Bian, H. Vrubel, V. Amstutz, K. Schenk, X. Hu, B. Liu, H. H. Girault, *Physical Chemistry Chemical Physics* **2013**, *15*, 2847–2857.

[17] B. Su, J.-P. Abid, D. J. Fermín, H. H. Girault, H. Hoffmannová, P. Krtil, Z. Samec, *Journal of the American Chemical Society* **2004**, *126*, 915–919.

[18] V. A. Turek, M. P. Cecchini, J. Paget, A. R. Kucernak, A. A. Kornyshev, J. B. Edel, *ACS Nano* **2012**, *6*, 7789–7799.

[19] R. A. W. Dryfe, *Physical Chemistry Chemical Physics* **2006**, *8*, 1869–1883.

[20] S. Ringe, N. G. Hörmann, H. Oberhofer, K. Reuter, *Chemical Reviews* **2021**, acs.chemrev.1c00675.

[21] P. Ren, J. Chun, D. G. Thomas, M. J. Schnieders, M. Marucho, J. Zhang, N. A. Baker, *Quarterly Reviews of Biophysics* **2012**, *45*, 427–491.

[22] J. D. Jackson, *Classical Electrodynamics*, 3rd edition, Wiley, **2012**.

[23] C. J. F. Boettcher, *Theory of Electric Polarization - Volume I*, 2nd edition, Elsevier, **1993**.

[24] J.-P. Hansen, I. R. McDonald, *Theory of simple liquids*, 3rd edition, Elsevier / Academic Press, **2007**.

[25] G. Malenkov, *Journal of Physics: Condensed Matter* **2009**, *21*, 283101.

[26] A. Nilsson, L. G. M. Pettersson, *Nature Communications* **2015**, *6*, 8998.

[27] D. J. Bonthuis, S. Gekle, R. R. Netz, *Physical Review Letters* **2011**, *107*, 166102.

[28] A. Ghoufi, F. Artzner, P. Malfreyt, *The Journal of Physical Chemistry B* **2016**, *120*, 793–802.

[29] L. Fumagalli, A. Esfandiar, R. Fabregas, S. Hu, P. Ares, A. Janardanan, Q. Yang, B. Radha, T. Taniguchi, K. Watanabe, G. Gomila, K. S. Novoselov, A. K. Geim, *Science* **2018**, *360*, 1339–1342.

[30] J.-F. Olivieri, J. T. Hynes, D. Laage, *The Journal of Physical Chemistry Letters* **2021**, *12*, 4319–4326.

[31] I. Benjamin, *Chemical Reviews* **1996**, *96*, 1449–1476.

[32] T.-D. Li, J. Gao, R. Szoszkiewicz, U. Landman, E. Riedo, *Physical Review B* **2007**, *75*, 115415.

[33] C. Schaaf, S. Gekle, *Physical Review E* **2015**, *92*, 032718.

[34] Y. Zhu, S. Granick, *Physical Review Letters* **2001**, *87*, 096104.

[35] Y. Levin, *Physical Review Letters* **2009**, *102*, 147803.

[36] B. C. Garrett, *Science* **2004**, *303*, 1146–1147.

[37] R. M. Noyes, *Journal of the American Chemical Society* **1962**, *84*, 513–522.

[38] M. V. Fedorov, A. A. Kornyshev, *Molecular Physics* **2007**, *105*, 1–16.

[39] D. V. Matyushov, *The Journal of Chemical Physics* **2014**, *140*, 224506.

[40] H.-B. Cui, K. Takahashi, Y. Okano, H. Kobayashi, Z. Wang, A. Kobayashi, *Angewandte Chemie* **2005**, *117*, 6666–6670.

[41] A. R. Haidar, A. K. Jonscher, *Journal of the Chemical Society Faraday Transactions 1: Physical Chemistry in Condensed Phases* **1986**, *82*, 3535–3551.

[42] C. Gerber, H. P. Lang, *Nature Nanotechnology* **2006**, *1*, 3–5.

[43] S. V. Kalinin, A. Gruverman, *Scanning Probe Microscopy: Electrical and Electromechanical Phenomena at the Nanoscale*, Springer Science & Business Media, **2007**.

[44] G. Gramse, I. Casuso, J. Toset, L. Fumagalli, G. Gomila, *Nanotechnology* **2009**, *20*, 395702.

[45] F. Deißenbeck, C. Freysoldt, M. Todorova, J. Neugebauer, S. Wippermann, *Physical Review Letters* **2021**, *126*, 136803.

[46] V. Ballenegger, J.-P. Hansen, *Europhysics Letters (EPL)* **2003**, *63*, 381–387.

[47] V. Ballenegger, J.-P. Hansen, *The Journal of Chemical Physics* **2005**, *122*, 114711.

[48] M. Neumann, O. Steinhauser, *Chemical Physics Letters* **1983**, *102*, 508–513.

[49] M. Neumann, *Molecular Physics* **1983**, *50*, 841–858.

[50] H. A. Stern, S. E. Feller, *The Journal of Chemical Physics* **2003**, *118*, 3401–3412.

[51] B. U. Felderhof, *Physica A: Statistical Mechanics and its Applications* **1979**, *95*, 572–580.

[52] B. U. Felderhof, *The Journal of Chemical Physics* **1977**, *67*, 493–500.

[53] C. Zhang, J. Hutter, M. Sprik, *The Journal of Physical Chemistry Letters* **2016**, *7*, 2696–2701.

[54] J. L. Aragones, L. G. MacDowell, C. Vega, *The Journal of Physical Chemistry A* **2011**, *115*, 5745–5758.

[55] D. Braun, S. Boresch, O. Steinhauser, *The Journal of Chemical Physics* **2014**, *140*, 064107.

[56] J. M. Caillol, D. Levesque, J. J. Weis, *The Journal of Chemical Physics* **1989**, *91*, 5555–5566.

[57] S. W. de Leeuw, J. W. Perram, E. R. Smith, J. S. Rowlinson, *Proceedings of the Royal Society of London. A. Mathematical and Physical Sciences* **1980**, *373*, 57–66.

[58] S. W. de Leeuw, J. W. Perram, E. R. Smith, J. S. Rowlinson, *Proceedings of the Royal Society of London. A. Mathematical and Physical Sciences* **1980**, *373*, 27–56.

[59] S. W. de Leeuw, J. W. Perram, E. R. Smith, J. S. Rowlinson, *Proceedings of the Royal Society of London. A. Mathematical and Physical Sciences* **1983**, *388*, 177–193.

[60] D. C. Elton, M.-V. Fernández-Serra, *The Journal of Chemical Physics* **2014**, *140*, 124504.

[61] P. H. Hünenberger, W. F. van Gunsteren, *The Journal of Chemical Physics* **1998**, *108*, 6117–6134.

[62] G. Lamoureux, E. Harder, I. V. Vorobyov, B. Roux, A. D. MacKerell, *Chemical Physics Letters* **2006**, *418*, 245–249.

[63] K. K. Mandadapu, J. A. Templeton, J. W. Lee, *The Journal of Chemical Physics* **2013**, *139*, 054115.

[64] M. Neumann, O. Steinhauser, *Chemical Physics Letters* **1983**, *95*, 417–422.

[65] M. Neumann, O. Steinhauser, *Chemical Physics Letters* **1984**, *106*, 563–569.

[66] M. Neumann, *The Journal of Chemical Physics* **1985**, *82*, 5663–5672.

[67] M. Neumann, *The Journal of Chemical Physics* **1986**, *85*, 1567–1580.

[68] M. Neumann, O. Steinhauser, G. S. Pawley, *Molecular Physics* **1984**, *52*, 97–113.

[69] G. Patey, D. Levesque, J. Weis, *Molecular Physics* **1982**, *45*, 733–746.

[70] M. Rami Reddy, M. Berkowitz, *Chemical Physics Letters* **1989**, *155*, 173–176.

[71] S. W. Rick, S. J. Stuart, B. J. Berne, *The Journal of Chemical Physics* **1994**, *101*, 6141–6156.

[72] D. van der Spoel, P. J. van Maaren, H. J. C. Berendsen, *The Journal of Chemical Physics* **1998**, *108*, 10220–10230.

[73] K. Watanabe, M. L. Klein, *Chemical Physics* **1989**, *131*, 157–167.

[74] C. Zhang, F. Gygi, G. Galli, *The Journal of Physical Chemistry Letters* **2013**, *4*, 2477–2481.

[75] D. V. Matyushov, *The Journal of Physical Chemistry B* **2021**, *125*, 8282–8293.

[76] M. Dinpajooh, D. V. Matyushov, *The Journal of Chemical Physics* **2016**, *145*, 014504.

[77] M. Dinpajooh, M. D. Newton, D. V. Matyushov, *The Journal of Chemical Physics* **2017**, *146*, 064504.

[78] S. Seyedi, D. R. Martin, D. V. Matyushov, *Journal of Physics: Condensed Matter* **2019**, *31*, 325101.

[79] M. Stengel, N. A. Spaldin, D. Vanderbilt, *Nature Physics* **2009**, *5*, 304–308.

[80] C. Zhang, M. Sprik, *Physical Review B* **2016**, *93*, 144201.

[81] C. Zhang, T. Sayer, J. Hutter, M. Sprik, *Journal of Physics: Energy* **2020**, *2*, 032005.

[82] P. A. Bopp, A. A. Kornyshev, G. Sutmann, *Physical Review Letters* **1996**, *76*, 1280–1283.

[83] A. A. Kornyshev, M. A. Vorotyntsev, *Surface Science* **1980**, *101*, 23–48.

[84] C. Schaaf, S. Gekle, *The Journal of Chemical Physics* **2016**, *145*, 084901.

[85] D. Frenkel, B. Smit, *Understanding molecular simulation: from algorithms to applications*, 2nd edition, Academic Press, **2007**.

[86] O. T. Unke, S. Chmiela, H. E. Sauceda, M. Gastegger, I. Poltavsky, K. T. Schütt, A. Tkatchenko, K.-R. Müller, *Chemical Reviews* **2021**, *121*, 10142–10186.

[87] P. Gkeka, G. Stoltz, A. Barati Farimani, Z. Belkacemi, M. Ceriotti, J. D. Chodera, A. R. Dinner, A. L. Ferguson, J.-B. Maillet, H. Minoux, C. Peter, F. Pietrucci, A. Silveira, A. Tkatchenko, Z. Trstanova, R. Wiewiora, T. Lelièvre, *Journal of Chemical Theory and Computation* **2020**, *16*, 4757–4775.

[88] P. S. Nerenberg, T. Head-Gordon, *Current Opinion in Structural Biology* **2018**, *49*, 129–138.

[89] W. L. Jorgensen, J. Tirado-Rives, *Journal of the American Chemical Society* **1988**, *110*, 1657–1666.

[90] G. Kaminski, W. L. Jorgensen, *The Journal of Physical Chemistry* **1996**, *100*, 18010–18013.

[91] G. A. Kaminski, R. A. Friesner, J. Tirado-Rives, W. L. Jorgensen, *The Journal of Physical Chemistry B* **2001**, *105*, 6474–6487.

[92] N. B. Kotadiya, A. Mondal, S. Xiong, P. W. M. Blom, D. Andrienko, G.-J. A. H. Wetzelaer, *Advanced Electronic Materials* **2018**, *4*, 1800366.

[93] S. Shi, L. Yan, Y. Yang, J. Fisher-Shaulsky, T. Thacher, *Journal of Computational Chemistry* **2003**, *24*, 1059–1076.

[94] Y. Zhang, H. Liu, S. Yang, R. Luo, H.-F. Chen, *Journal of Chemical Theory and Computation* **2019**, *15*, 6769–6780.

[95] W. D. Cornell, P. Cieplak, C. I. Bayly, I. R. Gould, K. M. Merz, D. M. Ferguson, D. C. Spellmeyer, T. Fox, J. W. Caldwell, P. A. Kollman, *Journal of the American Chemical Society* **1995**, *117*, 5179–5197.

[96] F. Jensen, *Introduction to computational chemistry*, 2nd edition, John Wiley & Sons, **2007**.

[97] F. London, *Zeitschrift für Physik* **1930**, *63*, 245–279.

[98] J. E. Lennard-Jones, *Proceedings of the Physical Society* **1931**, *43*, 461–482.

[99] A. Rahman, *Physical Review* **1964**, *136*, A405–A411.

[100] M. A. van-der-Hoef, P. A. Madden, *The Journal of Chemical Physics* **1999**, *111*, 1520–1526.

[101] X. Wang, S. Ramírez-Hinestrosa, J. Dobnikar, D. Frenkel, *Physical Chemistry Chemical Physics* **2020**, *22*, 10624–10633.

[102] W. L. Jorgensen, J. Chandrasekhar, J. D. Madura, R. W. Impey, M. L. Klein, *The Journal of Chemical Physics* **1983**, *79*, 926–935.

[103] G. Raabe, R. J. Sadus, *The Journal of Chemical Physics* **2011**, *134*, 234501.

[104] S. Plimpton, *Journal of Computational Physics* **1995**, *117*, 1–19.

[105] M. E. Tuckerman, *Statistical mechanics: theory and molecular simulation*, Oxford University Press, **2010**.

[106] M. P. Allen, D. J. Tildesley, *Computer simulation of liquids*, 2nd edition, Oxford University Press, **2017**.

[107] S. Nosé, *The Journal of Chemical Physics* **1984**, *81*, 511–519.

[108] W. G. Hoover, B. L. Holian, *Physics Letters A* **1996**, *211*, 253–257.

[109] A. P. Thompson, H. M. Aktulga, R. Berger, D. S. Bolintineanu, W. M. Brown, P. S. Crozier, P. J. in 't Veld, A. Kohlmeyer, S. G. Moore, T. D. Nguyen, R. Shan, M. J. Stevens, J. Tranchida, C. Trott, S. J. Plimpton, *Computer Physics Communications* **2022**, *271*, 108171.

[110] W. Shinoda, M. Shiga, M. Mikami, *Physical Review B* **2004**, *69*, 134103.

[111] G. J. Martyna, D. J. Tobias, M. L. Klein, *The Journal of Chemical Physics* **1994**, *101*, 4177–4189.

[112] M. Parrinello, A. Rahman, *Journal of Applied Physics* **1981**, *52*, 7182–7190.

[113] M. E. Tuckerman, J. Alejandre, R. López-Rendón, A. L. Jochim, G. J. Martyna, *Journal of Physics A: Mathematical and General* **2006**, *39*, 5629–5651.

[114] N. Bonnet, T. Morishita, O. Sugino, M. Otani, *Physical Review Letters* **2012**, *109*, 266101.

[115] H. A. Lorentz, *Annalen der Physik* **1881**, *248*, 127–136.

[116] P. Mazur, B. Nijboer, *Physica* **1953**, *19*, 971–986.

[117] S. R. De Groot, J. Vlieger, *Physica* **1965**, *31*, 125–140.

[118] S. R. de Groot, J. Vlieger, *Physica* **1965**, *31*, 254–268.

[119] D. J. Bonthuis, S. Gekle, R. R. Netz, *Langmuir* **2012**, *28*, 7679–7694.

[120] Y. R. Shen, V. Ostroverkhov, *Chemical Reviews* **2006**, *106*, 1140–1154.

[121] S. Nihonyanagi, T. Ishiyama, T.-k. Lee, S. Yamaguchi, M. Bonn, A. Morita, T. Tahara, *Journal of the American Chemical Society* **2011**, *133*, 16875–16880.

[122] S. Nihonyanagi, J. A. Mondal, S. Yamaguchi, T. Tahara, *Annual Review of Physical Chemistry* **2013**, *64*, 579–603.

[123] L. Eyges, *Annals of Physics* **1975**, *90*, 266–282.

[124] D. Kivelson, H. Friedman, *The Journal of Physical Chemistry* **1989**, *93*, 7026–7031.

[125] F. O. Raineri, H. L. Friedman, *The Journal of Chemical Physics* **1993**, *98*, 8910–8918.

[126] I. P. Omelyan, *Molecular Physics* **1996**, *87*, 1273–1283.

[127] G. B. Arfken, H. J. Weber, *Mathematical Methods for Physicists*, 6th edition, Academic Press, **2005**.

[128] P. Madden, D. Kivelson in *Advances in Chemical Physics*, (Eds.: I. Prigogine, S. A. Rice), John Wiley & Sons, Inc., Hoboken, NJ, USA, **2007**, pp. 467–566.

[129] R. L. Fulton, *The Journal of Chemical Physics* **1975**, *63*, 77–82.

[130] J. G. Kirkwood, *The Journal of Chemical Physics* **1934**, *2*, 351–361.

[131] P. J. Steinbach, B. R. Brooks, *Journal of Computational Chemistry* **1994**, *15*, 667–683.

[132] A. W. Appel, *SIAM Journal on Scientific and Statistical Computing* **1985**, *6*, 85–103.

[133] L. Greengard, V. Rokhlin, *Journal of Computational Physics* **1987**, *73*, 325–348.

[134] J. Barnes, P. Hut, *Nature* **1986**, *324*, 446–449.

[135] K. E. Schmidt, M. A. Lee, *Journal of Statistical Physics* **1991**, *63*, 1223–1235.

[136] T. Darden, D. York, L. Pedersen, *The Journal of Chemical Physics* **1993**, *98*, 10089–10092.

[137] J. W. Eastwood, R. W. Hockney, D. N. Lawrence, *Computer Physics Communications* **1980**, *19*, 215–261.

[138] V. Ballenegger, J. J. Cerda, O. Lenz, C. Holm, *The Journal of Chemical Physics* **2008**, *128*, 034109.

[139] H. Kornfeld, *Zeitschrift für Physik* **1924**, *22*, 27–43.

[140] J. Kolafa, J. W. Perram, *Molecular Simulation* **1992**, *9*, 351–368.

[141] H. G. Petersen, *The Journal of Chemical Physics* **1995**, *103*, 3668–3679.

[142] D. J. Adams, I. R. McDonald, *Molecular Physics* **1976**, *32*, 931–947.

[143] R. P. Bell, *Transactions of the Faraday Society* **1931**, *27*, 797.

[144] R. Kubo, *Journal of the Physical Society of Japan* **1957**, *12*, 570–586.

[145] D. Levesque, G. Patey, J. Weis, *Molecular Physics* **1977**, *34*, 1077–1091.

[146] G. N. Patey, J. P. Valleau, *The Journal of Chemical Physics* **1974**, *61*, 534–540.

[147] J. Barker, R. Watts, *Molecular Physics* **1973**, *26*, 789–792.

[148] D. J. Adams, E. M. Adams, G. J. Hills, *Molecular Physics* **1979**, *38*, 387–400.

[149] D. Adams, *Molecular Physics* **1980**, *40*, 1261–1271.

[150] D. Adams, E. Adams, *Molecular Physics* **1981**, *42*, 907–926.

[151] A. Ghoufi, A. Szymczyk, R. Renou, M. Ding, *EPL (Europhysics Letters)* **2012**, *99*, 37008.

[152] H. Zhu, A. Ghoufi, A. Szymczyk, B. Balannec, D. Morineau, *Physical Review Letters* **2012**, *109*, 107801.

[153] A. Schlaich, E. W. Knapp, R. R. Netz, *Physical Review Letters* **2016**, *117*, 048001.

[154] Z. Liu, T. Stecher, H. Oberhofer, K. Reuter, C. Scheurer, *Molecular Physics* **2018**, *116*, 3409–3416.

[155] S. Varghese, S. K. Kannam, J. S. Hansen, S. P. Sathian, *Langmuir* **2019**, *35*, 8159–8166.

[156] Y. Wu, H. L. Tepper, G. A. Voth, *The Journal of Chemical Physics* **2006**, *124*, 024503.

[157] Z. Liu, J. Timmermann, K. Reuter, C. Scheurer, *The Journal of Physical Chemistry B* **2018**, *122*, 770–779.

[158] S. H. Jamali, T. v. Westen, O. A. Moultos, T. J. H. Vlugt, *Journal of Chemical Theory and Computation* **2018**, *14*, 6690–6700.

[159] W. L. Jorgensen, D. S. Maxwell, J. Tirado-Rives, *Journal of the American Chemical Society* **1996**, *118*, 11225–11236.

[160] W. J. Orville-Thomas, *Internal rotation in molecules*, London, New York, Wiley-Interscience, **1974**.

[161] J. S. Rowlinson, B. Widom, *Molecular Theory of Capillarity*, Courier Corporation, **2013**.

[162] A. P. Willard, D. Chandler, *The Journal of Physical Chemistry B* **2010**, *114*, 1954–1958.

[163] F. Bresme, E. Chacón, P. Tarazona, *Physical Chemistry Chemical Physics* **2008**, *10*, 4704–4715.

[164] S. Senapati, M. L. Berkowitz, *Physical Review Letters* **2001**, *87*, 176101.

[165] E. Chacón, P. Tarazona, *Physical Review Letters* **2003**, *91*, 166103.

[166] M. Sega, B. Fábián, P. Jedlovszky, *The Journal of Chemical Physics* **2015**, *143*, 114709.

[167] C. A. Croxton, *Fluid Interfacial Phenomena*, Wiley, **1986**.

[168] S. W. Sides, G. S. Grest, M.-D. Lacasse, *Physical Review E* **1999**, *60*, 6708–6713.

[169] J. L. Rivera, C. McCabe, P. T. Cummings, *Physical Review E* **2003**, *67*, 011603.

[170] S. S. Jang, S.-T. Lin, P. K. Maiti, M. Blanco, W. A. Goddard, P. Shuler, Y. Tang, *The Journal of Physical Chemistry B* **2004**, *108*, 12130–12140.

[171] W. E. Lorensen, H. E. Cline, *ACM SIGGRAPH Computer Graphics* **1987**, *21*, 163–169.

[172] D. Muñoz-Santiburcio, D. Marx, *Physical Review Letters* **2017**, *119*, 056002.

[173] A. Chandra, M. E. Tuckerman, D. Marx, *Physical Review Letters* **2007**, *99*, 145901.

[174] M. E. Tuckerman, D. Marx, M. Parrinello, *Nature* **2002**, *417*, 925–929.

[175] Z. Liu, J. Timmermann, K. Reuter, C. Scheurer, **2018**, 8.

[176] J. W. Cooley, J. W. Tukey, *Mathematics of Computation* **1965**, *19*, 297–301.

[177] G. Cicero, J. C. Grossman, E. Schwegler, F. Gygi, G. Galli, *Journal of the American Chemical Society* **2008**, *130*, 1871–1878.

[178] A. C. Dávila López, T. Eggert, K. Reuter, N. G. Hörmann, *The Journal of Chemical Physics* **2021**, *155*, 194702.

[179] C.-Y. Lee, J. A. McCammon, P. J. Rossky, *The Journal of Chemical Physics* **1984**, *80*, 4448–4455.

[180] G. Tocci, L. Joly, A. Michaelides, *Nano Letters* **2014**, *14*, 6872–6877.

[181] J.-J. Velasco-Velez, C. H. Wu, T. A. Pascal, L. F. Wan, J. Guo, D. Prendergast, M. Salmeron, *Science* **2014**, *346*, 831–834.

[182] M. F. Toney, J. N. Howard, J. Richer, G. L. Borges, J. G. Gordon, O. R. Melroy, D. G. Wiesler, D. Yee, L. B. Sorensen, *Nature* **1994**, *368*, 444–446.

[183] J. N. Israelachvili, R. M. Pashley, *Nature* **1983**, *306*, 249–250.

[184] Z. Liu, PhD thesis, Technische Universität München, **2018**.

[185] T. Ishiyama, Y. Sato, A. Morita, *The Journal of Physical Chemistry C* **2012**, *116*, 21439–21446.

[186] N. A. Murugan, H. W. Hugosson, H. Ågren, *The Journal of Physical Chemistry B* **2008**, *112*, 14673–14677.

[187] D. K. Hore, D. S. Walker, G. L. Richmond, *Journal of the American Chemical Society* **2008**, *130*, 1800–1801.

[188] P. Jedlovszky, Á. Vincze, G. Horvai, *The Journal of Chemical Physics* **2002**, *117*, 2271–2280.

[189] G. Hantal, M. Darvas, L. B. Pártay, G. Horvai, P. Jedlovszky, *Journal of Physics: Condensed Matter* **2010**, *22*, 284112.

[190] L. B. Pártay, G. Hantal, P. Jedlovszky, Á. Vincze, G. Horvai, *Journal of Computational Chemistry* **2008**, *29*, 945–956.

[191] F. Aurenhammer, *ACM Computing Surveys* **1991**, *23*, 345–405.

[192] T. G. Scholte, *Physica* **1949**, *15*, 437–449.

[193] P. P. Klein, *Applied Mathematics* **2012**, *03*, 1634–1640.